



Technische Universität München

The present work was submitted to the Chair of Space Propulsion and Mobility

presented by

B.Sc. Fabiola Olsacher

Student ID No.: 03687016

Master Thesis

Investigation of TBC on CH₄/O₂ Rocket Combustion Engines

Munich, June 20, 2024

Supervising professor: Prof. Dr.-Ing. Chiara Manfretti

Assistant supervisor: Dr.-Ing. Rahand Dalshad

1st examiner: Prof. Dr.-Ing. Chiara Manfretti

Abstract

The propulsion system has always been a critical and challenging component of space flight, particularly due to the extreme thermal loads in the combustion chamber, which push the materials used to their limits. As a result, rocket engines require advanced cooling techniques. One option for reducing the thermal load on the engine are thermal barrier coatings, which possess a higher operating temperature than the combustion chamber liner and provide an insulating effect. These coatings are easy to apply without changing the engine design and help the chamber to cope with hot gas temperatures of up to 3500 K and temperature gradients of up to 1000 K/mm near the chamber wall [43]. These severe conditions make conventional physical property measurements difficult or impossible. In the case of capacitively cooled chambers in rocket engine design, the primary focus is on the heat flux from the combustion gases through the wall. Traditionally, heat flux determination has relied on empirical correlations and global calorimetric measurements. However, the inverse heat transfer method can be applied to reconstruct the heat flux from experimental data. In this case of a small in-space thruster using the propellants methane and oxygen.

This research aims to enhance the performance and protection of the rocket chamber by exploring the potential of two different thermal barrier coating systems. A ceramic system consisting of a YSZ/NiCrAlY and a metallic system composed of a Rene80/NiCuCrAl material were applied to a capacitively cooled copper chamber segment and hotfire experiments were conducted. The choice of coatings was based on an extensive research into suitable materials and manufacturing techniques. In order to evaluate the gathered data, an evaluation method based on an inverse heat conduction method combined with a conjugate gradient algorithm was implemented and validated. Both coatings showed a reduction in the heat flux distribution and the copper substrate temperatures were lowered, the amount of reduction depending on the load point. For a pressure point of 10 bar and an Ratio-Oxidizer-Fuel (ROF) of 3.1 the ceramic coating reduces the heat flux on average over the length of the coated segment of about 14.6% and the metallic coating of 11.2%. Suggestions for further investigation are given.

Kurzfassung

Das Antriebssystem ist seit jeher eine kritische und anspruchsvolle Komponente der Raumfahrt, insbesondere aufgrund der extremen thermischen Belastungen in der Brennkammer, die die verwendeten Materialien an ihre Grenzen bringen. Daher benötigen Raketentriebwerke fortschrittliche Kühlmechanismen und Kombinationen dieser. Eine Möglichkeit, die thermische Belastung des Triebwerks zu reduzieren, sind Wärmedämmschichten, die eine höhere Betriebstemperatur als das Brennmaterial aufweisen und isolierend wirken. Diese Beschichtungen lassen sich leicht aufbringen, ohne dass die Konstruktion des Antriebs großartig geändert werden muss, Sie helfen der Kammer, mit Heißgastemperaturen von bis zu 3500 K und Temperaturgradienten von bis zu 1000 K/mm in der Nähe der Kammerwand zurechtzukommen [43]. Diese schwierigen Bedingungen machen herkömmliche Messungen physikalischer Eigenschaften schwierig oder unmöglich. Bei kapazitiv gekühlten Kammern in Raketentriebwerken liegt das Hauptaugenmerk auf dem Wärmestrom der Verbrennungsgase zur und dann durch die Wand. Traditionell stützt sich die Bestimmung des Wärmestroms auf empirische Korrelationen und globale kalorimetrische Messungen. Die Methode der inversen Wärmeübertragung ermöglicht nun jedoch eine lokale Analyse des Wärmestroms anhand von experimentellen Daten, was die Klassifizierung von Wärmedämmschichten für ein kleines Weltraumtriebwerk mit den Treibstoffen Methan und Sauerstoff ermöglicht.

Ziel dieser Forschungsarbeit ist es, die Leistung und den Schutz der Raketenkammer zu verbessern, indem das Potenzial von zwei verschiedenen Wärmedämmschichtsystemen untersucht wird. Ein keramisches System, bestehend aus YSZ/NiCrAlY, und ein metallisches System, bestehend aus einem Rene80/NiCuCrAl-Material, wurden auf ein kapazitiv gekühltes Kupferkammersegment aufgebracht und experimentelle Daten wurden gesammelt. Die Wahl der Beschichtungen beruhte auf einer umfassenden Untersuchung geeigneter Materialien und Herstellungsverfahren. Zur Auswertung der gesammelten Daten wurde eine Bewertungsmethode auf der Grundlage einer inversen Wärmeleitungsmethode in Kombination mit einem konjugierten Gradientenalgorithmus implementiert und validiert. Beide Beschichtungen zeigten eine Verringerung der Wärmestromverteilung und die Temperaturen des Kupfersubstrats wurden gesenkt, wie viel hängt vom jeweiligen Lastpunkt ab. Bei einem Druckpunkt von 10 bar und einer ROF von 3.1 verringert die keramische Beschichtung den Wärmestrom im Durchschnitt über die Länge des beschichteten Segments um etwa 14.6% und die metallische Beschichtung um 11.2%. Es werden Vorschläge für weitere Untersuchungen gemacht.

Acknowledgements

I would like to thank the Institute of Space Mobility and Propulsion, Prof. Dr. C. Manfretti, and the members of DeltaOrbit for making this work possible.

Further thanks go to the cooperation with the Technical University of Braunschweig and especially to Dr. T. Fiedler, who not only took on the challenge of installing the metallic thermal barrier coating, but was also always open for discussion and questions.

I am grateful to rhv-Technik, especially C. Hofmann and M. Dauner, for being open-minded and supporting this project and supplying the professionally applied ceramic coating.

A big thank you to my friend Maren, who has been by my side through the good times and the bad and made me laugh even when I didn't feel like it.

Another thank you goes to my friend David, a true motivational speaker and companion.

My deepest appreciation goes to my family, without your support these studies would never have been possible in this form. Thank you for believing in me.

Thank you for following your dreams and fighting for them. Reaching for the stars.

Contents

Abstract	I
Kurzfassung	III
Acknowledgements	V
List of Figures	I
List of Tables	V
List of Symbols	VII
1. Introduction	1
1.1. Motivation and Scope of the Thesis	1
1.2. Structure of the Thesis	1
2. State of the Art	3
2.1. TBC Applications	3
2.1.1. Turbomachinery	3
2.1.2. Rocketry	3
2.2. Historical Background of TBCs	4
2.3. TBC Structure	4
3. Basic Principles	7
3.1. Basics of Rocket Propulsion	7
3.2. Thrust Chamber Design	8
3.3. Heat Transfer in Rocket Engines	8
3.3.1. Performance and Heat	9
3.3.2. Adiabatic Wall Temperature	10
3.3.3. Convective Heat Transfer	11
3.3.4. Conductive Heat Transfer	12
3.3.5. Measurement Methods	12
3.4. Cooling Methods	13
3.4.1. Capacitive Cooling	13
3.4.2. Thermal Barrier Coatings	14
4. Experimental Setup	17
4.1. Fluid Supply System	18

4.2. Combustion Chamber	20
4.2.1. Injector	21
4.2.2. Igniter	21
4.3. Combustion Chamber Sensors	21
4.4. Testing Procedure and Testplan	23
4.4.1. Test Configurations	25
4.5. Data Post-Processing	27
5. Thermal Barrier Coatings	29
5.1. Guidelines for Coating Selection	29
5.2. Area of Application	30
5.3. Ceramic Materials	30
5.3.1. Top Coats for a Ceramic TBC System	31
5.3.2. Bond Coats for a Ceramic TBC System	31
5.4. Metallic Materials	32
5.4.1. Top Coats for a Metallic TBC System	32
5.4.2. Bond Coats for a Metallic TBC System	33
5.5. Manufacturing Techniques	33
5.5.1. Ceramic Coating Techniques	34
5.5.2. Metallic Coating Techniques	35
5.6. Failure mechanisms	36
5.7. Thermal Simulation	37
5.7.1. Coating Modelling	38
5.7.2. Convective Heat Transfer Modelling	41
5.7.3. Heat Transfer Coefficient Correlation Comparison	44
5.7.4. Coating Thickness Analysis	45
5.8. Coating Manufacturing Process	47
5.8.1. Ceramic Coating Approach	48
5.8.2. Metallic Coating Approach	49
6. Inverse Heat Conduction Method	53
6.1. Basic Concepts of Inverse Heat Transfer Problems	53
6.2. Conjugate Gradient Method Optimization	54
6.3. Implementation Overview	56
6.4. Direct Problem Implementation	57
6.4.1. Data Input	58
6.4.2. Numerical Physical Model Implementation	59
6.4.3. Boundary Conditions	59
6.5. Conjugate Gradient Method Implementation	60
6.5.1. Conjugate Gradient Validation Process	60
6.5.2. Iterative First Guesses	61
6.5.3. Sensitivity Matrix	62
6.5.4. Stopping Criteria	64

6.6. Inverse Heat Conduction Method Sensitivity Analysis	65
6.6.1. Spatial Discretization	66
6.6.2. Temporal Discretization	68
6.6.3. Sensitivity Matrix Parameter Analysis	71
6.6.4. Results in Case of Missing Throat Sensors	76
6.6.5. Initial Heat Flux Distribution Conditions	77
6.7. Mesh Study	80
7. Results	83
7.1. Thermal Barrier Coating Visual Inspection	83
7.1.1. Ceramic Thermal Barrier Coating	83
7.1.2. Metallic Thermal Barrier Coating	85
7.2. Temperature Distribution	89
7.2.1. Axial Profiles	89
7.2.2. Expected versus real Temperature Reduction	91
7.2.3. Circumferential Profiles	92
7.3. Specific Heat Flux Evaluation	93
7.3.1. 5 bar Tests	94
7.3.2. 10 bar Tests	98
7.3.3. 12 bar Tests	101
7.3.4. 15 bar Tests	104
7.3.5. Summarized Observations	104
7.3.6. Relative Heat Flux Comparison	105
7.3.7. Temporal Heat Flux Evaluation	108
7.4. Load Point Evaluation	110
7.4.1. ROF, Mass Flow Rate and Chamber Pressure	111
7.4.2. Pressure Drop over Injector	113
7.5. Performance Analysis	113
7.5.1. Evaluation Process	113
7.5.2. Integral Heat Load Evaluation	115
7.5.3. Characteristic Velocity	117
7.5.4. Combustion Efficiency	118
7.5.5. Specific Impulse	119
7.6. Inverse Heat Conduction Method Error Analysis	120
7.6.1. Thermocouple Accuracy	120
7.6.2. Thermocouple Precision	121
7.6.3. Thermocouple Positioning	121
7.6.4. Material Properties	124
7.6.5. Inverse Method Error	126
7.6.6. Total Error	126
8. Conclusion and Outlook	131
8.1. Conclusion	131
8.2. Outlook	132

Bibliography	133
A. Uncoated Configuration IHCM evaluation	137
B. Ceramic Configuration IHCM evaluation	147
C. Metallic Configuration IHCM evaluation	157

List of Figures

2.1. TBC structure with top and bond coat	5
3.1. Heat loss across a rocket engine [43]	8
3.2. Typical axial heat transfer rate in a rocket engine [43]	9
3.3. Visualization of an adiabatic wall [21]	10
3.4. Visualization of an adiabatic wall [21]	12
3.5. Wall temperature for a regeneratively cooled rocket with and without TBC [16]	14
4.1. Exemplary Hotfire Test Setup	17
4.2. Test Setup Flowchart	18
4.3. Combustion chamber setup from left	20
4.4. Geometrical dimensions of the combustion chamber	21
4.5. Thermocouple nomenclature and layout	22
4.6. Thermocouple positions at the first plane of CC1 facing the injector	22
4.7. Generic test sequence example with IHCM, mass flow and ROF evaluation duration	24
4.8. Comparison of the uncoated hotfire flames at 10 <i>bar</i> at night and for low and high ROF	25
4.9. Comparison of the metallic hotfire flames at 10 <i>bar</i> and ROF 3.5 (last test)	26
5.1. Microstructure of PS and EB-PVD technique [16]	35
5.2. Thermal conductivity and specific heat capacity of copper from [6]	39
5.3. Thermal conductivity and specific heat capacity of Yttrium Stabilized Zirconia (YSZ) from [35]	39
5.4. Thermal conductivity and specific heat capacity of NiCrAlY from [1]	40
5.5. Thermal conductivity and specific heat capacity of Rene80 from [9]	40
5.6. Thermal conductivity and specific heat capacity of NiCuCrAl from [9]	40
5.7. Comparison of the Sinyarev and Bartz Heat Transfer Coefficient (HTC) correlation with a 12 <i>bar</i> and $ROF = 3.1$ load point heat flux	44
5.8. Temperature profiles of the copper surface along the z -axis for different TBC systems with a focus on CC1	45
5.9. Radial temperature profiles of TBC and copper for different TBC systems with a focus on the interface	46
5.10. Masking of the segment, after sand blasting and after bond coat application	48
5.11. High-Velocity-Oxygen-Fuel Method (HVOF) robot setup with rotary table and robot guiding in x -direction from [45]	50
5.12. First pilot test from [45]	51
5.13. Effect of heat treatment on third pilot test from [45]	52

6.1. Inverse heat conduction algorithm workflow	56
6.2. Filtered temperature data of TC-CC1-1a from run 10	58
6.3. Conjugate Gradient Method (CGM) validation setup and results	60
6.4. CGM first guess heat flux	61
6.5. Sensitivity Matrix (SM) with start and end domain point and all available sensors	63
6.6. SM comparison for the different test cases for a different amount of sensor positions	63
6.7. Optimization point configurations from low to high spatial resolution	67
6.8. Optimized heat flux and absolute error for Sinyarev and uncoated data	67
6.9. Optimized heat flux and absolute error for ceramic and metallic data	68
6.10. Comparison of heat flux distribution for last time step for uncoated hotfire	69
6.11. Comparison of heat flux distribution for last time step for ceramic hotfire	70
6.12. Comparison of heat flux distribution for last time step for metallic hotfire	70
6.13. Comparison of the magnitude deviation of ϵ on the Heat Flux (HF)	72
6.14. SM reference HF evaluation	73
6.15. Overview of converged heat fluxes for each K_t	74
6.16. Zoom in on the cylindrical part solution of the SM time factor analysis with the legend of Figure 6.15	74
6.17. SM evaluation time comparison	75
6.18. Comparison of results found by the CGM with and without measurement positions missing in the critical throat area	76
6.19. Uncoated run Nr. 10 no sensors in throat with altered material model	77
6.20. Comparison of effect on \dot{q} different first heat flux guesses	78
6.21. Comparison of effect on \dot{q} different first heat flux guesses	79
6.22. Percental temperature difference to the finest mesh over every sensor	80
6.23. Investigated meshes for mesh study from coarsest to finest	81
7.1. Ceramic TBC condition before and after hotfires	83
7.2. Ceramic TBC thickness close-up before and after hotfire	84
7.3. Metallic TBC condition of inlet and outlet before post-processing	85
7.4. Metallic TBC condition before and after hotfires	86
7.5. Metallic TBC thickness close-up before and after hotfire	86
7.6. Metallic TBC crack condition before and after hotfires	87
7.7. Metallic TBC delamination condition before and after hotfires	88
7.8. Metallic TBC crack condition at outlet before and after hotfires	88
7.9. Axial temperature profile of uncoated case at the condition with the highest temperatures	89
7.10. Axial temperature profile of ceramic case at the condition with the highest temperatures	90
7.11. Axial temperature profile of metallic case at the condition with the highest temperatures	90
7.12. Axial temperature profile comparison at 3 s at 1 mm from the wall for run 9	91
7.13. Axial temperature difference for coated versus uncoated for experimental and simulated data at 3 s at 1 mm from the wall in the coated CC1 segment and their deviation in prediction	92
7.14. Circumferential temperatures at the condition with the highest temperatures	93
7.15. Heat flux comparison of the test configurations at 5 bar and target ROF of 2.7	95

7.16. Heat flux comparison of the test configurations at 5 <i>bar</i> and target ROF of 3.1	96
7.17. Heat flux comparison of the test configurations at 5 <i>bar</i> and target ROF of 3.5	97
7.18. Heat flux comparison of the test configurations at 10 <i>bar</i> and target ROF of 2.7	98
7.19. Heat flux comparison of the test configurations at 10 <i>bar</i> and target ROF of 3.1	99
7.20. Heat flux comparison of the test configurations at 10 <i>bar</i> and target ROF of 3.5	100
7.21. Heat flux comparison of the test configurations at 12 <i>bar</i> and target ROF of 2.7	101
7.22. Heat flux comparison of the test configurations at 12 <i>bar</i> and target ROF of 3.1	102
7.23. Heat flux comparison of the test configurations at 12 <i>bar</i> and target ROF of 3.5	103
7.24. Heat flux comparison of the test configurations at 15 <i>bar</i> and target ROF of 3.1	104
7.25. Heat flux evolution of uncoated test at 10 <i>bar</i> and target ROF of 3.1	108
7.26. Heat flux evolution of ceramic test at 10 <i>bar</i> and target ROF of 3.1	109
7.27. Heat flux evolution of metallic test at 10 <i>bar</i> and target ROF of 3.1	110
7.28. Visualized load point evaluation of a coated (ceramic) hotfire run 15 with a target pressure of 12 <i>bar</i> and target ROF of 3.1	111
7.29. Visualized pressure drop of the ceramic hotfires	113
7.30. \dot{Q}_{CC} over the whole combustion chamber length for p_{cc} and ROF for all tests and all configurations	115
7.31. \dot{Q}_{CC1} over the first segment CC1 for p_{cc} and ROF for all tests and all configurations . . .	115
7.32. c^* over p_{cc} and c^* over ROF for all tests and all configurations	117
7.33. η_{c^*} over p_{cc} and η_{c^*} over ROF for all tests and all configurations	118
7.34. Vacuum Isp over p_{cc} and Isp over ROF for all tests and all configurations	119
7.35. Relative heat flux error due to a 1 K Thermocouple (TC) accuracy error	121
7.36. Relative heat flux error due to a $\Delta r = 0.5mm$ TC positioning error for the uncoated case over time	122
7.37. Relative heat flux error due to a $\Delta r = 0.5mm$ TC positioning error for the ceramic case over time	123
7.38. Relative heat flux error due to a $\Delta r = 0.5mm$ TC positioning error for the metallic case over time	123
7.39. Relative heat flux error due to a material uncertainties of $\Delta\alpha = 10\%$ for the uncoated case over time	124
7.40. Relative heat flux error due to a material uncertainties of $\Delta\alpha = 10\%$ for the ceramic case over time	124
7.41. Relative heat flux error due to a material uncertainties of $\Delta\alpha = 10\%$ for the metallic case over time	125
7.42. Summed relative heat flux error uncoated case	127
7.43. Relative heat flux error contributions uncoated case	127
7.44. Summed relative heat flux error ceramic case	128
7.45. Relative heat flux error contributions ceramic case	128
7.46. Summed relative heat flux error metallic case	129
7.47. Relative heat flux error contributions metallic case	129

List of Tables

4.1. Orifice parameters	19
4.2. Orifice upstream pressures in [bar]	19
4.3. Sensor coordinates and numbers in [mm] for the uncoated and ceramic test case for CC1	23
4.4. Sensor coordinates in [mm] for the uncoated and ceramic test case for CC3	23
4.5. Load point overview for test configurations	24
4.6. Test details for uncoated configuration	26
4.7. Test details for ceramic configuration	27
4.8. Test details for metallic configuration	27
4.9. Excluded sensors per hotfire case	28
5.1. Operating conditions for rocket engines, gas turbines from and the DO engine	30
5.2. Main features of ceramic coating techniques PS and EB-PVD	35
5.3. Thickness variation	38
5.4. Original and from Silvestri optimized Sinyarev HTC correlation parameter	43
5.5. Original and from Silvestri optimized Bartz HTC correlation parameter	44
5.6. Important metallic coating material parameter	49
5.7. HVOF feeding and process settings	50
6.1. First heat flux guess and sensitivity matrix heat flux curves [MW/m^2]	61
6.2. Spatial discretization decision matrix	69
6.3. Default parameter of the SM analysis	71
6.4. Results of the SM analysis for ϵ	71
6.5. Results of the SM analysis for \dot{q}_{sm}	72
6.6. Results of the SM analysis for K_t	73
6.7. Mesh study parameters	80
7.1. Overview of the test durations for 5 bar and ROF 2.7	95
7.2. Overview of the test durations for 5 bar and ROF 3.1	96
7.3. Overview of the test durations for 5 bar and ROF 3.5	97
7.4. Overview of the test durations for 10 bar and ROF 2.7	98
7.5. Overview of the test durations for 10 bar and ROF 3.1	99
7.6. Overview of the test durations for 10 bar and ROF 3.5	100
7.7. Overview of the test durations for 12 bar and ROF 2.7	101
7.8. Overview of the test durations for 12 bar and ROF 3.1	102
7.9. Overview of the test durations for 12 bar and ROF 3.5	103
7.10. Relative heat flux comparison of the 5 bar tests in percent	106

7.11. Relative heat flux comparison of the 10 <i>bar</i> tests in percent	106
7.12. Relative heat flux comparison of the 12 <i>bar</i> tests in percent	107

List of Symbols

General Symbols

\dot{m}	[kg/s]	Mass flow
\dot{q}	[W/m ²]	Heat flux
\dot{Q}	[W]	Integral heat flux
A	[m ²]	Area
c^*	[m/s]	Characteristic velocity
C_d	[-]	Discharge coefficient
c_p	[J/kgK]	Specific heat capacity
d	[m]	Diameter
F	[N]	Thrust
g_0	[m/s ²]	Standard gravitational acceleration
h	[J/kg]	Specific enthalpy
H	[J]	Enthalpy
I_{sp}	[s]	Specific impulse
L^*	[m]	Characteristic length
M	[g/mol]	Molar mass
Ma	[-]	Mach number
Nu	[-]	Nusselt number
p	[bar]	Pressure
Pr	[-]	Prandtl number
r	[-]	Recovery factor
r	[m]	Radius
Re	[-]	Reynolds number
ROF	[-]	Ratio oxidiser/fuel

T	[K]	Temperature
t	[s]	Time
t_{tbc}	[m]	TBC thickness
t_w	[m]	Wall thickness
z	[m]	Axial combustion chamber length

Greek Symbols

α	[W/m ² K]	Heat transfer coefficient
η	[-]	Efficiency
κ	[-]	Heat capacity ratio
λ	[W/mK]	Thermal conductivity
μ	[Pas]	Dynamic viscosity
ρ	[kg/m ³]	Density

Subscripts

\square_{avg}	Averaged value
\square_{aw}	Adiabatic wall temperature
\square_{calc}	Calculated value
\square_{cc}	Combustion chamber
\square_{cer}	Ceramic configuration
\square_{con}	Converging nozzle section
\square_c	Combustion
\square_{div}	Diverging nozzle section
\square_{eff}	Effective
\square_{end}	End of domain
\square_{ex}	Experimental or real value
\square_e	Exhaust
\square_{fu}	Fuel
\square_f	Final
\square_{hg}	Hot gas
\square_h	Hydraulic

\square_{ig}	Ignition
\square_{inv}	Inverse method
\square_i	Initial
\square_{met}	Metallic configuration
\square_{ox}	Oxidizer
\square_{rms}	Root mean square
\square_{sm}	Sensitivity matrix
\square_{std}	Standard deviation
\square_{th}	Nozzle throat
\square_{tot}	Total or summed value
\square_{unc}	Uncoated configuration
\square_w	Wall temperature
\square_{inf}	Ambient pressure

Abbreviations

APS	Atmospheric-Plasma-Spraying Method.
CC	Combustion Chamber.
CEA	Chemical Equilibrium with Applications.
CGM	Conjugate Gradient Method.
DO	DeltaOrbit.
FEM	Finite Element Method.
HF	Heat Flux.
HTC	Heat Transfer Coefficient.
HVOF	High-Velocity-Oxygen-Fuel Method.
IHCM	Inverse Heat Conduction Method.
IHTM	Inverse Heat Transfer Method.
IHTP	Inverse Heat Transfer Problem.
NASA	National Aeronautics and Space Administration.
ODE	Ordinary Differential Equation.
PDE	Partial Differential Equation.
RMS	Root Mean Square.
ROF	Ratio-Oxidizer-Fuel.
SM	Sensitivity Matrix.
TBC	Thermal Barrier Coating.
TC	Thermocouple.
TCA	Thrust Chamber Assembly.
TUM	Technical University of Munich.
YSZ	Yttrium Stabilized Zirconia.

1. Introduction

This chapter delivers insights into the motivation propelling this thesis and its scope of what was achieved, followed by an overview of the structure of this work.

1.1. Motivation and Scope of the Thesis

The Chair of Space Propulsion and Mobility, more specific the Technical University of Munich (TUM) VentureLab spin-off DeltaOrbit (DO), is currently developing a methane-oxygen propulsion system for in-space applications, featuring an actively cooled combustion chamber. The nominal vacuum thrust of 500 N is to be achieved at a combustion chamber pressure of 12 bar with a oxidizer-to-fuel ratio of 3.1. The propellant mass flow rates generated at this design load point are significant limiting factors for the engine's cooling capacity. Initial experiments with a capacitively cooled copper chamber indicated that the integral heat loads to the chamber wall might exceed the system's cooling capacities. As a result, reducing the total length of the thruster or L^* has been considered. However, this solution compromises the thruster's performance and efficiency, as chemical reactions require sufficient residence time. Another approach is to select moderate operating points, which also affects performance.

To address these challenges, Thermal Barrier Coating (TBC) present a promising option. The coatings are applied on the inside surface of the combustion chamber, providing thermal isolation from the hot gas stream. By applying a thin protective layer to the hot surface, these ceramic or metallic-based coatings, already successfully used in gas turbine components, can withstand higher temperatures than the substrate, in this case copper. Their low thermal conductivity allows for a high-temperature gradient within the layer, reducing the specific heat flux and protecting the surface from reactive hot gas products.

This research aims to enhance the performance and protection of the rocket chamber by exploring the potential of TBCs and applying them to a capacitively cooled copper chamber segment and gathering experimental data. The choice of coatings should be based on an extensive research regarding appropriate materials and manufacturing techniques that are feasible in this context. In order to evaluate the collected data, an evaluation method based on a the inverse heat conduction method should be implemented and validated. This thesis should deliver an adequate basis on the effects and the feasibility of employing a TBC system and a recommendation for further research.

1.2. Structure of the Thesis

Background information about TBCs can be found in the "State of the Art" chapter, while the next chapter contains knowledge about rocket propulsion and combustion, heat transfer phenomena and cooling methods used in rocket engines.

Chapter 4 includes facts regarding the experimental setup, explaining the test procedure and details concerning the measurement arrangement. It involves planning and conducting hotfire experiments with the uncoated and both coated segments.

In this thesis, a segment of an existing capacitively cooled multi-segment combustion chamber was coated with two different TBC systems. Chapter 5 holds a detailed literature review on state-of-the-art protective coatings to identify a suitable material. The selection process considered various criteria, such as resistance to thermal shocks, compatibility with the substrate material and layer thickness. A special focus was on manufacturing techniques that had to be assessed in terms of feasibility, time and financial budget.

Chapter 6 describes the evaluation method for the experimental data, where the Inverse Heat Conduction Method (IHCM) using a CGM algorithm was implemented and validated. Multiple sensitivity analysis concerning different parts of the algorithm were carried out.

The next section is dedicated to the results, where temperature distributions and specific heat fluxes for all test cases are presented. A load point evaluation is followed by a performance analysis. This chapter concludes with an error analysis of the IHCM.

In the last chapter concluding statements and propositions for further research are made.

2. State of the Art

This chapter provides an overview of the different applications of thermal barrier coatings with a focus on aerospace and aviation applications. A selection of historical evolutions in the research regarding thermal barrier coatings is presented, followed by an explanation of the different components and layers of a TBC and their role in the concept of protective layers.

2.1. TBC Applications

Thermal barrier coatings are currently employed in various engineering applications, including internal combustion engines, gas turbine blades of jet engines, pyrochemical reprocessing units and rocket engines. Every application comes with its own challenges, boundary conditions and requirements. The development of new materials and deposition techniques fitting the application, aims to enhance the lifespan of the underlying substrates. The coating materials are materials with a higher operational temperature limit than the substrate, for example the rocket combustion chamber liner material, and a lower thermal conductivity. Consequently, the performance of these coatings is crucial for extending the life of the substrates and enabling higher load points and thus the efficiency of the whole system. [46]

2.1.1. Turbomachinery

Thermal Barrier Coatings have been used in the hot sections of aero turbine engines for over three decades. Their initial application was driven by the need to mitigate component degradation caused by excessive thermal gradients in the vane airfoils. It had to withstand severe temperature, environmental, thermal cycling and stress conditions over numerous aircraft take-offs and landings. These commercially used coating systems consist of a two layer system of a ceramic top coat and a metallic bond coat. [14]

2.1.2. Rocketry

Rocket engine designers around the world are continually challenged to meet increasing demands for higher performance, improved reliability and reduced cost. Among the various methods proposed to extend the life of combustion chamber liners, thermal barrier coatings stand out as highly attractive. Their application is typically straightforward and requiring minimal modifications to the established manufacturing processes of regeneratively cooled liners. Already progress in understanding the behaviour of thermal barrier coatings under conditions of high thermal stress and significant temperature gradients has been done [16], while more recent research is focused on understanding the failure mechanisms and their severity in the context of rocket engines [13]. To extend the life of the combustor for improved reusability and efficiency, and to increase hot gas temperatures and pressures, a thermal barrier coating can

be applied to protect the combustor walls. This coating reduces the maximum temperature experienced by the chamber wall material while shielding it from the oxidising atmosphere. [7]

2.2. Historical Background of TBCs

Despite the proven efficacy of thermal insulation coatings in aircraft engines and gas turbines, their use in rocket combustion chambers has thus far been limited to experimental applications. In 1978, the NASA Lewis Research Center conducted research into protective coatings for copper combustion chambers in cryogenic rocket engines. The objective was to reduce the surface temperature of the copper combustion chamber of the Space Shuttle Main Engine. In this study, zirconium oxide was investigated as a top coat, while nickel-chromium was examined as a bond coat [33].

At National Aeronautics and Space Administration (NASA)'s Glenn Research Center, the development of coatings for the copper combustion chamber of the "Third Generation Reusable Launch Vehicle" commenced in 1998. Initially, these included NiCrAlY and NiAl top layers on an aluminium bond coat layer of pure copper [23]. Further investigations at the same research center revealed the development of copper/chromium top coat layers on NiCrAlY bond coat, among others. These layers demonstrated promising results in terms of oxidation protection and the reduction of the doghouse effect [19].

At the Keldysh Research Centre in Moscow, a series of ceramic coatings, including ZrO₂, TiN and AlN, was subjected to testing on copper substrates with varying bond coats [15]. Due to the low thermal conductivity of ceramics, overheating in rocket engines occurs with considerable rapidity.

An alternative approach is to utilise a coating material with a higher thermal conductivity, such as metals. Simulations conducted in [3] have demonstrated that the application of a fully metallic coating would be sufficient to reduce the maximum temperature of the copper substrate to a level below its maximum operating temperature, while maintaining the surface temperature of the layer below its maximum permissible limit [3].

Still a lot of research needs to be done to characterize appropriate TBC systems for the use in rocket engines. There is significant potential for advancement in TBC, and ongoing efforts are focused on producing more improved and durable coatings [46].

2.3. TBC Structure

In coating technology, materials such as forced ceramics, reinforced polymers, and reinforced metals are utilized. Coatings are further classified based on their architecture into single layer, bi-layer, and functionally graded coatings. [46]

TBCs typically consist of an adhesion layer (bond coat) and an insulation layer (top coat), which makes them a two-component and two-layer system, visualized in Figure 2.1. The bonding layer acts as a transition zone between the topcoat and the base material. Its primary functions include facilitating chemical adhesion of the topcoat, providing corrosion resistance to the base material, and compensating for the different coefficients of thermal expansion of the topcoat and the base material. The top coat is functioning as the actual thermal barrier. [16]

Other concepts like the gradient layer structure were not included in this work. As explained in [8], these coating systems showed in isothermal and laser cycling tests at comparatively low temperatures, delamination and bulging effects. A different approach would be a multilayer system, including a thermal barrier layer, an erosion resistant layer as the outer layer, a thermal stress control layer, a corrosion-oxidation resistant layer and a diffusion resistant layer. However this approach is not yet matured and the feasibility for this work is questionable. [2]

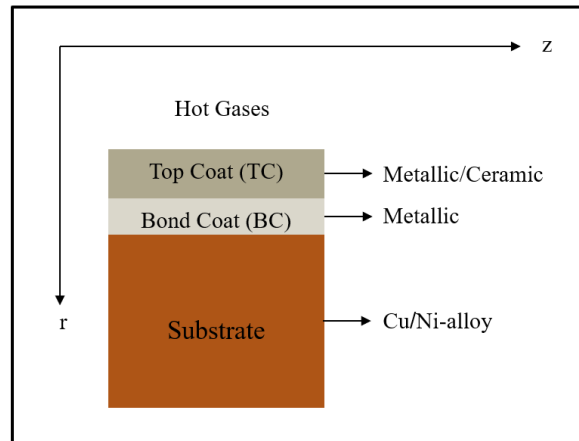


Figure 2.1.: TBC structure with top and bond coat

3. Basic Principles

This chapter lays the base of knowledge, useful for understanding the research topic. A general overview of the basics of rocket propulsion and a brief introduction into the thrust chamber design of a rocket is given, although the relevant formulas concerning the rocket performance are found in the subchapters of Section 7.5. Important heat transfer phenomena in rocket engines, as well as their measurement methods are discussed along with appropriate cooling techniques.

3.1. Basics of Rocket Propulsion

The mathematical basis for space flight were developed by Tsiolkovsky. His equation, known as the Tsiolkovsky equation, links the change in rocket velocity to the exit velocity of the propellant and the initial and final mass of the rocket. The equation is derived by considering a rocket with a mass and velocity that exhausts part of its propellant at an effective exhaust velocity c_{eff} , from Equation (3.4). This process occurs at a mass flow rate, incrementally reducing the mass and increasing the velocity by an increment. Through integration, the Tsiolkovsky Equation is derived, Equation (3.1), showing that the change in speed Δv equals c_{eff} multiplied by the natural logarithm of the initial mass m_i divided by the final mass m_f . The so called Δv is used to express the total change in velocity that is required for a space mission, like for example an orbit transfer.

$$\Delta v = c_{eff} \cdot \ln \left(\frac{m_i}{m_f} \right) \quad (3.1)$$

Two essential parameters for rocket development are thrust F and efficiency, expressed through the specific impulse I_{sp} . Thrust Equation (3.2) is composed of a velocity part and a pressure part. The velocity part involves multiplying the mass flow rate \dot{m} by the average exit velocity v_e , which differs from the effective exhaust velocity c_{eff} . The effective exhaust velocity combines both the velocity and pressure parts as a reference value. The pressure part is the difference between the nozzle exit pressure p_e and the ambient pressure p_{inf} , multiplied by the nozzle exit area A_e . The specific impulse is defined as the effective exhaust velocity of the propellant c_{eff} divided by the standard gravity g_0 . If $p_e = p_{inf}$, the pressure term becomes zero and in vacuum $p_{inf} = 0$, the thrust becomes a maximum.

$$F = \dot{m} \cdot v_e + (p_e - p_{inf}) \cdot A_e \quad (3.2)$$

$$I_{sp} = \frac{c_{eff}}{g_0} \quad (3.3)$$

These design parameters are largely influenced by the pressure and temperature of the combustion process. Understanding and controlling heat fluxes in the combustion chamber is essential for designing these parameters, making it a crucial aspect in the development of new rocket engines. [17]

3.2. Thrust Chamber Design

In the rocket engine, fuel and oxidizer are conveyed through pipes from the tanks to the injector plate and injected into the combustion chamber. Upon ignition, the flame anchors and the gas undergoes combustion, converting chemical energy into thermal energy. A portion of this thermal energy contributes to thrust generation, while a fraction is lost as heat transferred to the chamber wall. An estimated energy distribution is illustrated in Figure 3.1. Approximately 2% of the energy transferred to the wall amounts to approximately 100 MW in a conventional engine [24], underscoring the necessity for efficient cooling systems.

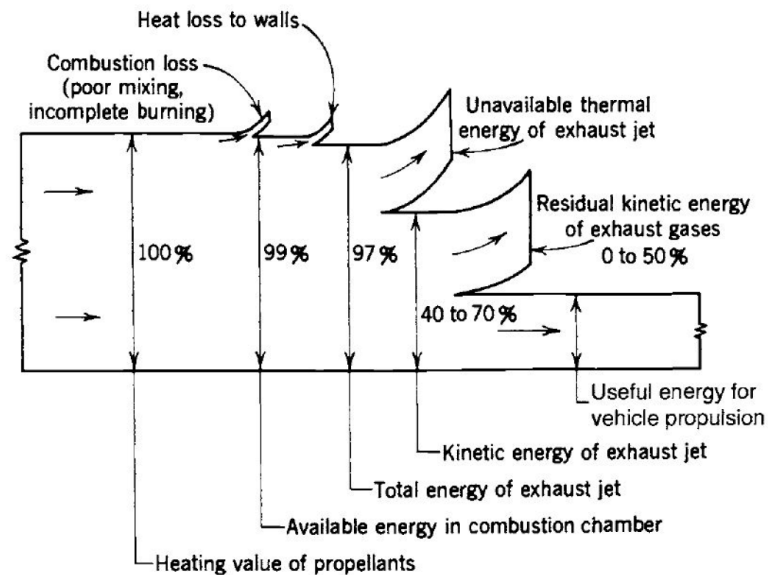


Figure 3.1.: Heat loss across a rocket engine [43]

Figure 3.2 highlights the expected heat flux distribution in a rocket engine, while the peak value is located at or slightly upstream of the throat, while the lowest value is to be found at the nozzle exit.

3.3. Heat Transfer in Rocket Engines

Rocket engines involve complex thermochemical processes. Within the combustion chamber, gas temperatures can exceed 3500 K. Due to the inability of any currently available material to withstand these extreme temperatures, cooling systems are essential [21]. In order to gain a holistic picture of the heat transfer in a rocket engine, different sub-topics have to be taken into account.

As a starting point the temperature, pressure, fluid properties and gas composition within the combustion chamber have to be determined analytically or by simulation. For the purpose of evaluating the heat transfer from hot gas to the wall, especially the HTC has to be identified. This may involve contributions

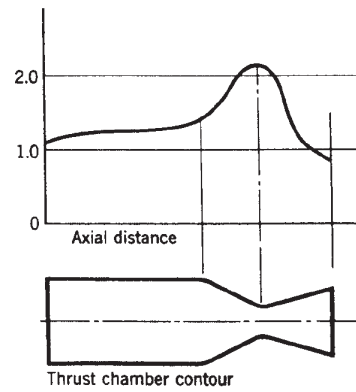


Figure 3.2.: Typical axial heat transfer rate in a rocket engine [43]

from both radiation and convection. Soot deposition might also be considered in the calculation of the hot gas side HTC. The heat conduction in the wall is assessed taking into account the effects of wall curvature, cavities and different chamber materials. Estimating the heat transfer into the coolant is done with a particular focus on fluid properties, especially when dealing with unstable and decomposing coolants. Lastly the heat transfer has to be evaluated from the outer chamber wall to the surrounding environment. While this can often be neglected if the outer wall temperature is rather low, it must be modelled for scenarios involving radiative cooled ceramics and nozzles. [20]

The following sections discuss the need to achieve high combustion temperatures, the functional principles and computational approaches, as well as models for various heat transfer phenomena and cooling techniques with the focus on the knowledge required for this work.

3.3.1. Performance and Heat

The primary objective of a rocket is to alter the velocity of the rocket to accomplish the intended mission. The change in the rockets velocity is directly proportional to the effective exhaust velocity c_{eff} . Assuming an adiabatic system, the effective exhaust velocity can be linked to the total enthalpy of the system $h_{tot} = h_c$ and thus the combustion temperature T_c :

$$c_{eff} = v_e \frac{p_e - p_a}{\dot{m}} A_e \quad (3.4)$$

$$v_e = \sqrt{2 \cdot (h_c - h_e)} = \underbrace{\sqrt{2c_p \cdot (T_c - T_e)}}_{\text{ideal rocket}} \quad (3.5)$$

The total enthalpy depends on the enthalpy change of the chemical reaction occurring during combustion. According to Hess's law, the enthalpy change for a reaction is independent of the reaction pathway and is determined by the enthalpies of formation of the reactants and products. Consequently, achieving high total enthalpies and temperatures in the combustion chamber is crucial for high-performance rocket engines. This is accomplished by using highly reactive propellants with high enthalpies of formation that burn to form products with low enthalpies of formation. [21]

3.3.2. Adiabatic Wall Temperature

The adiabatic wall model is applicable to uncooled structures under steady-state conditions. While this concept lacks practical significance in rocket engines as material limitations would be significantly exceeded, the adiabatic wall temperature serves as a reference case for heat transfer models. Consequently, the adiabatic wall temperature T_{aw} is also occasionally referred to as the recovery temperature of the hot gases near the wall.

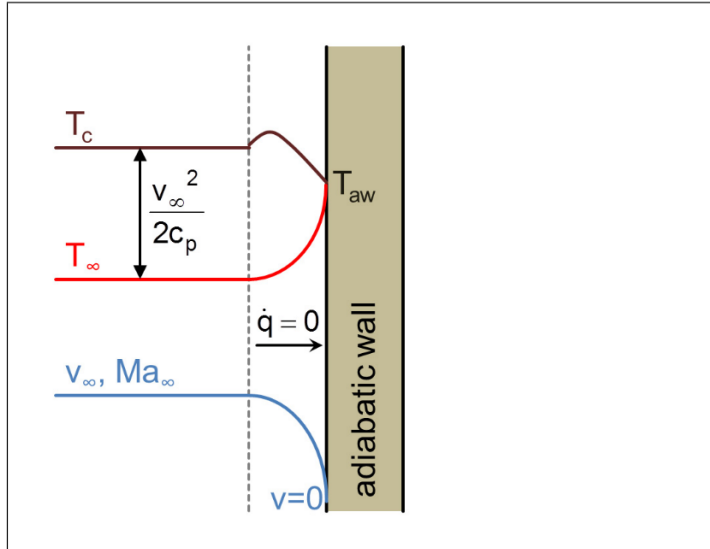


Figure 3.3.: Visualization of an adiabatic wall [21]

The adiabatic wall model, visualized in Figure 3.3, assumes, according to its name, that there is no heat transfer to or from the wall. The hot gases flow with a velocity $v_{inf} = v_{hg}$ and are associated with a temperature $T_{inf} = T_{hg}$, while the total temperature is $T_c = T_{hg_{tot}}$. In the boundary layer, represented by a dotted line, the velocity drops to zero, due to the no-slip wall condition. The static temperature rises to the adiabatic wall temperature T_{aw} , as it loses its velocity portion.

Opposed to ideal and isentropic flows, the real total temperature is not fully recovered at the wall. Radiative heat transfer within the boundary layer causes losses, resulting in a marginally lower adiabatic wall temperature than T_c . The recovery factor r expresses this deviation between the total temperature and the adiabatic wall temperature.

r is determined as a function of the Prandtl number Pr , which depends on the intensity of turbulence and can be related to boundary layer theory. The Prandtl number is dimensionless and relates kinematic viscosity to thermal diffusivity. [21]

laminary:

$$r = \sqrt{Pr} \quad (3.6)$$

turbulent:

$$r = \sqrt[3]{Pr} \quad (3.7)$$

The adiabatic wall temperature T_{aw} can be calculated as:

$$T_{aw} = T_{hg} \left[1 + r \left(\frac{T_{hg_{tot}}}{T_{hg}} - 1 \right) \right] \quad (3.8)$$

$$\frac{T_{hg_{tot}}}{T_{hg}} = \frac{\kappa - 1}{2} Ma_{hg}^2 + 1 \quad (3.9)$$

3.3.3. Convective Heat Transfer

Convective heat transfer is subjected to the transport of masses. Forced convection occurs when the fluid movement is caused by external forces like a pressure gradient. This heat transport phenomena is the main driver for the heat transfer from the hot combustion gases to the chamber walls in a rocket engine. The heat flux, described in Equation (3.10) is proportional to the convective heat transfer coefficient α_{hg} and is driven by the temperature gradient of the hot gas temperature and the wall temperature T_w .

$$\dot{q} = \alpha \cdot (T_{aw} - T_w) \quad (3.10)$$

Fluid properties as well as flow characteristics determine the HTC. As a result convective heat transfer is influenced by the design features of the chamber, which influence combustion pressure and turbulence, and thermochemical properties of the propellants. Dimensionless numbers are used describing this form of heat transfer. The Reynolds number represents the ratio of inertial forces to frictional forces. The Prandtl number describes the ratio of momentum propagation to thermal propagation, while the Nusselt number quantifies the ratio of convective heat transfer to diffusive heat transfer. [21]

$$Re = \frac{\rho \cdot v \cdot d_h}{\mu} \quad (3.11)$$

$$Pr = \frac{\mu \cdot c_p}{\lambda} \quad (3.12)$$

$$Nu = \frac{\alpha \cdot d_h}{\lambda} \quad (3.13)$$

In order to design a thermal barrier coating, a suitable HTC correlation has to be applied. As Bartz [4] proposed common correlations for heat transfer in rocket engines, these correlations are taken as a reference. The coefficients a , b and C characterize the particular engine. They allow potential adjustments for traits like wall roughness or curvature. Also the reference conditions utilized to determine fluid properties are taken into account.

$$Nu = \frac{\alpha_{hg} \cdot d_h}{\lambda_{hg}} = C \cdot Re^a \cdot Pr^b \cdot \text{corrections} \quad (3.14)$$

Correlations found in existing literature are generally adequate only for initial rough estimates, and the semi-empirical adjustments developed by rocket engine operators remain closely guarded proprietary knowledge. Various methodologies employ different definitions for reference temperatures and pressures, and they also differ in their descriptions of chemical reactions and gas compositions. The correlations applied in this thesis are detailed in Section 5.7.2. [21]

3.3.4. Conductive Heat Transfer

Heat conduction is the process through which thermal energy is transferred due to temperature variations. Unlike convection, which involves the movement of mass, conduction deals with the transfer of energy via molecular vibrations and free electrons. In the context of rocket engines, conduction predominantly affects heat transfer within the combustion chamber walls, although it also occurs in the hot gas. The principles of heat conduction are described by Fourier's law, with the assumption of constant thermal conductivity, λ . The differential form of Fourier's law is typically written as [43]:

$$\vec{q} = -\lambda \cdot \nabla T \quad (3.15)$$

This reduces to the one-dimensional scenario radially through the combustion chamber wall, where the wall thickness is t_{hg} , with T_{w1} as the temperature of the hotter wall and T_{w2} as the temperature of the cooler wall, as illustrated in Figure 3.4.

$$\dot{q} = \frac{\lambda}{t_{hg}} (T_{w1} - T_{w2}) \quad (3.16)$$

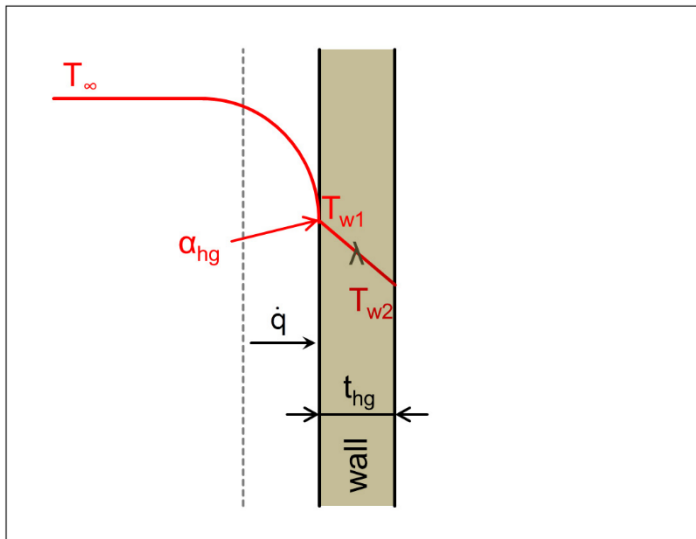


Figure 3.4.: Visualization of an adiabatic wall [21]

3.3.5. Measurement Methods

Heat transfer from the combustion gases to the chamber wall is a crucial element in designing the chamber and its subsystems. To optimize cooling systems while minimizing pressure drop, it is essential to thoroughly understand the heat transfer processes along the engine wall. Beyond affecting cycle performance, cooling design, and engine lifespan, wall heat flux also reflects the combustion processes. This data can be obtained by installing sensors, enabling a deeper insight into combustion dynamics and aiding in the optimization of engine performance and durability.

The hot gas flow in rocket combustion chambers exhibits two-dimensional variability, both axially and circumferentially. Axial development is primarily influenced by chemical reactions, while circumferential

heat transfer varies due to changes in flow composition and temperature, particularly in the stratified flow near the injector plate. These considerations highlight the need for realistic, high spatial resolution experimental heat transfer data under representative conditions. Different methods to evaluate the heat transfer in rocket engines exist. [26]

Gradient Method: In experimental rocket thrust chambers, a straightforward method for assessing wall heat flux is the gradient method. This approach entails placing multiple temperature sensors at various radial positions within the chamber wall. By assuming steady-state heat transfer within the material, the analytical formula Equation (3.16) for heat flux can be applied.

Calorimetric Method: In regenerative cooling systems, which are frequently employed in most sub-scale demonstrators, heat absorption data for the coolant can be easily obtained by measuring the inlet and outlet pressures and the coolant temperature. The rise in coolant enthalpy correlates with the average wall heat flux, typically providing a circumferentially and axially averaged heat flux, which offers limited resolution. Nevertheless, even with this limited resolution, axial heat flux profiles derived from the calorimetric method are useful for assessing injector and film cooling performance. Additionally, they facilitate quantitative comparisons with numerical simulations. [26]

Inverse Heat Transfer Method: One of the most sophisticated methods for determining wall heat loads in rocket thrust chambers is through the use of inverse methods. These techniques involve placing thermocouples at various locations within the chamber material, akin to the gradient method. The core principle of inverse methods revolves around iteratively adjusting unknown boundary conditions to minimize the difference between calculated and measured temperatures at multiple sensor positions. In each iteration, the heat transfer problem is solved using Finite Difference, Finite Volume, or Finite Element methods, utilizing boundary conditions from the previous iteration. The boundary conditions are refined based on the disparity between the newly computed temperature field and the experimental measurements, continuing until convergence is achieved. This iterative approach accommodates both transient and steady-state scenarios and facilitates the estimation not only of hot gas wall heat flux but also of the wall heat transfer coefficient within the cooling channels. To expedite the iterative process, optimization algorithms such as the Conjugate Gradient Method, Newton-Raphson Method, or Levenberg-Marquardt Method are often employed. [26]

3.4. Cooling Methods

While higher pressures offer performance advantages, their feasibility may be limited by the continuous increase in expected heat fluxes. Reliable operation of rocket combustors under such intense thermal and mechanical loads requires highly efficient cooling mechanisms. [26]

3.4.1. Capacitive Cooling

Capacitive cooling, also known as heat sink cooling, is a passive cooling technique in which heat transferred to the chamber walls diffuses into the structure, raising its temperature. For this method to be effective, the chamber material must have a high thermal conductivity to efficiently dissipate heat away from the hot gas wall. In addition, a high heat capacity and density are required to ensure effective heat absorption without exceeding the operating temperature of the material. Copper alloys are commonly used for this

purpose as they satisfactorily meet these requirements. The temperature gradient over time can be given by Fourier's law of heat conduction:

$$\frac{\delta T}{\delta t} = \frac{\lambda}{\rho c_p} \nabla^2 T \quad (3.17)$$

The result is a transient rising temperature profile that does not reach a steady state during the hot run. Consequently, the maximum duration of the test is limited in order to maintain the thermal and mechanical integrity of the chamber liner. In addition, the bulky dimensions of the capacitive hardware required to provide a sufficiently large heat sink, makes this cooling method impractical for flight hardware. Hence it is primarily used in laboratory-scale experimental combustors. [26]

3.4.2. Thermal Barrier Coatings

In the context of a rocket combustion chamber liner, the elevated operational temperature of the top layer facilitates a higher wall surface temperature, T_w . By maintaining the hot gas temperature T_{hg} , in Figure 3.5 depicted as T_c , as constant and permitting the hot-gas side of the wall to operate at a heightened temperature, the convective heat flux $\dot{q} = \dot{q}_{conv}$ from Equation (3.10), in Figure 3.5 \dot{q}_1 , applied to the wall is diminished [16].

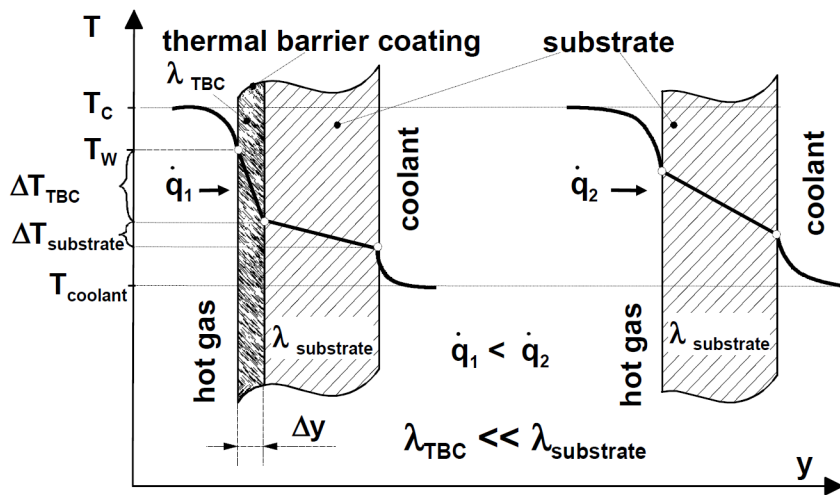


Figure 3.5.: Wall temperature for a regeneratively cooled rocket with and without TBC [16]

Without considering radiative heat transfer, we can set the convective heat flux equal to the total wall heat flux: $\dot{q} = \dot{q}_{conv}$. Therefore, the thermal gradient across the wall can be approximated using Equation (3.16). Here, λ represents the thermal conductivity, which is lower than that of the substrate, $(T_{w1} - T_{w2}) = \Delta T$ denotes the temperature gradient across the wall or layer, and $t_{hg} = \Delta y$ stands for the coating or wall thickness, illustrated in Figure 3.5.

$$\dot{q} = \lambda \frac{\Delta T}{\Delta y} \quad (3.18)$$

Equation (3.18) suggests that a lower heat conductivity of the coating, given a constant wall heat flux

\dot{q} , results in a greater thermal gradient $\Delta T/\Delta y$, as depicted in . Consequently, this increase in thermal gradient leads to higher wall temperatures T_w .

The decrease in \dot{q} offers two avenues to enhance system efficiency in the context of a regeneratively cooled rocket, which is the ultimate objective of applying the TBC for the DO engine. Firstly, by maintaining a consistent substrate temperature in both coated and uncoated scenarios, it becomes feasible to lower the coolant mass flow rate and consequently reduce pressure drop within the cooling system. This reduction enables a decrease in turbo-pump power requirements, allowing for the use of smaller pumps or prolonging their operational lifespan. Secondly, by keeping the coolant mass flow rate constant in both scenarios, substantial reduction in the base material wall temperature can be achieved. This decrease significantly diminishes thermal stresses and enhances material strength, thereby extending the service life of the combustion chamber liner. [16]

4. Experimental Setup

This chapter includes information about the experimental campaign. The general setup and the different hotfire configurations will be discussed as well as their respective goals and means to reach them. An overview of the test plans, test preparation and an exemplary test sequence are also provided, together with details about the data post processing. The goal of the hotfire experiments was to gather data that provides information about the influence of two different thermal barrier coatings, a ceramic and a metallic one, on the heat flux and performance of a capacitively cooled test chamber of the DeltaOrbit rocket engine.

The design load point for this configuration is 12 *bar* and a mixture ratio (ROF) of 3.1, which is not far of the optimum ratio 3.2 in [43] for a maximum specific impulse. In rocket propulsion systems, it is not beneficial to operate with the oxidizer and fuel at their stoichiometric mixture ratio, for methane an oxygen this would be a ROF of 4. Instead, they often operate fuel-rich ($\text{ROF} < 4$), as this is the best way to preserve low molecular mass molecules like hydrogen from reacting. This approach lowers the average molecular mass of the reaction products, boosting their exhaust velocity. [43]

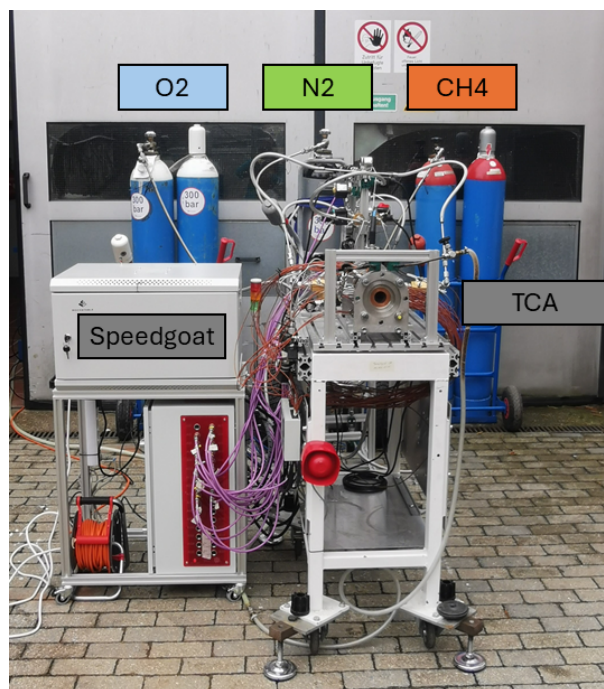


Figure 4.1.: Exemplary Hotfire Test Setup

The hotfire tests were conducted at the rocket test facility of the Institute of Space Propulsion, located at TUM's campus in Garching. The mobile test bench setup, depicted in Figure 4.1, consists of a real-time data acquisition system of the company Speedgoat, the gas supply and regulation system and the actual

rocket engine test setup. The tests are carried out from a safety distance of a control room, operating the tests with ready-to-use test sequences. As a visual safety measure during the tests, a video camera broadcasts to the control room. Oxidizer (oxygen), purge gas (nitrogen) and fuel (methane), are securely supplied by dedicated high-pressure gas cylinders. The Thrust Chamber Assembly (TCA) uses a spark torch ignition system, hosted in a copper ignition ring, and a single swirl injector. The capacitive copper combustion chamber consists of two segments. The first one has a constant diameter, while the second transitions after approximately the half of its total length into a convergent/divergent part, which is the nozzle.

4.1. Fluid Supply System

The purpose of the fluid supply system, illustrated in Figure 4.2, was to provide the gases in their required ROF and pressure to the injector and igniter. The respective load points, documented in Section 4.4, are adjusted by the second pressure regulator downstream the oxygen and methane bottles and are controlled by the second pressure and temperature measurement point. Through this upstream pressure level, the mass flows into the system, through choked orifices, are managed. All supply lines can be opened to the environment in sections by two magnetic valves, which are also used to enforce the test sequence on the system. It is crucial to observe the bottle pressures and their pressure drop during the tests, in order to grant a sufficient high pressure level for downstream operations. The purge line was used to purge part of the main chamber supply tubes and the igniter itself. Here each downstream pressure was only set in the beginning of each hot fire configuration.

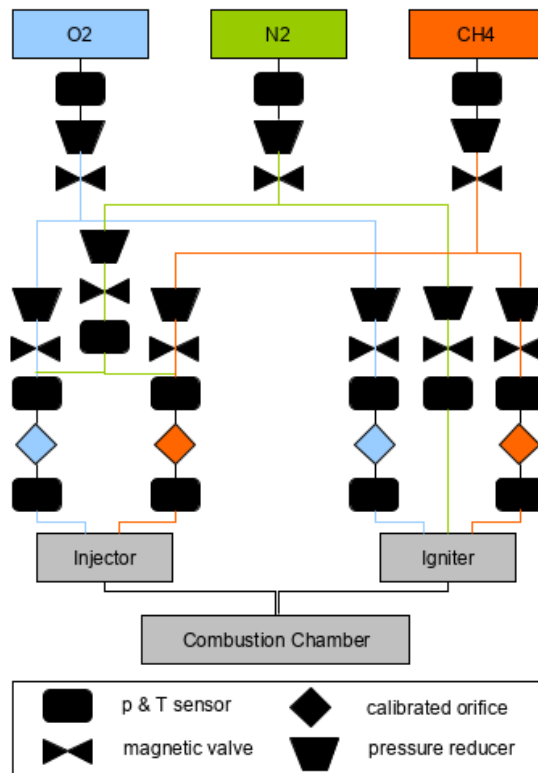


Figure 4.2.: Test Setup Flowchart

The pressure sensors at the bottles have an upper limit of 400 *bar* for methane and nitrogen, and 350 *bar* for oxygen, for all three of them with bottles with a maximum pressure of 300 *bar*. The sensors inside the feedlines, before the main and igniter orifices limit at 100 *bar*.

Propellants: The oxidizer consists of gaseous oxygen (GO_2) and the fuel of gaseous methane (GCH_4). For the tests, the gases were supplied at ambient temperature, so no conditioning took place. As a purge gas GN_2 was used.

Calibrated orifices: In total four orifices are used to control the mass flow. Prior to this thesis, the calibration and design of the geometric parameters, shown in table Table 4.1, as well as a stable and sufficient load point for the igniter, specified in Section 4.2.2, has been developed. The discharge coefficients of the igniter orifices show values > 1 , which result from measurement inaccuracies during calibration due to the marginal mass flow rates necessary for ignition. Thus only the upstream pressures of the orifices for oxidizer and fuel were determined.

Table 4.1.: Orifice parameters

	Injector Oxidizer	Injector Fuel	Igniter Oxidizer	Igniter Fuel
d [mm]	4.0	2.7	0.3	0.2
C_d [-]	0.9133	0.8998	1.09	1.02

The pressure calculation for the upstream main orifices, was carried out for three different ROF at respective three p_{cc} , which were aspired to be tested and are described more detailed in Section 4.4. These inputs were fed into a rocket-problem of the Chemical Equilibrium with Applications (CEA) tool of NASA, describing the characteristics of the existing engine with a finite area combustor and the contraction ratio, subsequently finding the desired oxidizer and fuel mass flows. In a non-linear minimization, the upstream pressure was optimized by evaluating the objective error function of the desired and computed mass flows. As the temperature of the gases during the test was not known, a constant assumption of 273 *K* was made. In reality the temperature decreases while flowing through the pipes, in average by around 10 *K*, therefore the influence, as can be seen in Section 7.4 is negligible. In Table 4.2 the calculated values, taken as reference setting points, were compared with the ones that were actually set. These were determined by comparing old test data, taking in account the pipe lengths and other inherent features of the setup, as well as the ambient temperature at the test days. In lower pressure load points the calculated values were over-predicted in comparison with previous values, while for higher load points more pressure has to be set to achieve the load point.

Table 4.2.: Orifice upstream pressures in [bar]

p_{cc}/ROF	5/2.7	5/3.1	5/3.5	10/2.7	10/3.1	10/3.5	12/2.7	12/3.1	12/3.5	15/3.1
$p_{ox_{ex}}$	16.1	17	17.9	31.7	33.9	35	40.7	42.9	45	52.2
$p_{ox_{calc}}$	16.3	17.3	18.2	32.9	33.9	35.6	38.3	40.43	42.48	49.8
$p_{fu_{ex}}$	18.9	17.4	16.3	36.4	34.4	31.4	46.3	42.8	40.1	51.6
$p_{fu_{calc}}$	19.1	17.73	16.5	37.1	34.3	32.1	43.9	40.73	38.1	48.7

4.2. Combustion Chamber

The following figures are depicting the assembled combustion chamber and relevant dimensions.

Figure 4.3 gives an overview of the thrust chamber. To accommodate thermal expansion of the chamber during the hotfires, the construction is only partially fixed on the mobile desk, as can be seen in Figure 4.1. The injector, igniter ring and chamber segments are pressed together between inlet and outlet flanges by the use of springs and four threaded rods; in the picture only one is depicted. The chamber assembly investigated in this thesis was composed of a swirl injector head with two separate inlets for oxidizer and fuel followed by a solid ring to mount the igniter, succeeded by the two Combustion Chamber (CC) segments. Conforming with old documentation [5], the cylindrical part is referred to as CC1 and the nozzle as CC3. For the different test configurations, the CC1 segment could be easily interchanged and pressure tightness was achieved by round sealing rings. The characteristic chamber length, L^* from Equation (4.1), an important comparative characteristic for different propellant combinations, of the investigated chamber can be adapted modularly, but for these experiments $L^* = 0.85 \text{ m}$, containing the igniter ring.

$$L^* = \frac{V_{cc}}{A_{th}} \quad (4.1)$$

The combustion chamber is equipped with six pressure sensors, as indicated in Figure 4.3. As the first segment was the subject of interest, most thermocouples were installed here. For this the thermoholders, evident in Figure 4.3, were designed and 3D printed. To accelerate cooling off during the tests and to avoid an insulation effect for the chamber, cut-outs were implemented. Space sleeves were used to prevent contact with the hot copper. Limited data ports in the data acquisition system lead to not being able to equip all TC-positions, indicated with red dots in Figure 4.3. The fuel manifold inlet can be seen in Figure 4.5, at the mirrored position of the oxidizer inlet. Details about sensors can be found in Section 4.3.

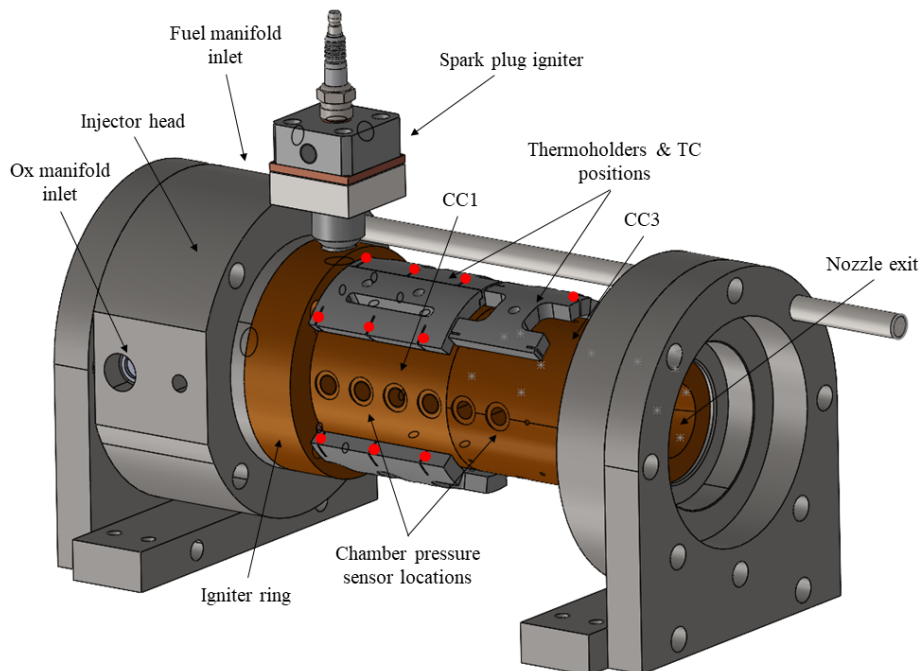


Figure 4.3.: Combustion chamber setup from left

Relevant dimensions can be retrieved from Figure 4.4. As the igniter ring was included in further evaluations of the hotfires, it is shown here too. The contraction half angle is $\Theta = 30^\circ$, the expansion half angle is $\alpha = 15^\circ$, the contraction ratio is $AR_{con} = 5$ and the expansion ratio is $AR_{div} = 4$.

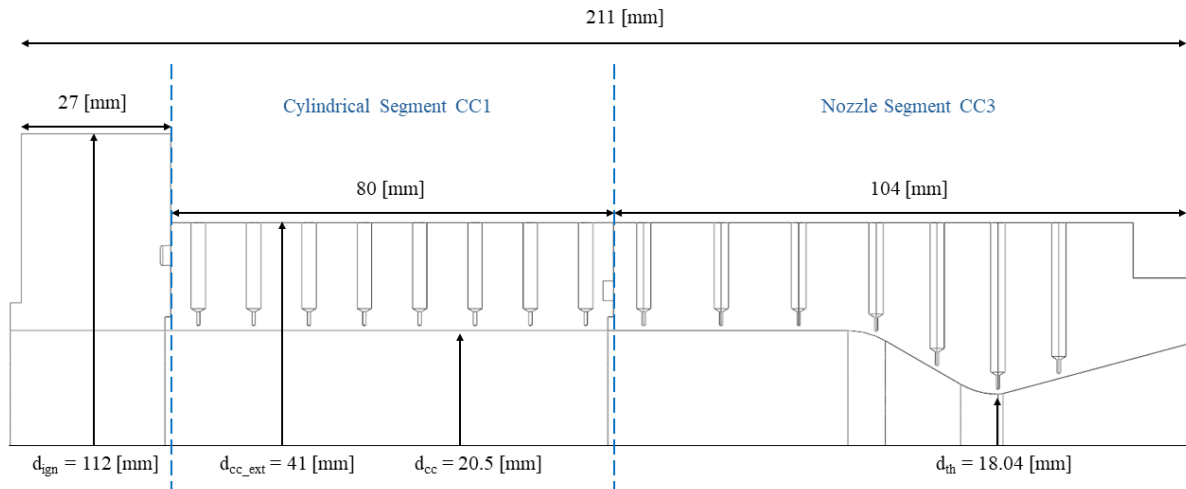


Figure 4.4.: Geometrical dimensions of the combustion chamber

4.2.1. Injector

The injector configuration is indicated as a "low" swirl configuration, as the project also tested another configuration with a different injection angle and less orifices, before this thesis [5]. The swirl number for the oxidizer and fuel are 2, while the total swirl number is 1. The "low" swirl configuration was chosen for this test series because of too high temperatures and heat loads in the inlet area of the "high" swirl case, compared to rather homogenous and constant ones throughout the cylindrical region with the "low" one.

4.2.2. Igniter

A spark torch igniter was used throughout the test campaigns to provide the thermal energy for chamber ignition. The igniter was supplied by a separate feed line, as indicated in Figure 4.2. The igniter hot gas was injected through the igniter ring perpendicularly to the main flow direction. The ROF of the igniter was 2.7 [–], with an oxygen upstream pressure of 47 bar and a fuel one of 57.9 bar, while the thermal power was approximately 14 kW, in total generating about 6 bar igniter pressure.

4.3. Combustion Chamber Sensors

The data sampling rate of the pressure sensors was 1 kHz. The six pressure sensors, four in CC1 and two in CC3 measuring the chamber pressure have a measurement range of 0 – 50 bar. The sensors in both manifolds, the oxygen post and the igniter chamber and ring pressure feature the same range.

The rate of the TC was approximately 45 Hz. The mounted thermocouples are from the type T class 1. They were installed in axial direction and at various circumferential positions for different radial distances from the hot gas wall, namely at 1 mm, 3 mm and 5 mm.

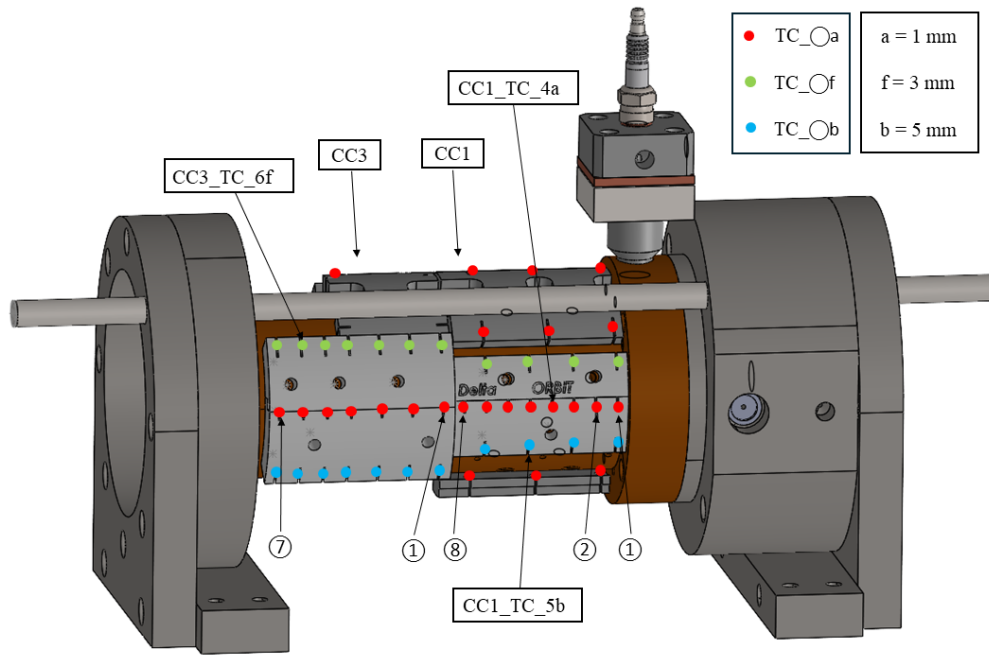


Figure 4.5.: Thermocouple nomenclature and layout

In order to gain an overview of the nomenclature and amount of sensors used, one should refer to Figure 4.5, which shows the chamber from the right hand side. A total of 53 TC were used, 31 by CC1 and 22 by CC3. The thermoholders on top in the middle of CC1 fit 9 sensors, the pair on the bottom contains 6. The holders, that can be seen frontal for CC1, in total 16 TC, and CC3, amounting to 21 TC, are equipped with the thermocouples that are later used as an input for the inverse heat transfer method in Chapter 6. These TC share the depicted nomenclature, additional ones are shown in Figure 4.6.

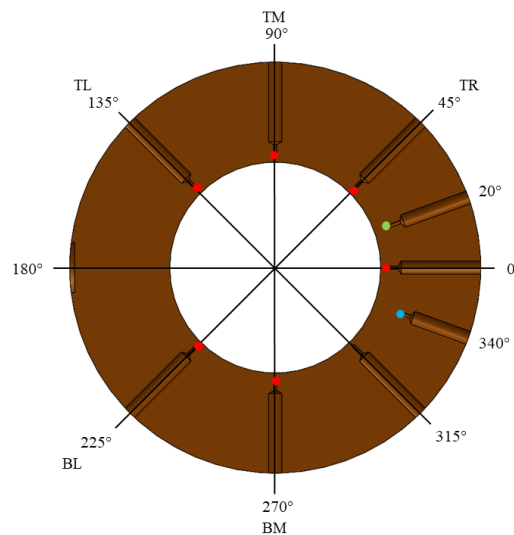


Figure 4.6.: Thermocouple positions at the first plane of CC1 facing the injector

The thermocouples of different thermoholders are at different circumferential positions but the same groups are in the same cross sectional plane. Thus they are numbered consecutively ranging for CC1 from

1 to 8 and for CC3 from 1 to 7. Some name examples are shown in Figure 4.5. The coloured dots indicate the occupied TC positions, while the colours signal the radial distance from the hot gas wall. The letter "a" is the closest to the wall, with $\Delta r = 1 \text{ mm}$, followed by "f" with $\Delta r = 3 \text{ mm}$ and "b" $\Delta r = 5 \text{ mm}$. The "a"-row of the TC-batch for the IHCM is at the same circumferential position, while the "f" and "b" rows in CC3 deviate by 30° and for CC1 by 20° , which is also illustrated in Figure 4.6, where the viewer faces the injector face plate. The shown plane is the first sensor plane in CC1. Here the naming of the top and bottom sensors is also demonstrated pursuing the logic of "T" being top, "B" bottom, "L" left and "R" right.

Table 4.3.: Sensor coordinates and numbers in [mm] for the uncoated and ceramic test case for CC1

Pos.	CC1 1	CC1 2	CC1 3	CC1 4	CC1 5	CC1 6	CC1 7	CC1 8
z	32	42	52	62	72	82	92	102
a r	21.5	21.5	21.5	21.5	21.5	21.5	21.5	21.5
f r	23.5		23.5		23.5		23.5	
b r	25.5		25.5		25.5		25.5	
Nr. a/f/b	1, 3, 2	4	5, 7, 6	8	9, 11, 10	12	13, 15, 14	16
Unc. Nr. a/f/b	-, 2, 1	3	4, -, 5	6	7, 9, 8	10	11, -, 12	13
Cer. Nr. a/f/b	1, -, 2	3	4, 6, 5	7	8, 10, 9	11	12, -, 13	14
Met. Nr. a/f/b	-, 1, -	2	3, 4, -	-	5, 7, 6	8	9, 10, -	11

In Table 4.3 and Table 4.4 the sensor position values used for the inverse method in Chapter 6 are listed. The radius is r is the radius of the chamber and the origin of the flow direction, namely the z -direction, is located at the injector face plate, which is the left plane of the igniter ring in Figure 4.4. As explained in Section 7.1.2, the metallic coated CC1 segment is shorter, but for reasons of clarity only the uncoated and ceramic hotfire case sensor coordinates are given. For the metallic configuration, there has to be deducted $\Delta z_{cc1} = 0.25 \text{ mm}$ from the first eight positions and $\Delta z_{cc3} = 0.25 + 1 \text{ mm}$ from the TC sensor positions of CC3. The 1 mm has to be deducted because the outlet of CC1, was shortened by that length. The numbering is not consistent with the physical positions of the sensor list, which was used for data evaluation and follows the letters. The last three rows of Table 4.3 and Table 4.4 explain the new sensor numbers after excluding the problematic ones from Table 4.9.

Table 4.4.: Sensor coordinates in [mm] for the uncoated and ceramic test case for CC3

Pos.	CC3 1	CC3 2	CC3 3	CC3 4	CC3 5	CC3 6	CC3 7
z	112.5	126.5	140.5	154.5	165.5	176.5	187.5
a r	21.5	21.5	21.5	20.5	15.8	10.0	12.8
f r	23.5	23.5	23.5	22.5	17.8	12.0	14.8
b r	25.5	25.5	25.5	24.5	19.8	14.0	16.8
Nr. a/f/b	17, 19, 18	20, 22, 21	23, 25, 24	26, 28, 27	29, 31, 30	32, 34, 33	35, 37, 36
Unc. Nr. a/f/b	14, -, 15	16, 18, 17	-, 20, 19	21, 23, 22	-, -, 24	-, 25, -	-, 27, 26
Cer. Nr. a/f/b	15, -, 16	17, 19, 18	-, 21, 20	22, 24, 23	-, 26, 25	-, -, 27	-, 29, 28
Met. Nr. a/f/b	12, -, 13	14, -, 15	-, -, 16	17, 18, -	-, 20, 19	-, 22, 21	-, 24, 23

4.4. Testing Procedure and Testplan

The general procedure for the testing was to go from low to high pressure levels and from low to high ROF. In this way the mechanical and thermal loads are raised continuously, pushing the unknown boundaries of

4. Experimental Setup

the TBCs. A common goal was to reach the first nine load cases, already portrayed in Table 4.2. The uncoated case was taken as a reference point for the data evaluation. The ceramic test case was completed without any problems and a load point at 15 *bar* and ROF 3.1 could be reached. During the metallic test campaign, issues occurred, explained in greater detail in the following paragraphs, and testing was aborted. For every load point two tests were done. An overview of the aspired ROF and chamber pressures p_{cc} for the uncoated (unc), ceramic (cer) and metallic (met) configuration is given in Table 4.5. In total 18 uncoated test runs were completed, 20 ceramic test runs and 12 metallic tests. The average ambient temperature was about 283 *K*.

Table 4.5.: Load point overview for test configurations

p_{cc}/ROF	2.7	3.1	3.5
5 <i>bar</i>	unc/cer/met	unc/cer/met	unc/cer/met
10 <i>bar</i>	unc/cer/met	unc/cer/met	unc/cer/met
12 <i>bar</i>	unc/cer	unc/cer	unc/cer
15 <i>bar</i>	-	cer	-

Figure 4.7 depicts a typical hotfire sequence. The magnetic valves used for purging are shown in green (MV_IF_3_N and MV_IG_3_N), the igniter sequence valves, both oxidizer (MV_IG_1_O) and fuel (MV_IG_2_F) in blue and both main valves (MV_IJ_1_O and MV_IJ_2_F) of the injector for the main sequence in red. To prevent spontaneous combustion the oxidizer is always injected into the chamber with a positive time offset regarding the fuel of $\Delta t_{ox} = 0.001$ *s*, and shut off with a negative one. As Δt_{ox} is small, it can not be seen in the figure.

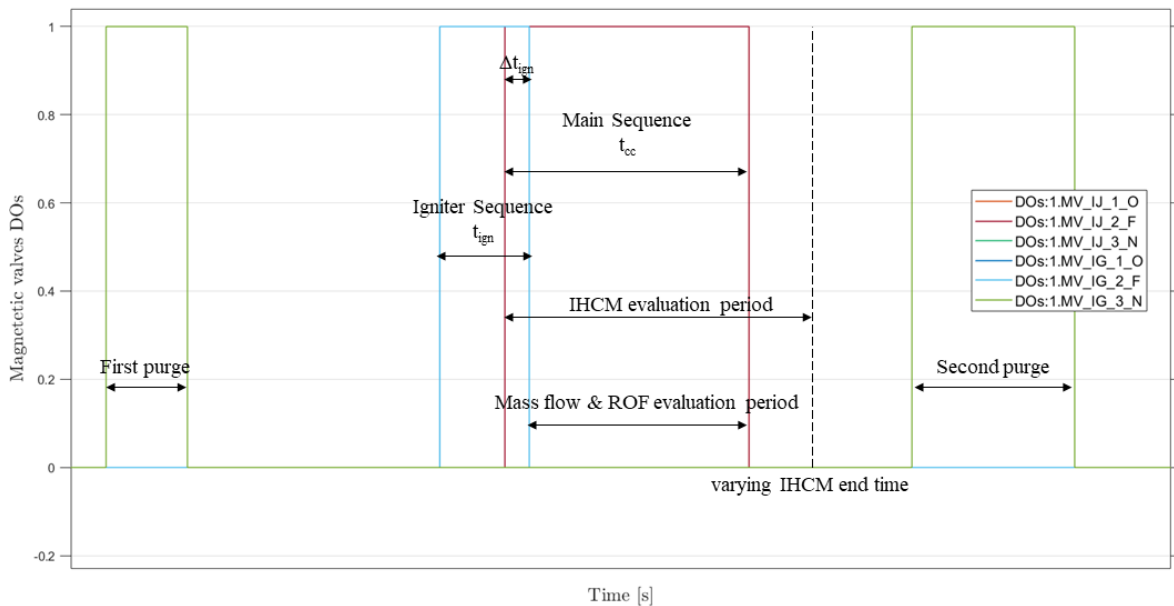


Figure 4.7.: Generic test sequence example with IHCM, mass flow and ROF evaluation duration

In the beginning a purge clears the lines from residuals of any propellant. After that the fuel, then the oxygen igniter valve open and the igniter sequence starts. The igniter is operated for a total duration of $t_{ig} = 1.1$ *s*, while the overlap of igniter and main chamber operation is $\Delta t_{ig} = 0.3$ *s*. The test duration t_{cc} itself was adapted for the tests and is shown in Table 4.6 for the uncoated, in Table 4.7 for the ceramic

and in Table 4.8 for the metallic tests. The procedure of getting these values is explained in greater detail in Section 7.4. The values in these tables are averaged over time. The averaging time span is taken as portrayed in the sequence. The start time is chosen as the closing time of the fuel igniter valve and the end time as the closing time of the main oxygen injector valve. The overlap of igniter and main sequence is ignored as the influence of the igniter distorts the overall mass flow and ROF test characteristics. t_{cc} is defined as the time both the main valve are open. Test durations varied from 2 – 8 s. After the main sequence a second purge is activated. For the IHCM evaluation the opening of the fuel main valve and the peak of a specific TC, further explained in Chapter 6, where the time varies for every run.

Before hotfires: Part of the testing routine is a valve check, testing whether the connections were done properly to prevent damaging the equipment. An extensive leak check is only done for the first testing day, as some piping connections were new. An igniter check happens for every new test series. Shortly before the actual hotfire there is an audiovisual signal of a siren and a light, indicating the test beginning. The light continues operating during the tests

In between hotfires: To accelerate cooling in between the experiments to reach a reasonable initial T_{cc} , indirectly observed by two surface temperature measurements on each segment, compressed air was utilized. This intermediate process serves to guarantee that the temperature in the copper chamber, especially the throat, does not reach more than about 550 K, after which the mechanical integrity of the material could be compromised [6] and to have nearly same initial conditions for the tests. Another reason is to wait long enough so that the temperature profile inside the CC is fairly homogenised, in order to have a clearly defined initial condition of a temperature field for the application of the IHCM. The state of the chamber and TBC were checked in between testing with an endoscope.

4.4.1. Test Configurations

Uncoated Tests: The testing of the uncoated segment ended with no noteworthy events. In Figure 4.8 the flame cones of 10 bar tests can be seen. It is interesting to note that a lower ROF, like in Figure 4.8b, generally exhibits a rather yellow and red flame as the fuel content is higher opposed to a blue and white flame for high ROF, like in Figure 4.8c. The tested load points can be seen in Table 4.6.



(a) Unc. 10 bar at night ROF 3.1



(b) Unc. 10 bar ROF 2.7



(c) Unc. 10 bar ROF 3.5

Figure 4.8.: Comparison of the uncoated hotfire flames at 10 bar at night and for low and high ROF

Lessons learned of Uncoated Case: After first testing the uncoated configuration, it became apparent that especially the drill holes of the thermocouples close to the hot gas wall, which are the deepest, showed temperature measurements lower than expected when compared with neighbouring TC positions. After visual inspection copper oxide from previous testing campaigns was found, which insulates the TC

Table 4.6.: Test details for uncoated configuration

No.	p_{cc} [bar]	ROF [-]	\dot{m}_{tot} [g/s]	t_{cc} [s]
1	4.35	2.63	64.39	3.00
2	4.34	2.60	64.39	5.00
3	4.63	3.01	67.89	3.00
4	4.61	2.99	67.47	3.00
5	4.60	3.44	67.65	3.00
6	4.55	3.42	66.93	3.00
7	8.82	2.68	128.80	3.00
8	9.03	2.57	131.91	3.00
9	9.41	3.03	136.14	3.00
10	9.39	3.04	135.77	3.00
11	9.38	3.44	136.14	3.00
12	9.35	3.45	135.70	3.00
13	11.40	2.61	165.88	3.00
14	11.36	2.62	165.21	3.00
15	11.67	3.02	168.33	3.00
16	11.63	3.02	167.77	3.00
17	11.99	3.41	173.40	3.00
18	11.95	3.41	172.69	3.00

from direct contact with the copper material. For the ceramic and metallic case, they were cleaned with isopropanol and a drill. This improved the response, but as can be found in Section 4.5 and Table 4.9 the TC in the throat area were still exhibiting lower values. One reason being that as the inner contour in this area is quite far from the outer one, the wire between the springs that push the thermocouples in place and the ferrule probably bent, reducing the contact pressure of the TC tip.

Ceramic Tests: As the boundaries of the ceramic coating were explored step by step, data could also be gathered for a higher load point than design point, namely 15 bar and ROF 3.1. The tested load points can be seen in Table 4.7.



(a) Met. 10 bar normal



(b) Met. 10 bar with TBC particles

Figure 4.9.: Comparison of the metallic hotfire flames at 10 bar and ROF 3.5 (last test)

Metallic Tests: During the last two tests it was noticed that the flames displayed white areas and the sound of the test suggested anomalous issues. The last test is displayed in Figure 4.9, where Figure 4.9a is happening shortly before the flame in Figure 4.9b. Here the upper part of the flame contains a white trail, parts of the coating being burned. After inspection, the TBC was found to have spalled and partially melted, therefore further testing was terminated.

Table 4.7.: Test details for ceramic configuration

No.	p_{cc} [bar]	ROF [-]	\dot{m}_{tot} [g/s]	t_{cc} [s]
1	4.48	2.62	65.97	2.00
2	4.40	2.57	65.32	5.00
3	4.49	2.93	66.13	3.00
4	4.63	3.05	68.05	4.99
5	4.65	3.40	68.33	3.00
6	4.59	3.38	67.55	5.00
7	8.68	2.63	126.79	3.00
8	8.67	2.64	126.80	5.00
9	9.30	3.10	134.66	3.00
10	9.27	3.11	134.27	3.00
11	9.16	3.53	133.35	3.00
12	9.11	3.51	132.60	3.00
13	11.80	2.66	171.18	3.00
14	11.88	2.68	172.41	4.71
15	12.02	3.04	173.22	3.00
16	12.00	3.02	173.02	4.11
17	12.18	3.41	175.79	3.00
18	12.20	3.43	176.20	4.45
19	15.04	3.12	216.18	3.00
20	14.83	3.10	213.19	3.08

Table 4.8.: Test details for metallic configuration

No.	p_{cc} [bar]	ROF [-]	\dot{m}_{tot} [g/s]	t_{cc} [s]
1	4.46	2.73	65.80	3.00
2	4.41	2.71	65.28	5.00
3	4.57	3.09	67.06	3.00
4	4.53	3.08	66.70	5.00
5	4.64	3.61	68.58	3.00
6	4.51	3.51	66.86	8.52
7	8.99	2.69	131.23	3.00
8	9.01	2.68	131.61	5.00
9	9.37	3.01	135.79	3.00
10	9.39	3.01	136.36	4.76
11	9.41	3.57	136.87	3.00
12	9.40	3.54	137.05	4.27

4.5. Data Post-Processing

As the IHCM is inherently ill-posed and very sensitive to the quality of the data input [29], the transient temperature profiles and level were thoroughly investigated. A general rule of thumb is that the TC display rather too low values, due to an improper contact with the specimen, if the reference temperature is equal to the other TC installed. If the sensors could be explicitly identified as problematic, they were not taken into account for the data evaluation. Every test case showed different problematic sensors, listed for all hotfire configurations in 4.9, as they were newly installed every time by changing the CC1 element. The influence of bigger hotspots was discarded for filtering the TC for the HF evaluation, as previous tests showed a good mixing of the propellants and the different circumferential positions for one axial planes were thus not taken into consideration, also stated in Section 7.2.3. Different problems, listed were

distinguished:

- the sensor was missing, due to clogged TC drill holes.
- the temperature maximum, compared in one axial plane was not correlating with the distance from the hot gas wall. For example the TC CC3_6a sensor is the closest to the throat and should have the maximum in the CC3_6 plane, which was not the case.
- the curve of the TC featured a very moderate slope.
- the temperature maximum was compared with two axially neighbouring TC located at the same radial distance. They were compared in either CC1 or CC3. If one was significantly lower it was excluded.

Table 4.9.: Excluded sensors per hotfire case

case/CC	CC_1	CC_3
uncoated	1a, 3a, 7f	1f, 3a, 5a, 5f, 6a, 6b, 7a
ceramic	1f, 7f	1f, 3a, 5a, 6a, 6f, 7a
metallic	1a, 1b, 3b, 4a, 7b	1f, 2f, 3a, 3f, 4b, 5a, 6a, 7a

5. Thermal Barrier Coatings

This chapter includes the literature research done with respect to different coating applications, materials and their respective best manufacturing techniques. It contains the thermal simulation to determine the desired coating thickness. Furthermore the actual manufacturing process, with their respective process parameters is presented.

5.1. Guidelines for Coating Selection

In this section, practical guidelines and requirements with respect to this project are formulated and summarized. The following points are related to the practical implementation and dimensioning of the coating.

- The surface roughness of the coating has to be as low as possible to provide similar flow conditions to an uncoated chamber
- The coating thickness has to be designed for the nominal load point of 12 *bar* and ROF of 3.1.
- The coating has to be manufactured externally, preferably by an industrial company or a research facility
- Options to investigate and analyse the coating after the experiments has to be assured
- The selection of the manufacturer and manufacturing technique is limited by the inner diameter of the CC segment and the maximum/minimum coating thickness
- The entire inner contour of the segment has to be coated
- The manufacturing process has to ensure a constant thickness over the surface

The following points are taken from [2] and treat the material requirements for thermal barrier coatings, while the first three are the most important ones, defining the material combinations and use cases.

- low thermal conductivity compared to the substrate
- similar thermal expansion coefficient to match the metallic substrate
- good adherence to the substrate
- high melting point
- minimal to no phase transition between room temperature and operating temperature, thereby minimizing significant volume changes that could otherwise result in cracking
- chemical inertness to the combustion products

5.2. Area of Application

Comparing the operating conditions in which the TBC should be used, with the respective fields of applying different coating strategies, is crucial as it gives a hint on the most suitable coating for this work. The operating conditions of a cryogenic rocket engine, gas turbines and the DO engine are compared in Table 5.1. It is important to note that most literature about TBC in rocket engine application are dedicated to medium to large cryogenic rockets, rather than capacitively cooled and low thrust engines, like it is the case for this work. The data concerning the DO engine is taken from [5], while the rocket engine and gas turbine data comes from [16].

Table 5.1.: Operating conditions for rocket engines, gas turbines from and the DO engine

	Rocket Engine	Gas Turbine	DO Engine
CC pressure [<i>bar</i>]	115	25	12
CC temperature [<i>K</i>]	3500	1600	≈ 3300
Wall heat flux [<i>MW/m²</i>]	≈ 80	≈ 2	≈ 4 – 12
Cooling temperature [<i>K</i>]	≈ 30 <i>lH₂</i>	> 300 air	≈ 300 <i>gO₂/gCH₄</i>
Total operational time	minutes	months	minutes
Substrate Material	copper alloy	nickel alloy	copper alloy
TBC system	metallic	ceramic	metallic and/or ceramic

Comparing the conditions in table Table 5.1, it can be deduced that both applications exhibit overlaps with the DO engine. The engine is close to the pressure condition, the heat flux values and the cooling temperature from the gas turbine coating application. On the contrary, the hot gas temperature, the total operational time and the substrate material are coinciding with a rocket engine application. For liquid rocket engines rather metallic coatings are used while gas turbines apply ceramic coatings [8].

As a consequence both coating options are pursued as a coating option for this work. Not only the type of material used for the application is of great importance, but also the combination of a suitable manufacturing technique with their respective minimum and maximum coating thickness.

For example, high heat flux combined with the low thermal conductivity of ceramic coatings will induce extreme temperature gradients, thereby imposing significant thermo-mechanical loads on the coating. As a result thermal overload can only be avoided with a thin coating [16]. The coating thickness for a ceramic coating in a high-heat-flux rocket engine would have to be in the order of 20 μm , which is not possible with conventional thermal spray processes. This leads to the proposition of using metallic coatings, with a higher thermal conductivity without exceeding the maximum operating temperature, thus a larger allowed coating thickness [8]. These factors as well as the feasibility of the solution were of great importance for this project.

5.3. Ceramic Materials

In contrast to metals, ceramics frequently exhibit greater resistance to oxidation, corrosion, and wear, while also offering superior thermal insulation properties. Apart from yttria-stabilized zirconia, other materials such as lanthanum zirconate and rare earth oxides show promise as candidates for thermal barrier coatings [2]. A here referred to as "ceramic" TBC system, consists of a metallic bond coat and a ceramic top coat, which provides thermal and oxidation protection [40].

Providing a low thermal conductivity, ceramics are most appropriate to reduce the heat load and increase the combustion chamber lifetime [7]. Some general features of ceramic materials in this context are:

- high-temperature resistance for high-temperature material degradation [46]
- high thermal stability [48]
- low thermal conductivity, ergo being a good insulator [48]
- high corrosion resistance in combination with metallic substrate materials [48]
- ceramic materials are permeable for oxygen, always needing a bond coat to protect the metallic substrate and facilitate adhesion [8]

5.3.1. Top Coats for a Ceramic TBC System

Different top coats are introduced and a choice is justified. [2]

YSZ: If ceramic coatings are in use, mostly Zirconia (ZrO_2) stabilized with 7 – 8 wt.% of Yttrium (Y_2O_3), also named 7-8YSZ, are used as a top coat, as they are widely studied and provide the best performance. They offer a high thermal expansion coefficient, a low thermal conductivity and are very thermal shock resistant. Their major drawback is the limited operational temperature of $< 1473\text{ K}$, which can be reached in long-term applications, like gas turbines, as the material starts to sinter. Phase transformation starts at 1443 K and the material is prone to corrosion as it is oxygen transparent. [2]

Mullite: Mullite is important as a ceramic material due to its combination of low density, high thermal stability, resistance to harsh chemical environments, low thermal conductivity and favourable strength and creep behaviour. It consists of silicon dioxide (SiO_2) and aluminium oxide (Al_2O_3). Compared to YSZ, mullite has a significantly lower coefficient of thermal expansion and higher thermal conductivity. In addition, mullite has a superior resistance to oxygen compared to YSZ. However, it's worth noting that above 1273 K , the thermal cycling life of mullite coatings is significantly shorter than that of YSZ.

Aluminium Oxide: This material is very corrosion-resistant, non oxygen-transparent and exhibits an elevated hardness. However it owns a high thermal conductivity, a rather low thermal expansion coefficient and starts its phase transformation at 1273 K . Although the application process is quite uncomplicated, it is not deemed the best option for a thermal barrier coating.

As an YSZ coating is the best option regarding performance, background information and accessibility, this TBC was chosen.

5.3.2. Bond Coats for a Ceramic TBC System

These commonly used top coats from Section 5.3.1 are recommended to be combined with an MCrAlY bond coat. The M stands for the elements Co, Cobalt or Ni, Nickel or a combination of the two Co/Ni. Although this TBC system is optimized for a nickel based substrate, the coating system is well characterized, which

makes it reliable coating. This bond coat, typically used in nickel-based aero engines, combines the substrate material Nickel and the top coats main component Yttrium. [40]

As the NiCrAlY bond coat is widely studied and mentioned in nearly all sources studied here, corresponding ceramic coatings, and it is commercially available, this bond coat was selected.

5.4. Metallic Materials

The harsh environment present in rocket combustion chambers necessitates the use of new coating concepts. While a ceramic topcoat normally provides adequate thermal insulation in standard thermal barrier coating applications, the significant cooling heat flux for regeneratively cooled engines, within the rocket combustion chamber, coupled with the high thermal conductivity of the copper wall (which is approximately 15 times greater than that of ceramic coatings), results in sufficient insulation provided by the metallic coatings alone. [7]

The main requirements for the metallic thermal barrier coatings are similar to the ceramic coatings. A low thermal conductivity, high melting temperature, good resistance to hot gas corrosion and sufficient strength even at high temperatures are desired. In addition, the coefficient of thermal expansion should be lower than that of the copper substrate in order to reduce the large differences in expansion due to the high thermal gradient. Metals that meet these requirements include, for example, the nickel-based Rene80 or Cobalt-rhenium alloys (CoRe). [8]

Other options tested in conjunction with rocket engines are different variations of NiAl or NiCrAlY as a stand-alone coating, as well chromium top coats, a mixture of copper and chromium or even copper, chromium and aluminium. These coatings offered a sufficient protection of the chamber wall, as well as a suitable oxidation resistance as reported in literature. For low heat fluxes and isothermal oxidation tests, these coatings exhibited no major damages. [7]

Due to the different chemical composition and material properties of the copper substrate and the thermal insulation layer, it is also advisable to use an adhesion promoter layer for metallic thermal insulation layers, similar to ceramic coatings. Also achieving a reduction of concentration gradients at the interface with the substrate. In addition, the coefficient of thermal expansion should be matched to both the substrate and the thermal barrier coating to reduce delamination due to thermal stresses. [8]

NiCrAlY bond coatings, which are commonly used in gas turbines and aero engines, are not suitable for a rocket engine application. On the one hand, the thermal expansion mismatch between the copper alloy and NiCrAlY leads to the formation of microcracks at the interface and, in severe cases, delamination of the coatings. On the other hand, the chemical gradient leads to interdiffusion between the layers, resulting in the formation of diffusion pores at the interface. Consequently another approach for bond coats had to be found, resulting in an experimental mixture presented in Section 5.4.2. [7]

5.4.1. Top Coats for a Metallic TBC System

Rene80: It is an alloy already frequently used in turbomachinery, although, more as a material for turbine blades. It exhibits a high solidus and thus service temperature of 1493 K , a good high thermal strength and oxidation and hot corrosion resistance. Rene80 is also commercially available as a coating powder with

the desired particle size and does not have to be laboriously manufactured as a custom-made product [8]. Even at surface temperatures of about 1350 K the coating withstands supersonic flows in rocket engines [13]. The chemical composition in weight percent is $Ni - 14\%Cr - 9.5\%Co - 5\%Ti - 4\%Mo - 4\%W - 3\%Al$ [11].

CoRe: Co-Re alloys have been specifically developed for applications beyond the temperatures of traditional Ni-based superalloys. These alloys can achieve melting temperatures of up to 1900 K , which facilitates higher coating thicknesses than with Rene80. Chromium is incorporated into the alloy composition to facilitate the formation of a protective Cr_2O_3 layer which provides robust protection against high temperature oxidation [44].

The coefficient of thermal expansion of both top coat alloys is in the range typical for NiCrAlY alloys and is therefore lower than the coefficient of thermal expansion of the NiCuCrAl bond coat, presented below, and copper substrate [44]. In a study examining the long term effects of heat exposure, in respect to the service time of a rocket engine, on a Rene80 and a CoRe system in combination with a NiCuCrAl bond coat. The first one identified a maximum service interface temperature of 900°C , while the latter only achieved one of 750°C before failure occurred [11]. Rene80 exhibits a superior boundary surface porosity, but in other aspects of coating behaviour there is no major difference. Another factor to include is the acquisition cost of CoRe powders being nearly nine times as much as for Rene80 [8]. Following these informations, and the fact that the technical university of Braunschweig was willing to share their knowledge about metallic TBC, the Rene80 coating was chosen.

5.4.2. Bond Coats for a Metallic TBC System

If the substrate is made of copper, which is the case in this work, the best option is to have a copper-alloy base material, that is chemically and mechanically suited as a connector between the substrate and top layer [16].

Starting from the typical NiCrAlY bond coat, the TU Braunschweig, modified this coating into a more suitable option for copper chambers, namely a new NiCuCrAl bond coat. With the chemical deposition in weight percent of $Ni - 30\%Cu - 6\%Al - 5\%Cr$ [11]. The copper addition enhances the chemical compatibility, crucial for a bond coat, causing better interdiffusion and hence adhesion of the coating on the copper substrate. This newly developed coating possesses an intermediate thermal expansion coefficient of the Nickel top coat alloy and the copper [7]. This bond coat is successfully tested in combination with a Rene80 top coat as a research project in the german SFB Transregio 40 project, deeming this combination as a good alternative to ceramic coatings in rocket engines, with a focus on cryogenic rocket engines [8].

5.5. Manufacturing Techniques

The specific operational requirements of rocket engines require a suitable coating technique. Following the choice of coatings from Section 5.3 and Section 5.4, an appropriate coating technique for a ceramic and a metallic coating had to be identified. For the ceramic coating it is necessary, that the manufacturing technique allows rather thin coatings, also in terms of future applications in a regeneratively cooled engine, where findings of this thesis should be applicable. While for the metallic coatings, due to their higher

thermal conductivity, the requirement was to determine a technique capable of producing a dense but preferably thicker coating than for the ceramic case. But before anything else the manufacturing processes had to be feasible with the existing geometry and the financial and time budget. The aim was to coat the inner cylinder of the cylindrical combustion chamber, not the throat segment with an even smaller geometry. Manufacturers located in Germany were preferred. Another factor to consider, was that both top and bond coat should be able to be coated with the same technique, minimizing the labour costs at each provider.

5.5.1. Ceramic Coating Techniques

Plasma spraying, physical vapour deposition and chemical vapour deposition are commonly used for ceramic coatings [16]. The latter is excluded here, as it only provides a low disposition rate, ergo a small coating thickness [25].

Plasma Spraying Method (PS): Plasma spraying involves melting powdered spray material using a plasma jet, which can be generated inside or outside the spray gun, before depositing it onto the workpiece surface. The plasma is typically produced by burning gases like argon, helium, nitrogen, hydrogen, or their mixtures. During this process, these gases undergo dissociation and ionization, resulting in high exhaust velocities that transfer heat energy to the spray particles upon recombination. The arc itself occurs within the spray gun between a centrally positioned electrode (cathode) and a water-cooled spray nozzle acting as the anode. This technique is versatile and applicable in various environments, including standard atmospheric conditions, inert gas flows (such as argon), vacuum chambers, and even underwater settings. Specialized nozzle attachments are also used to generate high-velocity plasma for specific applications. It is a line of sight process, meaning that the area that can be coated needs to be accessed in a direct path by the plasma jet [37]. The high temperatures facilitate a significant volume of particle melt, which, when combined with high particle velocities, results in exceptional deposition densities, low porosity coatings, and improved bonding between the coating and substrate compared to other thermal spraying processes.

In plasma spraying, the average grain diameter of the spray powder is typically around $50\mu m$, with a maximum grain diameter of up to $80\mu m$. The resulting coatings have a roughness of about $3\mu m$, resulting in melting the particles. As a result, plasma spray coatings are approximately one order of magnitude thicker than the desired thickness for high-heat-flux regeneratively cooled rocket engine. Although this might not be suitable for engines of this caliber, it would be very much appropriate for the DO use case, which ranges between a high-thrust rocket engine and a gas turbine application in terms of coating, see Section 5.2. [16]

Electron Beam Physical Vapour Disposition (EB-PVD): In the process of Electron Beam Physical Vapor Deposition, a target anode is subjected to bombardment by a highly energised electron beam generated by a charged tungsten filament within a high-vacuum environment. The electron beam induces a transition of the target atoms into the gaseous phase. Subsequently, the highly energised atoms condense onto surfaces within the vacuum, forming a thin, solid coating composed of the material from the anode [25]. The minimal thickness that is able to be achieved is much smaller than the ones with the plasma spraying technique, making it an interesting candidate for rocket engine coatings as well [16]. As described

in [41] this technique is also a line of sight process, which limits the application for small interior geometries.

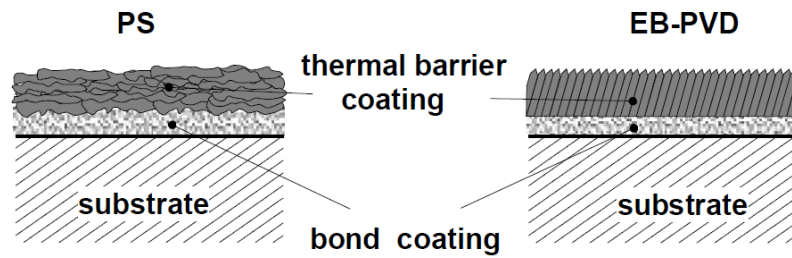


Figure 5.1.: Microstructure of PS and EB-PVD technique [16]

Technique Comparison: The Plasma Spraying technique is typically associated with the production of a lamellar structure in coatings. This structure is characterised by the presence of an extensive network of microcracks between individual lamellae, which contributes to the coating's strain tolerance, depicted in Figure 5.1. In contrast, the electron beam physical vapor deposition technique results in the formation of a columnar microstructure of the coating. Although the grain boundaries between individual columns may be weak, they still provide effective strain tolerance for the brittle ceramic material, providing it with a good tolerance against thermo-shocks. This feature gives it a considerable advantage in lifetime compared with the plasma spraying technique. It has been demonstrated that zirconia coatings applied by electron beam physical vapour deposition exhibit a cyclic life approximately one order of magnitude greater than plasma sprayed coatings in gas turbine airfoils. [16]

Table 5.2.: Main features of ceramic coating techniques PS and EB-PVD

	PS	EB-PVD
Microstructure	lamellar	columnar
Thickness [mm]	0.2 – 3	0.1 – 0.3
Bonding	mechanical	chemical
Surface [K]	rough	smooth

The main differences are elucidated in Table 5.2. Summarizing these findings, both methods would be applicable to this work, while EB-PVD would be a better choice regarding the lifetime of the coating. This method was not chosen, for the simple reasons of financial and acquisition issues, as no provider could be found that was willing to coat the single piece, with such a restricted geometry for a reasonable price. In succeeding projects, this technique could be evaluated again. Thus the focus lied on the plasma spraying method, which is also deemed the most versatile in respect to components of any dimension in [46].

5.5.2. Metallic Coating Techniques

The method mostly mentioned in connection with metallic coatings is the HVOF, thus presented here. High-speed flame spraying involves a continuous combustion process in a combustion chamber at elevated pressure. Powdered spray material is introduced into the centre axis of this chamber. The high pressure generated by the combustion of the fuel gas-oxygen mixture, coupled with the downstream expansion nozzle, produces the desired high gas jet velocity. As a result, the spray particles are propelled at significant

speeds, resulting in densely coated surfaces with excellent adhesion properties. The moderate temperature input ensures minimal metallurgical alteration of the sprayed material during the process, such as the formation of mixed carbides. As a result, this process produces exceptionally thin coatings with precise dimensional accuracy. [37]

The primary advantage of HVOF spraying over other atmospheric spraying processes is its high particle velocity. This characteristic results in a short exposure of the particles to the oxidizing flame, resulting in low oxide content in the coatings, typically less than 1%. In addition, the high kinetic energy of the particles facilitates relatively good adhesion and contributes to the formation of a dense coating structure with porosity typically less than 1%. A thermally grown oxide at the interfaces, similar to that observed in gas turbine coatings is unlikely for a metallic coating applied with HVOF. This can be explained as an effect of the relatively dense HVOF coatings resulting in low oxygen permeability. [7] Using HVOF as a the manufacturing method of choice for metallic coatings will enhance the critical stress intensity factor for crack propagation for the better, because of its lamellar structure [13]. The optimal coating parameters are contingent upon a number of factors, including the melting temperature, heat capacity, particle size and oxidation resistance of the coating material. Consequently, it is only possible to ascertain these parameters through comprehensive parameter studies [8].

5.6. Failure mechanisms

This section is included, because the test campaign of the metallic coating had to be interrupted due to failure of the coating.

When designing coatings for high-heat-flux regeneratively rocket engines, it is critical to predict whether cracks will propagate into the substrate. This has to be done with extensive studies of the coatings themselves. Crack propagation into the substrate can result in critical damage to the cooling channels and even failure of the entire rocket engine. However, it is also possible for cracks to bend as they reach the substrate and propagate along the substrate/coating interface. This propagation can occur in Mode I, where bending moments are caused by the stress gradient, or Mode II, where tensile loads act in the coating. Understanding and predicting these crack propagation mechanisms is essential to ensure the reliability and longevity of rocket engine components. [7]

Failure Mechanisms of Ceramic Systems: For experiments involving large heat fluxes and resulting significant temperature gradients the occurrence of delamination, buckling and spalling of coatings in general can be expected. Especially, for the bond coat of a ceramic system, as used in aero engines, the thermal expansion between the copper and the NiCrAlY bond coat can lead to microcracks at the interface [7]. The high pressure and temperature of the hot gas can induce sintering of the porous ceramic top layer, leading to an increase in thermal conductivity and subsequent ageing of the coating. The extreme temperature differences across the coatings, coupled with the cyclic operation of the rocket engine, contribute to a reduction in the life of the coatings due to material fatigue. When for example liquid hydrogen (LH_2) is used as a cooling medium, it can cause thermal expansion of the liner, resulting in significant thermo-mechanical stresses on the coating. This has to be considered for any regeneratively cooled application. [16]

For the common NiCrAlY bond coat and YSZ top coat system on a copper substrate, the formation of thermally grown oxide at the bond coat/substrate interface is unlikely, which excludes this failure mechanism. That effect can further be prevented if the bond coat is mullite or alumina based [2]. This can be attributed to the relatively short operating times in rocket engines. On the other hand this plays a key role in the failure mechanisms of thermal barrier coatings on nickel-based substrates in turbomachinery as the operating times are significantly longer than in rocket engines. [40]

Failure Mechanisms of Metallic Systems: When metallic coatings in rocket engines are subjected to thermal shocks and significant heat fluxes, two primary failure modes can occur: vertical cracking and buckling. Buckling happens when materials are under major compression and deform suddenly. These failures result from the significant thermal gradient induced by the large heat flux. Vertical cracks are formed due to tensile strains in regard to thermal shocks induced by regenerative cooling. The buckling happens due to compressive strains caused by the different coefficients of thermal expansion during thermal cycling. [7]

In "classical" TBC applications in gas turbines, the ingress of hot gas into cracks is a relevant concern, as the cracks tend to open during the hot gas phase. However, in rocket combustor walls, the greater temperature gradient results in significant compressive loads on the coatings during the hot gas phase. As a result, the cracks are often closed again, reducing the risk of hot gas ingress. [13]

Consideration of Crack Formation: During the design process of the coatings thicknesses, the topic of crack estimation during hot fire, arose and a crack propagation analysis was considered. If the porosity of the coating is not significantly higher than for a coating made with a spraying angle of 90° , at least the mechanical properties are comparable to the respective empirical material data [8]. However during the coating process, thermal stresses are introduced into the coating itself, due to thermal cycling of the iteratively building the coating iterations and the fact that the powder is undergoing a phase conversion. The residual stresses after the manufacturing process can not be estimated without precise knowledge of the temperatures in the layer and substrate during the coating process. A superposition of compressive stresses due to the high impact of the particles, tensile stresses due to cooling and stresses caused by the hotfire itself occur. Additionally also the different coefficients of thermal expansion of the layer and substrate would have to be taken into account. [1]

An analysis of this kind was however discarded after consulting with the Technical University of Braunschweig. A decent crack propagation analysis is a rather complicated process, including way more tests and experiments with the coating itself, determining variables like thermal cyclic behaviour, exact material properties, cavities etc. A simple analytical approach would not deliver reliable data. As a result, this was not deemed necessary for this thesis.

5.7. Thermal Simulation

In order to properly predict the effect of the coatings on the combustion chamber setup, a thermal simulation, realized in Matlab, was done. The hot gas properties needed for the convective heat transfer

coefficient correlation, in order to simulate the combustion process were obtained from the NASA program CEA, developed by Sanford Gordon and Bonnie McBride..

This program facilitates the calculation of the fluid temperature and the ideal characteristic velocity, using its built-in rocket problem feature. Within this framework, the "injector" plane is assumed to correspond to the injector face plate, while the "combustion end" denotes the termination point of the cylindrical chamber section. In particular, the temporal evolution of temperature resulting from reaction kinetics and atomisation processes is often neglected due to the limitations of CEA in capturing such dynamics. The fluid properties required for heat transfer analysis are then derived from the output of this computational tool, while assuming an equilibrium composition [20]. In equilibrium flow, it is assumed that the local gas composition depends solely on the local thermodynamic conditions. This theoretically necessitates an infinite residence time of the gases or an infinite chemical reaction rate. In practice, this assumption holds true to a large extent within the combustion chamber for all non-complex rocket fuels. [21]

The physical model domain is created and set-up the same as described in Section 6.4.2, with a cross sectional profile of the igniter ring and the two combustion chamber segments. The major difference between these two models is the fact that this simulation includes two additional domains, adjacent to the first, the completely cylindrical segment, CC element. The two domains, the top and bond coat span over the whole length of the first combustion chamber segment, namely 80 *mm*. The boundary conditions are set analogous to Section 6.4.3, apart from the convective hot gas boundary condition, elaborated in Section 5.7.2, that were simulated and not subjected to optimization. The simulation was set for a duration of 3 *s* as this was the aspired testing time. The initial condition for the domain was set at 293 *K* as the expected initial temperature.

Special care was taken in respect to the mesh in the coating area, as the dimensions differ significantly at the transitional zone to the combustion chamber segment, because of the major discrepancy of coating versus chamber thickness. As a consequence, the mesh was refined in the coatings and for the minimal case of a top coat and bond coat thickness (ceramic case) both being 50 μm , two cells in radial direction were the minimum. Even after a variation of the mesh parameters, this amount could not be increased.

5.7.1. Coating Modelling

For the analysis, the bond coat was set to a constant value of 50 μm for both coating systems throughout the parameter variation. In [8], this thickness is deemed optimal for a metallic coating system, while in [46] similar thicknesses are recommended for the bond coat. As the bond coat is not crucial for reducing temperature itself, this analysis focuses on the variation of different top coat thicknesses. The top coat thickness was evaluated in $\Delta d_{tc} = 50 \mu m$ increments for five cases for each coating configuration, which are listed in Table 5.3. Taking into account all the information gathered on coating thicknesses, with specific reference to [8] for metallic and [2] for ceramic systems, and consultation with coating manufacturers, this range of topcoat thicknesses has been selected.

Table 5.3.: Thickness variation

	d_{tc_1}	d_{tc_2}	d_{tc_3}	d_{tc_4}	d_{tc_5}
Ceramic Configuration	50 μm	100 μm	150 μm	200 μm	250 μm
Metallic Configuration	150 μm	200 μm	250 μm	300 μm	350 μm

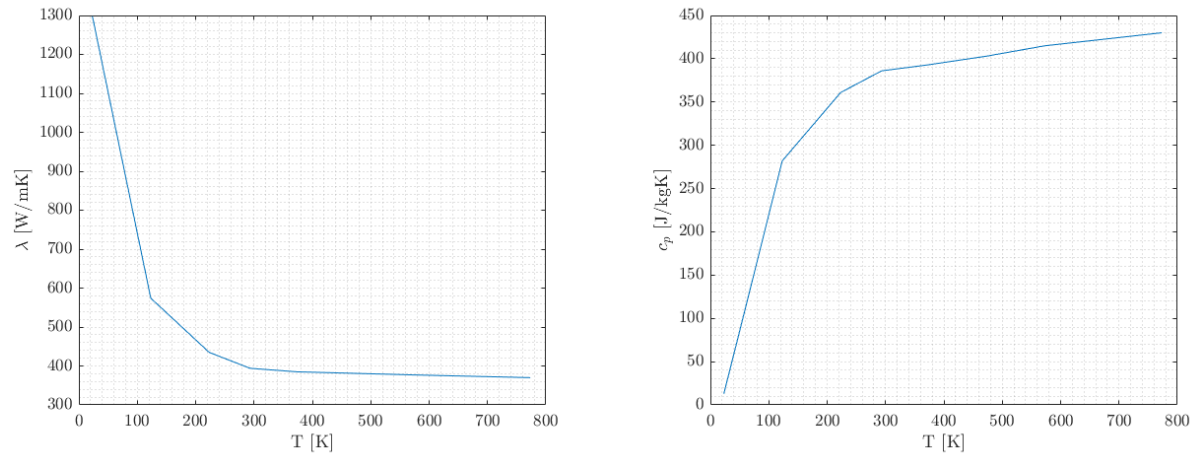


Figure 5.2.: Thermal conductivity and specific heat capacity of copper from [6]

In general the material properties were linearly inter- and extrapolated. The density was taken as a constant value for all materials. During the evaluation attention was also paid to the maximum service temperature of the materials, to determine the upper limit of the top coat thickness range, therefore this data is given too. The copper substrate was modelled with [6] as a source, the density is extracted as 8930 kg/m^3 and is depicted in Figure 5.2.

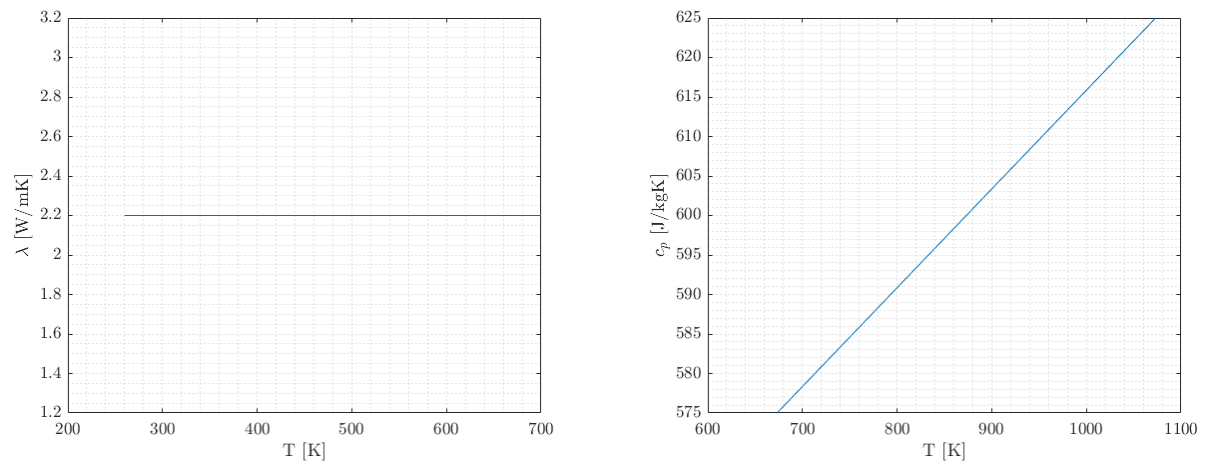


Figure 5.3.: Thermal conductivity and specific heat capacity of YSZ from [35]

The material parameters for the metallic coating system of the ceramic YSZ top coat from [35], shown in Figure 5.3, and the NiCrAlY bond coat from [1], shown in Figure 5.4. The density of the top coat was taken as 6000 kg/m^3 and the bond coat thickness as 6900 kg/m^3 . The maximum service temperature of the bond coat is given as 1250 K in [1] and the top coat as 1470 K where sintering occurs, originating from [2].

The material parameters for the metallic coating system of the Rene80 top coat, shown in Figure 5.5, and the NiCuCrAl bond coat, shown in Figure 5.6, which is an experimental mixture, are extracted from [9]. The density of the top coat was assumed as 7930 kg/m^3 and the bond coat thickness as 7670 kg/m^3 . The maximum service temperature of the bond coat is given as 1170 K in [10] and the top coat as 1270 K [27].

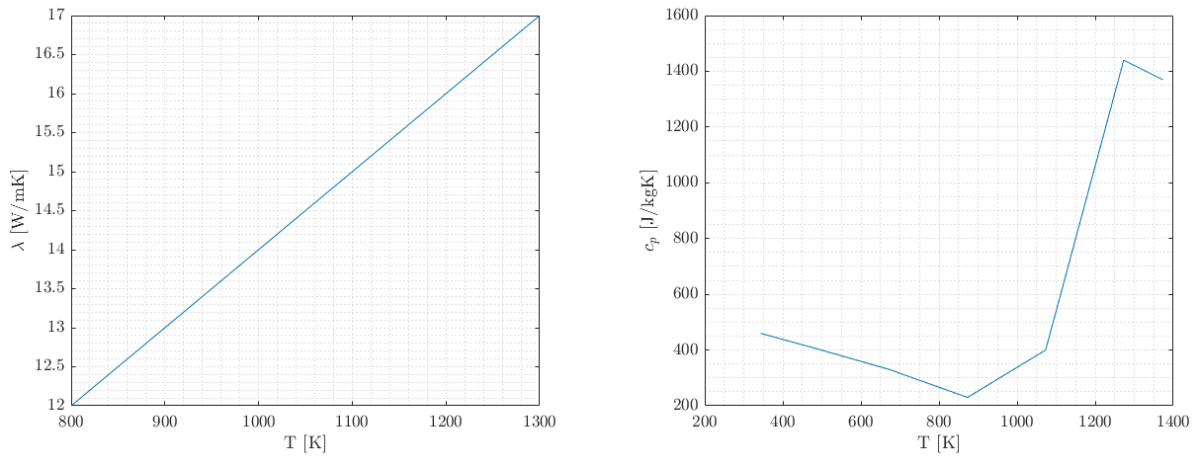


Figure 5.4.: Thermal conductivity and specific heat capacity of NiCrAlY from [1]

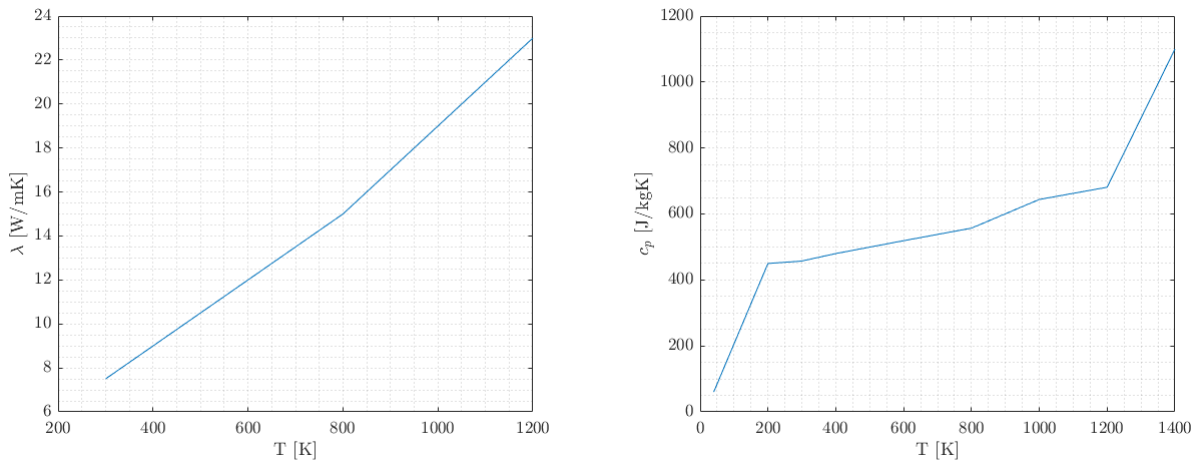


Figure 5.5.: Thermal conductivity and specific heat capacity of Rene80 from [9]

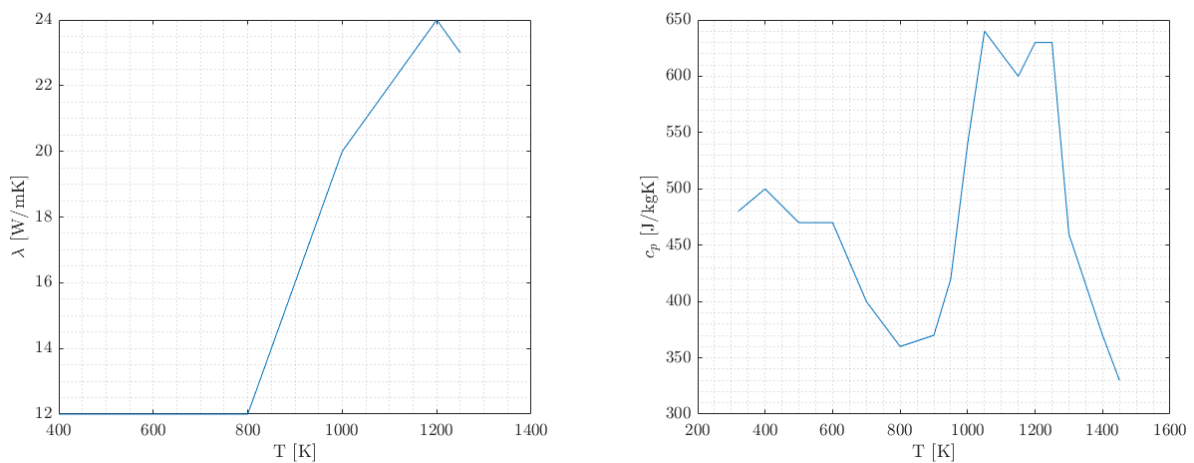


Figure 5.6.: Thermal conductivity and specific heat capacity of NiCuCrAl from [9]

5.7.2. Convective Heat Transfer Modelling

The modelling of heat transfer within a capacitively cooled structure of a combustion chamber can be divided into the following sub-problems, which are taken as an orientation for the heat transfer modelling [20]:

- Determination of fluid properties and gas composition.
- Evaluation of the heat transfer coefficient at the inner wall of the CC.
- Calculation of heat conduction within the chamber wall.
- Evaluation of the heat transfer from the outer CC wall to the ambient environment. This might be neglected in case the outer wall temperature is low.

The first two items are evaluated in this section, although radiation was neglected as the main driver of heat transfer from the hot gases to the CC walls is forced convection [21]. The third component was done by the Matlab solver itself and point number four was neglected, as the outside chamber wall did not reach temperatures for which radiation would be important (maximum wall temperatures of about 380 K), neither included was natural convection as it is deemed insignificant (values in the order of 10 [W/m²K] [32] versus expected heat fluxes of 4 – 12 [MW/m²]).

Important effects and connections of convective heat transfer are extracted from [20] and are the following:

- a) Impact of the wall temperature on the heat flux
 - b) Impact of choice of heat flux coefficient correlation
 - c) Influence of imperfect mixing and reaction kinetics
- a)** The reference temperature (T_{ref}) used for calculating the physical properties of the hot gas in the correlations can either raise or lower the heat transfer coefficient, and consequently the heat transfer, depending on the gas composition and temperature regime. The wall temperature is determined by the energy balance, which is influenced by factors such as the heat flux coefficient, recovery temperature (as shown in Equation (5.2)) and thermal conductivity. In the case of transient behavior, the specific heat capacity of the chamber and TBC material, need to be modelled as well, to depict time dependent material behaviour. [20]
- b)** Since the heat flux coefficient is directly proportional to the heat flux, the choice of formula is crucial. The Sinyarev correlation [42], which was ultimately used, was developed and tested for metal-based combustors at low to moderate wall temperatures. However, like most heat flux correlations, it inadequately models or entirely overlooks factors such as soot deposition on the chamber wall, materials of the combustor with low thermal conductivity, and effects within the turbulence and boundary layer, including wall roughness. As a result, in these scenarios, the calculated heat transfer coefficient can significantly differ from experimental results. [20]
- c)** As previously noted, the effects of mixing, atomization, and reaction kinetics are neglected because these factors are not included in the underlying CEA program, which is used to calculate the hot gas

temperature and fluid properties. However, the Bartz [4] and Sinyarev [42] correlations incorporate axial positions and local speed into their calculations, as shown in Section 5.7.3. [20]

Assumptions: From [43] a combustion efficiency η_{c*} of 95% was assumed. A recovery factor of $r = 0.8$ is used, details in Section 3.3.2, more detailed explanation in Section 3.3.2. This is an empirical value that normally varies between 0.7 – 0.9 and a value of 0.8 was found to be conservative but rather realistic in the past [20]. The hot gas properties (T_{hg_i} , Ma_i and κ_i), used in Equation (5.2), were calculated one time beforehand for the whole combustion chamber length and interpolated for the respective axial position (i) for the following equations. Assumptions for the CEA program were: the estimations of a sea level application, 12 *bar* and an ROF of 3.1 for a methane and oxygen combustion, which corresponds to the design point of the engine, and the geometric parameters of the nozzle. In this way, using Equation (5.1), also the mass flow was determined.

$$\dot{m} = \frac{p_{cc} A_{th}}{c^*} \quad (5.1)$$

Both HTC correlations presented here, Bartz and Sinyarev, use the adiabatic wall temperature in their equations, outlined in Section 3.3.2. Combining Equation (3.8) and Equation (3.9), Equation (5.2) was altered equal as in [42], to accommodate the recovery temperature, which is taking imperfect combustion and incomplete heat recovery into account.

$$T_{aw_i} = T_{hg_i} \left(1 + r \cdot \left(\left(1 + \frac{\kappa_i - 1}{2} \cdot Ma_i^2 \right) \cdot \eta_{c*}^2 - 1 \right) \right) \quad (5.2)$$

The mean of the adiabatic wall temperature and the respective current wall temperature at the axial position, to be found in Equation (5.3), are used to evaluate the hot gas properties for the correlations, as proposed in [21], which is an adaptation done from the original definitions. Through T_{ref_i} , the hot gas properties, the thermal conductivity of the hot gas λ , the specific heat capacity c_p , the dynamic viscosity η and the Prandtl number Pr , utilized in the correlations are calculated.

$$T_{ref_i} = \frac{T_{w_i} + T_{aw_i}}{2} \quad (5.3)$$

Two correlations, namely the Bartz and Sinyarev correlation were employed to predict the effect of the coating on the combustion chamber. In principle these two correlations are quite similar, although they incorporate different boundary conditions. Bartz takes the impact of the Mach number and the temperature gradient inside of the boundary layer into account, while Sinyarev only considers the latter. The Sinyarev model was developed for low to moderate CC wall temperatures and Bartz model is used for various operating conditions [42]. While they have proven rather good agreement with kerosene-oxygen mixtures [21], they need adjustment for the methane-oxygen combination, which is why it was referred to [42].

The original formulations of the correlations are found in Equation (5.4) for Sinyarev [42] and Equation (5.5) and Equation (5.6) for Bartz from [4]. d_{th} is the diameter of the throat, d_h is the local diameter and r_c is the radius of the curvature at the throat, both taken from the actual geometry.

$$Nu = 0.0162 \cdot (Re \cdot Pr)^{0.82} \left(\frac{T_{aw}}{T_w} \right)^{0.35} \quad (5.4)$$

For Bartz d_{th} is the diameter of the throat and r_c is the radius of the curvature at the throat, both taken from the actual geometry.

$$Nu = 0.026 \cdot Re^{0.8} \cdot Pr^{0.4} \left(\frac{d_{th}}{r_c} \right)^{0.1} \cdot \sigma \quad (5.5)$$

$$\sigma = \left[\frac{1}{2} \cdot \frac{T_w}{T_{aw}} \left(1 + \frac{\kappa - 1}{2} Ma^2 \right) + \frac{1}{2} \right]^{-0.68} \cdot \left[1 + \frac{\kappa - 1}{2} Ma^2 \right]^{-0.12} \quad (5.6)$$

Sinyarev Correlation: The parameters C_1 , C_2 and C_3 from Equation (5.7) can be adapted and optimized for the specific combustion chambers and propellant combinations. The parameters were taken from [42] as there is as well a methane oxygen propellant combination used, although it is to note that in this literature a coaxial injector was used. Due to a lack of other sources providing information about the heat flux correlation coefficients that would better fit the configuration of a swirl injector, a TBC and the methane-oxygen mixture, this correlation was used to provide a first estimation of the influence of the TBC on the heat flux.

$$\alpha_{Sinyarev} = C_1 \cdot \frac{\lambda^{(1-C_2)} \cdot (\dot{m} \cdot c_p)^{C_2}}{d_h^{(1+C_2)}} \cdot \left(\frac{T_{aw}}{T_w} \right)^{C_3} \quad (5.7)$$

In order to understand the constraints of the Sinyarev model, the coefficients are explained and portrayed in Table 5.4. The coefficient C_1 is used to adapt variations associated to the units. The factor C_2 is a indicator of the interaction of the individual flames. C_2 stands for the expected reduction of the pressure dependency and is directly proportional to the mass flow. As the enthalpy flow ($\dot{m} \cdot c_p$) is reduced in [42], the hot gas properties are over-estimated and thus are corrected by lowering the original C_3 coefficient marginally. The parameters are taken from table 7.1 in [42], while the adaptation of the HTC for an undeveloped flame near the face plate and a reduced adiabatic wall temperature at the same location was not taken into consideration, as a swirl injector does not enforce such behaviour due to better mixing.

Table 5.4.: Original and from Silvestri optimized Sinyarev HTC correlation parameter

	C_1	C_2	C_3
Original	0.01975	0.82	0.35
Silvestri optimized	0.01750	0.79	0.33

Bartz Correlation: Considering the same ideas as mentioned above for the Sinyarev model, the parameters for the Bartz correlation were also extracted from [42]. The coefficients own the rather similar physical explanations.

$$\alpha_{Bartz} = B_1 \cdot \left(\frac{c_p}{\eta} \right)^{B_2/2} \cdot \frac{\lambda^{(B_2-0.2)} \cdot \dot{m}^{B_2}}{d_h^{(1+B_2)}} \cdot \left(\frac{d_{th}}{r_c} \right)^{0.1} \cdot \sigma \quad (5.8)$$

$$\sigma = \left[\frac{1}{2} \cdot \frac{T_w}{T_{aw}} \left(1 + \frac{\kappa - 1}{2} Ma^2 \right) + \frac{1}{2} \right]^{-(B_2+B_3)} \cdot \left[1 + \frac{\kappa - 1}{2} Ma^2 \right]^{-B_3} \quad (5.9)$$

Finally Equation (3.10) was used to calculate the heat flux along the CC axis and imposed as a boundary condition on the physical domain.

Table 5.5.: Original and from Silvestri optimized Bartz HTC correlation parameter

	B_1	B_2	B_3
Original	0.0315	0.8	-0.12
Silvestri optimized	0.0183	0.79	-0.1283

5.7.3. Heat Transfer Coefficient Correlation Comparison

With the purpose of identifying an appropriate HTC correlation to predict the influence of the TBC on the system, the Sinyarev and Bartz correlation from Section 5.7.2 were compared with a 12 bar and $ROF = 3.1$ load point heat flux from [5]. This load point is the design point of the engine.

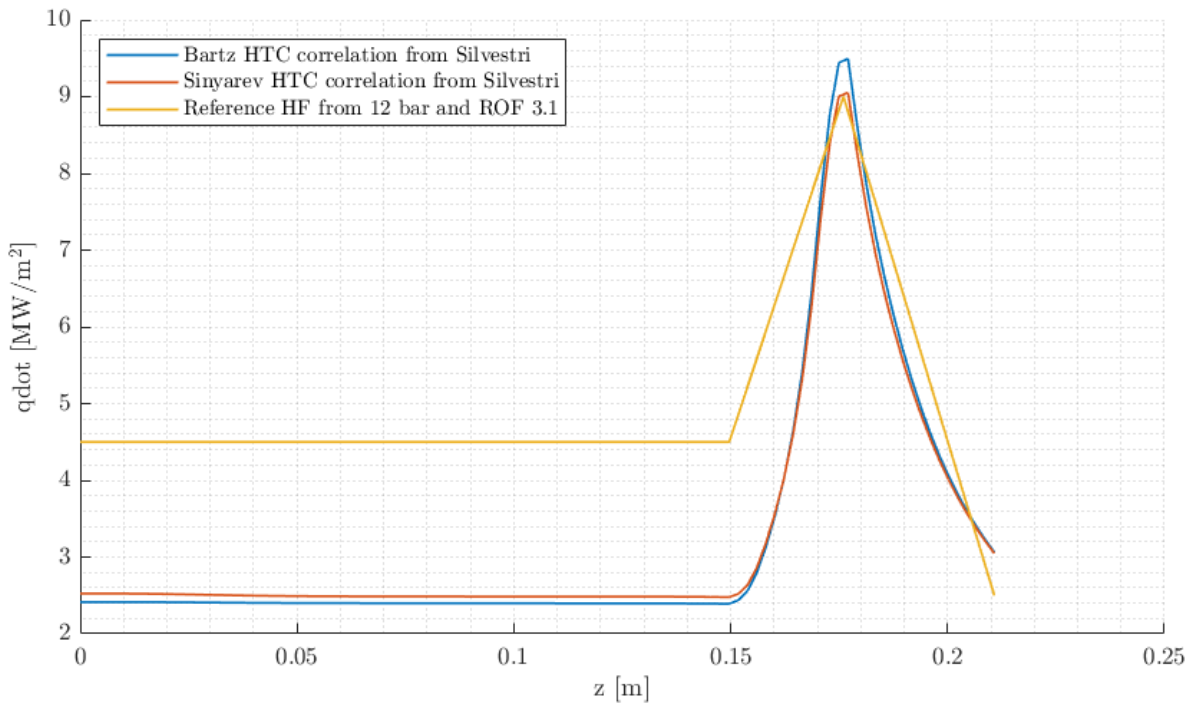
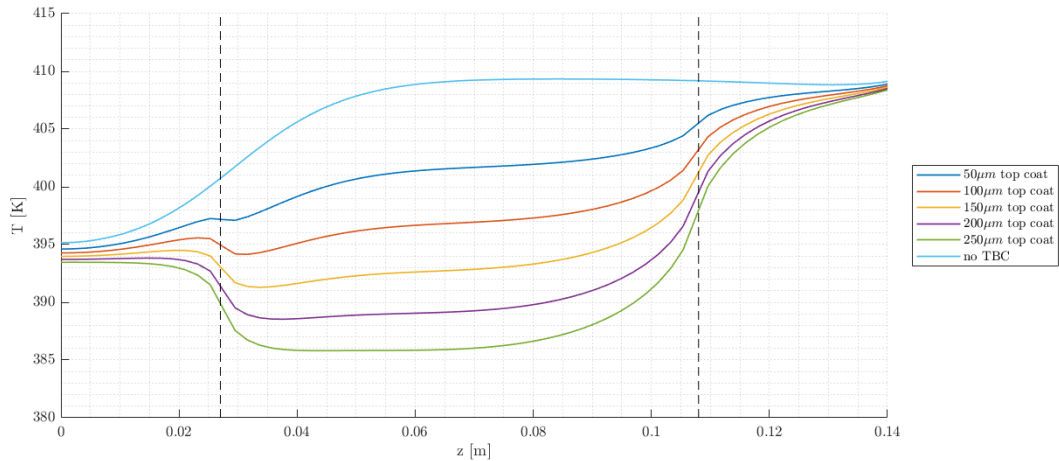


Figure 5.7.: Comparison of the Sinyarev and Bartz HTC correlation with a 12 bar and $ROF = 3.1$ load point heat flux

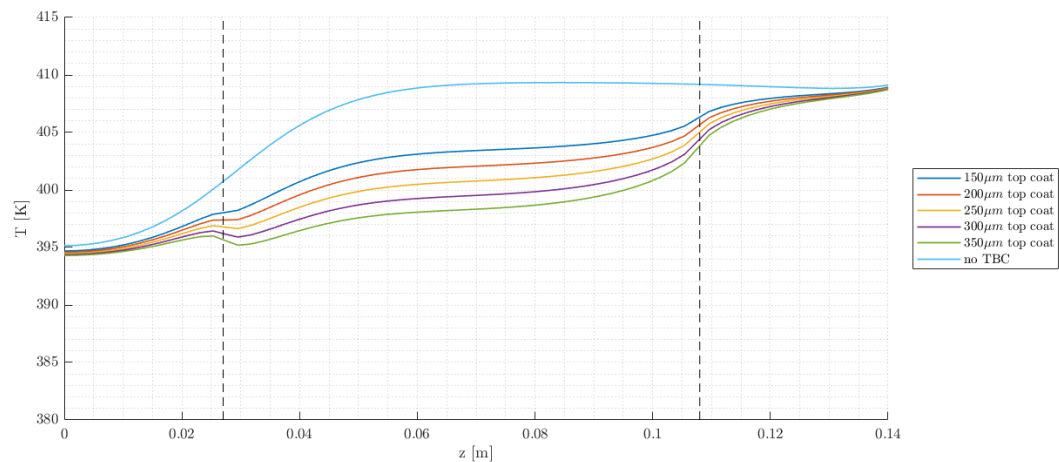
As can be derived from Figure 5.7, both correlations are under-predicting the heat flux in the cylindrical part of the chamber and thus constant in the heat flux value of about 44%. Since the parameters for these correlations were sourced from [42] and specifically adapted for their methane-oxygen engine, the similarity between the correlations is understandable. As there was no heat transfer coefficient (HTC) correlation evaluation conducted at DO, these existing correlations were used.

The under-prediction is most likely caused by the fact that [42] uses a coaxial injector and thus, the optimization of both parameter sets focused on different aspects of the combustion behaviour. The Bartz correlation over-predicts the heat flux value in the throat of circa 5.5%, compared to the Sinyarev correlation, agreeing nearly accurately. For this reason and as the Sinyarev correlation exhibits a slightly higher heat flux in the constant cross section, this correlation is used for further purposes.

5.7.4. Coating Thickness Analysis



(a) Temperature profile of the copper surface along the z -axis for a ceramic TBC system

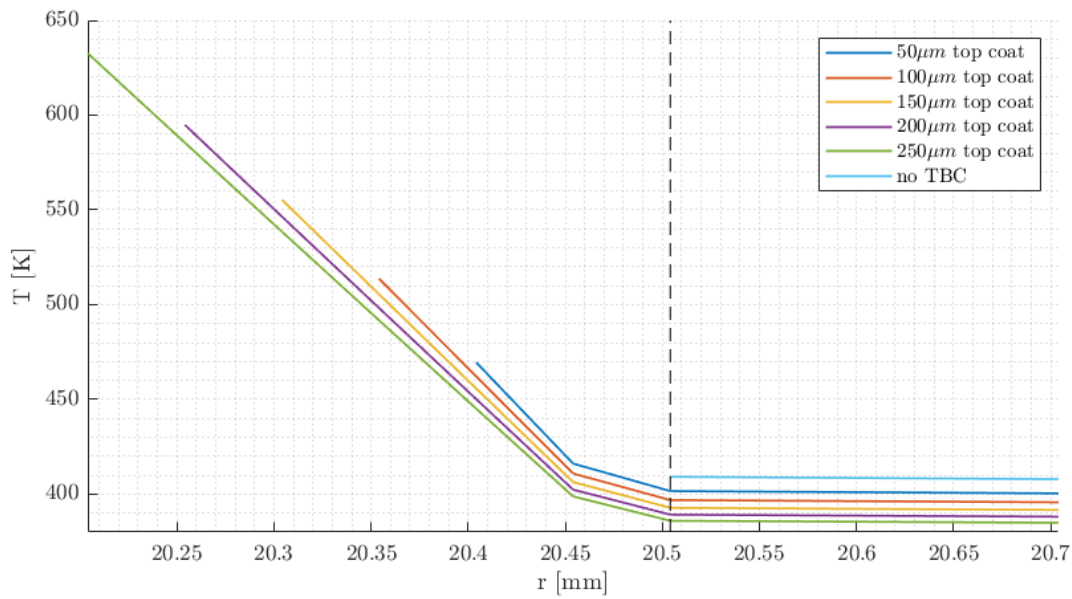


(b) Temperature profile of the copper surface along the z -axis for a metallic TBC system

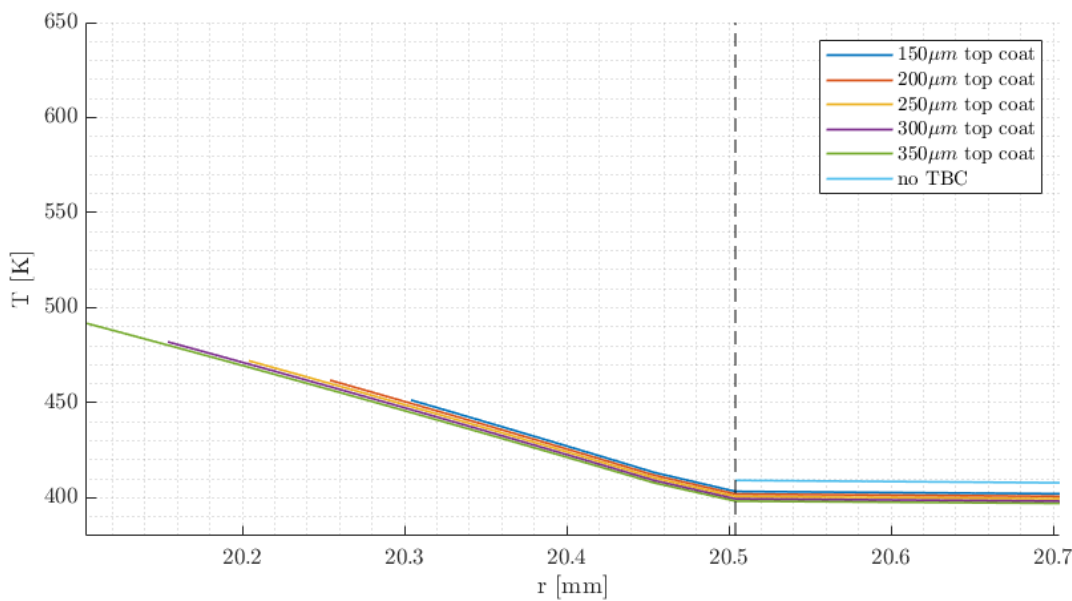
Figure 5.8.: Temperature profiles of the copper surface along the z -axis for different TBC systems with a focus on CC1

The following results were generated with the information of the materials and HTC correlations described prior. Figure 5.8 shows the influence of different thicknesses on the temperature profiles of the copper surface after 3 s. As the temperatures align with the ones of the uncoated configuration shortly downstream (most of CC3 except the beginning) of the depicted domain, this is no focus of the analysis. Especially temperatures in CC1, between the dashed lines are of interest. It can be seen that the biggest difference in temperature is found in the middle of CC1, which is why Figure 5.9 is plotted at this axial position

radially.



(a) Radial temperature profile of the TBC and copper for a ceramic TBC system



(b) Radial temperature profile of the TBC and copper for a metallic TBC system

Figure 5.9.: Radial temperature profiles of TBC and copper for different TBC systems with a focus on the interface

If Figure 5.8a and Figure 5.8b are compared directly it is striking that the ceramic coating provides a greater temperature reduction by an addition of $50 \mu m$. As the temperature reduction effect sinks, ergo is detrimental to increasing coating thickness for both systems, the maximum difference achieved from $50 \mu m$ to $100 \mu m$ for the ceramic coating and $150 \mu m$ to $200 \mu m$ for the metallic coating is about $\Delta T_{met,max50\mu m} = 1.36 K$, while the ceramic configuration provides $\Delta T_{cer,max50\mu m} = 4.75 K$. This results in a factor of 3.5 in temperature reduction per $50 \mu m$. The minimum is established in a value of

$\Delta T_{cer,min50\mu m} = 3.24 K$ for the ceramic system and of $\Delta T_{met,min50\mu m} = 1.19 K$ for the metallic system for the last two coating thicknesses respectively. As explained in paragraph a) in Section 5.7.2, this effect originates in a reduced heat transfer due to a higher coating wall temperature, whose increase over the different coating thicknesses can be taken from Figure 5.8.

Figure 5.8a exhibits a rather striking drop for the maximum coating thickness analysed and the temperature along the copper surface only starts rising significantly, two thirds downstream of CC1, while even for the maximum thickness in Figure 5.8b, the temperature continues rising over the whole CC1, after a marginal drop.

If equal thicknesses ($150 \mu m$) for both TBC systems are compared (Figure 5.9), applying a ceramic coating reduces by a maximum temperature by $15.53 K$, while the metallic only achieves a maximum reduction of $8.06 K$. This is also visible in Figure 7.13, as only the selected thicknesses are depicted. To underline the major differences in coating surface thicknesses of the ceramic coating system in Figure 5.9a and Figure 5.9b, the axis ranges were chosen to be equal. For a thickness of $250 \mu m$, the ceramic coating reaches a temperature of $630 K$ and the metallic one of only $470 K$, which for both coatings below the maximum service temperature given in Section 5.7.1. The transition from top to bond coat, created by the different thermal conductivities is way more visible in Figure 5.9a than Figure 5.9b for the metallic system.

The heat flux for the nominal load point is under-predicted, Figure 5.7, meaning that for real conditions at the same load point, the surface temperatures of the coatings will be differ significantly, which also has a positive impact on the insulation effect of the TBC, resulting in expecting a better result for the design load point of the engine, referring to Section 7.2.1. This has to be also taken into account regarding the maximum service temperature of the YSZ and the Rene80. With rising coating thickness also the cooling effect sinks relatively, as demonstrated above and thermal strain may become so dominant that it leads to cracks, as pointed out in [2] and [1]. As a consequence, a trade-off between a desired reduction in temperature and avoiding failure of the coating has to be done. The appropriate thickness ranges were researched and after analysing the temperature reductions, and taking information about feasible coating thicknesses from the manufacturers into account, this leads to the conclusion that a top coat thickness of $t_{cer,tc} = 150 \mu m$ and $t_{met,tc} = 250 \mu m$ are optimal. They were combined with a bond coat thickness of $t_{cer/met,bc} = 50 \mu m$ for each system, explanations in Section 5.7.1.

5.8. Coating Manufacturing Process

This section gives an overview of the application specific manufacturing processes for ceramic and metallic coatings as well as details on the manufacturing procedure of the selected coatings.

Overall it proved difficult to find a company or university partner to coat the segments. The major problem turned out to be the exceptionally limited space to be coated. The small diameter of $41 mm$, the fact that the surface to be coated was an inner cylinder and the ratio of diameter to length being 2, turned out to be the significant problems. This was limiting the mode of application, the choice of manufacturing process, as the application device had to be either operating from a distance or being equipped with a small dimension itself, without compromising the quality of the coating. The diameter to length ratio entailed the need for a creative solution approach as coating from one side of the part and in

one stroke seemed difficult. In both manufacturing processes, the coating was applied from both openings to the half of the cylinder by an angle of about 45° from the rotary axis, as a vertical application was not possible. The angle was defined by the diameter to length ratio. Coating a single piece is generally not economically feasible.

The requirements for the manufacturing technique included that the front and back face, which were sealing surfaces were not to be coated. Neither the outside of the segment should be coated, as the pressure sensor threads and thermocouple drilling holes needed to stay clear from coating remains. On the inside, the pressure sensor holes to measure the combustion chamber pressure needed to stay unclogged.

5.8.1. Ceramic Coating Approach

The company of choice was rhv-Technik [36], agreeing to coat the CC segment as a "sample part", while being extremely generous and professional.

Final Process: Some pilot tests on flat test pieces were done by the company, to gain knowledge about the manufacturing parameters in combination with the copper substrate. Before the coating could be applied, the inner cylinder surface was sand blasted to roughen the surface as a preparation to facilitate adhesion.

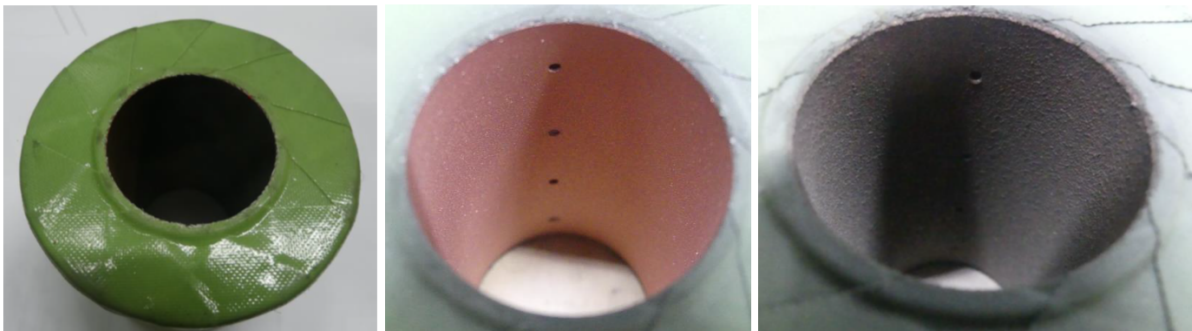


Figure 5.10.: Masking of the segment, after sand blasting and after bond coat application

As a next step, the NiCrAlY bond coat was applied with an approximate thickness of $\approx 50 - 70 \mu m$, after which the top coat made of zirconium oxide with an approximate thickness of $\approx 150 \mu m$ was layered above. Both materials were supplied in powder form. The part was masked with a heat-resistant adhesive tape in order to protect the non-coated areas, depicted in Figure 5.10 in green. During the application process the copper chamber got cooled with liquid carbon dioxide, to keep the thermal load inside the copper substrate as low as possible, because the manufacturing technique itself is based on a high heat input into the coating powders. The layers were built up from both sides at an angle deviating 45° from the rotary axis, covering the same surfaces multiple times for each coat, while the part itself was clamped on a rotary table.

For the ceramic coating no diffusion annealing was necessary, as the coating technique guaranteed a satisfactory adhesion. With the aim of reducing the effect of surface roughness on the convective heat transfer as much as possible, the manufacturer polished the surface. In this way also the overlap created by the manner of application was removed.

Surface Roughness: The arithmetic mean roughness value is abbreviated with R_a and the mean roughness depth with R_z . After sanding, the copper exhibited an $R_a = 6.6\mu\text{m}$ and $R_z = 40.5\mu\text{m}$. The bond coat had an $R_a = 6.0\mu\text{m}$ and $R_z = 47.1\mu\text{m}$, similar to the copper surface, and the top coat had an $R_a = 4.2\mu\text{m}$ and $R_z = 23.5\mu\text{m}$ before and $R_a = 0.9\mu\text{m}$ and $R_z = 7.9\mu\text{m}$ after polishing.

5.8.2. Metallic Coating Approach

The metallic coating was done by Dr. T. Fiedler from the Materials Science Institute of the Technical University Braunschweig [45]. For this experimental work the close cooperation with the Technical University of Braunschweig provided more insight into the manufacturing process and is thus described in greater detail. Details to the coating are provided in Table 5.6.

Table 5.6.: Important metallic coating material parameter

	Bond Coat	Top Coat
Name	NiCuCrAl	Rene80
Manufacturer	Nanoval (custom powder)	Oerlikon Metco (Diamalloy 4004NS)
Composition [wt%]	Ni-Cu30-Al6-Cr5	Ni-Cr14-Co9.5-Ti5-Mo4-W4-Al3
Powder size [μm]	+20/ - 50	+11/ - 45
Manufacturing technique	HVOF	HVOF

Pre-manufacturing Steps: As the coating technique was not as precise, that only the inside of the cylinder could have been coated, an attempt to mask the test cylinder with a glass-fiber reinforced high-temperature tape was made. The idea to manufacture a cask cover encasing the CC was discarded because of time issues. Instead, the risk that excessive material would be removed from the sealing surfaces, was taken. The aftermath of this is described in Section 7.1.2.

As a preparation for the coating, a chamfer on the inner edges of the cylinder of approximately 0.3×45 was sanded. Then the part was cleaned with isopropanol and was immersed in an ultrasonic bath in ethanol. For each side of the sub-layer the sealing surfaces were covered with tape, the lower half of the inner surface covered with an aluminium cylinder. Then the inner surface was sandblasted and cleaned with compressed air and ethanol. For every iteration the masking was renewed. After cooling down, the part was turned over, the masking removed and cleaned in ethanol. No ultrasonic bath was used because of the already existing layer. Then the whole process was repeated.

Set-up Description All the test pieces were clamped on a rotary table and were unevenly cooled with pressured air, as an aspiration system is used to transport the exhaust gases of the manufacturing process out of the enclosure containing the coating robot. As a consequence, the flame of the robot was slightly diverted from the to be coated object, reducing the precision with which the flame could be aimed at the surfaces. In order to create a homogenous coating layer, the robot had to move perpendicular to the rotary axis in x -direction, depicted in Figure 5.11. Hence the flame overlapped with the mask, which resulted in a high thermal load on the tape.

Pilot Tests: In total three different tests were conducted, determining the manner of application, meaning movement in $x - y - z$ -direction of the robot, depicted in Figure 5.11, the number of layers to achieve the

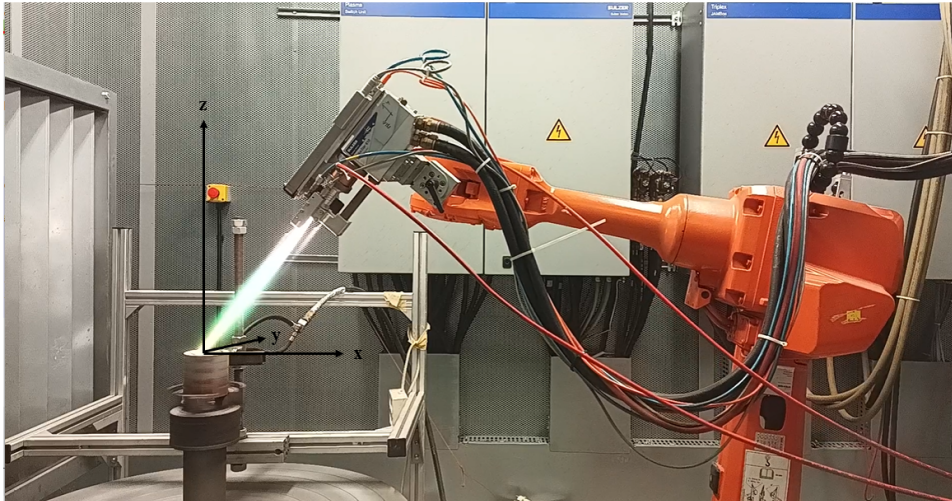


Figure 5.11.: HVOF robot setup with rotary table and robot guiding in x -direction from [45]

Table 5.7.: HVOF feeding and process settings

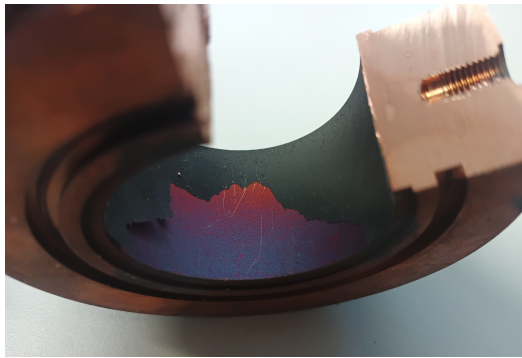
	kerosene [l/h]	oxygen [slpm]	stoichiometry	CC pressure [MPa]	spray distance [mm]	angle
Bond Coat	16.2	650	0.8	5.0	400	45°
Top Coat	18.0	680	0.8	5.5	300	45°

desired layer thicknesses for bond and top coat, as well as the robot crossing speed over the segment. The feeding and process settings can be taken from Table 5.7, more background information about the process parameter can be found in [12].

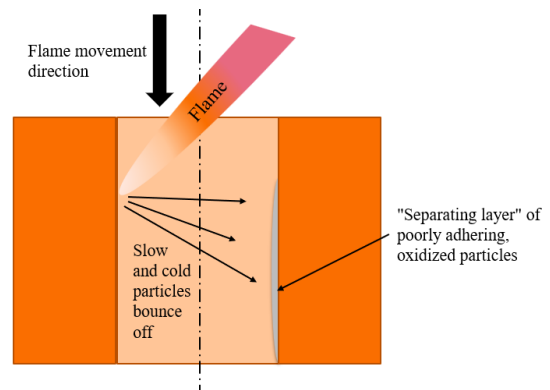
Two translational speeds in x -direction were tested, namely 22 mm/s and 44 mm/s . The first test coating was done for both top and bond coat with the low velocity and an iteration of layering of 2, while the direction of spraying was from along the z -axis, so from bottom to top. For the second test, these values were doubled. The third pilot test used the fast proceeding velocity and four layers for the bond coat and the low speed and three layers for the top coat. The direction of spraying for the last two pilot tests was from down the z -axis, so from top to bottom. For the pilot tests only one side needed to be coated, as the pilot cylinder was by far shorter than the actual CC segment.

First Pilot Test: The reason why the z -direction of the coating process got changes was because the first pilot case exhibited a very poor layer adhesion on the bottom of the cylinder, the part coated last. The coating was easy to remove with nearly no force, while on the contrary the upper part stayed. Below the peeled off coating, combustion products deposited on the surface and an oxidized layer was formed on the copper, visible in Figure 5.12a. The reason for this to happen is visualized in Figure 5.12b. The flame is getting swirled inside of the cylinder while coating, because the specimen mount only allows for the gases to exit through the cylinder and the flow is deflected nearly 90°, leading to a higher pressure inside of the cylinder. These effects lead to a strong heating of neighbouring surfaces and hence oxidation. Through the swirl, slow and cold particles from the outer part of the flame bounce off and collide with the opposite surfaces, not yet coated. This leads to a separating layer of copper oxide build-up, which hinders the coating to adhere. As the flame is pointed downwards into the cylinder and for this test it the flame

movement direction was from top to bottom, this effect developed.



(a) First pilot test with poor layer adhesion due to process errors



(b) First pilot test process error

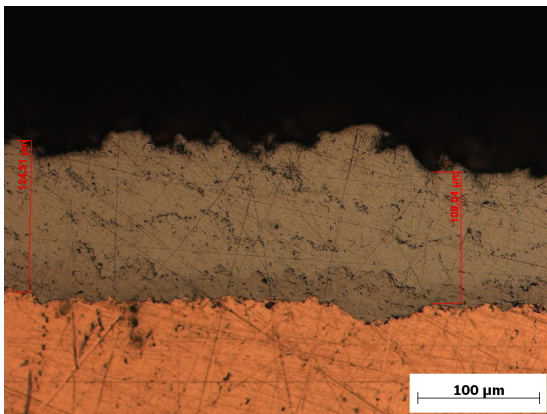
Figure 5.12.: First pilot test from [45]

For further tests the direction of the flame movement was reversed, so that potentially cold and slow particles land on the already coated surface. Furthermore the coating speed was increased, to avoid heating up the copper substrate as much and the specimen was cooled with pressurized air. This change in settings was successful.

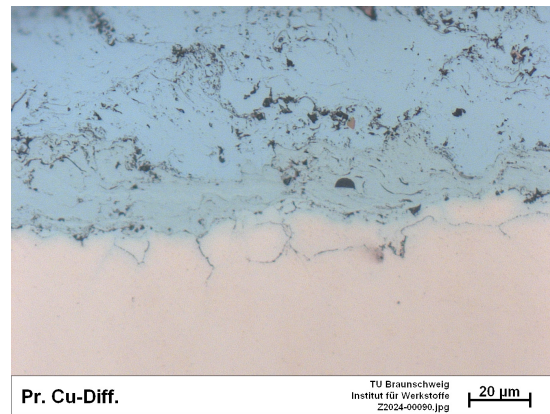
Second Pilot Test: The second pilot test exhibited a rather ripply and rough surface. The ripple seems to depend on the robot's traversing speed. At slower speeds, the freshly applied, still hot and therefore soft, layer components are likely to be flattened by the following particles. At higher speeds, on the other hand, the formation of roughness peaks is favoured because the new layer products are not developed quickly enough and the particles cool down. The solution is to apply the bond coat quickly to reduce the heating of the copper substrate and quickly achieve a covering protective layer. The top coat is applied slowly because the copper surface is already protected and the layer is reasonably smooth.

Third Pilot Test: This test was used to confirm the statements made prior. A cross cut of the coating was done and a very low porosity was noticed. To enhance layer adhesion a trial of diffusion heat treatment at 700°C at $6h$ at an argon inert gas atmosphere was done. This effect on the metallic bond coat, also reducing the growth of delamination cracks, can be found in [18]. No major cracks were found and a good interdiffusion could be observed, documented in Figure 5.13b. Smaller cavities and oxidation at the interface between copper and coating are noticed, which were to be expected for a spraying angle of 45° .

Final Process: The final product used 22 mm/s of robot forward velocity for the top coat, coated in 4 iterations, and 44 mm/s for the bond coat, coated in 7 iterations for each of the two sides to achieve the final layer thickness. The bond coat was $45 - 50\ \mu\text{m}$ and the top coat approximately $250\ \mu\text{m}$ thick, resulting in a total thickness of approximately $300\ \mu\text{m}$. The coating was done from both sides, using an aluminium cylinder inside of the CC segment, sealed with high-temperature tape, to mask and protect the side, that was not to be coated. This resulted in a bulge in the middle of the chamber, which was sanded but not removed completely. After coating the diffusion heat treatment was done. Post-manufacturing steps are described in Section 7.1.2.



(a) Final pilot test with respective process parameters before heat diffusion treatment



(b) Final pilot test with respective process parameters after heat diffusion treatment

Figure 5.13.: Effect of heat treatment on third pilot test from [45]

6. Inverse Heat Conduction Method

An essential factor in the design of a regeneratively and subsequently also a capacitively cooled chamber is the maximum specific heat flux, typically found around the smallest chamber diameter more precisely in the throat region [43]. This chapter describes the theory and the process of determining the specific heat flux from available temperature data. Details regarding the direct solver employed and an overview of the code is given.

For this problem the inverse heat conduction method in combination with a conjugate gradient algorithm is utilized, where a special focus was put on defining the conditions for a suitable sensitivity matrix, stopping criteria and a mesh study. A sensitivity analysis concerning the spatial and temporal discretization was done. In this document the specific heat flux is referred to as heat flux for reasons of simplicity.

6.1. Basic Concepts of Inverse Heat Transfer Problems

Inverse Heat Transfer Problem (IHTP) utilize temperature and/or heat flux measurements to estimate unknown quantities in the analysis of thermal engineering issues. For example, inverse problems in heat conduction typically involve estimating an unknown boundary heat flux using temperature measurements taken below the boundary surface. In a classical direct heat conduction problem, the cause (boundary heat flux) is known and the effect (temperature field in the body) is determined. Conversely, the inverse problem involves estimating the cause based on the known effect. The difficulties encountered in solving IHTPs should be acknowledged. Mathematically, IHTPs are generally classified as ill-posed because their solutions can become unstable due to errors inherent in the measurements used in the analysis. [29]

When a physical domain with time-dependent boundary conditions, a given initial condition and possessing the thermophysical properties c_p , ρ and λ is given and the temperature distribution $T(x, t)$ within the solid is computed over time and position, this is called the Direct Problem, which is usually described by Partial Differential Equation (PDE).

Consider a similar problem to the one described above, with the same properties, except that this time the time-dependent boundary condition at the surface is unknown. The goal is to determine the unknown boundary condition resolved in time and space. To compensate for the lack of information on the boundary condition, in the domain measured temperatures are used over a specified time interval. This is referred to as an Inverse Problem, more precisely to a boundary IHTP because it involves estimating the unknown surface conditions. [29]

"In the direct problem the causes are given, the effect is determined; whereas in the inverse problem the effect is given, the cause (or causes) is estimated." [29]

IHTP can be tackled through either parameter estimation or function estimation methodologies. When

there is partial knowledge about the functional form of the unknown quantity, the inverse problem simplifies to the estimation of a limited set of unknown parameters. They can be linear or non-linear, one-, two or three-dimensional. IHTP can be classified into the nature of heat transfer process involved, for example IHTP of conduction, or the type of causal characteristics, such as IHTP of boundary conditions. If a boundary heat flux is to be resolved in time, the full time domain approach should be used as the time discretisation can be as small as desired. [29]

The direct problem can be solved, for example, by numerical or polynomial approaches. The inverse problems are solved by minimising an objective function. This objective function contains the difference between the measured and estimated temperature vectors, whose result is subject to minimisation. The point at which minimization is satisfactory is decided by a stopping criteria. [29]

For this thesis the Finite Element Method (FEM) solver of Matlab was used to solve the Direct problem, while the Inverse Problem was computed by a CGM.

6.2. Conjugate Gradient Method Optimization

Different optimization algorithms exist, that could be used. The Newton-Raphson method, the Levenberg-Marquardt method and the Conjugate Gradient method were examined, however the latter was reckoned to be most feasible for this problem, being the only method reaching convergence.

The CGM is a robust iterative technique used to address both linear and non-linear inverse problems in parameter estimation. In each iteration, an optimal step size is combined with a descent direction to minimize the objective function, which is the temperature difference between measured and estimated values. The descent direction is calculated by linearly combining the negative gradient direction of the current iteration with the descent direction from the previous iteration. This ensures that the angle between the descent direction and the negative gradient direction is less than 90° , which guarantees minimization of the objective function. When equipped with an appropriate stopping criterion, determining when the error, based on the temperature difference between measured and estimated temperatures, is sufficiently small, the CGM is considered an iterative regularization technique. These algorithms typically involve a reasonably large number of iterations to achieve stable solutions for the inverse problem [29]. For this use case of the CGM, the parameter in question is the heat flux at the hot gas wall of the CC.

The dynamics of IHCM is inherently unstable, which implies that small variations in input variables, such as temperature, lead to significant and oscillating fluctuations in output variables, such as heat flux [32]. Therefore a careful validation of the method and cautious choice of input data, detailed explanation in Section 4.5, to avoid data incongruity is essential.

In general for problems like this, the heat flux is a continuously applied boundary condition across all points of a geometry. However, optimizing the heat flux value individually at each point in contact with the fluid would significantly increase computational costs and exacerbate the problem's ill-posed nature [32]. The more optimization points are set, the higher the problem's degrees of freedom. But this happens without augmenting the information input, when the setup is not changed, as no additional thermocouple measurements are added. Therefore, in the approach selected and outlined here, parameters are only assigned to locations where at least one temperature sensor is present. As a result no optimization points at $z = 0$ and $z = z_{end}$ were set, and these domains outside of the other points were modelled, see

Section 6.4.3. If the number of parameters N remains smaller than the number of spatially independent thermocouples M , an over-determined problem formulation is formed. At each time step and iteration, adjustments are made to the values of these N parameter points to minimize the residuals ϵ_{rms} and ϵ_{std} , described in Section 6.5.4.

Theoretical Background: Following equations are all extracted from [29]. $k = 1, 2, \dots, K$ stands for the number of iterations, $j = 1, 2, \dots, N$ for the number of parameter points to be optimized and $i = 1, 2, \dots, M$ for the number of measurement points or sensors.

In order to determine a new heat flux distribution \dot{q}^{k+1} (a vector containing the heat flux values at the parameter points which are subject to optimization) the following equations have to be used. The number and location along the hot gas wall of the spatial discretization points is found in Section 6.6.1. At these locations a variation of the heat flux value is performed for the CGM. J stands for the SM, from Equation (6.12), which does not change over the evaluation of a run so, $J^k = J$, as the SM in [32] was found to be approximately constant over time and thus does not have to be recalculated for every iteration, saving computational time. T_{exp} are the interpolated temperatures for the sensors at the relevant time step. The determined temperatures per sensor are for further clarification written as:

$$T_{calc} = T(\dot{q}^k) \quad (6.1)$$

After solving the direct problem for the initial heat flux distribution and the initial temperature field, the residual is calculated and compared to the stopping criteria and if they are failed to meet, the algorithm proceeds using the following equations.

First the gradient direction ∇S , a vector, is evaluated at iteration k :

$$\nabla S(\dot{q}^k) = -2(J)^T [T_{exp} - T_{calc}] \quad (6.2)$$

Then the conjugation coefficient γ , a value, after Fletcher-Reeves is computed:

$$\gamma^k = \frac{\sum_{j=1}^N (\nabla S(\dot{q}^k))_j^2}{\sum_{j=1}^N (\nabla S(\dot{q}^{k-1}))_j^2} \quad (6.3)$$

The next step consists of the calculation of the direction of descent d :

$$d^k = \nabla S(\dot{q}^k) + \gamma^k d^{k-1} \quad (6.4)$$

Followed by the evaluation of the step size β in a matrix form:

$$\beta^k = \frac{[Jd^k]^T [T_{calc}^k - T_{exp}]}{[Jd^k]^T [Jd^k]} \quad (6.5)$$

With these steps, the new heat flux guess \dot{q}^{k+1} can be calculated with:

$$\dot{q}^{k+1} = \dot{q}^k - \beta^k d^k \tag{6.6}$$

This procedure gets repeated until a stopping criterion is satisfied. The next iteration reuses the old values:

$$\dot{q}^k = \dot{q}^{k+1} \tag{6.7}$$

$$d^{k-1} = d^k \tag{6.8}$$

$$\nabla S(\dot{q}^{k-1}) = \nabla S(\dot{q}^k) \tag{6.9}$$

6.3. Implementation Overview

Matlab was the environment of choice to set up the Inverse Heat Transfer Method (IHTM) and the direct solver. An overview of the workflow of the code is provided in Figure 6.1.

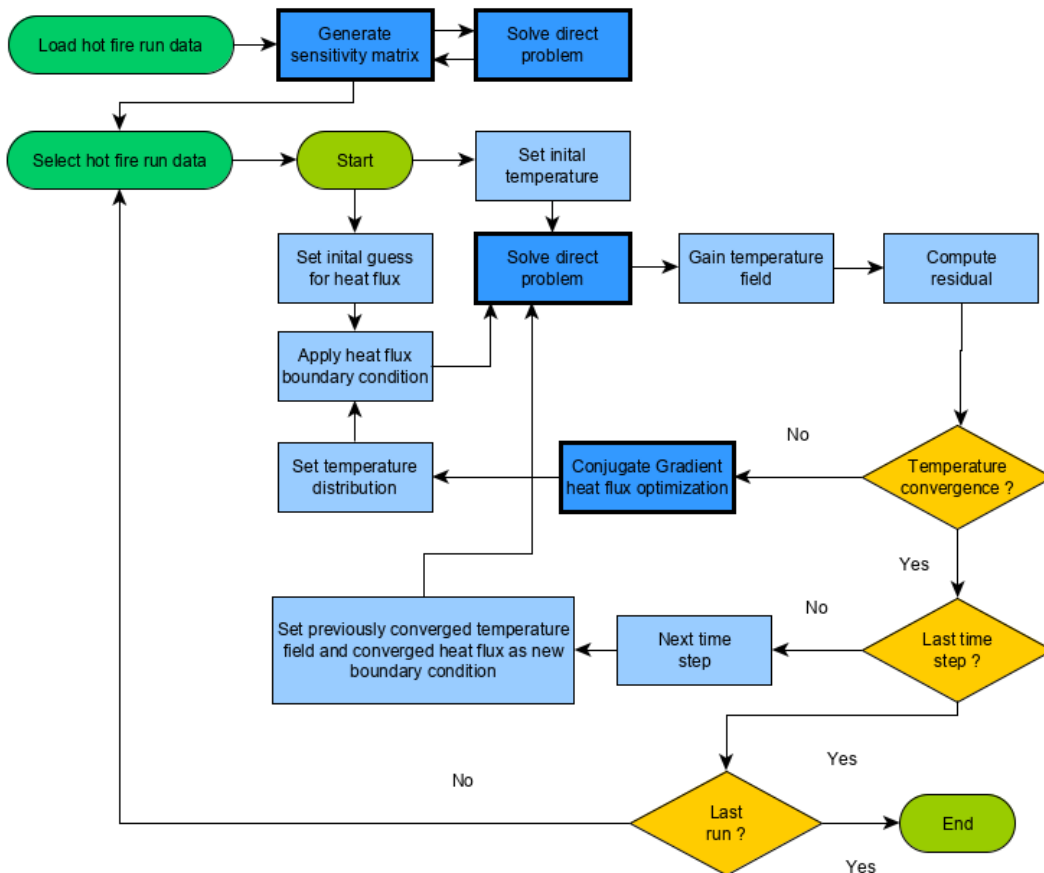


Figure 6.1.: Inverse heat conduction algorithm workflow

Simulation Preparation: As every hotfire configuration has a different amount of data, as explained in Chapter 4, the type of experiment case has to be distinguished. Furthermore a distinction in the sensor lists, containing the r and z coordinates, has to be done, as the metallic configuration is shorter. A choice whether to include optimization points at the very beginning and end of the spatial domain, where no measurement points are available, can be taken. And if no last one is selected, it is possible to specify how the end should be treated, either linearly extrapolated to zero or constantly extrapolated, taking the last known heat value. A desired time discretization can be chosen too. File path and data saving management is done. As the code is written to treat the data of a batch of experiments, the workflow in Figure 6.1 starts with the data input after that, necessary steps for the temporal and spatial discretization of the problem and preparations for the sensitivity matrix calculation are done.

Sensitivity Matrix Calculation: In the next step the sensitivity matrix is generated, using the basic structure of the direct problem with specified initial SM conditions. The matrices are inputs to the actual simulation and are explained in greater detail in Section 6.5.3.

IHCM outer Hotfire Loop: In this loop every hotfire run is handled subsequently. For the first time step of each run, the first heat flux guesses are set accordingly to the pressure load points and the respective SM is loaded. An initial temperature is set for the direct problem. After every successful run, the results are saved and if the batch of data is calculated successfully, the IHCM is ended.

IHCM Time Step Loop: Accordingly to the time discretization the next time step gets initialized to be computed and the previously converged heat flux and the temperature profile is initialised before using again the direct problem for calculation. The direction of descent is set to zero.

IHCM inner iterative Optimization Loop: The altered heat flux guess is treated with linear interpolation as a boundary for the direct problem and is retrieved in compliance with the CGM, described in Section 6.2. After successful computation by multiple iterations, defined by a stopping criteria in Section 6.5.4 testing the convergence, the code proceeds to the next time step or hotfire run. For the first iteration the conjugation coefficient is set to zero.

6.4. Direct Problem Implementation

Depending on how a real problem is modelled, different results can be expected. A hotfire, especially in a capacitively cooled CC is in-stationary in time [31]. This behaviour is reflected by discretizing the run in multiple time steps, which are analysed transiently by finding one heat flux distribution representing the change in temperature over this increment, assuming the HF distribution to be steady state over the time increment. Spatial variations of the temperature and heat flux can be expected as the axial measurement points are distributed in a thin circumferential segment. But they are being projected and modelled in one plane, omitting the 3D profile. The material properties are obtained from temperature dependent correlations from literature. Multiple sensors are used for discrete measurements. The direct solver is employed to address the heat conduction PDE within a simplified geometry, comprising solely the combustion chamber without the fluid domain.

6.4.1. Data Input

As both the temperature and the heat flux are transient values, an evaluation window must be chosen in order to carry out the evaluation of the axial profiles of these values. In regeneratively cooled CC the cooling simplifies the IHTM evaluation as there the problem can be defined as steady-state, opposed to a capacitively cooled chamber, which needs to be resolved transiently [31]. Hence the minimum evaluation window is the operational hotfire duration.

Temperature Data: For the IHCM, the temperature data during the IHCM sequence, found in Figure 4.7, needs to be extracted at the points in time of choice. To realize this, the spatial information of the sensors, that were not excluded from the data set, found in Table 4.9, is loaded. Through the specified discretization, the time data gets determined accordingly and then the temperature for each sensor if necessary interpolated. The data was smoothed on a trial basis, which was done with an Savitzky-Golay filter and smooths according to a quadratic polynomial that is fitted over the evaluation window. But as it can be seen in Figure 6.2, no major effect can be observed except at the beginning of the temperature curve, where the start-up process of the hotfire takes places. As we wanted to capture this effect, no filtering was done. The low data acquisition rate acts as smoothing in time itself. Neither was decided for a weighting of any sensor measurement in the IHCM, as no sensor location or TC can be identified as more trustworthy or significant than another.

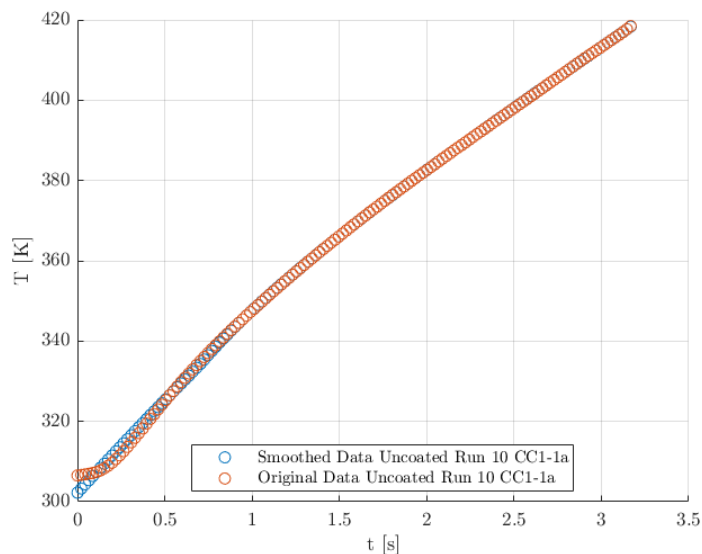


Figure 6.2.: Filtered temperature data of TC-CC1-1a from run 10

Evaluation Window: The data has to be cropped, as only the main sequence is of interest for the IHCM evaluation. Due to thermal inertia of the CC and the dynamics of the fluid system, the closing of the main valves is not conclusive enough to capture the hottest states, the TC peaks. For every run, the end time is different, as for one, the total hotfire run duration varies, and second the value of the end cropping condition differs. As a trimming end criterion, the TC peak of CC1_TC_8a was chosen. Details of the nomenclature is found in Section 4.3. This TC is valid in every configuration, is near to the hot gas wall,

so reacts the fastest to the drop in the combustion chamber pressure and shows higher temperatures than "f" and "b". In the coated configurations it has the highest value, due to cross heat conduction from CC3.

6.4.2. Numerical Physical Model Implementation

The physics of the problem gets defined by a "ThermalModel" PDE object [47], while the type of thermal analysis is specified by "transient-axisymmetric", the axis of symmetry being the rotational axis of the CC. The axis symmetry is used because the dimensional reduction from 3D to 2D saves computational time.

Geometry: The physical domain gets modelled by the longitudinal profile of the CC, describing the igniter ring and the two CC-segments as one 2D geometry, reducing the number of boundary conditions to the exterior ones to the environment, described in Section 6.4.3. A "decomposed solid geometry model" gets created from a "decomposed geometry matrix" and was included into the PDE model. The hot gas wall gets modelled with 100 sections to guarantee a smooth shape. A mesh, details in Section 6.7, is established. Matlab automatically assigns the axis of symmetry as the y -axis, which will be further named z . The zero-point of reference for the z -axis was set at the igniter rings side to the injector face plate. The x -axis is referred to as r -axis.

Material Parameter: Here also the material properties, originating from [6], are assigned to the domain. For this type of simulation the density, thermal conductivity and the specific heat capacity are necessary. The two latter are defined over a range of temperature to model the temperature dependent behaviour of the copper material, which are significant for particularly high and low temperatures as the behaviour gets non-linear.

6.4.3. Boundary Conditions

Except for the boundary condition of the hot side wall, which is the variable of interest, all other boundary conditions must be predetermined and are represented using a Neumann boundary condition. The model was simplified omitting two interfaces: 1. between igniter ring and first; 2. first to second segment, as the parts are pressed together and it was assumed that the high thermal conductivity of copper justifies this approach. The latter was also found to be true by [32], where the difference between an adiabatic and a spatially dependent heat flux, was insignificant. The other walls were imposed with an adiabatic thermal boundary condition, detailed information about this choice in Section 5.7.2.

The optimized heat flux distribution is being linearly interpolated between the defined optimization points. As the algorithm ran into issues with the extrapolation, more details in Section 6.6.1, a start and an end condition was forced, Equation (6.11). The heat flux value to the face plate is getting extrapolated constantly, while the nozzle side is linearly extrapolated ending at zero. The following method was used in this thesis: opt_z containing the z -coordinates of the optimization points, z_{inv} the z -coordinates used for the definition of the boundary condition and z_{end} describing the end of the domain. So the entries of the vector q^k are being optimized, but the boundary condition for the direct solver is given in this form:

$$z_{inv} = [0, opt_z, z_{end}] \quad (6.10)$$

$$q^k = [q^k(1), q^k, 0] \quad (6.11)$$

6.5. Conjugate Gradient Method Implementation

This section provides an insight into the measures taken to formulate and implement the optimization algorithm in the context of this thesis.

6.5.1. Conjugate Gradient Validation Process

The inverse algorithm's objective is to determine the unknown applied heat flux based on temperature readings. Therefore, in order to validate it, it is necessary to provide data generated with a precisely defined boundary condition. If the results from the inverse algorithm agree with the pre-defined conditions, then the algorithm can be considered as validated [32]. Therefore, a direct calculation with a defined wall heat flux is performed and the temperature data at the experimental sensor locations are mapped. Afterwards the IHCM is used to reconstruct the heat flux.

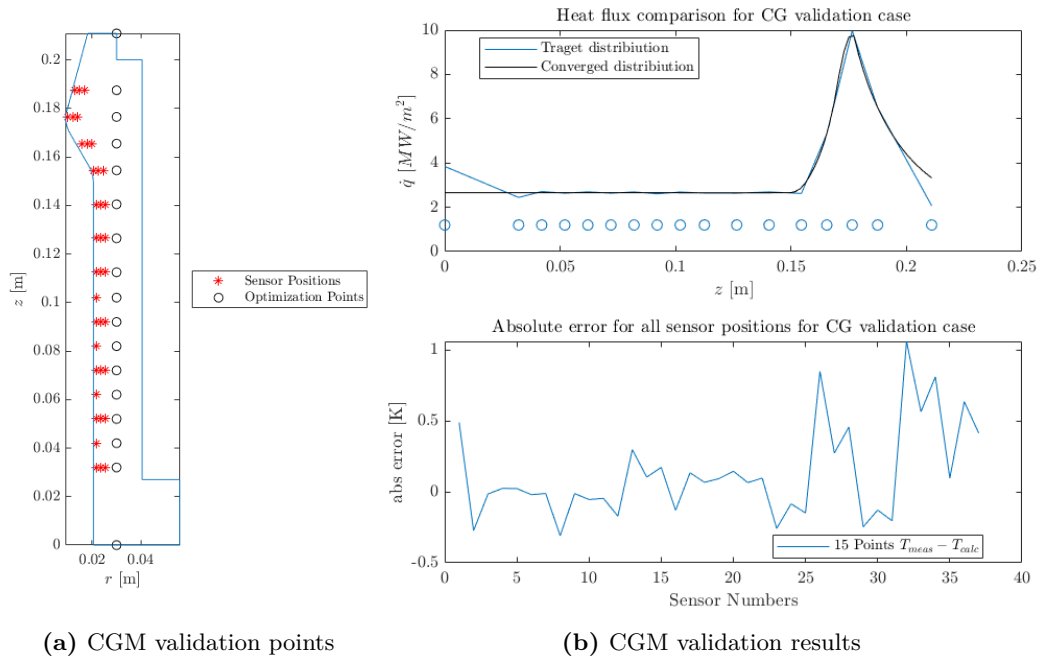


Figure 6.3.: CGM validation setup and results

The wall heat flux for the direct case is generated from the Sinyarev HTC, upper subfigure in Figure 6.3b, and is simulated for a total of 1 s at an initial temperature of 300 K. The data is recorded at the respective measurement points and used as input for the CGM. The SM is evaluated at the same conditions for 0.5 s with the reference heat flux distribution of the 10 bar load point. The stopping criteria (further information in Section 6.5.4) are possible to be refined, as the method is expected to generate more accurate results, because of lacking the systematic errors of real data. Therefore an $\epsilon_{rms} = 0.1 K$ was chosen, which drops to an absolute value of 0.35 K in the last iteration, and $\epsilon_{std} = 0.01 K$ was selected. In terms of optimization points, contrary to Section 6.4.3, it was feasible due to the "clean" simulated

data to set an optimization point at the beginning of the domain at $z = 0 \text{ m}$ and at the end. One point was set for every projected sensor position at the respective z -coordinate, visible in Figure 6.3a. This gives the opportunity to observe the behaviour of the method for a high spatial resolution, additionally to the phenomena that happen for start- and end-domain points. Unphysical behaviour in the beginning of the top figure in Figure 6.3b is observed due to a lack of measurement points. The end-domain point is under-predicting the heat flux. As the same setup caused problems in Section 6.6.1, the start and end points were modelled. The highest ϵ_{rms} is found in the sensor position nearest to the hot gas wall in the throat and in the sensor position to the transition from cylindrical to convergent.

In the beginning of the domain the solution of the IHCM method deviates 44%, this difference is reduced drastically in the cylindrical section, where the heat flux values differ a maximum of 1.5%. In the cylindrical-convergent transition it deviates for 11.2% and in the throat of 2.3%. Overall, the CGM can be considered validated since the converged solution represents the imposed heat flux boundary condition for the vast majority.

6.5.2. Iterative First Guesses

Every time step needs an initialisation of a heat flux and a starting temperature field for the domain. In the first time step, the temperature data is taken from experimental data. The first guess for the heat flux is shown in Table 6.1 and Figure 6.4.

Table 6.1.: First heat flux guess and sensitivity matrix heat flux curves [MW/m^2]

p-case/z-coordinate	0	z_{conv}	z_{th}	z_{end}
5 bar	2	2	4	0.5
10 bar	4	4	7	2
12 bar	4.5	4.5	9	2.5
15 bar	5	5	10.5	3

Initial Heat Flux Distribution at $t > 0 \text{ s}$: For these time steps, the algorithm uses the optimized heat flux from the previous time step as a starting guess for the heat flux.

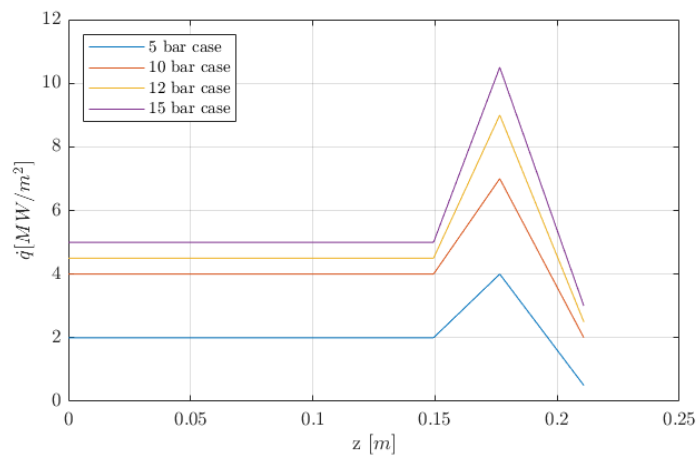


Figure 6.4.: CGM first guess heat flux

Initial Temperature Distribution at $t = 0$ s: For the IHCM every run needs an initial temperature distribution for the first time step, this is done by the arithmetic mean of the very first temperatures of all sensors. At this point the temperatures only deviate marginally.

Initial Temperature Distribution at $t > 0$ s: Following initial temperature distributions at the remaining time steps are taken from the transient thermal results prior to the current time step and get initiated by updating the initial conditions object of the PDE.

6.5.3. Sensitivity Matrix

A SM is a Jacobian Matrix, which describes the small change of the temperature as a result of an alteration of one heat flux value at the specific optimization point. The structure of this matrix is outlined in Equation (6.12). A sensitivity study in [30] showed that the computation of the Jacobian matrix outside of the optimization loop is legitimized due to the linearity of the Fourier heat conduction equation. The matrix remains unaltered, if the number and location of the measurement points and the optimization point locations do not change. Hence the matrix is determined once and used throughout the optimization procedure. This approach saves computational time.

Reference Heat Flux Distribution: Selecting a reasonable reference guess for the heat flux vector P is not crucial to maintaining the linearity of the problem, as can be found in Section 6.6.3. As a matter of simplicity, distributions from old data in Section 6.5.2, Figure 6.4, are used.

Mathematical Background: The SM is a $M \times N$ matrix. M = number of sensors and N = number of unknown parameters. As the matrix in Equation (6.12) is not re-evaluated for every time step, only one SM exists, unlike in [29].

$$J(P) = \begin{bmatrix} \frac{\delta T_1}{\delta P_1} & \cdots & \frac{\delta T_1}{\delta P_N} \\ \vdots & \ddots & \vdots \\ \frac{\delta T_M}{\delta P_1} & \cdots & \frac{\delta T_M}{\delta P_N} \end{bmatrix} \quad (6.12)$$

There exist several approaches of determining the sensitivity coefficients (the SM entries). For this thesis the finite forward difference approximation from [29] according to Equation (6.13) was implemented. First a reference case using the direct problem in Section 6.4, with no change in the vector P is calculated, which can be found in the right side of the numerator in Equation (6.13). Then, iteratively one parameter position is changed by adding the amount ϵP_j to the respective j -position, the problem is solved and the corresponding temperatures at the sensor positions are being interpolated. This is done N times. The choice of ϵ , can be found in Section 6.6, is given in [29] as $\epsilon \approx 10^{-5}$ or 10^{-6} . In this work $\epsilon = 10^{-5}$.

$$J_{ij} = \frac{T_i(P_1, P_2, \dots, P_j + \epsilon P_j, \dots, P_N) - T_i(P_1, P_2, \dots, P_j, \dots, P_N)}{\epsilon P_j} \quad (6.13)$$

The visualization of the SM can be found in Figure 6.5, which is the SM of Section 6.5.1. The effect of the domain start and end point, being the first and last column, is nearly zero, meaning the influence of

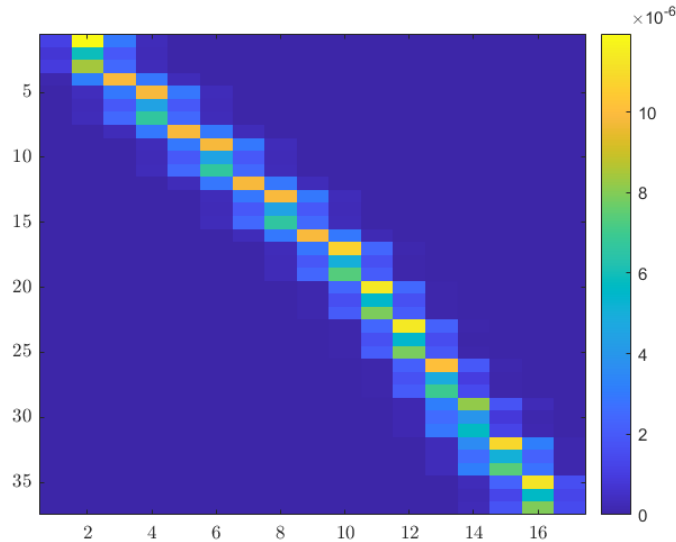
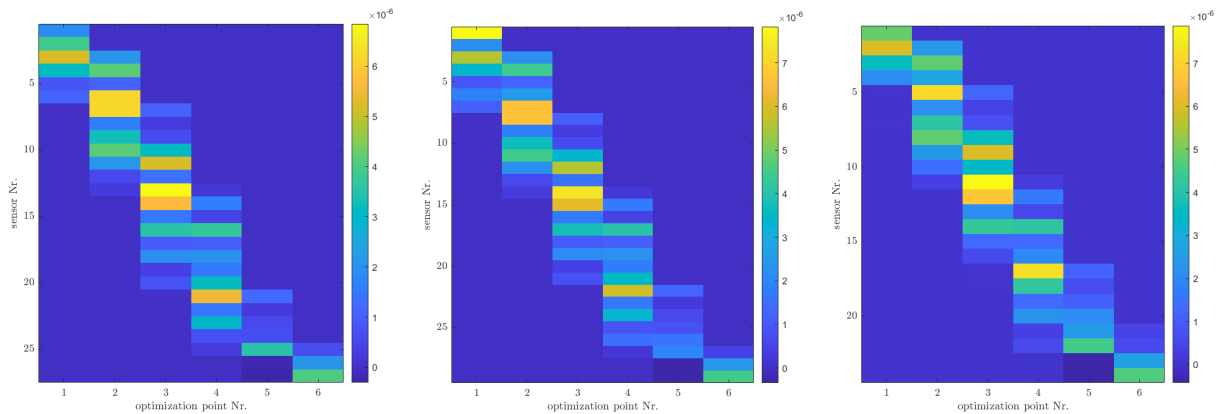


Figure 6.5.: SM with start and end domain point and all available sensors

a change in heat flux at this position is hardly detected by the measurement points. This concludes a higher predicting uncertainty for heat flux values in these areas.

Other parameters regarding the evaluation duration of the matrix in respect to the target time step of the IHCM, the initial temperature, alternative reference heat flux distributions, temperature and pressure relations as well as the proportional deviation ϵP_j , were investigated in Section 6.6. As one sensitivity matrix is used per pressure load point, hence three for the uncoated, four for the ceramic and two for the metallic case had to be calculated for evaluating the experiments of one test case.



(a) SM of 10 bar uncoated test case (b) SM of 10 bar ceramic test case (c) SM of 10 bar metallic test case

Figure 6.6.: SM comparison for the different test cases for a different amount of sensor positions

Figure 6.6 underlines the different amount of rows, as a different amount of sensor positions is used to calculate the matrixes. Figure 6.6 still exhibits the diagonal behaviour of Figure 6.5, but the entries around the diagonal are not as dominant, when the spatial discretization points are set in one line with the sensor points. For example the striking yellow points in the third column are in all cases the sensors

CC1_8a and CC3_1a.

Sensitivity Matrix Initial Temperature: The initial temperature is chosen to be set to the mean initial temperature of all test runs of one pressure load point as the initial one. This is the best way to exclude convergence problems.

Sensitivity Matrix Evaluation Duration: The same approach, like to find one common initial temperature, was used for the time duration the SM should be evaluated. The mean of the time discretization steps of one load category was calculated and divided by two, justification found in Section 6.6. As in some load point categories the length of the test runs differs by a factor of about 2.5, a security step was built in to ensure that the matrix stays valid and a solution can be found. If the smallest time increment of one run of one pressure category is smaller than calculated time step for the SM, this minimal value is multiplied by a factor of 0.8 and set as the new time step of the SM. Because if the SM is calculated for a longer duration than the individual time steps of the IHCM evaluation, abortion was observed. Hence this safety measure was set in order that the simulation duration of the SM is always smaller than the shortest time increment in a batch of measurements. If the experiment durations vary a lot for one pressure case, (for example for the 5 *bar* case, the test durations were from 3 – 8.5 *s*) it should be considered excluding the remarkably short or long runs, and assess them solitarily.

Sensitivity Matrix Calculation: Saving computational time, one SM was evaluated for six data sets. But as mentioned in Section 6.5.3, the state at which the SM are computed should be as similar as possible to the real case, on that account heat flux curves for all pressure load points were taken from old data, found in Table 6.1. These are reused as an initial heat flux guess for the actual optimization. The heat flux, interpolated linearly for the required positions, is set as a boundary condition for the hot gas wall and the reference case with an unaltered distribution is calculated. It gets solved by an Ordinary Differential Equation (ODE)-solver for the finite element model.

6.5.4. Stopping Criteria

In the iterative inverse method, achieving an exact solution is unfeasible. Instead a criterion based on a certain behaviour of the defined error is used to indicate an acceptable level of approximation.

In this work three error definitions were used, one mainly for debugging and two as actual stopping criteria, where the calculation was stopped depending on which criteria was fulfilled first. The definitions use an end time error formulation, taking the raw temperature data at the point of time in question. No weighting of a sensor position is done and the temperature deviations get summarized to a scalar, losing its location information. Setting a fixed value as a favourable end temperature difference to be reached, in form of an absolute Root Mean Square (RMS) error, turned out to be problematic. The hot fire runs, depending on the pressure levels, could achieve different minimal errors (ΔT), for the lower pressures a smaller (around 4 *K*) than for higher ones (around 7 *K*). Setting various thresholds for every hotfire configuration and load point was considered incommensurable, hence relative criteria were defined. Furthermore due to over-determination of the system, this "hard-limit" criteria would possibly have never

been met. The catching mechanisms act after a certain number of iterations. The following definition of temperature deviations or errors was used:

$$\Delta T = |T_{calc} - T_{exp}| \quad (6.14)$$

$$\Delta T_{avg} = \frac{1}{M} \sum_{i=1}^M \Delta T_i \quad (6.15)$$

Diverging Optimization: This criterion was used for debugging purposes and the algorithm validation, to obtain information on the behaviour of the algorithm in combination with the test data and is similar to the definition in [24]. This criterion compares the average temperature difference ΔT_{avg} of the current iteration with that of the previous one. If this value increases for four consecutive iterations, the system is considered to be diverging and the simulation is terminated. To prevent premature abortion due to localized divergence of a single sensor, it is relied on accumulated divergence over multiple successive iterations. This approach ensures that the simulation is aborted only when a persistent trend of divergence is detected. For the evaluation of the specific heat flux presented in Section 7.3, this criterion was not used.

Local Minimum: A local minimum, see [24] is identified when the standard deviation σ of the average temperature difference ΔT_{avg} over the last four iterations, divided by the mean of the last four ΔT_{avg} values, falls below the threshold value of $\epsilon_{std} < 0.1 K$, f being the current iteration.

$$\epsilon_{std} = \frac{\sigma}{\frac{1}{4} \sum_{k=f-3}^f \Delta T_{avg,k}} \quad (6.16)$$

RMS Criterion: The most dominant stopping criterion was formulated with the root mean square error difference between the current and previous iteration. RMS was used as it possesses the same unit as the error quantity. This stopping criterion prohibits the IHCM from oscillating around a possible solution. If for example the error between two close measurement points can not be reduced as a result of inherent temperature data acquisition errors, the algorithm can not find a heat flux solution that meets both data points. The solution was considered sufficiently accurate when $\epsilon_{rms} < 0.01 K$.

$$\Delta T_{rms,k} = \sqrt{\frac{1}{M} \sum_{i=1}^M \Delta T_i^2} \quad (6.17)$$

$$\epsilon_{rms} = |\Delta T_{rms,k} - \Delta T_{rms,k-1}| \quad (6.18)$$

6.6. Inverse Heat Conduction Method Sensitivity Analysis

This section provides information about the parameter development process for the discretization of the hotfire runs as well as details about the validation of the conjugate gradient method on numeric data. A

focus was also the determination of relevant variables concerning the sensitivity matrix and their validity area.

6.6.1. Spatial Discretization

In order to understand more about the specific heat flux alongside the CC, an appropriate spatial resolution has to be provided without interfering with the evaluation methods stability, as the nature of the algorithm is ill-posed. This circumstance limits the resolution of the axial heat flux distribution.

For the problem to be well-posed, the number of optimization variables N on the unknown boundary, the heat flux, should not exceed the number of available on the hot gas wall projected measurement positions. As for some points along the shape, three temperature measurements are available, but are only describing one axial position M_{ax} , N has to be $N \leq M_{ax}$. Typically, selecting optimization parameter positions as close as possible to the location of the thermocouples is advantageous to maximize sensitivity and minimize parameter interference. [31]

Predefined Optimization Point Locations: Some pre-considerations were done to narrow down the quantity of possible variations for the purpose of finding the optimal point locations.

Points suggested by Geometry: As the heat flux in the cylindrical part is assumed to be relatively constant [43], the transition point to the convergent part of CC3, was identified as one suitable parameter point. Moreover as the maximum specific heat flux value is expected at the throat of the nozzle or slightly upstream due to axial heat conduction [43], one optimization point was placed at the axial position of the nozzle throat.

Points suggested by Sensor Positions: In alignment with prior statements, one optimization point was chosen at the first axial sensor position in the first segment. CC1 being of major interest, one optimization point position coincides with the last sensor of CC1. Another point is selected at the last accessible data point, the last sensor of CC3.

Points excluded: Since the lowest heat flux value is near or at the end of the nozzle, but its exact value is not known (due to mounting issues no TC could be applied at the nozzle exit) an assumption had to be made. Setting this location as an optimization point without any boundary condition, resulted in runaway values due to the linear extrapolation of the data. As old data did not provide answers to this topic, because there the end point was subject to modelling as well, the solution of setting the end point value to zero was taken. Similar problems were encountered with the optimization in the igniter ring missing temperature measurement points as well. Here the assumption of a constant heat flux, taking the first optimization point value, was made. Equation (6.11) summarizes this.

Optimization Point Analysis: The decision process is outlined in this subsection. In total three different point configurations were investigated, depicted in Figure 6.7. The throat area was not subject of variation as not many data points were available, in consequence of faulty sensors, found in Table 4.9. Figure 6.7a is the lowest resolved configuration, case 1, that possesses the essential points mentioned in Section 6.6.1

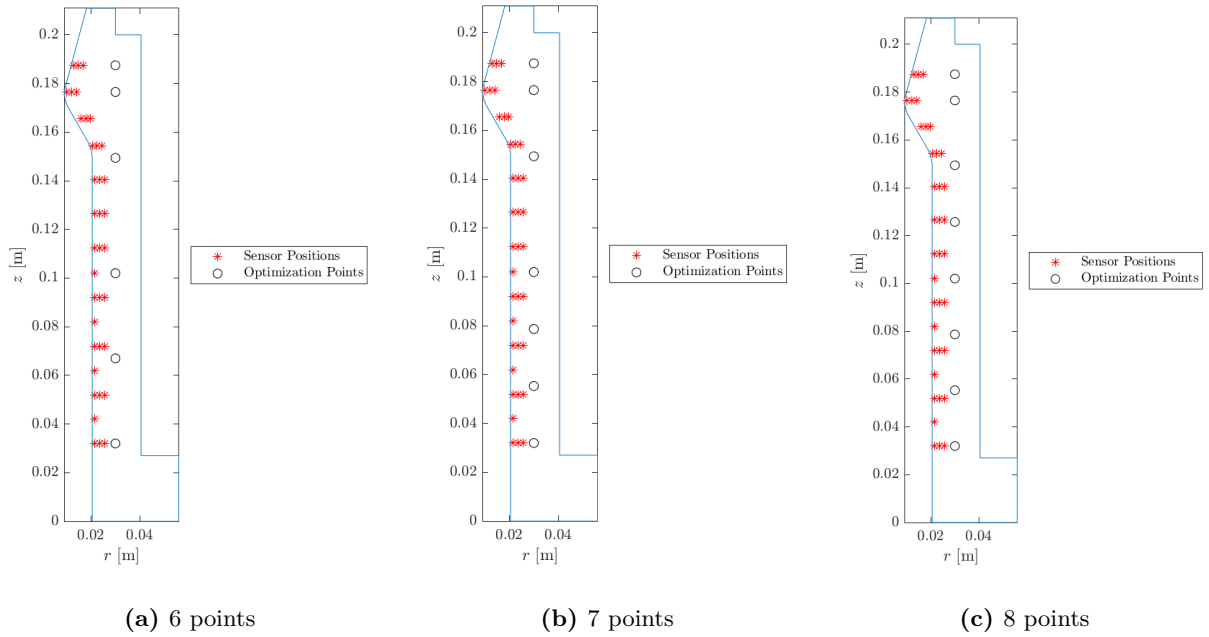


Figure 6.7.: Optimization point configurations from low to high spatial resolution

and an additional point in the cylindrical part of CC1. Figure 6.7b, case 2, exhibits two points in this part and Figure 6.7c, case 3 combines the middle configuration with an extra point in the cylindrical part of CC3.

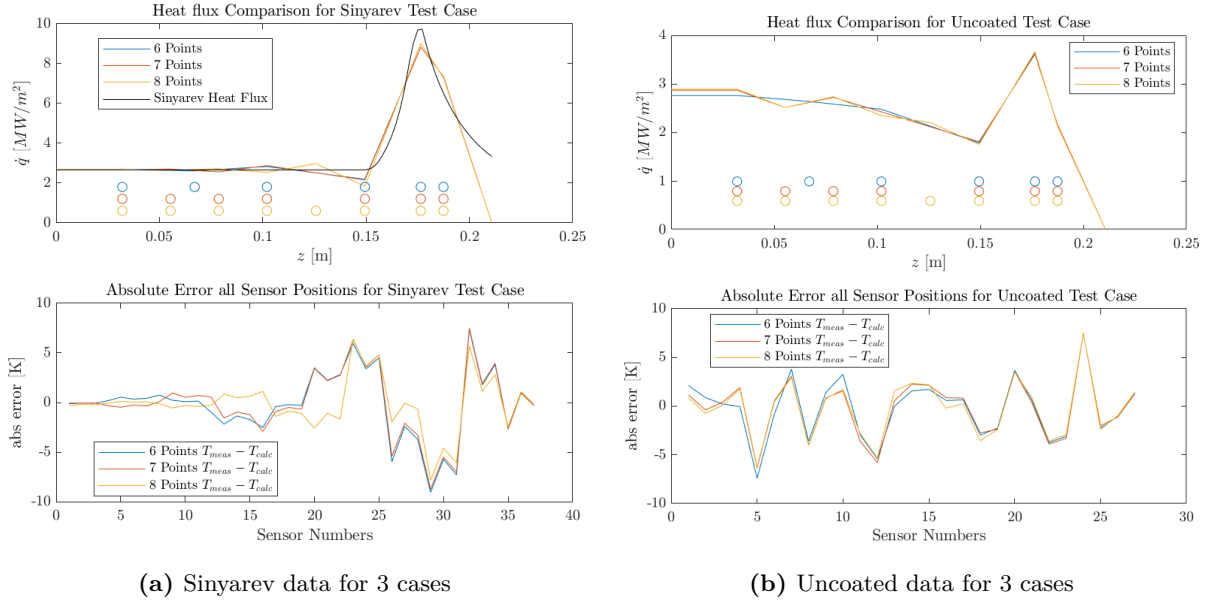


Figure 6.8.: Optimized heat flux and absolute error for Sinyarev and uncoated data

In order to find appropriate optimization points at first numeric data has to be used and be later compared with experimental data. The domain was implemented with a simulated heat flux distribution from the Sinyarev HTC correlation and was employed as the "experimental" target data. The initial temperature was 283 K and it was simulated for 0.5 s. The resulting temperature profiles at the sensor locations were

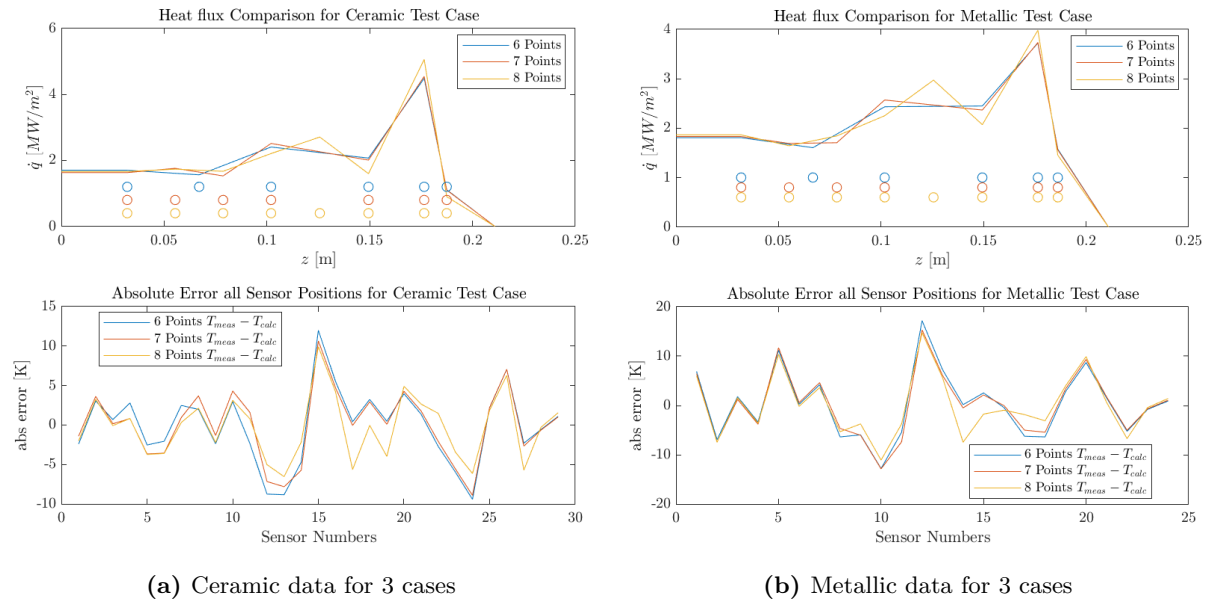


Figure 6.9.: Optimized heat flux and absolute error for ceramic and metallic data

interpolated and used as an input. Figure 6.8a shows the converged distributions of the configurations and their respective parameter points. The next second subfigure in Figure 6.8a portrays the absolute error, which varies especially in CC3, while case 3 offers better results for the constant part of CC3.

As experimental trial data, temperature measurements of hotfire run number 10 from the uncoated, ceramic and metallic configuration was utilized. The problematic sensors are already excluded. This run was selected as it exists in all three cases and is with an ROF of approximately 3.1 closest to the actual CC design point. The data was evaluated with only one time increment, 1 s into the hotfire main sequence.

In Figure 6.8b the uncoated case is best represented by either case 2 or 3, the lowest resolution produces slightly bigger errors. In the ceramic case in Figure 6.9a the magnitude of the errors produced by cases 1 and 2 are alike, while case 1 shows more smaller ones according to amount in the CC1 segment (sensor numbers 1 – 14) than case 2. Case 3 does not deliver good results for the second segment and exhibits more deflections than the lower resolved cases. Figure 6.9b manifests good results for cases 1 and 2, while case 3 exhibits the same behaviour as in the ceramic data.

These observations result in the decision matrix Table 6.2, comparing the best solutions for a data set with each other and weighing it from best 3 to 1 lowest. Case 1 with the six optimization points is chosen in consequence of prior explanations, and as the most important resolution of data sets, are the coated ones while also reducing the computational time significantly.

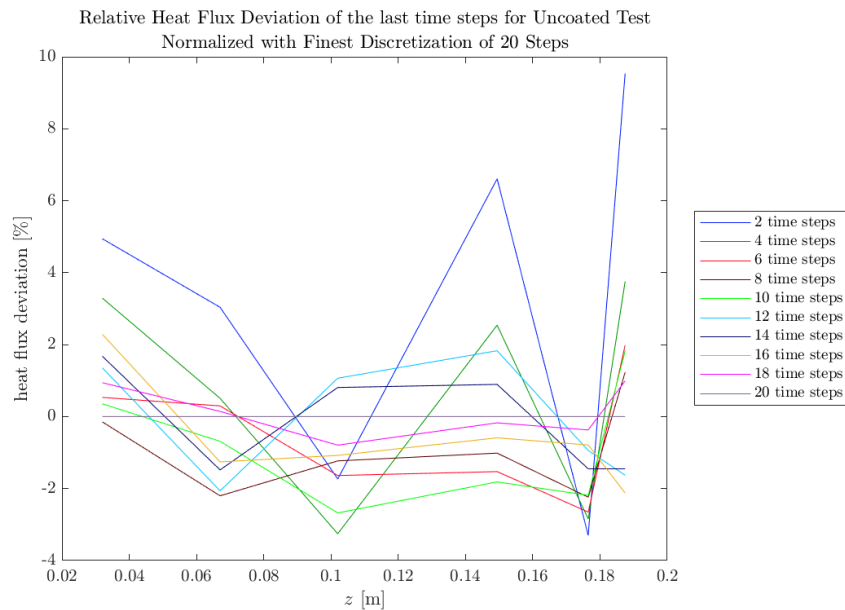
6.6.2. Temporal Discretization

The right temporal discretization is as crucial as the spatial one with the aim of rendering the time dependency of the data as accurate as possible without demanding excessive computational resources. The heat flux distribution gets time averaged over the analysed time increment. Given the fact that the effect

Table 6.2.: Spatial discretization decision matrix

	6 points	7 points	8 points
Sinyarev	3	3	2
Uncoated	2	3	3
Ceramic	3	2	1
Metallic	3	3	2
Sum	11	11	8

of the TBC on the transient heat flux distribution development is not clear, no weighting of a specific time period, for example start-up or shut-off, is done. This uniform time spacing is hence used for all data sets. For this analysis the spatial discretization of 6 points was already used.

**Figure 6.10.:** Comparison of heat flux distribution for last time step for uncoated hotfire

For this evaluation once again run number 10, with 10 *bar* and ROF 3.1 is used. All three runs were calculated with 2, 4, 6, 8, 10, 12, 14, 16, 18, 20 time increments. The increment values were depending on the total hot fire run duration. The only common point in time is the last one and following the logic of the last one being the most accurate, because the least time averaging had happened, this heat flux distribution was selected and compared to the respective values of each optimization point of finest time discretization with 20 time step. The percental heat flux deviation was calculated by subtracting the respective cases from case 20 and normalizing it by case 20. The discretization of 14 time steps turns out to be the most favourable.

Time Increments Uncoated: The smallest difference, visible in Figure 6.10, hence the closest distribution to the 20 time step case, and the lowest number of increments, which equals the least computational time were taken as selection criteria. This is best met by the 12 and 14 time steps discretization varying approximately a maximum of 2 or respectively 1.5%. Both under-predict mainly in the cylindrical part of CC3 and over-predict in the middle of CC1.

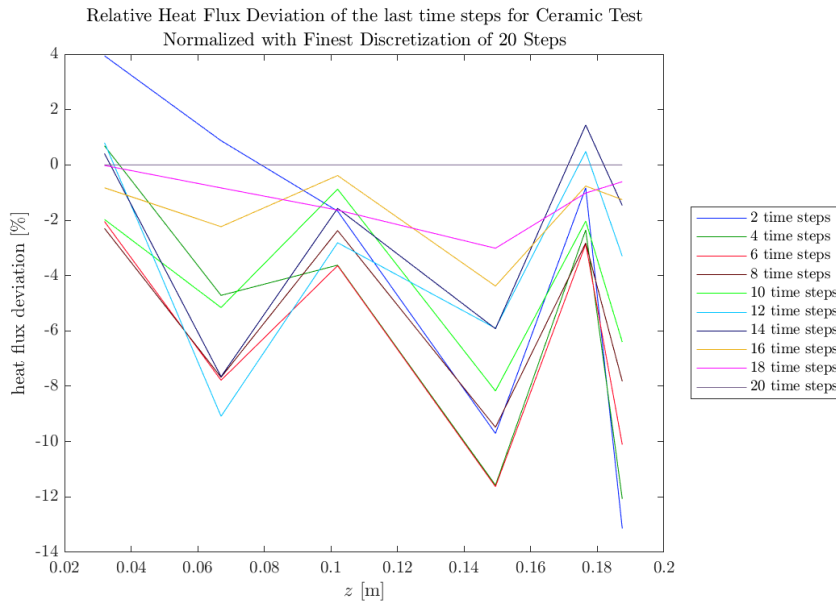


Figure 6.11.: Comparison of heat flux distribution for last time step for ceramic hotfire

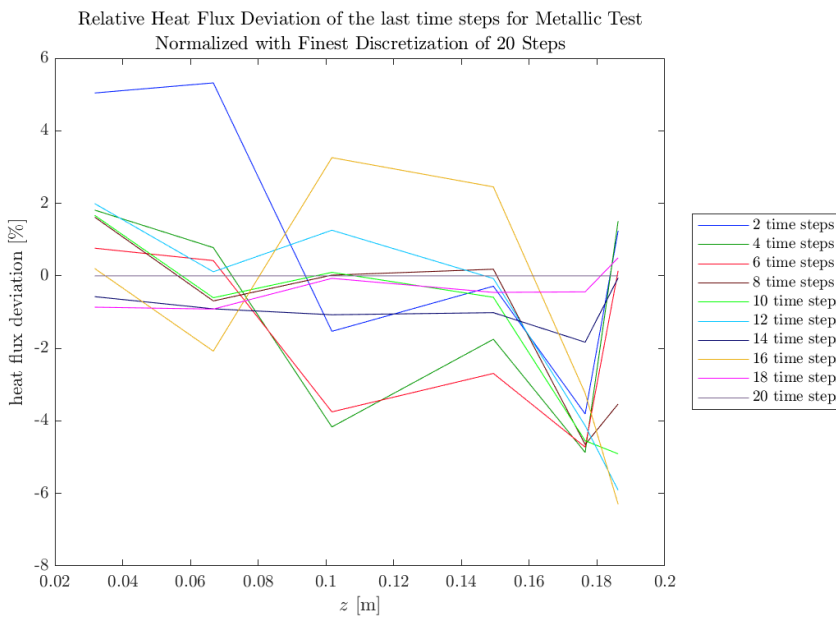


Figure 6.12.: Comparison of heat flux distribution for last time step for metallic hotfire

Time Increments Ceramic: The lowest deviation, visible in Figure 6.11, versus computational time ratio show the 14 and 16 time steps discretization varying approximately maximum 7 or respectively 4%. Both over-predict the heat flux distribution.

Time Increments Metallic: The best deviation versus computational time ratio, visible in Figure 6.12, shows by far the 14 step discretization varying approximately maximum 2 percent. The heat flux distribution gets over-predicted.

6.6.3. Sensitivity Matrix Parameter Analysis

As not much about the range of validity of the SM in this specific experimental context is known, an analysis regarding multiple parameters was done. The matter of updating the SM for every time step was not investigated as given in [30]. The same data set as in Section 6.5.1 as well as stopping criteria were used, a target heat flux created with a Sinyarev HTC, at an initial temperature of 300K simulated for 1 s. In this analysis only the parameter of the SM are altered.

- ϵ : magnitude of heat flux deviation per parameter point
- \dot{q}_{sm} : which magnitude and form of distribution has to be selected to guarantee the best result
- $K_t = \frac{\Delta t_{sm}}{\Delta t_{inv}}$: interrelation between duration of a time increment of the IHCM and the simulation duration of the SM in order to still provide a relative linearity

For every parameter analysis the default mode, if not specified otherwise can be collected from Table 6.3 and only the parameter in question is modified. The first guess for the inverse calculation was always the 12 bar guess form Table 6.1.

Table 6.3.: Default parameter of the SM analysis

	K_t	ϵ	\dot{q}_{sm} [MW/m ²]
Value	0.5	10 ⁻⁵	12 bar Table 6.1

ϵ : This parameter influences the relative change of the heat flux at a specific optimization point, which induces a change in temperature. This ratio, the entries of the sensitivity matrix, is assumed to be constant for small changes. However different definitions were found of this parameters interpretation of "small". In [29] this value is given between 10⁻⁵ and 10⁻⁶, but in [24] a value of 1.5 × 10⁻¹ is set. As there were no further information in [29] of the exact validity range, concerning other parameters like initial temperature of the experiments or material parameters, were given, a study, given in Table 6.4 was done.

Table 6.4.: Results of the SM analysis for ϵ

ϵ	Stopping criterion	Iterations
10 ⁻¹	RMS criterion fulfilled	8
10 ⁻²	RMS criterion fulfilled	8
10 ⁻³	RMS criterion fulfilled	8
10 ⁻⁴	RMS criterion fulfilled	8
10 ⁻⁵	RMS criterion fulfilled	8
10 ⁻⁶	RMS criterion fulfilled	8
10 ⁻⁷	RMS criterion fulfilled	8

It can be taken from Figure 6.13 that there are no differences caused by varying this parameter, concluding that the broad definition of "small" is valid in any case and the linearity of the matrix is kept constant. In the end the proposed value from [29] of $\epsilon = 10^{-5}$ is chosen. There are also no discrepancies in terms of computational efficiency, as Table 6.4 shows.

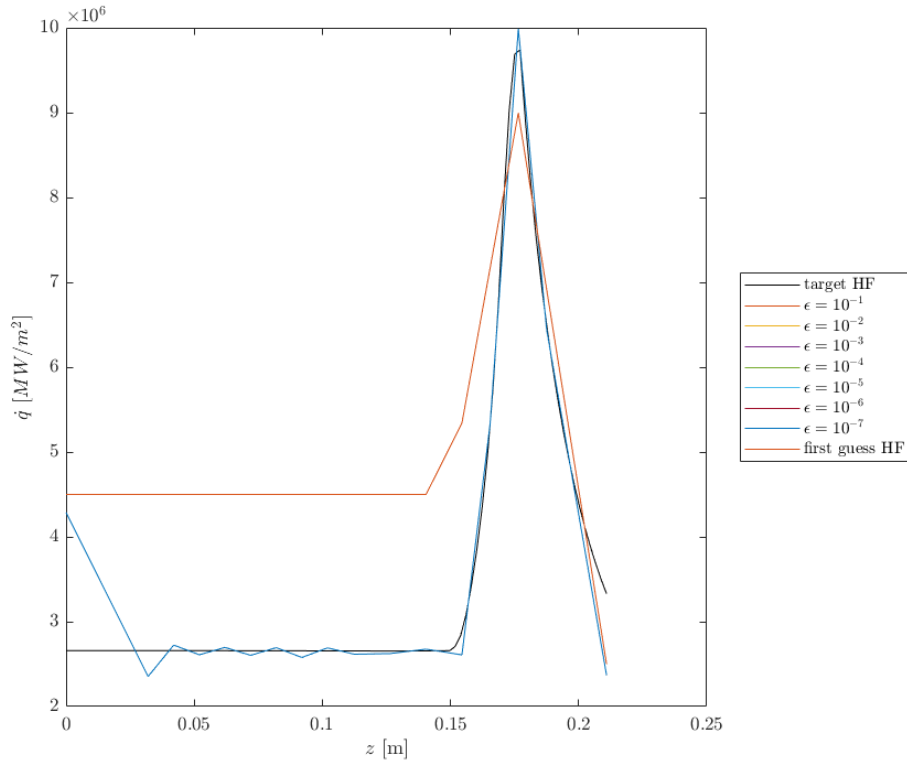


Figure 6.13.: Comparison of the magnitude deviation of ϵ on the HF

\dot{q}_{sm} : Even though the previous section, hints that changes in the magnitude of \dot{q}_{sm} , do not disturb the linearity of the SM, another study, listed in Table 6.5 was conducted, as oppositional information in reference to this topic was found in [31].

Table 6.5.: Results of the SM analysis for \dot{q}_{sm}

\dot{q}_{sm} [MW/m^2]	Stopping criterion	Iterations
[1, 1, 1, 1]	RMS criterion fulfilled	8
[8, 8, 8, 8]	RMS criterion fulfilled	8
[4.5, 4.5, 9, 2.5]	RMS criterion fulfilled	8
[6, 6, 12, 4]	RMS criterion fulfilled	8
[0.5, 0.5, 3, 0.25]	RMS criterion fulfilled	8

The influence of the reference heat flux at which the SM is computed was evaluated. The distributions points in Table 6.5 are at the start point of the domain, the convergent transition point, the throat and the end domain point.

Looking at Figure 6.14, it becomes apparent that the choice of reference heat flux neither has an effect on the computational time nor on the quality of the result. As a consequence, for an ideal data set it inflicts no difference. As a result of simplicity, the same reference heat flux for the SM and for the CGM was applied.

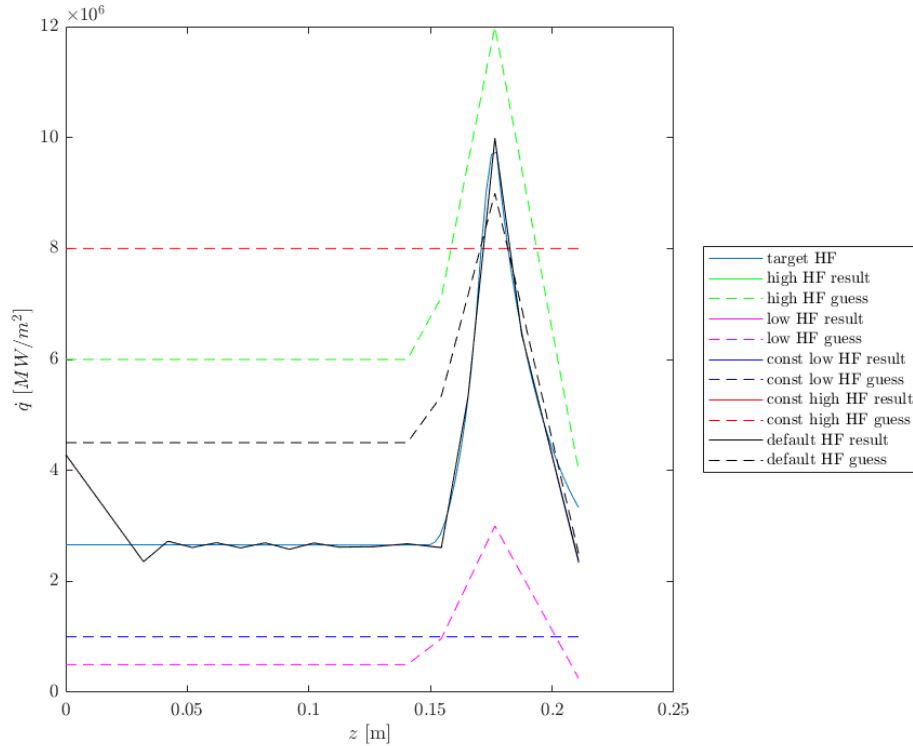


Figure 6.14.: SM reference HF evaluation

K_t : The question of linearity, i.e. which time factor K_t is suitable to obtain good results with respect to the desired evaluation period, is treated here. The test matrix and the outcome can be seen in Table 6.6.

Table 6.6.: Results of the SM analysis for K_t

K_t	Stopping criterion	Iterations
0.2	Optimization diverging	5
0.4	RMS criterion fulfilled	12
0.6	RMS criterion fulfilled	8
0.8	RMS criterion fulfilled	8
1	RMS criterion fulfilled	8
1.2	RMS criterion fulfilled	9
1.4	RMS criterion fulfilled	10
1.6	RMS criterion fulfilled	12

The results can be seen in Figure 6.15, where $K_t = 0.2$ is not plotted as the result did not converge. From Figure 6.15 it can be concluded that there are no major global differences in the ration of the time for the SM and for the evaluation window. If a closer look is taken in Figure 6.16 the smoothest solution is $K_t = 0.4$. The other factors tend to behave similarly to each other. Bearing in mind that these data are not subject to errors due to data collection, a smooth solution is essential. The peak is over-predicted in any time factor cases.

Another factor to consider is the number of iterations, which can be seen as a measure of computation time, although it is not exactly the same for each case. Thus a low number of iterations is favourable to

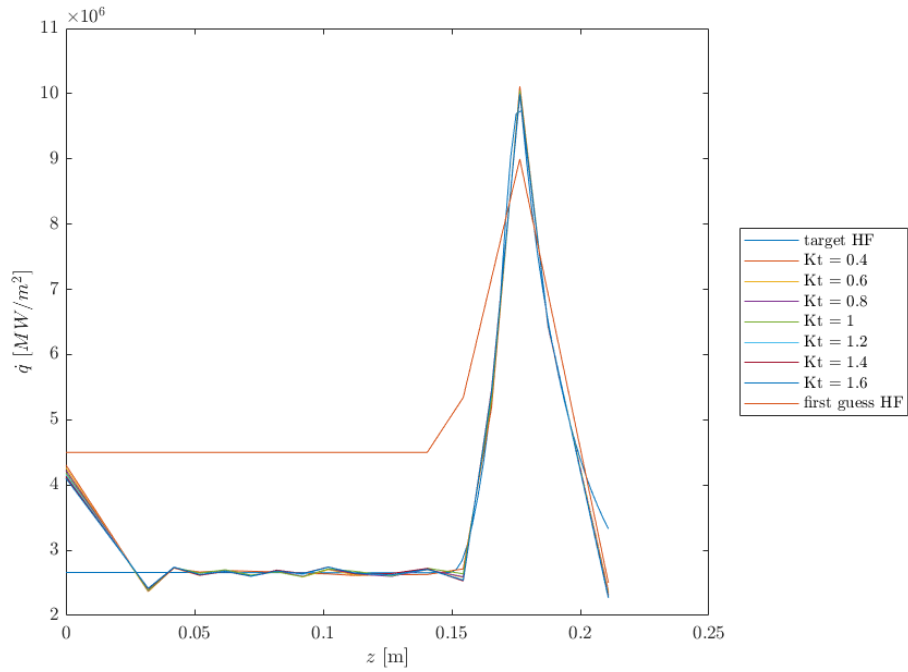


Figure 6.15.: Overview of converged heat fluxes for each K_t

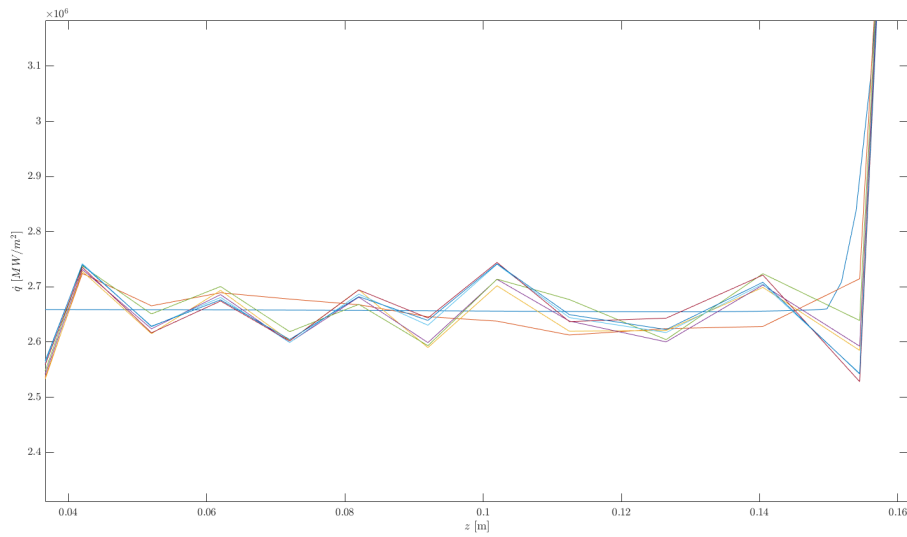


Figure 6.16.: Zoom in on the cylindrical part solution of the SM time factor analysis with the legend of Figure 6.15

compute large quantities of data. Which is why the optimal K_t lies between $K_t = 0.4$, for a smooth distribution and $K_t = 0.6$, for a little amount of iterations. Hence $K_t = 0.5$ is chosen, taking 8 iterations.

In the wake of the time factor analysis it is interesting to point out the physical meaning of simulating the SM for a shorter or longer time, which is depicted in Figure 6.17. Larger evaluation times, Figure 6.17b,

lead to affecting not only punctual the change in temperature, like the more diagonal form in Figure 6.17a suggests, but also affects the neighbouring sensors more. This phenomenon is caused by the high thermal diffusivity of copper, which smoothes out any temperature peaks by quickly transferring heat from the source to the surrounding material.

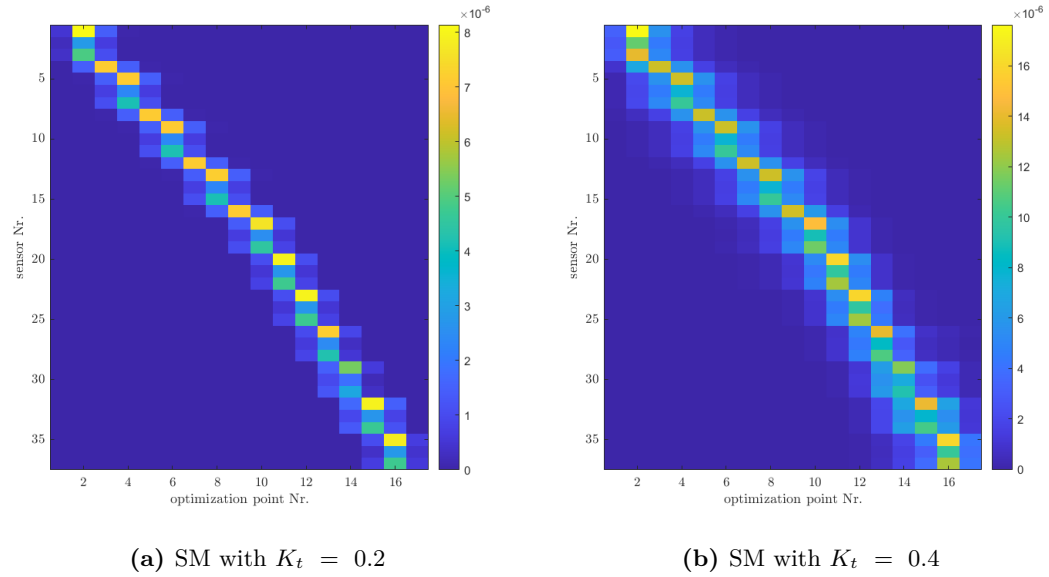
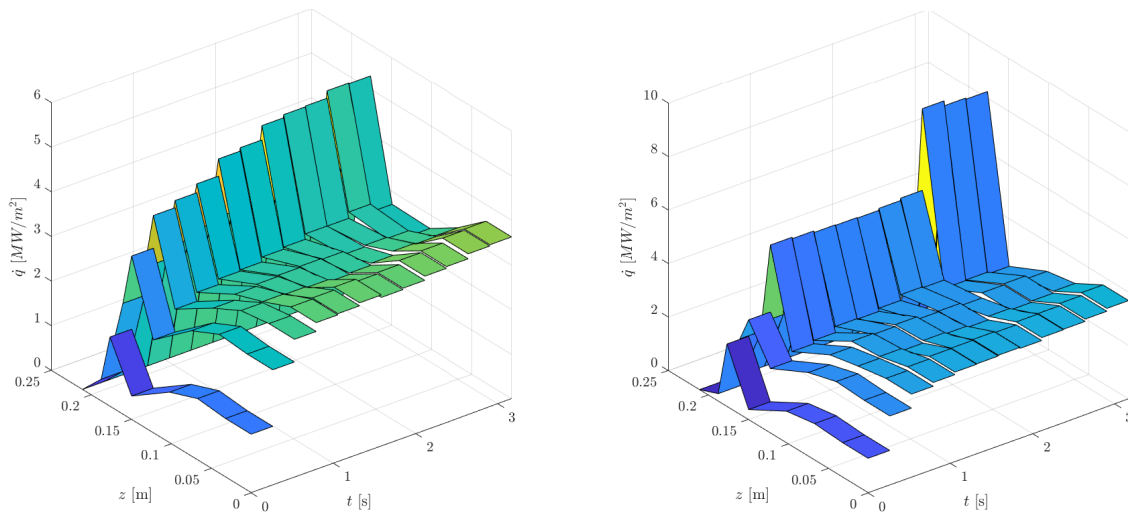


Figure 6.17.: SM evaluation time comparison

6.6.4. Results in Case of Missing Throat Sensors

Not only the heat flux values of the cylindrical part were of interest, which were unaffected by this phenomenon, but also the heat flux distribution in the throat was needed to correctly calculate the performance of the whole engine. Additionally this analysis was deemed to be part of the validation process of the algorithm implemented in this thesis.

The graphs shown in this section are only taken for a qualitative comparison. At first during data evaluation a qualitative issue concerning the heat flux distribution arose. It manifested in the uncoated hotfire configuration as all sensors in CC3 position 6, the throat position, were considered problematic hence missing. The one least off-value was CC3_6f. In the beginning, these sensors were not included into the computation leading to significant jumps in the converged heat flux, depicted in Figure 6.18b. No exceptional physical effect is taking place in the temperature data, supporting such a jump. Neither the logged variables, like stopping criteria or error variables exhibit abnormalities. These runs, were evaluated with the iterative initial condition from the previous result and 12 time increments, as this evaluation took place before the temporal discretization study.



(a) Uncoated run Nr. 10 with CC3_6f sensor in throat

(b) Uncoated run Nr. 10 no sensors in throat

Figure 6.18.: Comparison of results found by the CGM with and without measurement positions missing in the critical throat area

Factoring the material model, in Figure 6.19, as it was done for the error analysis in Section 7.6, shifted the jump to two time increments earlier. It can be inferred that if the configuration is modified slightly to circumvent potentially unfavourable factors in the data aligning with the method and to evaluate it with the same method, resulting in the same behaviour, the issue lies with the data input rather than the evaluation method. This is also strongly suggested by Figure 6.18a, as the issue does not occur here. As the optimization point in the throat, in case of the case without any CC3_6 sensors, is located in the vicinity of only three measurement points, namely CC3_5b, CC3_7b and CC3_7f, which are also located further away. This probably provokes a reverse or envelope reaction in the optimizer, initiated by a marginal change in one of the sensors in respect to the others.

This incident could not be explained other than with an optimization point being in the throat area,

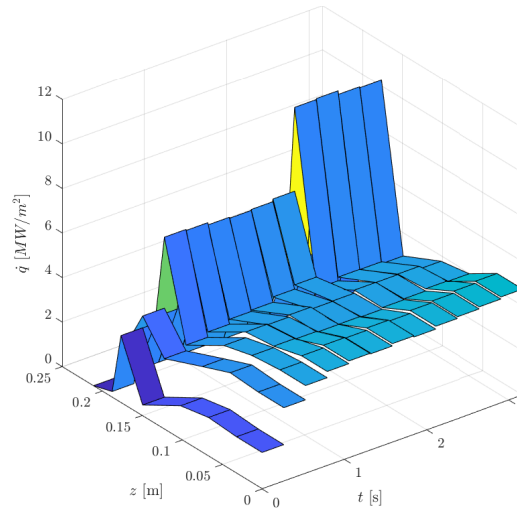


Figure 6.19.: Uncoated run Nr. 10 no sensors in throat with altered material model

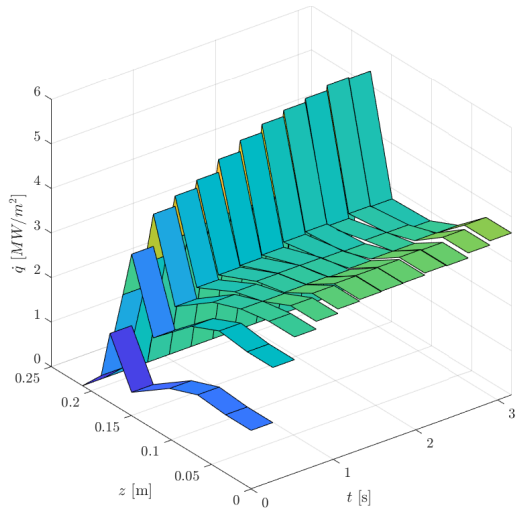
a critical optimization point as the peak heat flux is expected here, but this point is missing data for comparison. It also illustrates why the cylindrical part seems untouched by the phenomena, in both Figure 6.18a and Figure 6.18b the end level is around 3.5 MW/m^2 . As a result of these observations, another analysis in Section 6.6.5, targeting the influence of the initial heat flux distribution was performed. In conclusion of both, the sensor CC3_6f was kept as a data input.

6.6.5. Initial Heat Flux Distribution Conditions

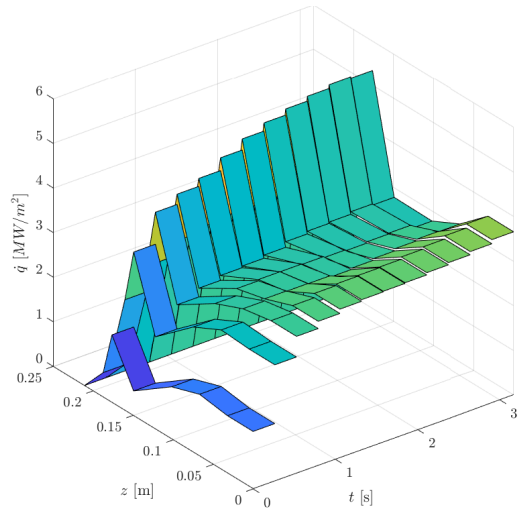
A topic of interest was the influence of the quantitative nature and manner of initiating the initial guess on each iteration. For example as another possible solution of the jump behaviour in Figure 6.18b. An explanation could have been a self-reinforcing feedback-loop of the iteratively implemented initial heat flux guess causing an instability. If the same heat flux distribution had been assumed in each time step, it could be deduced that the solution would deviate too much from the actual heat flux to be considered appropriate. Thus this option of modifying the magnitude of the first guess was explored additionally.

The first analysis, depicted in Figure 6.20, was done with the final sensor set of the uncoated run Nr. 10 and 12 time discretization steps. In contrast to the final procedure, the initial guess for every time step was either set with a constant value or the same heat flux distribution from Table 6.1 of the 10 *bar* case. To vary the magnitude of the constant value, 0 MW/m^2 , 2 MW/m^2 and 8 MW/m^2 were selected. No influence on the heat flux distribution compared in Figure 6.20 emerges from different first guesses, which concludes that the method of implementing a stabilizing sensor measurement at the throat plays the major role in solving the issue of Figure 6.18b.

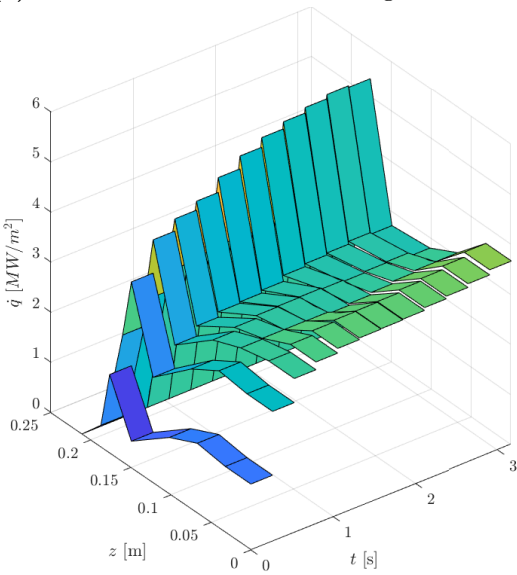
The second analysis, lacking all CC3_6 sensors, is illustrated in Figure 6.21. Figure 6.21a demonstrates the clear tendency of approaching the first guesses magnitude, which is given with 4 MW/m^2 in the cylindrical part compared to 3.5 MW/m^2 and 7 MW/m^2 for the peak compared to 7 MW/m^2 . This solution deviates from the final result in Figure 6.18a supporting the idea of converging to the given first guess. The implementation of a constant initial guess for each time step results in similar heat flux distributions in the final time steps, yet distinct temporal evolutions. Figure 6.21b and Figure 6.21c



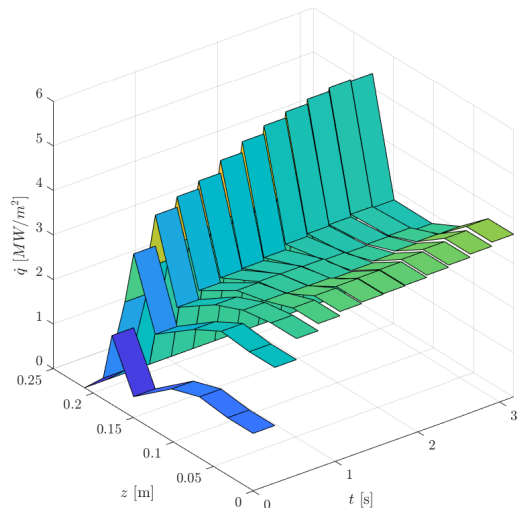
(a) Uncoated run Nr. 10 same first guess Table 6.1



(b) Uncoated run Nr. 10 first guess 0 MW/m^2



(c) Uncoated run Nr. 10 first guess 2 MW/m^2



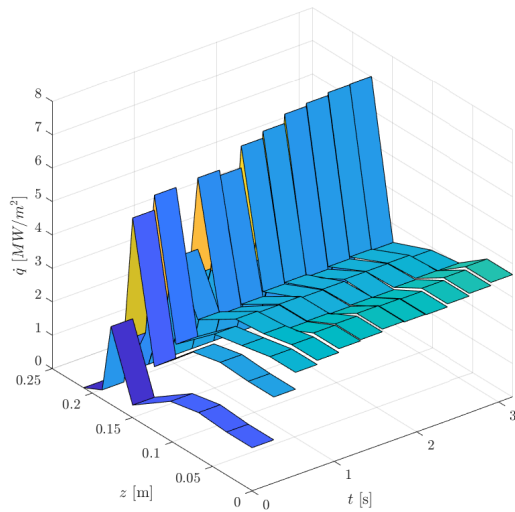
(d) Uncoated run Nr. 10 first guess 8 MW/m^2

Figure 6.20.: Comparison of effect on \dot{q} different first heat flux guesses

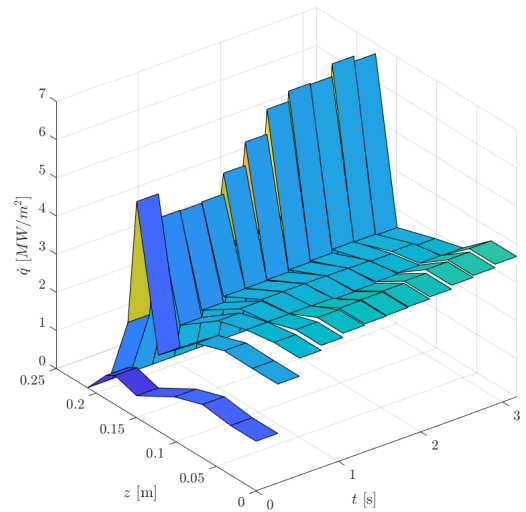
demonstrate comparable outcomes, with the exception of the second time step jump. The occurrence of the aforementioned jump can be attributed to the absence of the sensor, rather than the initial condition. The application of a higher initial boundary condition of 8 MW/m^2 results in the occurrence of the jump at an earlier point in time. This analysis reveals two key impacts. Firstly, there is a tendency for the magnitude of the initial guess to converge to a higher value the earlier it is applied. Secondly, the jumps themselves disrupt the distributions.

The decision regarding this topic, which is also in accordance with the recommendations set forth in various literature sources, including [32], was to iteratively implement the heat flux distribution of the prior time step. Supported by the first analysis in Figure 6.20. This approach was also taken in order to accelerate the calculation process. This analysis points out the importance of the data input quality and

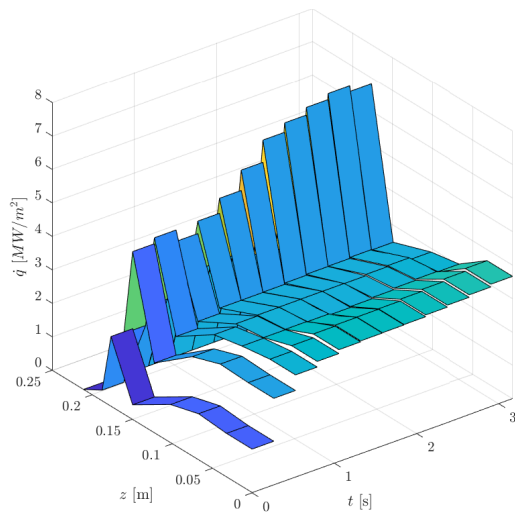
the sensitivity of the throat area to insufficient measurement data, which in succession also affects the whole temporal evolution of the heat flux uniquely in the throat area.



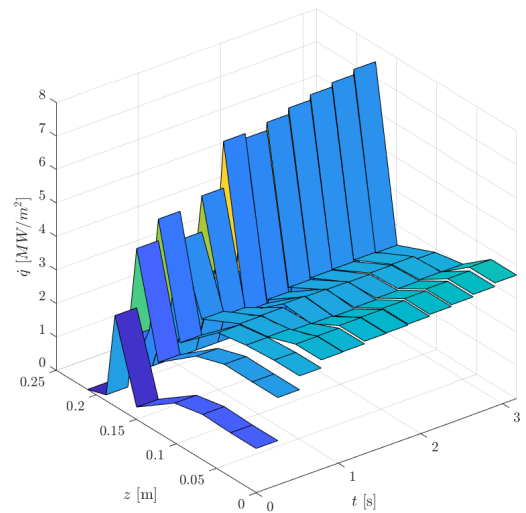
(a) Uncoated run Nr. 10 same first guess Table 6.1 no CC3_6 sensors



(b) Uncoated run Nr. 10 first guess 0 MW/m^2 no CC3_6 sensors



(c) Uncoated run Nr. 10 first guess 2 MW/m^2 no CC3_6 sensors



(d) Uncoated run Nr. 10 first guess 8 MW/m^2 no CC3_6 sensors

Figure 6.21.: Comparison of effect on \dot{q} different first heat flux guesses

6.7. Mesh Study

A mesh study was conducted in order to calculate the IHCM results as accurately as possible. A mesh study is essential to assess the influence of the element size on the accuracy and reliability of the simulation results, but also affects the computational time. Coarse meshes may lead to significant errors, especially in regions with steep gradients or high-curvature geometries, whereas fine meshes can provide more accurate results, but typically need more computational resources and time to solve.

The meshes were systematically refined, each time approximately doubling the amount of cells, until convergence was reached, where further mesh refinement would produce negligible changes in the results. An automatic refinement at the hot gas wall edges takes places, which coincides with the area of interest, as all data points are located 5 mm at most from the edges. The computed temperature data at the sensor locations of four different meshes were compared by using a heat flux distribution generated with a Sinyarev HTC-correlation.

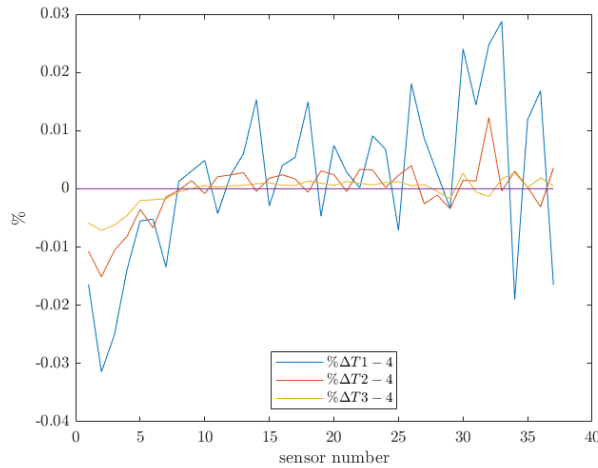


Figure 6.22.: Percental temperature difference to the finest mesh over every sensor

Table 6.7 sums up the parameters used for the mesh study. The element geometry generates tetrahedrons with nodes at its corners and edge centres. Hmax being the target maximum mesh edge length, Hmin the minimum one and Hgrad the mesh growth rate.

Table 6.7.: Mesh study parameters

	Element geometry	Hmax	Hmin	Hgrad	Elements
Mesh 1	tetrahedron	0.0095	0.0045	1.15	309
Mesh 2	tetrahedron	0.0065	0.003	1.05	595
Mesh 3	tetrahedron	0.0045	0.002	1.05	1182
Mesh 4	tetrahedron	0.004	0.00025	1.005	2060

The mesh and their detailed resolution can be seen in Figure 6.23. As observed especially in Figure 6.23b, Figure 6.23c and Figure 6.23d, the hot gas side has a higher resolution. As the finest mesh is supposed to obtain the best results in terms of accuracy, the sensors, 37 in total, percentaged temperature error is shown in Figure 6.22. In general the differences are marginal, so the second mesh, depicted in red, was used as a mesh for upcoming calculations.

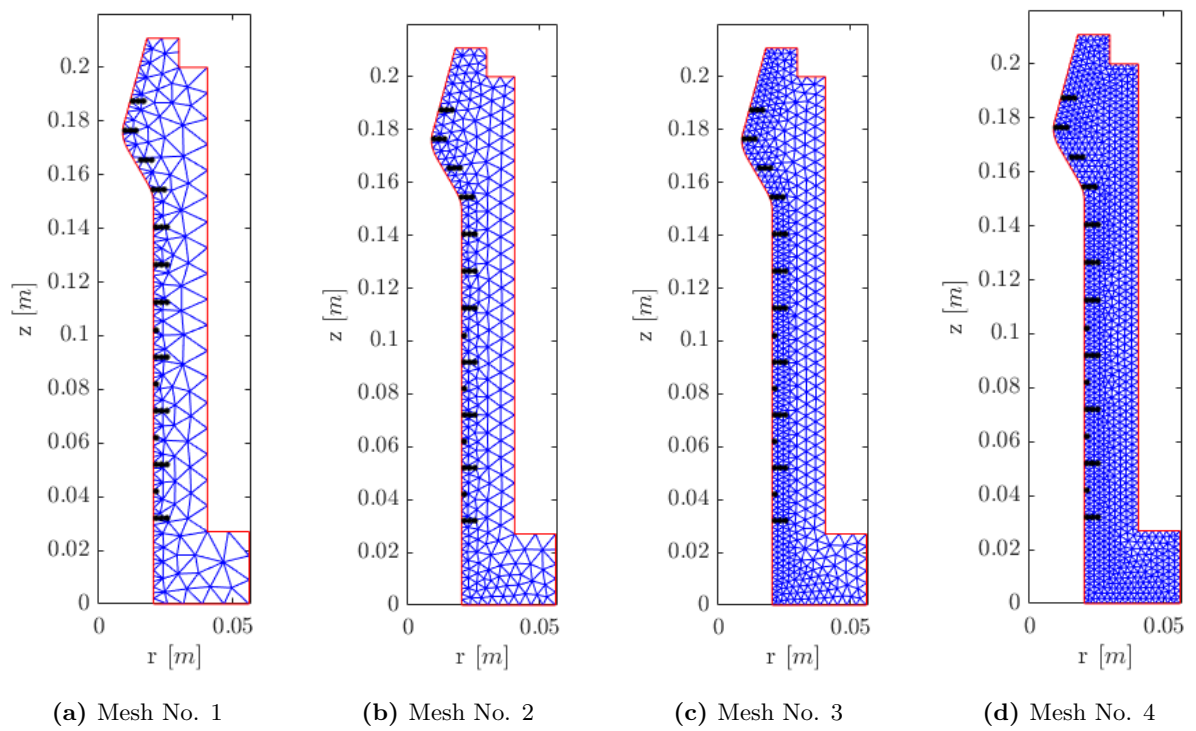


Figure 6.23.: Investigated meshes for mesh study from coarsest to finest

7. Results

This chapter includes the visual inspection of the coatings before and after the hot fires. The axial and circumferential temperature profiles and an evaluation of the simulated thermal barrier coating temperatures are incorporated. The main results of the IHCM, the specific heat fluxes and their temporal evolution are presented. The load points of all the hot fire runs are summarized and followed by the performance analysis including values like the integral heat load, the combustion efficiency, the characteristic velocity and the specific impulse. A critical analysis of the IHCM errors is presented as well.

7.1. Thermal Barrier Coating Visual Inspection

Three different kinds of visual inspections were done. One without visual magnification, capturing more holistic pictures of the CC segments with a camera. Most images were done with a digital microscope, measuring the crack lengths and delamination areas as well as the layer thickness. The surface roughness was evaluated with a 3D confocal laser scanning microscope. The microscope measurements were performed at the Chair of Metal Forming and Casting at TUM. More information about the specific microscopes is provided in [22]. The microscope pictures were taken at the same location before and after the hotfire to ensure coherence.

7.1.1. Ceramic Thermal Barrier Coating



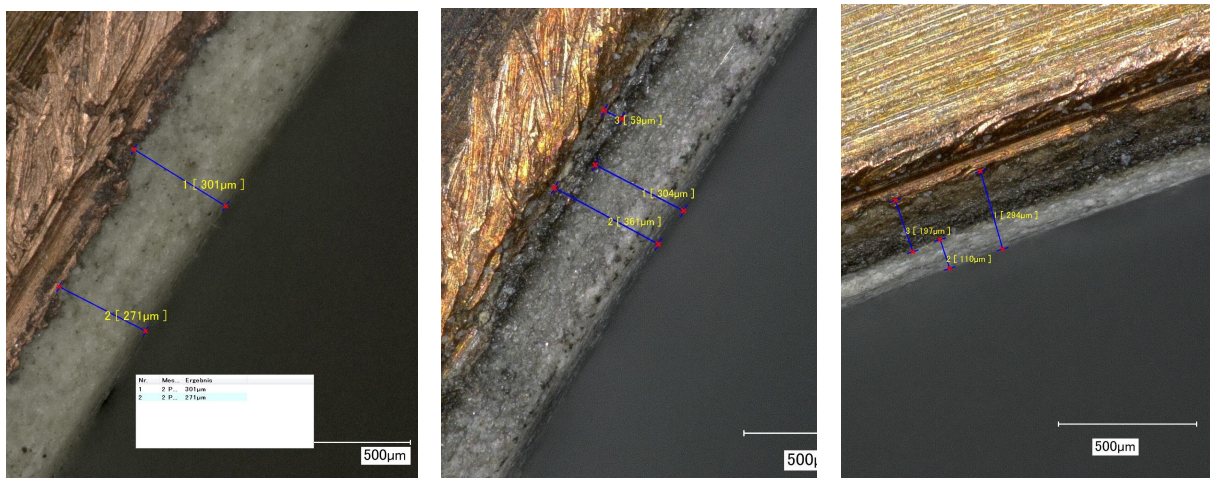
(a) Ceramic TBC condition before

(b) Ceramic TBC condition after

Figure 7.1.: Ceramic TBC condition before and after hotfires

General Condition: The ceramic coated segment was done professionally by the company rhv-Technik. As can be concluded from Figure 7.1a the surface is even and no cracks or delamination could be found by visually inspecting the TBC. Both perspectives in Figure 7.1 were taken looking to the injector, ergo looking into the outlet. For easier orientation both show the drilling holes of the pressure sensors into the chamber, which are in Figure 4.6 taken as a reference at 180° . The black mark in the picture after the hotfire test series, starts upstream at about 45° and ends at about 0° at the outlet, suggesting a clockwise turn of the stream in direction of the outlet. This mark was probably left by the fuel-rich igniter, while the whirl originates from the swirl injector.

The naked eye examining the ceramic TBC can assert that the coating does not end in the same plane as the inner surface of the cylinder, resulting in a very small round edge, instead of a sharp one. This is most likely a product of the manufacturing technique and can be seen in Figure 7.2.



(a) Ceramic TBC thickness inlet before hotfire (b) Ceramic TBC thickness inlet after hotfire (c) Ceramic TBC thickness outlet after hotfire

Figure 7.2.: Ceramic TBC thickness close-up before and after hotfire

Layer Thickness and Edges: The layer thickness could be analyzed through the microscope, measuring at a 0° angle. It can be seen in Figure 7.2, that the exact thickness of the layer is difficult to determine, because of the overlap of the copper and irregularities at the edges. Here, a thickness before the hotfire at the inlet of $271 - 301 \mu m$ was measured. It is interesting to note the structure of the coating after the hot fire, visible for the inlet in Figure 7.2b and the outlet in Figure 7.2c. Comparing Figure 7.2b and Figure 7.2a it can be deduced that the layer changed at the interface to the copper substrate. Whether it is an oxidation of the boundary surface itself, or if it is superficial, can only be evaluated by destructive methods. This was not done as the part may be used in the future. A similar pattern is visible at the outlet after the hotfires in Figure 7.2c, where the altered layer accounts for approximately the half of the layer thickness. As stated in [8], the oxygen permeable ceramic coating, especially for coatings sprayed with the Atmospheric-Plasma-Spraying Method (APS) technique, can exhibit an oxidation of the bond coat after thermal cycling.

Cracks and Delamination: In general no cracks or delaminations could be determined. Neither by visual inspection, nor by the microscopic examination.

Surface Roughness: The surface roughness was both times measured at the inlet with the laser scanning microscope at an angle of 30° in the curvature of the cylinder, which both affects the magnitude of the following values. Nevertheless as they were measured at the same conditions, a relative statement can be formed. Before the test the roughness was $R_a = 4.5\mu m$ and $R_z = 28.9\mu m$ and after the test $R_a = 2.9\mu m$ and $R_z = 20.8\mu m$. This concludes that the combustion products probably smoothed the surface by sedimentation. It is to be noted that the first 5 mm from the inlet and outlet going inwards exhibit a slightly rougher surface than the inner part.

7.1.2. Metallic Thermal Barrier Coating

The metallic coating was done by Dr. T. Fiedler from the Materials Science Institute of the technical university Braunschweig.

Post-manufacturing Condition: As mentioned in Section 4.3, there had to be taken 0.25 mm off of the inlet, Figure 7.3b, on the lathe, while the outlet had to be stripped of 1 mm , re-working the original contour. Reworking both face surfaces of the parts, resulted for a rather defined edge for the coating at the inlet, because it could be chipped off using a chisel, and the lathe for the edges, taking the material inwards. On the other hand, the face surface of the outlet, was also reworked using a chisel, but the inwards motion at the inner notch, resulted in the spalling of the coating at the edges. As the metallic coating is made from a very brittle and hard material, only using the lathe, without the chisel first, was not feasible.



(a) Metallic TBC condition of outlet before post-processing

(b) Metallic TBC condition of inlet before post-processing

Figure 7.3.: Metallic TBC condition of inlet and outlet before post-processing

General Condition: Figure 7.4a depicts the condition of the TBC post-manufacturing and after the necessary post-processing steps to remove excess coating that accumulated during the production process.

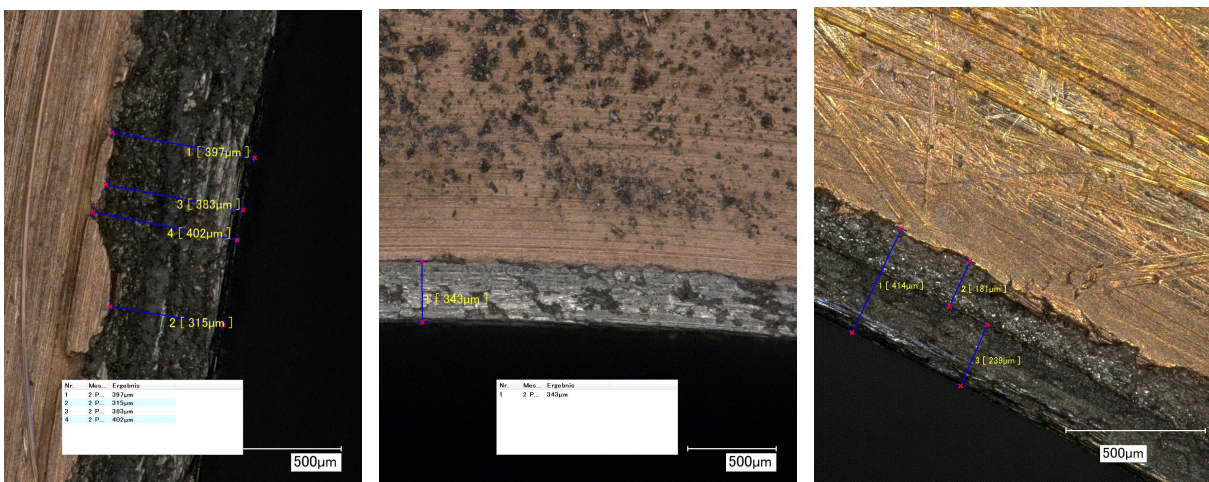


(a) Metallic TBC before hotfires and after post-processing

(b) Metallic TBC after hotfires

Figure 7.4.: Metallic TBC condition before and after hotfires

Layer Thickness and Edges: The layer thickness could be analysed through the microscope, measuring at a 0° angle. It can be seen in Figure 7.5, that the exact thickness of the layer is difficult to determine, equal to the ceramic coating, especially for the inlet. Measuring such small thicknesses with no real references, as the copper surface is quite wavy and the transition from TBC to inner cylinder is complicated to pinpoint. The values were measured about $250 \mu m$ from each other and vary quite a bit. As the outlet was reworked on the lathe, the cut to the coating was more defined, also visible in Figure 7.4a.



(a) Metallic TBC thickness inlet before hotfire

(b) Metallic TBC thickness outlet before hotfire

(c) Metallic TBC thickness inlet after hotfire

Figure 7.5.: Metallic TBC thickness close-up before and after hotfire

For the inlet thicknesses of $315 - 402 \mu m$, Figure 7.5a, and for the outlet $343 \mu m$, Figure 7.5b were measured. It is interesting to note the structure of the coating after the hot fire, visible for the inlet in Figure 7.5c, which similar to the ceramic coating is visibly divided into two layers, the top one with a thickness of $239 \mu m$ and the bottom one with $181 \mu m$. Comparing Figure 7.5c and Figure 7.5a it can be deduced that the layer changed at the interface to the copper substrate. Taking into account that the inlet is depicted and the top coat thickness is about $250 \mu m$, this visible difference in coating structure is

probably the top and bond coat, whereas the exact division varies depending on the exact measurement location, leading to a higher "supposed bond coat" value.

Cracks and Delamination: After the post-processing steps done at TUM a circumferential strip of about 7 mm average thickness was spanning from (referencing Figure 4.6) about 45° to 230° was uncoated. This means the top part at this axial position was uncoated, which can be seen in Figure 7.6a. This figure is taken from the inlet, which is why the pressure sensor drill holes are located on the right instead of on the left. Meaning that there was an uncoated part of the chamber in the middle of CC1 exposed to the hot gas stream. It was located where the bulge was attempted to be reduced on the lathe. However while doing so the coating delaminated completely at this weak spot, leaving a broad strip of missing coating.



(a) Metallic TBC crack condition before

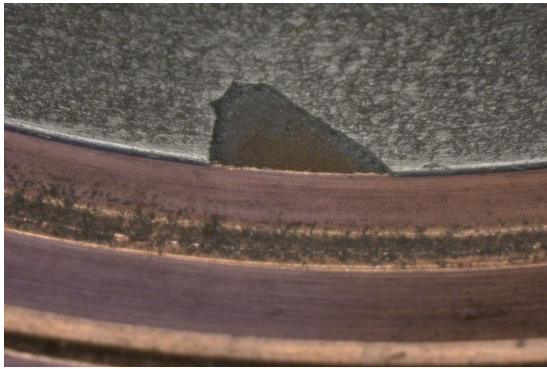
(b) Metallic TBC crack condition after

Figure 7.6.: Metallic TBC crack condition before and after hotfires

After the hotfire experiments the strip was missing along the whole circumference, while melting at some locations. This phenomenon can best be seen in Figure 7.6b, which is approximately at the end position of the delaminated area at the beginning of the experiments, at about 230°. Through the elevated convective heat transfer due to the step in the surface most likely creating a small recirculation zone, the material melted and was transported by the hot gas stream out of the CC, which can also be seen in Figure 4.9b. Around both breaking lines thermal discolouration can be observed, a witness of the very same incident happening. This weak spot in the coating resulted in a premature termination of the hotfire experiments, such that the behaviour of the coating at the engine design load point could not be evaluated.

Due to post-processing, the inlet was nearly without major problem areas. Here, the edge of the coating was rather round than sharp.

The documented cracks and delamination were all located at the outlet of the segment. The cracks started radially at the sealing surface of the chamber, propagating to the inside of the chamber, visible in 7.3a. According to [8], if the coating adhesion is not affected, the cracks are not likely to cause delamination as long as they are vertical. The reason for these cracks is not clear, most likely caused by thermal strains because of the different thermal expansion coefficients of the nickel based coating and the copper



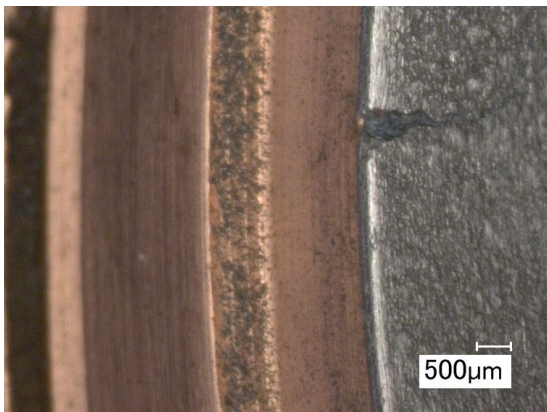
(a) Metallic TBC delamination condition before



(b) Metallic TBC delamination condition after

Figure 7.7.: Metallic TBC delamination condition before and after hotfires

substrate. It is not clear if they already existed before the heat diffusion treatment as they were only visible afterwards. The delamination and microscopic crack pictures are taken with an angle of 30° to the rotational axis. One delamination and one crack is analysed in detail, while there were also minor delaminations observed at 0° , 185° , 270° and 350° at the outlet.



(a) Metallic TBC crack condition at outlet before



(b) Metallic TBC crack condition at outlet after

Figure 7.8.: Metallic TBC crack condition at outlet before and after hotfires

The delamination documented in Figure 7.7 was located at the outlet, following prior conventions, at 45° . Contrasting the before Figure 7.7a and after Figure 7.7b, it becomes apparent that the delamination did not grow marginally. Remains of the coating were removed and the copper is completely exposed.

The crack in the metallic coating before the hotfires visible in Figure 7.8a and after in Figure 7.8b, did grow from $2520 \mu\text{m}$ to $3750 \mu\text{m}$ in length. This implies that if vertical cracks are existing, the effect of thermal cycling is not to be neglected and cautious observation has to be done.

Surface Roughness: The surface roughness was both times measured at the inlet with the laser scanning microscope at an angle of 30° in the curvature of the cylinder, which both affects the magnitude of the following values. Nevertheless as they were measured at the same conditions, a relative statement can be formulated. Before the test the roughness was $R_a = 4.7 \mu\text{m}$ and $R_z = 26.8 \mu\text{m}$ and after the test $R_a = 2.2 \mu\text{m}$ and $R_z = 15.6 \mu\text{m}$ were measured. This concludes similar reasoning as for the ceramic

coating. Probably the combustion products smoothed the surface by deposition thereof.

7.2. Temperature Distribution

To compare all configurations, run 9 was chosen as it provides the same testing duration and data for every case is available. The target point is ROF 3.1 and the pressure is 10 *bar*. The time point of evaluation is the same as for the end time of the IHCM calculations, indicating the condition with highest temperatures during the test.

7.2.1. Axial Profiles

All TC readings, that were not corrupted and available for the respective configuration, were plotted. "a" being 1 *mm*, "f" being 3 *mm* and "b" being 5 *mm* from the surface of the hot gas wall. This TC information is to be found in Table 4.9. Missing sensor positions are interpolated linearly, meaning that if the temperature lines cross, this is not a physical issue, but a presentational one.

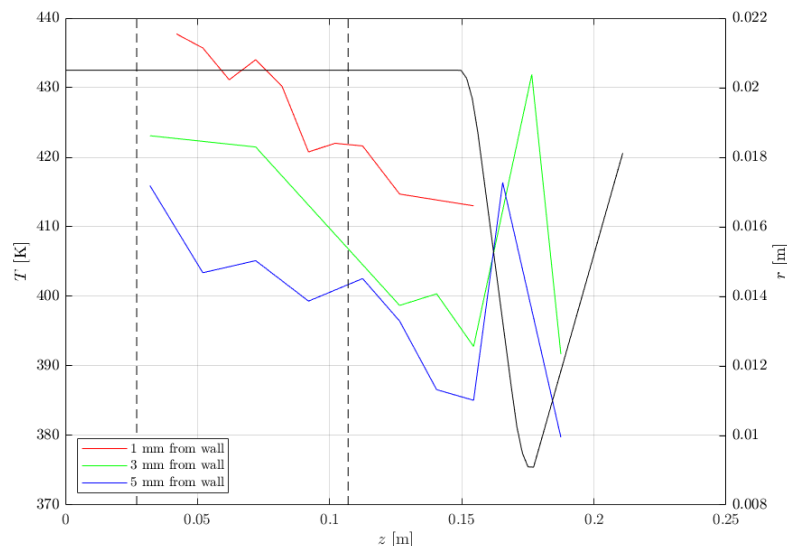


Figure 7.9.: Axial temperature profile of uncoated case at the condition with the highest temperatures

From Figure 7.9 the temperature distribution in relation to the distance to the hot gas wall can be clearly deduced. The temperature profiles show a similar trend to the heat flux in Figure 7.19, with a sinking tendency along the CC axis. The temperatures sink downstream in the cylindrical part and start rising in the convergent part, till the throat.

Figure 7.10 visualizes the effect of the ceramic TBC on the temperature profile. In the cylindrical part of the chamber, temperatures are nearly kept constant, just at the end of CC1, they start rising due to lateral heat conduction from CC3. In CC3 temperatures decrease again, but still being higher than in CC1. Excluding the peak, there is a temperature difference of about 18 *K* between the coated and uncoated segments in the ceramic hot fire 1 *mm* from the wall. Comparing the first data point of the red line in the uncoated versus ceramic case, a temperature reduction of 32 *K* is achieved.

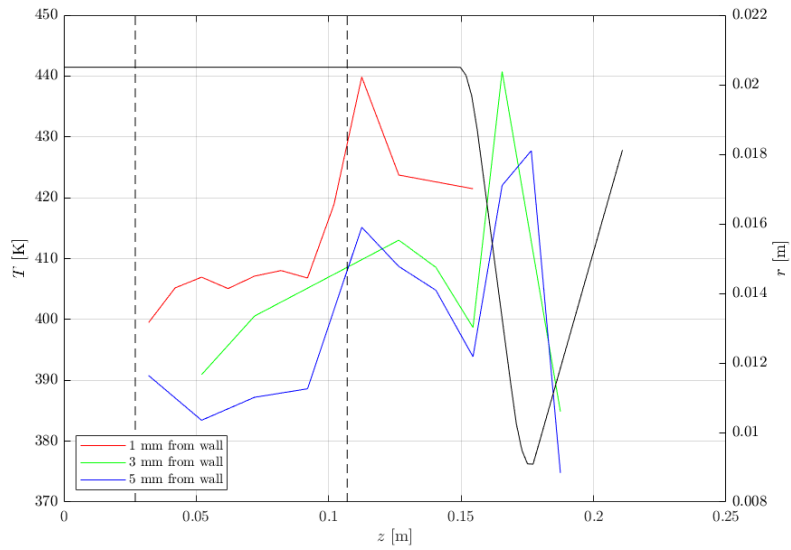


Figure 7.10.: Axial temperature profile of ceramic case at the condition with the highest temperatures

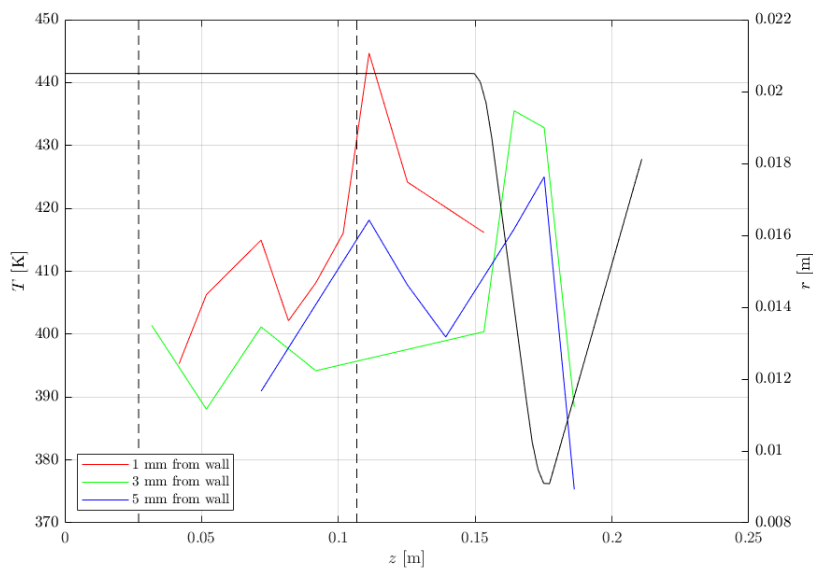


Figure 7.11.: Axial temperature profile of metallic case at the condition with the highest temperatures

Figure 7.11 shows similar behaviour to Figure 7.10, but exhibiting a peak of temperature in the middle of CC1, attributed to the fact that half of the circumference at this point is not covered by the coating. This does not directly affect the sensor positions shown in this graph, but circumferential heat conduction can be assumed. This effect is also captured by Figure 7.14c with the red line at position 45° for "f" and 0° for "a", featuring a higher temperature at the first position. Comparing the first data point of the red line in the uncoated versus metallic case, a temperature reduction of 42 K is achieved.

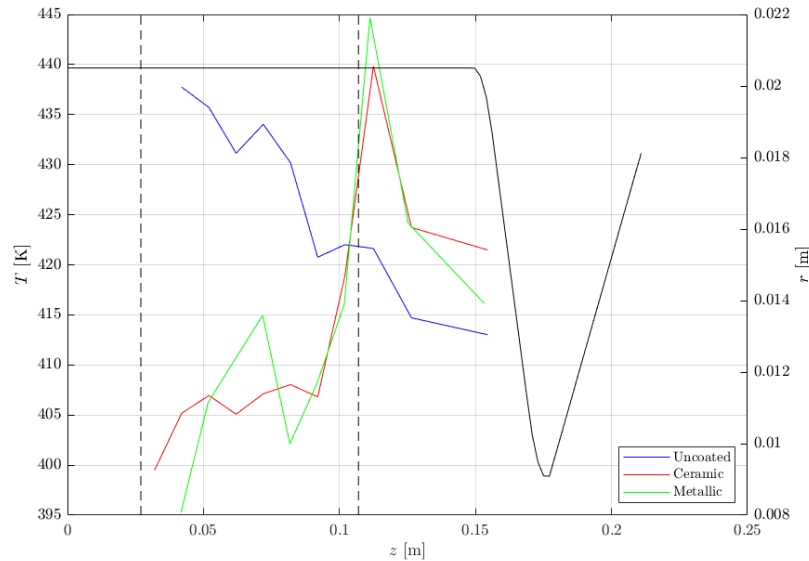


Figure 7.12.: Axial temperature profile comparison at 3 s at 1 mm from the wall for run 9

Figure 7.12 provides a direct comparison of the temperature distributions at 1 mm away from the wall. The big discrepancy between the temperatures in CC1 is visible, while shortly before the end of the segment showing hotter temperatures than the uncoated version. At the end of the cylindrical part of CC3 the ceramic version is 8 K warmer and the metallic 3 K.

7.2.2. Expected versus real Temperature Reduction

As Section 5.7.3 and Figure 5.7 elucidate, the with the help of the Sinyarev correlation simulated heat flux magnitude for the cylindrical part was a constant value of about 2.5 [MW/m^2]. In order to enhance a possible comparison, not the load point at which Figure 5.7 was generated (12 bar and $ROF = 3.1$), but the temperature reduction for a similar heat flux is compared and the same testing/simulation time is chosen. In order to compare the two coatings run number 5 is taken, because as can be obtained from Figure 7.17, this heat flux distribution for the final point in time is the most similar to the distribution in Figure 5.7. Here a target ROF of 3.5 and a pressure of 5 bar was reached.

The real achieved temperature reduction for both coatings in the cylindrical segment can be seen in Figure 7.13, the TC at 1 mm from the wall are taken. The mean temperature reduction for the experimental ceramic version is 15.41 K over the CC1 segment length and the metallic one 11.22 K, which was expected in qualitative terms. The mean temperature reduction for the simulated ceramic version is 13.79 K over the CC1 segment length and the metallic one 7.12 K. The mean temperatures are not deviating as much for the ceramic case with 10.5%, while for the metallic case the difference is 36.5%, which indicates an issue with the material properties of the TBC, which most likely changed during the manufacturing process, while also taking into consideration that part of the coating was missing in the CC1 segment, as described in Section 7.1.2.

Both, the experimental data as well as the simulated data shows the diminution in temperature difference to the end of the segment, where an assimilation of the temperatures in CC3 for all three versions starts,

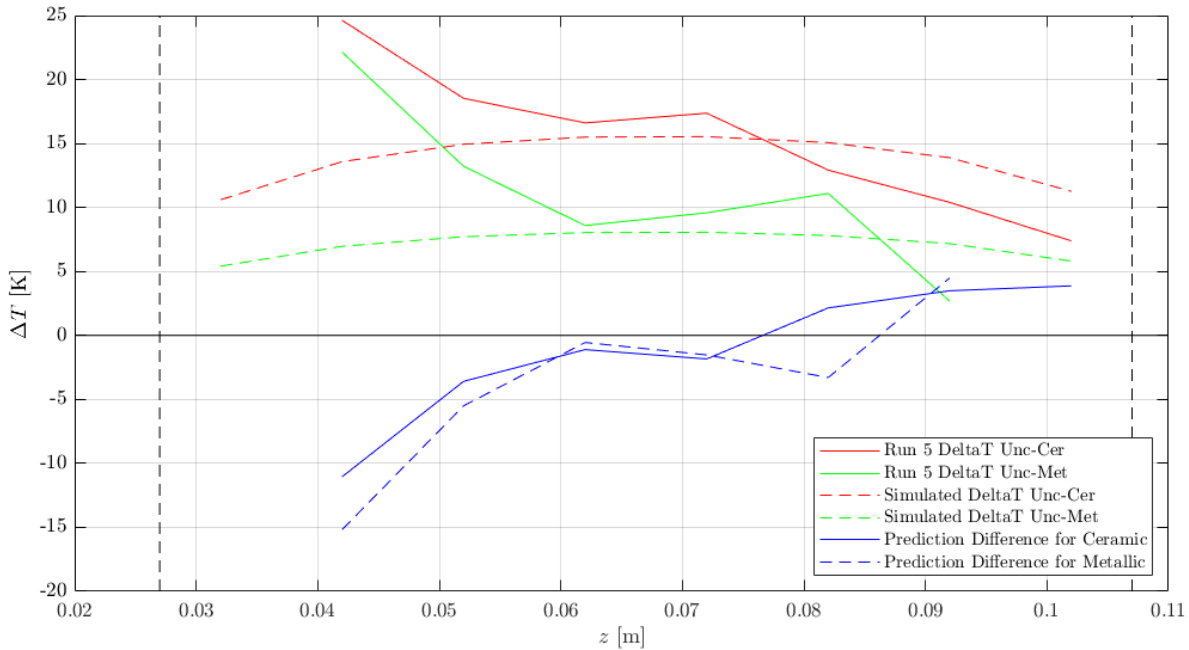


Figure 7.13.: Axial temperature difference for coated versus uncoated for experimental and simulated data at 3 s at 1 mm from the wall in the coated CC1 segment and their deviation in prediction

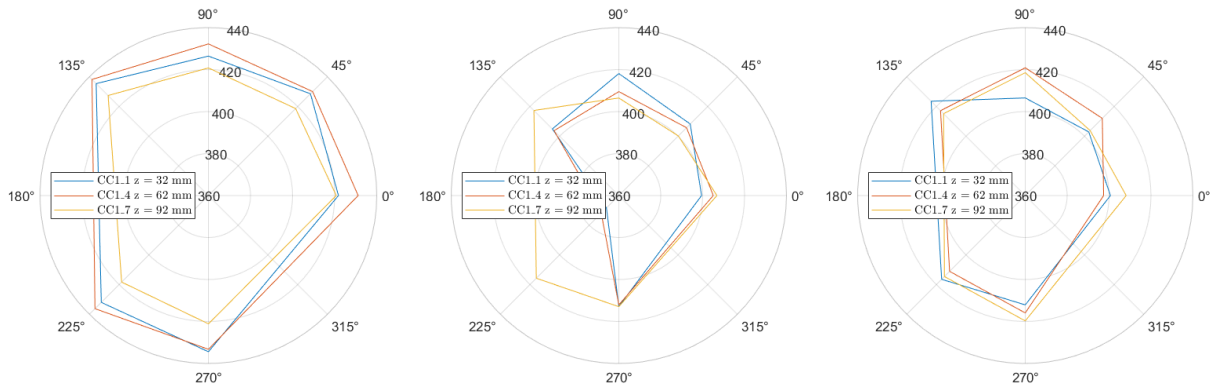
as can be seen for example in Figure 5.8. In Figure 7.13 it becomes apparent that the distribution over the length of the segment can not be predicted by the simulation. This is probably owed to the bigger heat fluxes alongside the chamber axis than supposed, while the fact that the chamber is treated as one bulk geometry, instead of three separated parts, reinforces this trend. Another additional explanation is the injector effect, which is not considered in analytic correlations. This exculpates the need for a closer look at possibly differently simulating the contact areas between the segments.

The difference in prediction is visualized with the blue lines. In general the prediction for the ceramic case is better than for the metallic configuration. In the beginning of the segment both temperature reductions get under-predicted and in the last quarter, rather over-predicted, explained by the previous statements made.

7.2.3. Circumferential Profiles

In total, data of three planes in the first combustion chamber segment was collected. The first one CC1_1 is the first plane after the igniter ring ($z = 32\text{mm}$), the second plane is located 5 mm before the middle plane of the CC element ($z = 62\text{mm}$) and the last plane sits 15 mm before the beginning of CC2 ($z = 92\text{mm}$). The view depicted in Figure 7.14 is equal to the view in Figure 4.6, looking from the nozzle into the chamber. The TC position at 0° was already used as an input for the IHCM.

Figure 7.14a shows the general trend of the temperature rising to the middle of the CC, with the second plane exhibiting the highest temperatures, and then a temperature drop to the end of the element with the lowest values in plane three. Sensor CC1_1a at 0° was taken from the evaluation, evidence in Table 4.9, showing too low values. The same problem seems to exist with CC1_4BM. Nevertheless the temperature



(a) Circumferential temperatures of uncoated case (b) Circumferential temperatures of ceramic case (c) Circumferential temperatures of metallic case

Figure 7.14.: Circumferential temperatures at the condition with the highest temperatures

profiles for the respective planes are quite uniform, not indicating any hot spots.

In Figure 7.14b clearly an issue occurs with the temperature measurements at CC1_1BL and CC1_4BL. The TC in CC1_7 exhibit the most uniform distribution, in alignment with the expected temperature distribution and can be taken as a point of reference for the other planes. As the sensors in 0° were not showing faulty values, their trend can be taken as a reference as well, even though the exact magnitude, as CC1_4a and CC1_7a lie closely within each other, is questionable. Here a temperature increase over the segment to CC3 would be detected, but this is contradicting the measurements of top right and top middle, which show a temperature decrease downstream the segment. Excluding the one sensor position on the bottom left, the first and second plane are rather uniform as well, but as the measurements are located in the same magnitude, it is difficult to gain a clear picture. Concluding the circumferential measurements of the ceramic case are not reliable.

As stated in Table 4.9, for the metallic version the sensors CC1_1a and CC1_4a at 0° were discarded, so most likely the blue and red positions are above or in the vicinity of the yellow one, as it is true for bottom left and top left. Throughout the most positions, the third plane shows higher temperatures than the second one. TL and BL coincide with the findings of the heat flux value, Figure 7.27. As explained in Section 7.1.2, the CC was exposed to the hot gas streams at about 45° to 230° , which is just a bit after plane two, which could explain the more asymmetric form of the CC1_4 plane.

7.3. Specific Heat Flux Evaluation

The final results for every run for every time step are found in the appendix. For the uncoated case it should be referred to Appendix A, the ceramic hotfires are found in Appendix B and the metallic in Appendix C.

In general it can be stated that the peak in the uncoated configuration is most likely under-predicted as the sensors CC3_5, CC3_6 and CC3_7 are showing values below the actual temperature as the drill holes of the TC were partly clogged with copper oxide, amplifying the insulation effect on the measurements. For that reason the focus lies on comparing the cylindrical part. When comparing all the metallic runs in

relation to the ceramic coating, it is striking that in the geometrical transition zone from the cylindrical part to the throat, the metallic coating is always showing higher HF values than the uncoated and ceramic version. Additionally the peak value in the throat of the metallic configuration exhibits always lower values than the ceramic configuration. As the nozzle was in all the cases uncoated and the same specimen, the reason for this effect is most likely a sensor issue which leads as a consequence to a numerical issue. While comparing temperature data from the same load points at the same time for the metallic and ceramic coating, it became apparent that the maximum temperatures of the metallic case are always higher (at an ROF of 3.5 at 10 *bar* for CC3_4a ≈ 16 K, for CC3_5b ≈ 18 K, for CC3_6b ≈ 17 K and for CC3_7b ≈ 10 K) than the ceramic case, which could be the reason that the IHCM finds a higher heat flux in the cylindrical part of the second segment. A higher HF there seems to initiate the algorithm to find a lower peak value than the ceramic case. A possible explanation could be the a too temperature in the throat in case of the metallic configuration in proportion to it's high temperatures in the cylindrical part. The effects seen in the results, of higher and lower HF in comparison to each other in the second segment could be a combination of partly clogged sensor holes, a measurement error as a consequence, which leads to find a numerical solution, that is not equal for this segment in the end. At least shortly after the first segment, the HF distributions should be similar.

The following HF distribution are evaluated at the last point in time, in order to find a common evaluation criterion for all the runs. Searching for the maximum value in the throat leads to observing fairly different instants in time, thus this approach has been discarded. The first test of each load point and configuration is shown by a continuous line, the second with a dashed one. In order to highlight the reproducibility of the results, a second evaluation of the second run at the last point in time of the first run for every configuration, if this was not already the case with the second run duration, is drawn with a dotted line.

As the nominal load point is a combustion chamber pressure of 12 *bar* and a ROF of 3.1, the different pressure points are compared to each other with the ROF as a variable, rather than the ROF as a first common trait, as this would lead to up to 12 different HF distributions in one plot instead of six.

7.3.1. 5 bar Tests

For this pressure load point the three ROF of all three configurations could be tested.

ROF 2.7 For this load point an average CC pressure of around 4.4 *bar* was reached. The ROF was under-accomplished by the uncoated and ceramic configuration, the metallic one reached the desired one rather accurate. A general tendency in the CC1 segment, spanning from 0.027 *m* till 0.107 *m*, is that the highest heat flux is found in the uncoated segment. The ceramic one has the effect of a rather constant low heat flux through the whole cylindrical part, also in CC3. The HF in the metallic coated CC1 drops to a minimum, also compared to the other HF in this part, in the middle of the CC1 section. However it rises in the CC3 part. The metallic configuration exhibits the largest HF value in the transition zone from the cylindrical to convergent geometry. The influence of the longer test durations shows in a higher HF value in the beginning of CC1 and thus also in the igniter ring. The uncoated and metallic case exhibit the best repeatability in the first segment and indicate that quasi steady-state was already reached at that point in time. The ceramic case is rather different from both, the first and the second run, which is probably owed to the fact, that the first run only continued for two instead of three seconds.

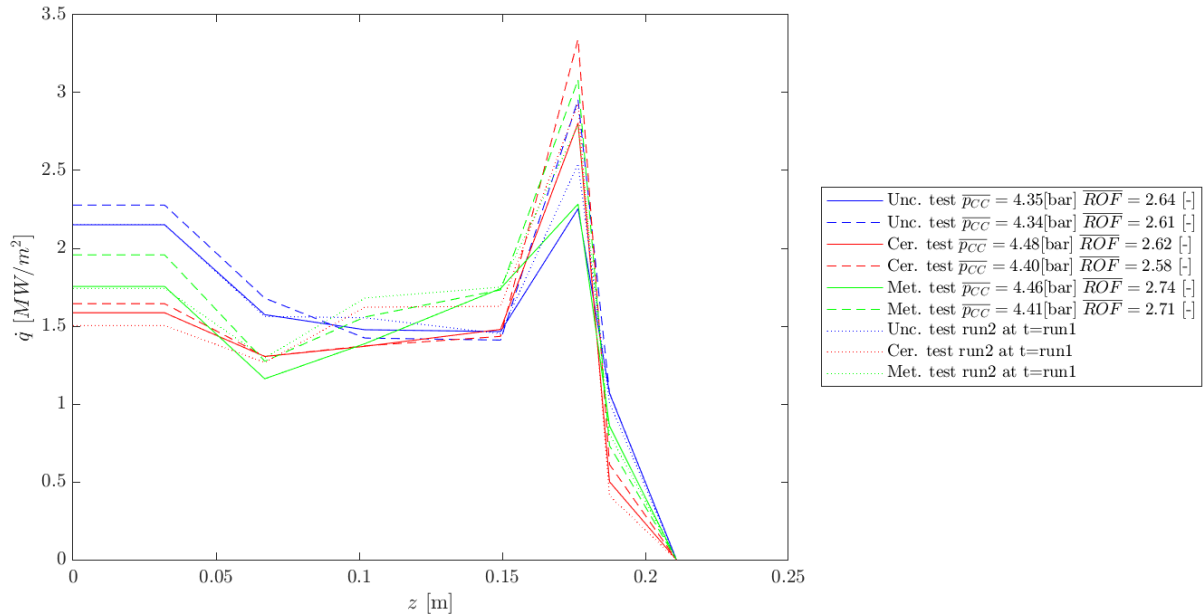


Figure 7.15.: Heat flux comparison of the test configurations at 5 bar and target ROF of 2.7

The HF in the nozzle part of the uncoated and the metallic configuration differ greatly for the peak value comparing the two tests with each other. Both intermediate time steps of run two of unc. and met. exhibit higher values than run one, restricting the repeatability more to the cylindrical part. Also the first ceramic test displays a lower peak than the second. This is due to the first tests being two to three seconds shorter than the second. The intermediate run, is although quite close in value. As the optimization point in the transition zone coincide regardless of the testing period it mainly manifests in the peak value. The last optimization point follows the same trend as the cylindrical part, with the uncoated test displaying the highest HF value, followed by the metallic and then the ceramic configuration. There seems to be a connection of a higher value in the optimization point from cylindrical to the throat area, to a lower peak value found by the algorithm, probably caused by the previously mentioned reasons.

Table 7.1.: Overview of the test durations for 5 bar and ROF 2.7

	Uncoated Config.	Ceramic Config.	Metallic Config.
1st run t_{cc}	3.00 s	2.00 s	3.00 s
2nd run t_{cc}	5.00 s	5.00 s	5.00 s
2nd run at $t_{cc_{run1}}$	3.00 s	2.00 s	3.00 s

ROF 3.1 For this load point an average CC pressure of around 4.5 bar was reached. The ROF was under-accomplished by the uncoated and ceramic configuration, the metallic one reached the desired one rather accurate. A general tendency in the CC1 segment, spanning from 0.027 m till 0.107 m, is that the highest heat flux is found in the uncoated segment. The ceramic one has the effect of a rather constant low heat flux through the whole cylindrical part, also in CC3. The HF in the metallic coated CC1 drops to a minimum, but not as much as for the ROF of 2.7, in the middle of the CC1 section. However it rises in the CC3 part. The metallic configuration exhibits the largest HF value in the transition zone from the cylindrical to convergent geometry, although less than for the ROF of 2.7. The influence of the longer test durations shows in a higher HF value in the beginning of CC1 and thus also in the igniter ring, yet the difference between the tests of one configuration are not as large as in the previous ROF. All cases exhibit good repeatability in the cylindrical part of the first segment and indicate that quasi steady-state in terms of heat flux distribution was already reached at that point in time.

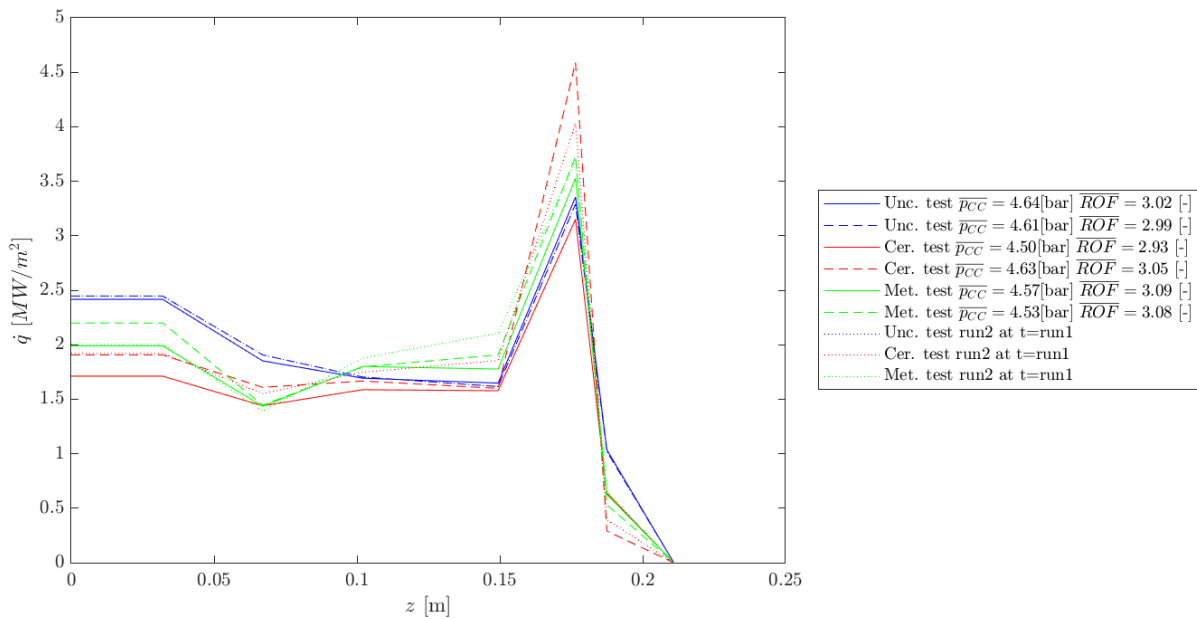


Figure 7.16.: Heat flux comparison of the test configurations at 5 bar and target ROF of 3.1

The HF in the nozzle part of the ceramic configuration differs greatly for the peak value comparing the two tests with each other, also for run two and t_{ccrun1} , similar to the previous test. The first test is shorter than the second, as it is for all the configurations, but in the ceramic configuration this seems to be a big driver of the peak value, compared to the rather small differences of the other configurations among each other. The last optimization point follows the same trend as the cylindrical part, with the uncoated test displaying the highest HF value, followed by the metallic and then the ceramic configuration.

Table 7.2.: Overview of the test durations for 5 bar and ROF 3.1

	Uncoated Config.	Ceramic Config.	Metallic Config.
1st run t_{cc}	3.00 s	3.00 s	3.00 s
2nd run t_{cc}	5.00 s	4.99 s	5.00 s
2nd run at t_{ccrun1}	3.00 s	3.00 s	3.00 s

ROF 3.5 For this load point an average CC pressure of around 4.5 bar was reached. The ROF was under-accomplished by the ceramic configuration, the uncoated one reached the desired one rather accurate and the metallic over-estimated. The general tendency in the CC1 segment, spanning from 0.027 m till 0.107 m, of the highest heat flux being in the uncoated segment also applies here. The ceramic one has the effect of a rather constant low heat flux through the whole cylindrical part, also in CC3. The HF in the metallic coated CC1 drops marginally, but not as much as for the ROF of 3.1, in the middle of the CC1 section and does not rise as much in the CC3 part. The metallic configuration exhibits the largest HF value in the transition zone from the cylindrical to convergent geometry, although less than for the ROF of 2.7. The influence of the longer test durations in the igniter ring are not as dominant as in the lower ROF any more. All cases exhibit good repeatability, the distributions are nearly identical between two runs, throughout the whole CC length and indicate that quasi steady-state was already reached at that point in time.

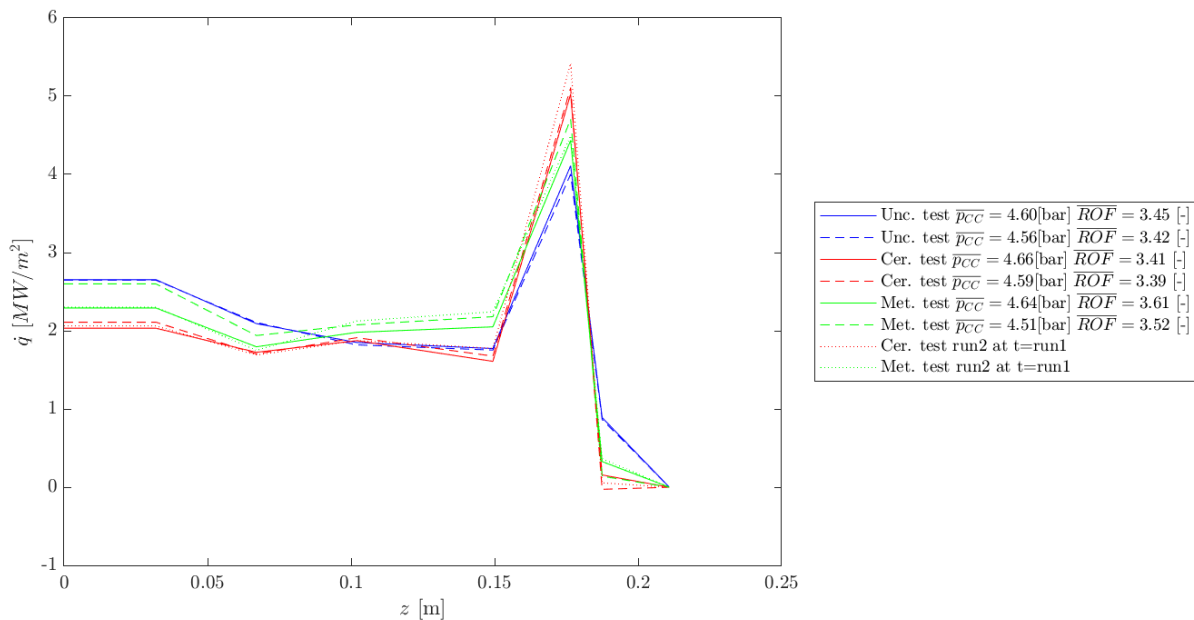


Figure 7.17.: Heat flux comparison of the test configurations at 5 bar and target ROF of 3.5

The HF in the nozzle part follows the same trend as before, from high to low with ceramic, metallic and then uncoated. This reverses in the last optimization point. The longest test duration in all the experiments of the second hot fire of the metallic case did not provoke an outstanding effect. Overall, the longer testing periods do not influence the magnitude of the tests in one configuration as much as for the lower ROF.

Table 7.3.: Overview of the test durations for 5 bar and ROF 3.5

	Uncoated Config.	Ceramic Config.	Metallic Config.
1st run t_{cc}	3.00 s	3.00 s	3.00 s
2nd run t_{cc}	3.00 s	5.00 s	8.52 s
2nd run at $t_{cc,run1}$		3.00 s	3.00 s

7.3.2. 10 bar Tests

ROF 2.7 For this load point an average CC pressure of around 8.9 bar was reached. The ROF was under-accomplished by the uncoated and ceramic configuration, the metallic one reached the desired one rather accurate. The highest heat flux in CC1 is found in the uncoated segment. The HF in the metallic and ceramic coated CC1 drops to a minimum in the middle of the CC1 section. The ceramic case exhibits lower magnitudes of HF in the cylindrical part compared to the metallic one. Both coated options show a constant HF distribution in the cylindrical part of CC3. The metallic configuration exhibits the largest HF value in the transition zone from the cylindrical to convergent geometry. The uncoated and ceramic cases are nearly equal. As in the 5 bar case the uncoated HF falls below the metallic one but has a similar magnitude than the ceramic one in the constant area of CC3. The influence of the longer test durations shows a higher HF value in the beginning of CC1 and thus also in the igniter ring, yet the difference nearly vanishes in the nozzle area. The uncoated and ceramic cases exhibit good repeatability, the distributions are nearly identical, throughout the whole CC length. Only the metallic distribution differs slightly in the cylindrical part.

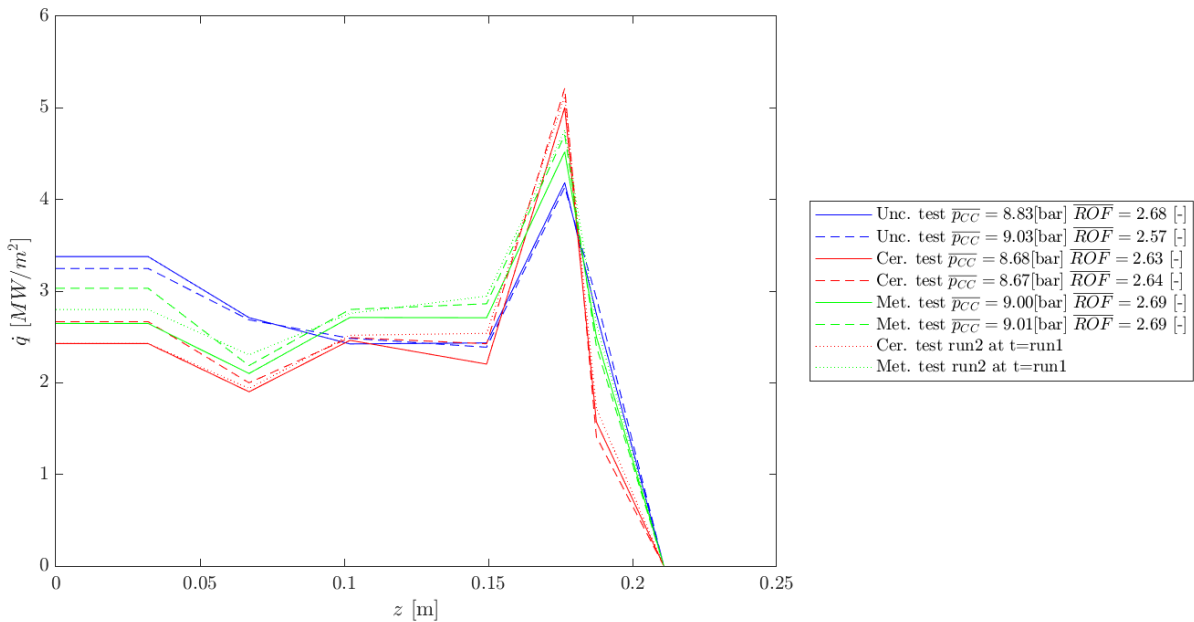


Figure 7.18.: Heat flux comparison of the test configurations at 10 bar and target ROF of 2.7

The peak value of the HF in the nozzle part are quite similar for each configuration in itself. The ceramic configuration demonstrates again the highest value, followed by the metallic and then uncoated case. The last optimization point follows the reversed trend.

Table 7.4.: Overview of the test durations for 10 bar and ROF 2.7

	Uncoated Config.	Ceramic Config.	Metallic Config.
1st run t_{cc}	3.00 s	3.00 s	3.00 s
2nd run t_{cc}	3.00 s	5.00 s	5.00 s
2nd run at t_{ccrun1}		3.00 s	3.00 s

ROF 3.1 For this load point an average CC pressure of around 9.3 *bar* was reached. The ROF was under-accomplished by the uncoated and metallic configuration, the ceramic one reached the desired one rather accurate. The highest heat flux in CC1 is found in the uncoated segment. The HF in the metallic and ceramic coated CC1 drops to a minimum in the middle of the CC1 section, equivalent to the lower ROF. The ceramic case exhibits lower magnitudes of HF in the cylindrical part compared to the metallic one. Both coated options show a constant HF distribution in the cylindrical part of CC3. The metallic configuration exhibits the largest HF value in the transition zone from the cylindrical to convergent geometry. The uncoated and ceramic cases are nearly equal. As in the 5 *bar* case the uncoated HF falls below the metallic one in CC3 but has a similar magnitude than the ceramic one in the constant area of CC3. Both HF distributions of the two distinct tests of the uncoated and ceramic case are nearly equivalent, as the load points and testing periods are alike. All cases exhibit good repeatability, the distributions are nearly identical, throughout the whole CC length and indicate that quasi steady-state was already reached at that point in time.

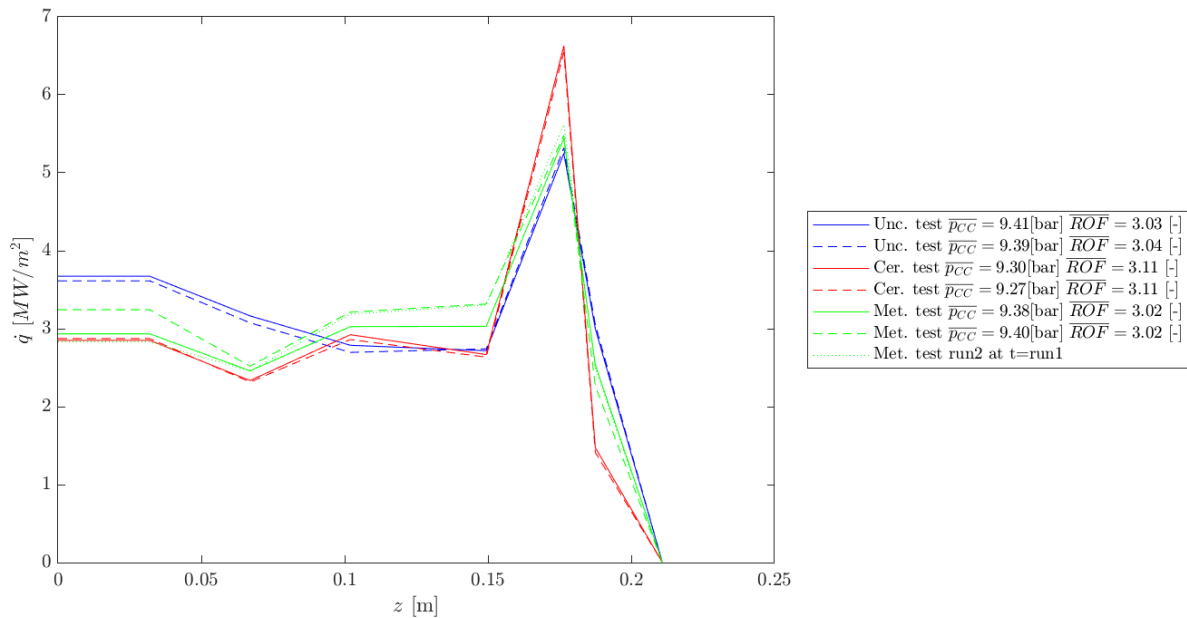


Figure 7.19.: Heat flux comparison of the test configurations at 10 *bar* and target ROF of 3.1

The peak value of the HF in the nozzle part are quite similar for each configuration in itself. The ceramic configuration is demonstrates this time by far the highest value, followed by the metallic and then uncoated case. The last optimization point follows the same trend as the cylindrical part, with the uncoated test displaying the highest HF value, followed by the metallic and then the ceramic configuration.

Table 7.5.: Overview of the test durations for 10 *bar* and ROF 3.1

	Uncoated Config.	Ceramic Config.	Metallic Config.
1st run t_{cc}	3.00 s	3.00 s	3.00 s
2nd run t_{cc}	3.00 s	3.00 s	4.76 s
2nd run at t_{ccrun1}			3.00 s

ROF 3.5 For this load point an average CC pressure of around 9.3 bar was reached. The ROF was under-accomplished by the uncoated configuration, the ceramic one reached the desired one rather accurate and the metallic one over-estimated. The highest heat flux in CC1 is found in the uncoated segment, although it gets overtaken at around 0.9 m from the metallic configuration. The HF in the metallic and ceramic coated CC1 drops to a minimum in the middle of the CC1 section, equivalent to the lower ROF. This time the minimum of the ceramic case is deviating more from the metallic case than for the lower ROF. This demonstrates the cooling effect of the ceramic case being quantitatively better than the metallic one. All options show a constant HF distribution in the cylindrical part of CC3. The metallic configuration exhibits the largest HF value in the transition zone from the cylindrical to convergent geometry. The ceramic case performs better in this point pointed out by a lower HF value. As in the 5 bar case the uncoated HF falls below the metallic one in CC3 but has a similar magnitude than the ceramic one in the constant area of CC3. Both HF distributions of the two distinct tests of the uncoated and ceramic case are nearly equivalent, as the load points and testing periods are alike. Except from the metallic case in the cylindrical part, the other cases exhibit good repeatability throughout the whole CC length and indicate that quasi steady-state was already reached at that point in time.

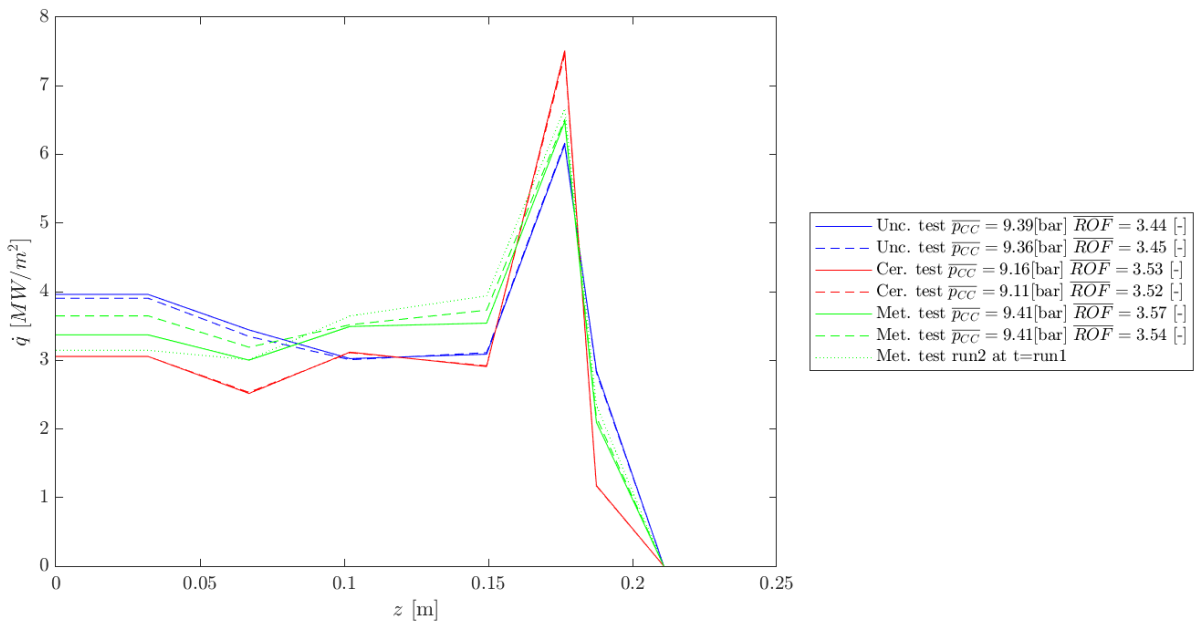


Figure 7.20.: Heat flux comparison of the test configurations at 10 bar and target ROF of 3.5

The peak value of the HF in the nozzle part are quite similar for each configuration in itself. The ceramic configuration is demonstrates by far the highest value, like for ROF 3.1, followed by the metallic and then uncoated case. The HF in the last optimization point reverse this order.

Table 7.6.: Overview of the test durations for 10 bar and ROF 3.5

	Uncoated Config.	Ceramic Config.	Metallic Config.
1st run t_{cc}	3.00 s	3.00 s	3.00 s
2nd run t_{cc}	3.00 s	3.00 s	4.27 s
2nd run at $t_{cc_{run1}}$			3.00 s

7.3.3. 12 bar Tests

ROF 2.7 For this load point an average CC pressure of around 11.6 *bar* was reached. The ROF was under-accomplished by both configurations. The highest heat flux in CC1 is found in the uncoated segment. At the end of part CC1, for the same testing period, the HF nearly correspond to each other. This also applies for the radially constant part in CC3. The second ceramic test duration was longer and due to that, the HF in CC3 exhibits a higher value there. The HF in ceramic coated CC1 drops to a minimum in the middle of the CC1 section. This demonstrates the cooling effect of the ceramic case compared to the uncoated case. Both options show a constant HF distribution in the cylindrical part of CC3. In the transition zone from the cylindrical to convergent geometry, both configurations show a similar HF value for the same test duration. Compared to the lower pressure points, the CC3 HF value is now higher than the value in the CC1 part. The ceramic case exhibits good repeatability in the beginning of the first segment, but diverges to the end of it and exhibits also different values in the cylindrical part of the second segment. Slight heat flux variations and an earlier point in time exhibiting higher HF values as can be seen in Figure 7.21 are a rather usual behaviour as the HF distribution is only quasi steady-state, which can also be taken from Appendix B.

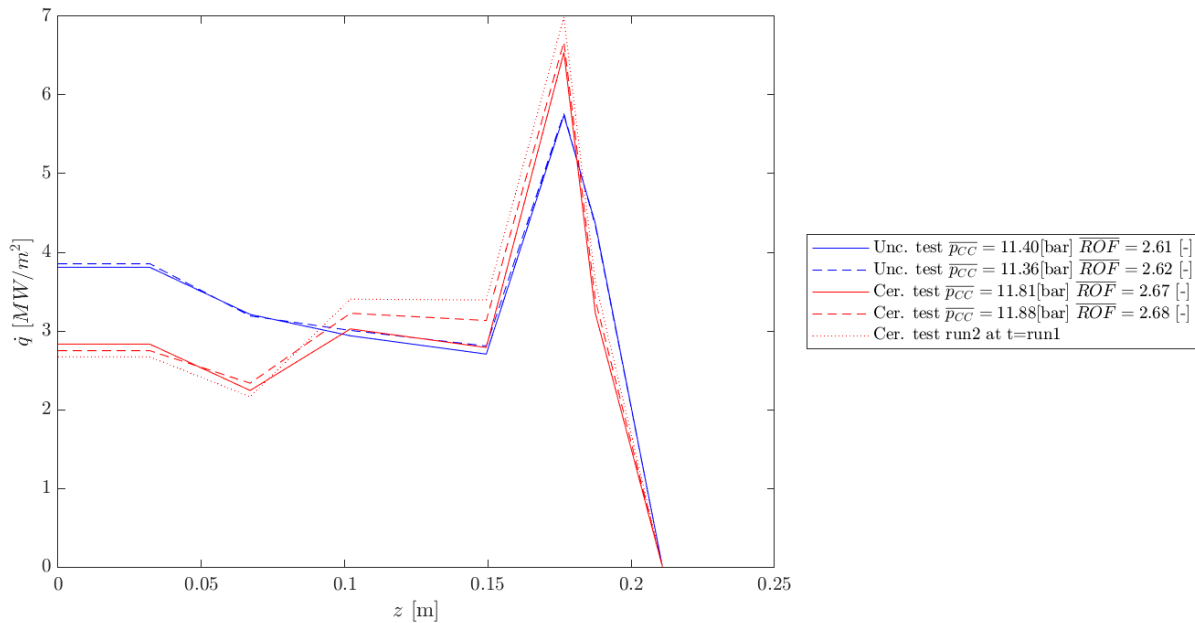


Figure 7.21.: Heat flux comparison of the test configurations at 12 *bar* and target ROF of 2.7

The peak value of the HF in the nozzle part are quite similar for each configuration in itself. In both cases, the magnitude is not as different as at the lower pressure points. The HF in the last optimization point reverse the order of magnitude for the cases in the peak.

Table 7.7.: Overview of the test durations for 12 *bar* and ROF 2.7

	Uncoated Config.	Ceramic Config.
1st run t_{cc}	3.00 s	3.00 s
2nd run t_{cc}	3.00 s	4.71 s
2nd run at $t_{cc_{run1}}$		3.00 s

ROF 3.1 For this load point an average CC pressure of around 11.8 *bar* was reached. The ROF was under-accomplished by both configurations. The highest heat flux in CC1 is found in the uncoated segment. At the end of part CC1, for the same testing period, the HF nearly correspond. This also applies for the radially constant part in CC3. The second ceramic test duration was longer and due to that, the HF in CC3 exhibits a higher value there. The HF in ceramic coated CC1 drops to a minimum in the middle of the CC1 section. This demonstrates the cooling effect of the ceramic case compared to the uncoated case. Both options show a constant HF distribution in the cylindrical part of CC3, which is compared to ROF 2.7 more upwards directed. In the transition zone from the cylindrical to convergent geometry, both configurations show a similar HF value for the same test duration. Compared to the lower pressure points, the CC3 HF value is now higher than the value in the CC1 part. The ceramic case exhibits good repeatability in the first segment, but shows higher values for the second segment.

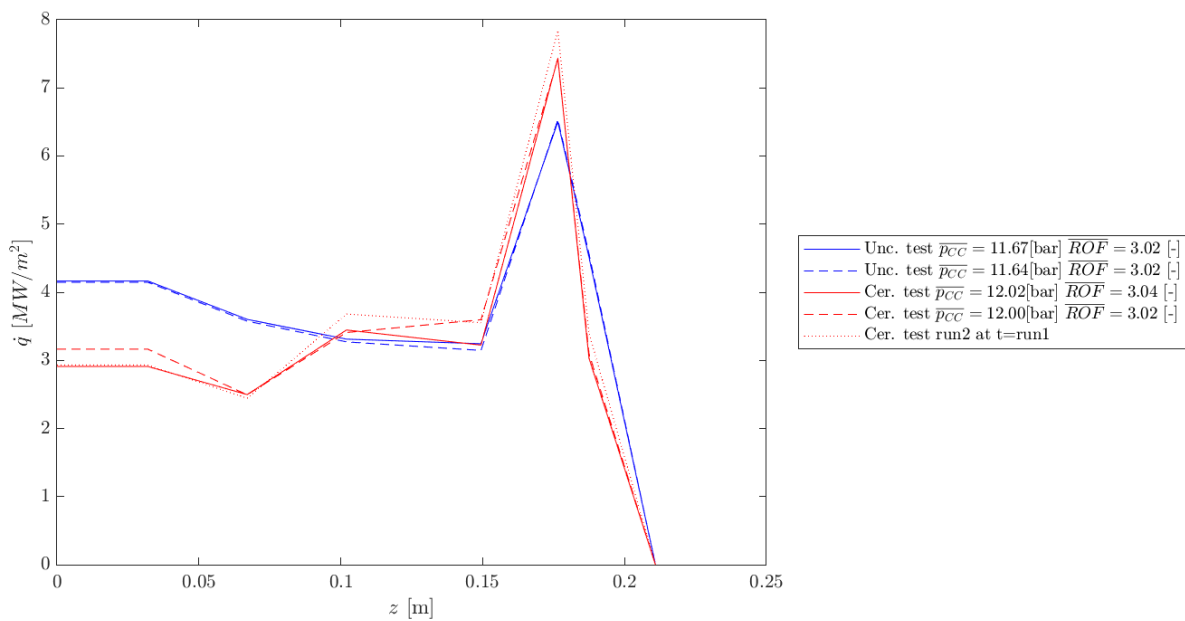


Figure 7.22.: Heat flux comparison of the test configurations at 12 *bar* and target ROF of 3.1

The peak value of the HF in the nozzle part are nearly similar for each configuration in itself. In both cases, the magnitude is not as different as at the lower pressure points and increases with the ROF. The HF in the last optimization point reverse the order of magnitude for the cases in the peak. The HF value is lower at the last point with rising ROF.

Table 7.8.: Overview of the test durations for 12 *bar* and ROF 3.1

	Uncoated Config.	Ceramic Config.
1st run t_{cc}	3.00 s	3.00 s
2nd run t_{cc}	3.00 s	4.11 s
2nd run at $t_{cc,run1}$		3.00 s

ROF 3.5 For this load point an average CC pressure of around 12.1 *bar* was reached. The ROF was nearly reached by both configurations. The highest heat flux in CC1 is found in the uncoated segment. At the end of part CC1, for the same testing period, the HF nearly correspond. This also applies for the radially constant part in CC3, where the difference is even less than for the previous ROF of 3.1. The second ceramic test duration was longer and due to that, the HF in CC3 exhibits a slightly higher value there. The HF in ceramic coated CC1 drops to a minimum in the middle of the CC1 section. This demonstrates the cooling effect of the ceramic case compared to the uncoated case. Both options show a constant HF distribution in the cylindrical part of CC3 and their values almost align. In the transition zone from the cylindrical to convergent geometry, both configurations show a similar HF value for the same test duration. Compared to the lower pressure points, the CC3 HF value is now higher than the value in the CC1 part. The ceramic case exhibits good repeatability in the first segment, but shows higher values for the second segment.

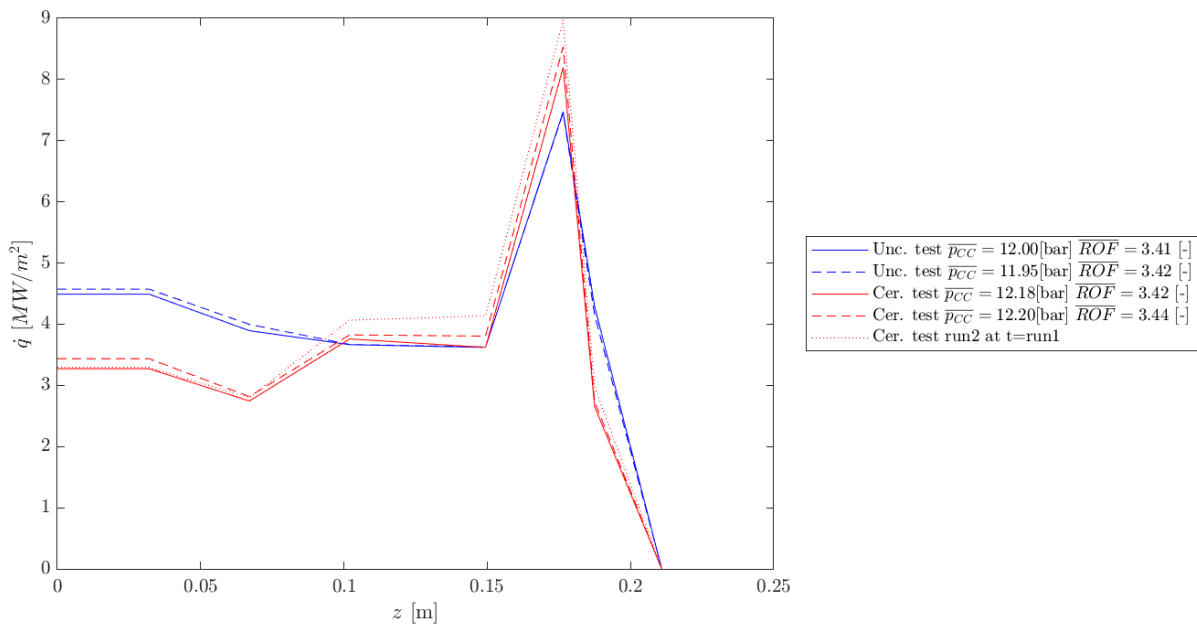


Figure 7.23.: Heat flux comparison of the test configurations at 12 *bar* and target ROF of 3.5

The peak value of the HF in the nozzle part are nearly similar for each configuration in itself. In both cases, the magnitude is not as different as at the lower pressure points. The HF in the last optimization point reverse the order of magnitude for the cases in the peak. The HF value is lower at the last point with rising ROF.

Table 7.9.: Overview of the test durations for 12 *bar* and ROF 3.5

	Uncoated Config.	Ceramic Config.
1st run t_{cc}	3.00 s	3.00 s
2nd run t_{cc}	3.00 s	4.45 s
2nd run at $t_{cc_{run1}}$		3.00 s

7.3.4. 15 bar Tests

For this pressure load point the nominal ROF 3.1 of the ceramic configuration could be tested. The first test took 3.00 s and the second 3.08 s.

ROF 3.1 For this load point an average CC pressure of around 14.9 bar was achieved. The ROF was nearly reached. The highest heat flux in CC1 is found in the uncoated segment. Along the axial direction, the HF is globally rising till the throat. Except that the HF in ceramic coated CC1 drops to a minimum in the middle of the CC1 section. Another constant HF distribution shows up in the cylindrical part of CC3.

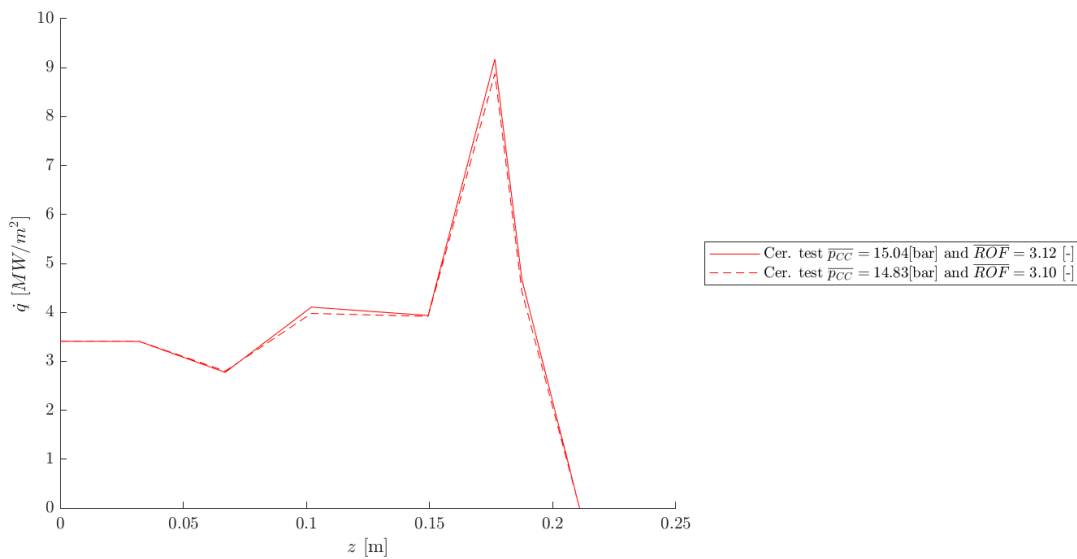


Figure 7.24.: Heat flux comparison of the test configurations at 15 bar and target ROF of 3.1

The peak value of the HF in the nozzle part are nearly similar for each configuration in itself. This test shows the maximum HF value achieved in the whole test series. This aligns with the fact that the heat flux is approximately linearly proportional to the combustion chamber pressure, $\dot{q} \propto_{cc}^{0.8}$ [43].

7.3.5. Summarized Observations

An insulation effect, thus a cooling effect can be stated as successful. The following statements are general observations summarizing the previous sections.

- A general trend that was observed is the fact that for all the pressure points an increasing value of ROF result in quantitative higher HF distributions.
- A common tendency of a lower heat flux value in the CC1 segment for the coated cases could be concluded from the results. In the coated configurations the HF values in the CC3 part were constant, but lower than in the igniter ring for low pressure points and higher than in the igniter ring for higher pressure points.
- The metallic case reaching the highest value in the geometric transition zone, from cylindrical to throat, and the uncoated and ceramic case being quite similar in value there.

- If all three test cases were be evaluated, the highest peak value in the throat was mostly found in the ceramic case, followed by the metallic and then the uncoated case. As mentioned earlier the peak in the uncoated case is probably under-estimated, for lower pressure points of about 28% and for the highest of approximately 11%. Nevertheless, the last optimization point, reversed this trend, by the lowest values in the ceramic case, succeeded by the metallic and then the uncoated case. At the last point the values drop with higher ROF.
- A drop in the middle of CC1 for the coated cases happens for higher load points than 5 bar, before that they exhibit rather constant HF distribution in the cylindrical part. For higher pressure points there could be detected a minimum in the middle of CC1 for the coated cases. This drop was lower for the ceramic than for the metallic configuration. This demonstrates the cooling effect of the ceramic case being quantitatively better than the metallic one. The local minimum in CC1 in the coated test cases originates from the insulation effect of the TBC, as from both side, one time from the igniter ring and one time from CC3 axial heat conduction occurs, but due to a lack of circumferential heat flux, because of the coating, a minimum occurs.
- In general, rising quantitative values of the HF with higher pressure load points but also with higher ROF could be detected.
- An influence of the experimental duration can be more clearly observed in lower pressure points.
- The HF value is lower at the last optimization point with rising ROF for all pressure points.
- At the end of part CC1, for the same testing period, the HF nearly correspond, which is due to cross heat conduction of the second segment, equalizing the temperature difference that developed because of the coating.
- With higher pressure points, the HF distribution in the ceramic and uncoated cases align in the cylindrical part of CC3, while the metallic case exhibits higher values. Both coated options show a constant HF distribution in the cylindrical part of CC3. The metallic configuration exhibits the largest HF value in the transition zone from the cylindrical to convergent geometry. The uncoated and ceramic case are nearly equal. This is most likely caused by sensor errors due to insufficient contact with the substrate in different parts along the chamber, which also differ per case. This error leads the algorithm to find solutions in the second segment, that are not nearly identical, which would have been expected as the same nozzle segment was used each time.
- Repeatability is not as evident for the 5 bar tests with low ROF as for higher pressure points. In general a rather good compliance throughout the CC length can be observed, which for one underlines the repeatability of the tests and shows that 3 s were enough to reach quasi steady-state conditions for the heat flux distribution in the engine.

7.3.6. Relative Heat Flux Comparison

In this section the different pressure and mixture ratio load points of the configurations are related to each other in order to quantify the reduction in the HF distribution. As far as possible, the same testing durations were evaluated. Solely the three optimization points i in CC1 were compared, and calculated with the Equation (7.1) for the comparison of coated (coa.) vs uncoated (unc.) and Equation (7.2) for the contrast between the coated versions. A positive value equals a reduction. For Equation (7.2) the

metallic configuration is taken as a reference, as in most cases it resulted in a higher heat flux distribution. The chosen tests are listed below. As there are no comparable results for the 15 *bar* tests, they were not included. The point in time of evaluation is the last time point, as in the sections above.

$$\Delta\dot{q}_{rel,i} = \frac{\dot{q}_{unc,i} - \dot{q}_{coa,i}}{\dot{q}_{unc,i}} \quad (7.1)$$

$$\Delta\dot{q}_{coa,i} = \frac{\dot{q}_{met,i} - \dot{q}_{cer,i}}{\dot{q}_{met,i}} \quad (7.2)$$

Table 7.10 presents an overview of the quantitative effect of installing a coating versus no coating and the influence of choosing a ceramic or a metallic coating for a 5 *bar* test. A general tendency for the 5 *bar* test case over all ROF is that for the first optimization point, the ceramic coating is reducing nearly double as much the heat flux compared to the metallic coating. The best cooling effect is thus to be found in the beginning of the CC1 geometry for all coatings. This discrepancy sinks a lot for the middle point, even reversing for ROF 3.1 and 2.7, resulting in a bigger heat flux reduction for the metallic coating compared to the ceramic one. For ROF 3.1 and 2.7 at the last point at CC1, the ceramic coating is still slightly reducing the heat flux, while not performing better for the highest ROF. The metallic coating under-achieves in all of the cases for the end geometry point, albeit only marginally. For the highest ROF and 5 *bar*, the ceramic coating is always the better choice.

Table 7.10.: Relative heat flux comparison of the 5 *bar* tests in percent

		CC1 start point	CC1 middle point	CC1 end point	Average
ROF 2.7	unc - cer	27.80%	22.26%	3.51%	17.85%
	unc - met	14.03%	24.12%	-9.50%	9.55%
	met - cer	16.02%	-2.45%	11.89%	8.48%
ROF 3.1	unc - cer	22.09%	15.61%	2.15%	13.28%
	unc - met	10.12%	24.20%	-5.45%	9.61%
	met - cer	13.31%	-11.33%	7.22%	3.06%
ROF 3.5	unc - cer	23.38%	17.55%	-1.28%	13.21%
	unc - met	13.64%	14.17%	-7.04%	6.92%
	met - cer	11.28%	3.92%	5.38%	6.86%

Table 7.11.: Relative heat flux comparison of the 10 *bar* tests in percent

		CC1 start point	CC1 middle point	CC1 end point	Average
ROF 2.7	unc - cer	28.10%	29.83%	-1.63%	18.76%
	unc - met	21.61%	22.47%	-11.91%	10.72%
	met - cer	8.28%	9.49%	9.18%	8.98%
ROF 3.1	unc - cer	22.39%	26.18%	-4.85%	14.57%
	unc - met	20.10%	22.25%	-8.59%	11.25%
	met - cer	2.85%	5.05%	3.44%	3.78%
ROF 3.5	unc - cer	22.82%	26.87%	-3.11%	15.52%
	unc - met	14.87%	12.77%	-15.47%	4.05%
	met - cer	9.34%	16.15%	10.69%	12.06%

Table 7.11 presents an overview of the quantitative effect of installing a coating versus no coating and the influence of choosing a ceramic or a metallic coating for a 10 *bar* test. A general tendency for the

10 *bar* test case over all ROF is that for the first and second optimization point, the ceramic coating is reducing the heat flux more compared to the metallic coating. The differences for the middle point and ROF 3.1 are not as striking as for the other cases. There is another common trend that the heat flux reduction is even better for the second point, opposed to the 5 *bar* test. The cooling effect for the first half of the segment is thus nearly constant for both coatings. For all ROF the last point at CC1 both coatings are losing their cooling function, although the effect is not as severe for the ceramic coating as for the metallic one. For all ROF and 10 *bar*, the ceramic coating is always the better choice.

Table 7.12.: Relative heat flux comparison of the 12 *bar* tests in percent

		CC1 start point	CC1 middle point	CC1 end point	Average
ROF 2.7	unc - cer	25.63%	30.11%	-2.97%	17.59%
ROF 3.1	unc - cer	30.10%	30.66%	-4.04%	18.90%
ROF 3.5	unc - cer	27.13%	29.50%	-2.56%	18.02%

Table 7.12 presents an overview of the quantitative effect of installing a ceramic coating versus no coating for a 12 *bar* test. A general tendency for the 12 *bar* test case over all ROF is that for the first and second optimization point, the ceramic coating is reducing the heat flux in reference to the uncoated version. The achieved decrease is the highest of all pressure load points and ROF test cases. There is another common trend that the heat flux reduction is even better for the second point similar to the 10 *bar* test, opposed to the 5 *bar* test. The cooling effect for the first half of the segment is thus nearly constant for the ceramic coating, with an approximate HF cutback of 28% in comparison with the uncoated version. For all ROF the last point at CC1 the coating loses its cooling function, although the effect is not major, only a few percent. The following list, gives insight in which runs were used to evaluate Table 7.10, Table 7.11 and Table 7.12.

- **5 bar test:** ROF 2.7 - run 2 / ROF 3.1 - run 4 / ROF 3.5 - run 5
- **10 bar test:** ROF 2.7 - run 7 / ROF 3.1 - run 9 / ROF 3.5 - run 11
- **12 bar test:** ROF 2.7 - run 13 / ROF 3.1 - run 15 / ROF 3.5 - run 17

7.3.7. Temporal Heat Flux Evaluation

Not only the magnitude and spatial distribution is of interest for evaluating the effect of the TBC on this capacitive chamber, but also the temporal evaluation compared between the uncoated and coated configurations and the coated configurations between each other, provides valuable insight.

As the comparison criteria was to assess all three configurations, run number 9 with a target CC pressure of 10 bar and a ROF of 3.1 was chosen, as there is data existing for all of the configurations and the testing time is the same, namely 3 s. This facilitates the comparison of the individual time steps. The heat flux evolution is fairly similar in terms of pressure cases, which is why the nominal load point of 12 bar and a ROF of 3.1 was not compared additionally.

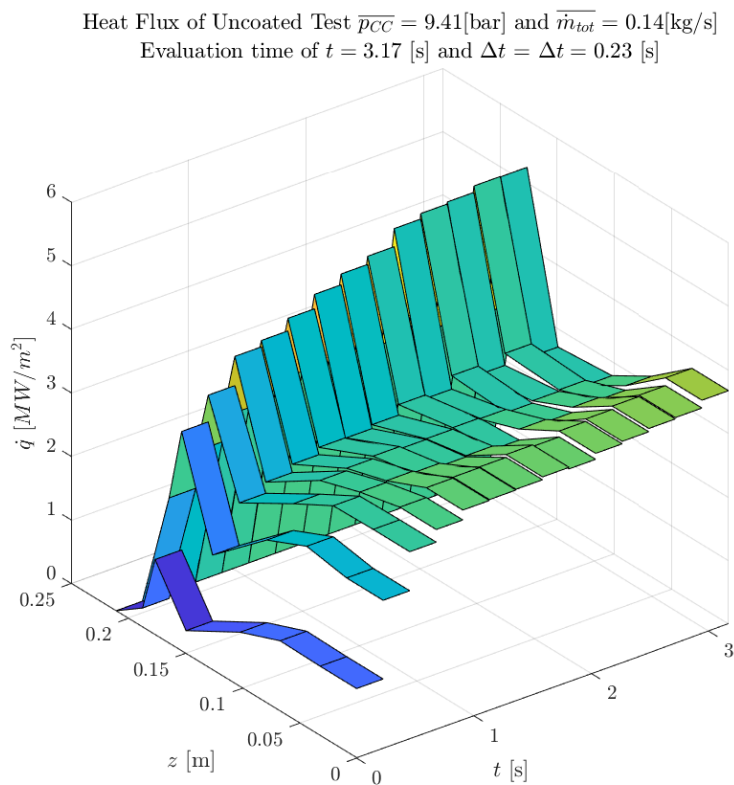


Figure 7.25.: Heat flux evolution of uncoated test at 10 bar and target ROF of 3.1

Figure 7.25 provides an insight into the temporal evolution of the HF in the uncoated case, used as a reference case. The start-up period of the engine can clearly be seen in the jump between the HF distribution of the first and second time step. This period also extends till the fourth time step for the throat value, even though the increase is not as noticeable any more. After that the peak value in the throat slowly but steadily rises till the tenth time step, followed by a rather constant HF distribution over time. In general the HF distribution in the cylindrical part of the CC exhibits an almost quasi steady-state behaviour, with minimal differences, primarily in the point of the transition zone to the convergent geometry part.

Heat Flux of Ceramic Test $\overline{p_{CC}} = 9.30[\text{bar}]$ and $\overline{\dot{m}_{tot}} = 0.13[\text{kg/s}]$
 Evaluation time of $t = 3.23 [\text{s}]$ and $\Delta t = \Delta t = 0.23 [\text{s}]$

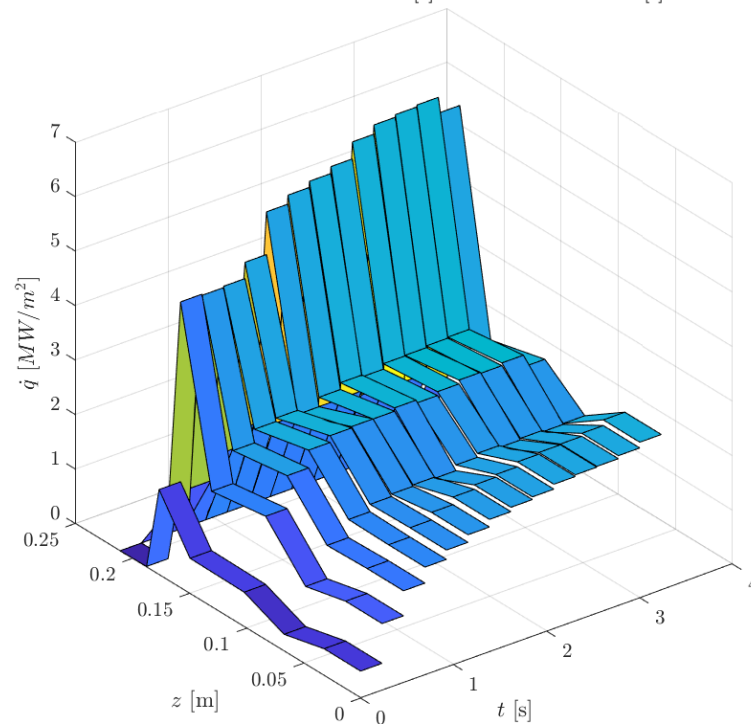


Figure 7.26.: Heat flux evolution of ceramic test at 10 bar and target ROF of 3.1

Figure 7.26 provides an insight into the temporal evolution of the HF in the ceramic coated configuration. The start-up period of the engine can clearly be seen in the jump between HF distribution of the first and second time step. This incident shows approximately the same ratio of change of the HF distribution values than in the uncoated case, which is times 3 in the throat and times 2 in the cylindrical part. The start-up period does not smoothly continue as in Figure 7.25 for the throat, however does so for the first four time increments for the cylindrical part. After this, the cylindrical part exhibits an almost quasi steady-state behaviour, not even with the minimal differences in the point of the transition zone to the convergent geometry part, as in Figure 7.25. The HF distribution rather demonstrates a plateau effect for the second till fifth throat value. After that the peak value in the throat slowly but steadily rises till the thirteenth time step, dropping for the last, as the experiment is already ended at this point in time.

Figure 7.27 provides an insight into the temporal evolution of the HF in the metallic case. In general the behaviour over time of the metallic test case is in its nature more comparable to the uncoated than the ceramic case. The start-up period of the engine can clearly be seen in the jump between the HF distribution of the first and second time step, also with similar ratios than in the ceramic case. This period also extends till the fourth time step for the throat value, even though the increase is not as noticeable any more. After that the peak value in the throat slowly but steadily rises till the tenth time step, followed by a rather constant HF distribution over time. In general the HF distribution in the cylindrical part of the CC exhibits an almost quasi steady-state behaviour beginning from the fifth time increment on. But with minimal differences, primarily in the point of the transition zone to the convergent geometry part.

Comparing Figure 7.25, Figure 7.26 and Figure 7.27 with each other they all evidence a rather quasi

Heat Flux of Metallic Test $\overline{p_{CC}} = 9.38[\text{bar}]$ and $\overline{\dot{m}_{tot}} = 0.14[\text{kg/s}]$
 Evaluation time of $t = 3.23 [\text{s}]$ and $\Delta t = \Delta t = 0.23 [\text{s}]$

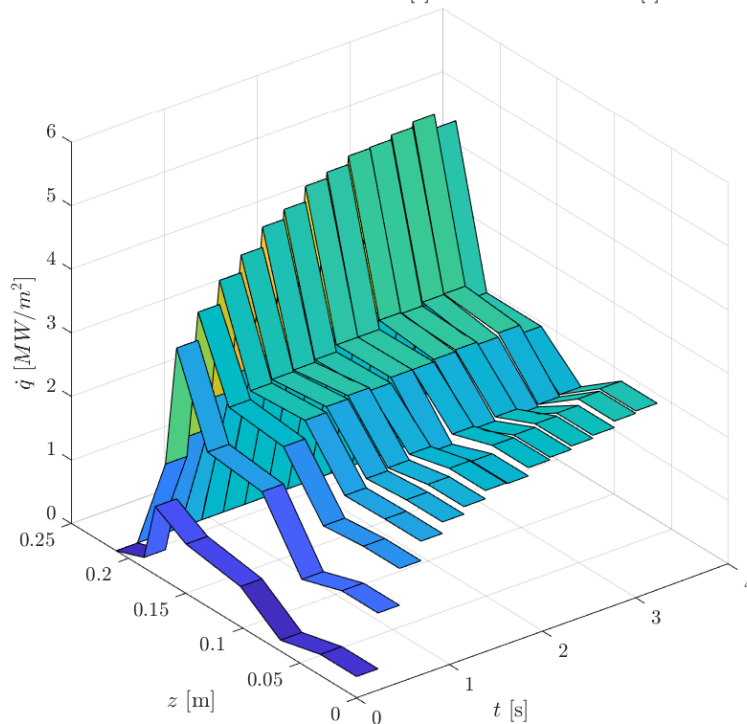


Figure 7.27.: Heat flux evolution of metallic test at 10 bar and target ROF of 3.1

steady-state HF distribution in the radially constant part of the geometry for the about two thirds of the total combustion time. The TBC do not inflict a transient behaviour in the cylindrical part, evidence is the comparably constant distribution in this part of the geometry with time. The throat values of the uncoated and metallic case are reaching an approximate quasi steady-state condition for the last second, dividing this temporal evolution in a start-up period, a transient period and a nearly-steady-state section. While for the ceramic case, after the start-up, a nearly-steady-state section is followed by a transient and again by a nearly-steady-state section.

7.4. Load Point Evaluation

When utilizing or referencing values such as thrust, specific impulse, propellant flow, and other performance parameters, it is essential to specify the conditions under which a particular value is applicable. The following parameters are important [43]:

- a) combustion chamber pressure
- b) ambient pressure or altitude or vacuum (space)
- c) nozzle expansion area ratio
- d) nozzle shape and exit angle
- e) propellants, their composition and ROF

f) initial ambient temperature of propellants prior to start

For item (b) standard sea level conditions, 1.0132 bar [43] can be taken, because of the marginal altitude of Munich. Item (c) and (d) are answered by the contraction half angle $\Theta = 30^\circ$, the expansion half angle $\alpha = 15^\circ$, the contraction ratio being $AR_{con} = 5$ and the expansion ratio being $AR_{div} = 4$. (f) equals the average ambient experiment temperature of 283 K.

In order to deliver a holistic performance assessment, values like the mass flow rates of fuel and oxidizer, the ROF (e) and the CC pressure points (a), provide contextual information. An overview of these values and the exact evaluation window is provided in chapter Section 4.4. In Table 4.6 the values are summarized for all the tests of the uncoated configuration, in Table 4.7 those of the ceramic and in Table 4.8 those of the metallic configuration.

7.4.1. ROF, Mass Flow Rate and Chamber Pressure

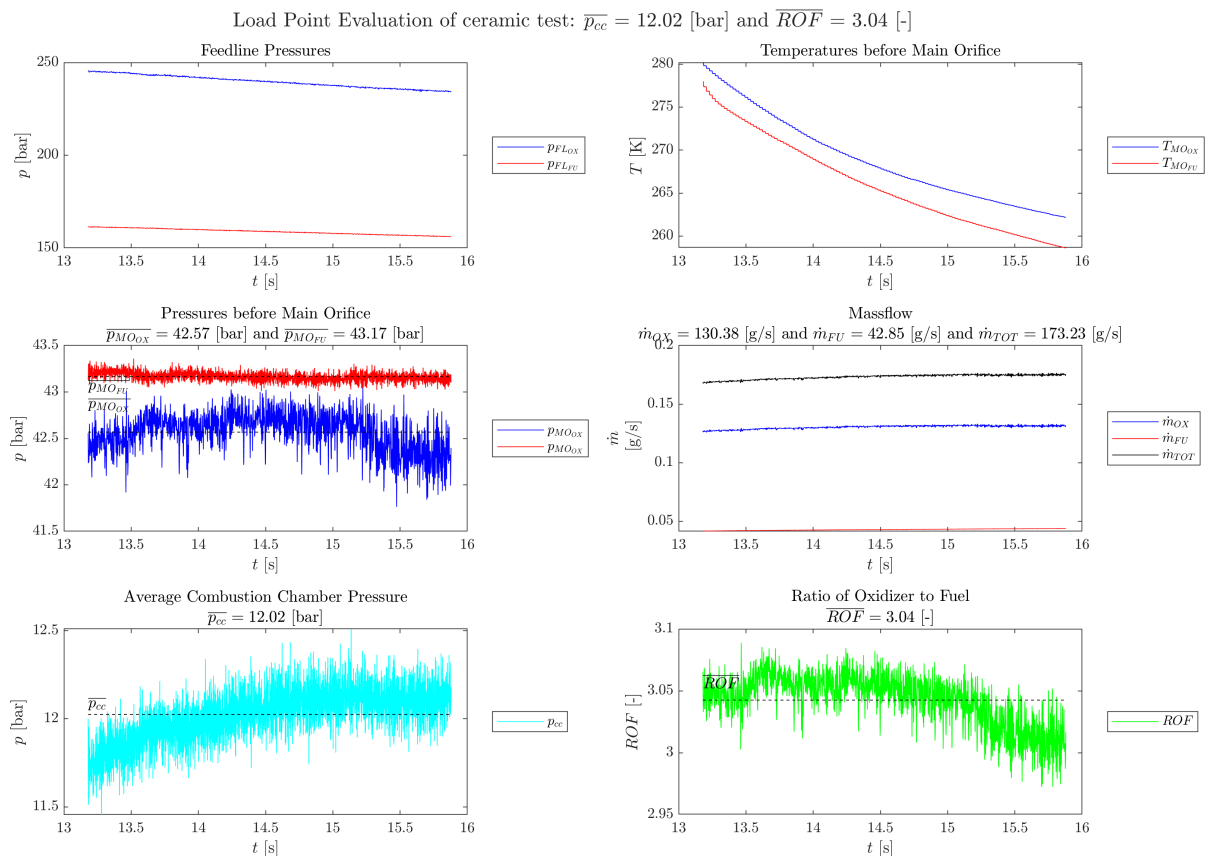


Figure 7.28.: Visualized load point evaluation of a coated (ceramic) hotfire run 15 with a target pressure of 12 bar and target ROF of 3.1

The starting time is chosen as the closing time of the fuel igniter valve and the end time as the closing time of the main oxygen injector valve. The overlap of igniter and main sequence is ignored as the influence of the igniter distorts the overall mass flow and ROF test characteristics. Due to the different sampling times, the temperature data necessary for the evaluation had to be interpolated. After that the pressure, temperature and magnetic valve data could be cropped.

Figure 7.28 gives an overview of the relevant parameters for the pre-performance evaluation of the mass flows, ROF and p_{cc} . The ceramic hotfire run 15 with a target pressure of 12 bar and target ROF of 3.1 was taken as an example, because it represents the design load point and a configuration of interest, not the uncoated reference configuration. Although it is to be noted, that the configuration does play a major role in these values. Providing such a diagram for every of the 50 hotfires would be too much. After sighting the data, most hot fires exhibit the same behaviour. Some display a bigger drop in the ROF than others.

Mass Flow Rate The same strategy as in Section 4.1 and the orifice data in Table 4.1 was used to calculate the mass flow rate. With the difference that no optimization had to be done, as the pressure point was an input this time, not the output. As a consequence, tabled fluid data for the oxidizer and fuel were used to determine the fluid density, also taking two-phase mixtures as an empirical correction factor w into account. The mass flow rate was determined by means of Equation (7.3)

$$\dot{m} = C_d \pi \frac{d_{orf}^2}{4} \rho w \quad (7.3)$$

In order to evaluate the oxygen mass flow through the main valve, the temperature sensor TC_M_O and the pressure sensor P_FL_4_O before the orifice were used as an input over time. To evaluate the fuel mass flow through the main valve, the temperature sensor TC_M_F and the pressure sensor P_FL_5_F before the orifice were used as an input over time. These values can be seen in Figure 7.28 in the first subfigure on the right for the temperatures and in the second row on the left for the pressures. There also the temperature drop, which is mentioned in Section 4.1, can be observed. The time averaged mass flows of fuel, oxidizer and the total mass flow, following Equation (7.4), were also calculated. The portions of the mass flows can be taken from Figure 7.28, subfigure four. It is clear that the mass flow is consistently stable, with no significant fluctuations.

$$\dot{m}_{tot} = \dot{m}_{ox} + \dot{m}_{fu} \quad (7.4)$$

ROF It is crucial to accurately know the chemical composition of the propellants and their relative proportion. This means above all, knowing the mixture ratio ROF. [43] Equation (7.5) was utilized for this purpose. Additionally a time averaged value was determined for every experiment. Figure 7.28 subfigure six, reports the ROF distribution over time. As it is built from the mass flow ratio, small mass flow fluctuations in both mass flows can add up and generate a higher noise, than the singular mass flow signals.

$$ROF = \frac{\dot{m}_{ox}}{\dot{m}_{fu}} \quad (7.5)$$

CC Pressure As the pressure drop in the chamber itself is negligible, an arithmetic mean of all six sensors was performed per hotfire and resulting in the reference chamber pressure distribution over time. This pressure is visualized in Figure 7.28 in blue, with the dotted line as the time averaged value.

7.4.2. Pressure Drop over Injector

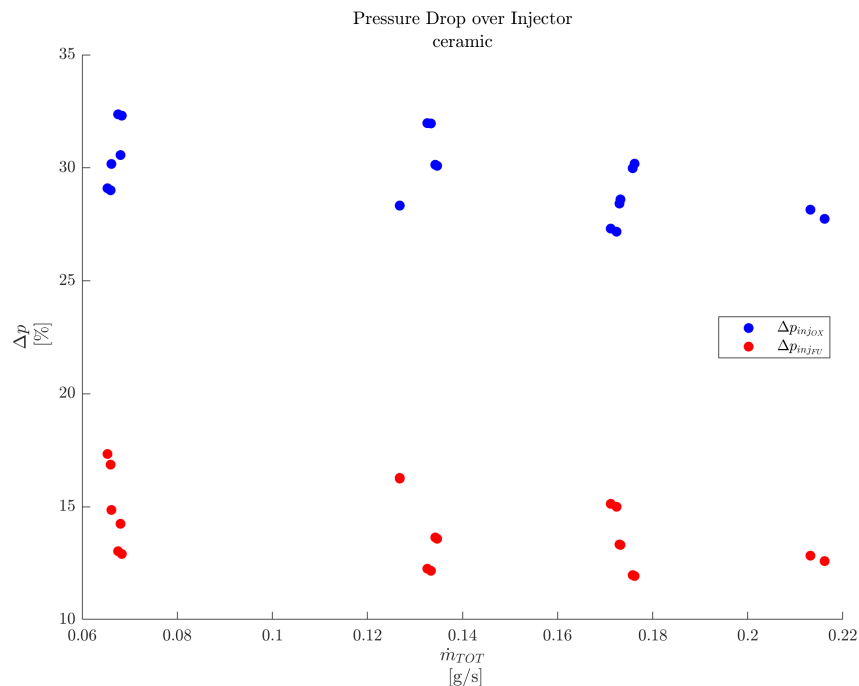


Figure 7.29.: Visualized pressure drop of the ceramic hotfires

The pressure drop across the injector is typically adjusted to fall within the range of 15% to 25% of the chamber pressure. This adjustment is made to achieve elevated injection velocities, which are crucial for enhancing atomization and droplet breakup during the combustion process. Furthermore feedback into the supply lines is avoided. [43]

Figure 7.29 depicts the pressure drops in the injector happening in the DO engine. The ceramic configuration was chosen as it contains the most data points. The blue points symbolize the injector pressure drop at the oxygen side with an average of around 29%, and the fuel in red with around 15%.

7.5. Performance Analysis

In this section, important engine parameters of the different configurations are compared and clustered in their respective testing conditions, introducing the combustion chamber pressure and the mixture ratio. The process of obtaining the results is described.

In general the performance values η_{c*} , c^* and I_{sp} had to be calculated with the integral heat load of the combustion chamber up until the throat, as the program in use CEA is limited to this input. The under-prediction of the heat flux distribution in the throat area in the uncoated configuration marginally skews the performance results.

7.5.1. Evaluation Process

The performance evaluation code was already part of the inventory of DO, and was solely adapted for the needs of this thesis. At first all the necessary experimental data is loaded. Then geometric parameters of

the main orifices and the injector are defined. After each test campaign the throat diameter was measured and serves as an input for the performance calculation, as well as the CC diameter. Followed by the integral heat flux calculation. After this, the performance parameters, c^* , Isp and η_{c^*} are evaluated for every hot fire experiment. These values are extracted of two distinct performance evaluations, being the output of this script. In the end the traits of an adiabatic swirl flow and a swirl flow with heat loss are calculated.

The tool of choice is a code incorporating the NASA tool CEA. As a general setting, the "problem" was defined as "rocket", "equilibrium" conditions were assumed and "fac", the finite area combustor was chosen. CEA can only calculate ideal processes, so it is necessary to convert the experimental values into corrected values that can be used by CEA, but still indicating the real scenario.

Input \dot{Q} This variable is used to back calculate the heat loss of an ideal versus a real combustion process. The total heat flux used for the calculation consisted of the integral heat loads over the surface till the throat, discretized and interpolated over hundred increments. The value was averaged over the last four time steps. As CEA only considers conditions spanning from the inlet to the throat, this interval was chosen, which is crucial for the program as it does a correction of the inlet conditions, incorporating heat loss, in order to evaluate the performance. [38]

Compute Inlet Conditions At first the inlet conditions for the runs are computed. With the aid of the orifice and the injector parameters, the mass flows and mixture ratios are computed for fuel and oxidizer. Followed by the respective injector velocities, the swirl number and the axial flame impact position. These corrections and values are important, as CEA assumes only axial velocity components in its calculations, which is not the case for a real swirl injector. As a consequence only the axial propagation of the angular momentum along the CC axis is relevant as an input, thus the impact of the swirl injector is given with a scalar value. In other words, the behaviour of the swirl injector, velocity components and hence static pressure, is transferred to the respective characteristics of a co-axial injector [39]. From this function, the total enthalpies of both fuel and oxidizer are used as an input for the actual performance calculation. For these quantities the state of the respective fuel in the injector manifold is used. Given that the experiments utilised a capacitive combustion chamber, the input enthalpies of the propellants needed to be altered in order to compensate the energy loss that would typically be prevented by regenerative cooling, as a closed system.

Compute Performance The fluid state in the combustor and nozzle, Mach number and sub- and supersonic area ratios, had to be corrected iteratively for the influence of the swirl injector. The static combustion chamber pressure had to be adapted to a theoretical one, as explained prior, using the real versus theoretical mass flow deviation as an objective function. After determining η_{c^*} with Equation (7.7), the "real" fluid properties (corrected for CEA program restrictions) but still "ideal" ones (because of the nature of CEA), were identified and fed back into a CEA rocket problem formulation. Followed by the evaluation of the vacuum Isp and c^* .

7.5.2. Integral Heat Load Evaluation

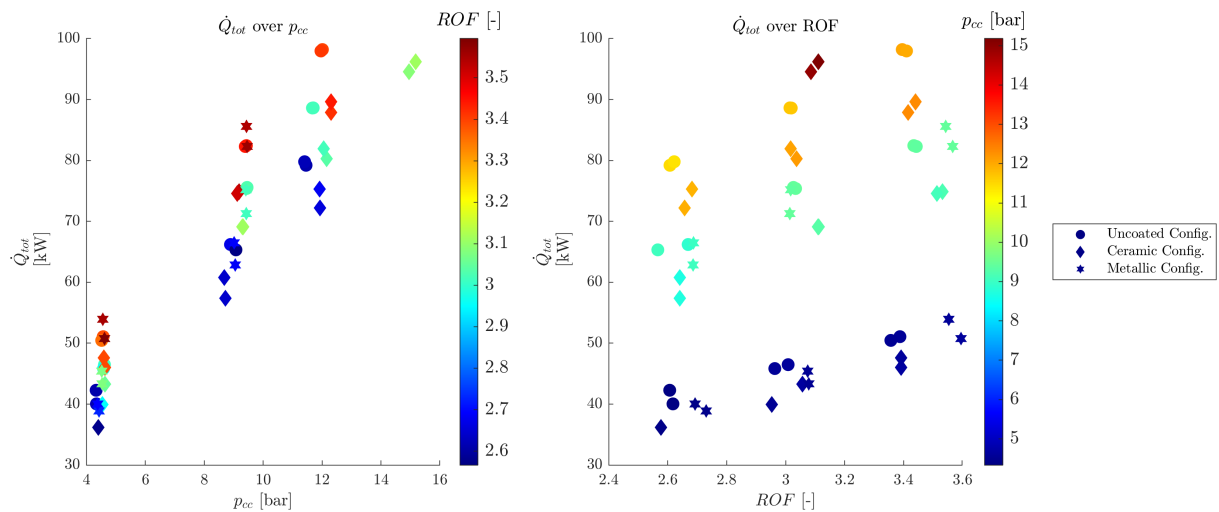


Figure 7.30.: \dot{Q}_{CC} over the whole combustion chamber length for p_{cc} and ROF for all tests and all configurations

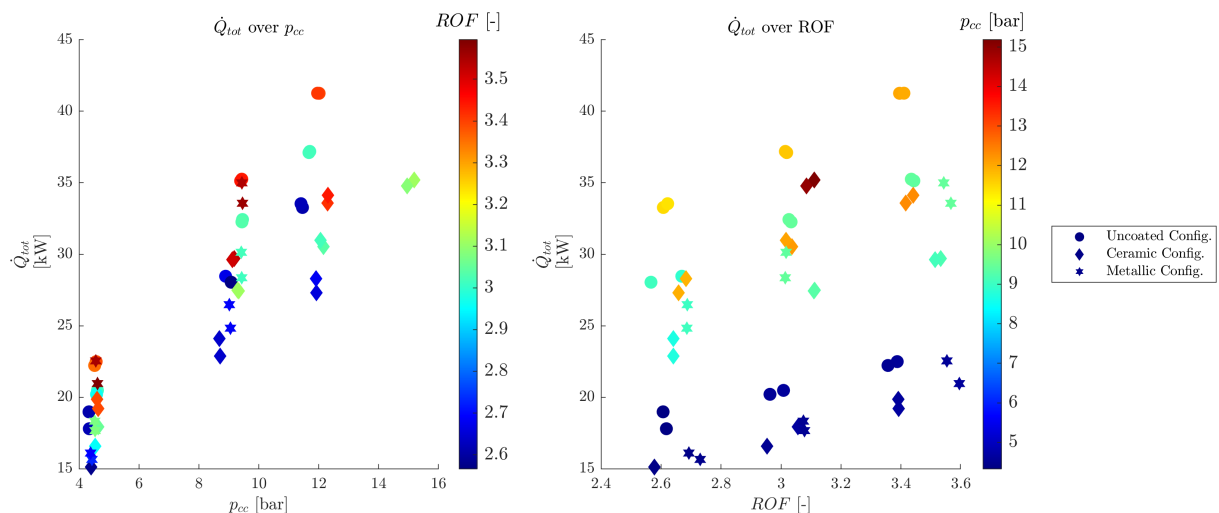


Figure 7.31.: \dot{Q}_{CC1} over the first segment CC1 for p_{cc} and ROF for all tests and all configurations

The integral heat load represents a strong indicator on the amount of coolant that would be required, transferring the capacitive cooling concept to a regenerative one. Two different parts of the CC were examined. A holistic picture is provided in Figure 7.30 as the whole CC length was evaluated, while Figure 7.31 is focused on the influence of the TBC on the integral heat reduction. Figure 7.31 can be referenced as the more meaningful data representation as the under-prediction of the heat flux distribution in the throat area in the uncoated configuration does not skew the performance results.

The integral heat load in Figure 7.30 was calculated for the last four time steps over the whole CC, where the heat flux distribution can be considered nearly steady-state. It was time averaged to provide a more representative value for the respective experiments. The heat flux values were integrated over the whole CC length, including the igniter ring and the whole nozzle. The same procedure was done with Figure 7.31 except for only evaluating CC1.

The data shows that around 90% of the total heat flux is released up until the nozzle throat, while the divergent nozzle part only receives the residual 10%, which is why this part is also included into the evaluation here. This is owed to the nozzle being short and due to the expansion, the temperature is dropping significantly.

For all configurations the integral heat flux increases as expected nearly linearly with rising combustion chamber pressure, as predicted by $\dot{Q} \propto p_{cc}^{0.8}$ [43], in the left figure of Figure 7.30 and Figure 7.31. An increasing tendency in this quantity can be observed with rising ROF, ergo a more oxygen-rich combustion.

Ceramic Configuration: Following this conceptual trend, it can be stated that the ceramic configuration exhibits the lowest total heat flux, per similar ROF and p_{cc} compared to the uncoated and metallic version. Especially for higher pressures (10 – 12 bar) the reduction for similar ROF is striking with a value of about 10 kW less for \dot{Q}_{CC} and 8 kW less for \dot{Q}_{CC1} for $ROF = 3.1$. Referencing the nominal engine design load point of $p_{cc} = 12$ bar and $ROF = 3.1$, a considerable reduction of about 10% difference in integral heat load over the whole CC to the uncoated configuration. For the same load point a reduction of circa 17% is achieved along the span of the CC1 segment. It is interesting to note that \dot{Q}_{CC1} of the 15 bar case lies even beneath the 12 bar load point for the uncoated case, visible in the right figure of Figure 7.31. Figure 7.31 underlines the statement, that the passive cooling effect of the ceramic coating is not negligible, especially when it comes to higher CC pressures.

Metallic Configuration: The metallic case shows a larger variance for the data at the same pressure load point than the uncoated case. In the metallic configuration compared from a standpoint including the whole CC in Figure 7.30, higher ROF result in higher total heat fluxes for the same pressure, than for the uncoated version and vice versa, resulting in the highest, ergo the worst solution for higher ROF. This does not hold true for the examination of only the first chamber segment CC1, where the metallic configuration is always the second best heat reduction method after the ceramic coating. For lower ROF for the whole engine, the metallic version is better than the uncoated one, but worse than the ceramic one. For the highest load point achieved, and the nominal ROF of 3.1, a reduction of about 9% for CC1 can be observed. A passive cooling effect is strongly dependent on its use case for the metallic configuration in terms of overall performance. Only considering the coated part itself, it represents an appropriate heat intake reduction measure.

7.5.3. Characteristic Velocity

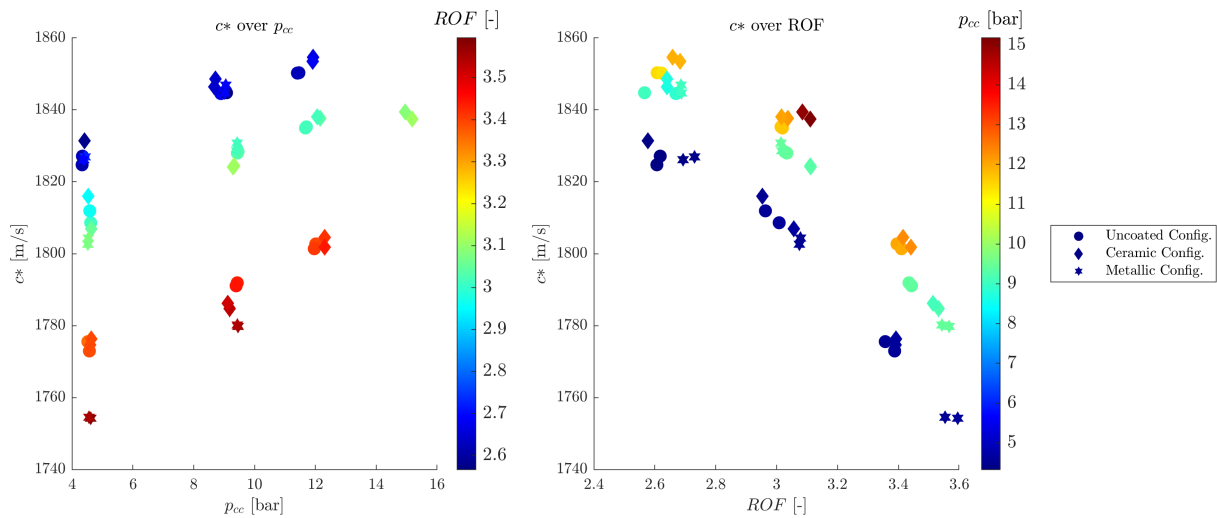


Figure 7.32.: c^* over p_{cc} and c^* over ROF for all tests and all configurations

This velocity, not a physical velocity though, is solely dependent on the characteristics of the propellant and combustion chamber, and ignores nozzle specifics. It can therefore be used as a benchmark for evaluating different propellant combinations in terms of combustion chamber efficiency. [43] In this case, the influence of a different cooling technique on the same chamber. In CEA Equation (7.6) is using the corrected combustion chamber pressure.

$$c^*_{exp} = \frac{p_{cc,exp} A_{th}}{\dot{m}} \quad (7.6)$$

As can be deduced from Figure 7.32, lower ROF for the same pressure are advantageous, creating a higher characteristic velocity, even though the lower and higher ROF around the nominal one are distributed equally with $\Delta ROF = 0.4$, the deviation in c^* is not equidistant. As can be seen from the left subfigure, c^* is slightly increasing with pressure, but decreasing with ROF, visualized in the right subfigure. For the examined pressures and increasing ROF, the metallic version is steadily deteriorating in value, except for 5 bar where the c^* are comparable with the uncoated case. The ceramic coating exhibits nearly continuously better characteristic velocity values referenced to the uncoated ones. This holds true for the nominal load point as well. Concluding an equal or even better performance in the use of a ceramic coating.

7.5.4. Combustion Efficiency

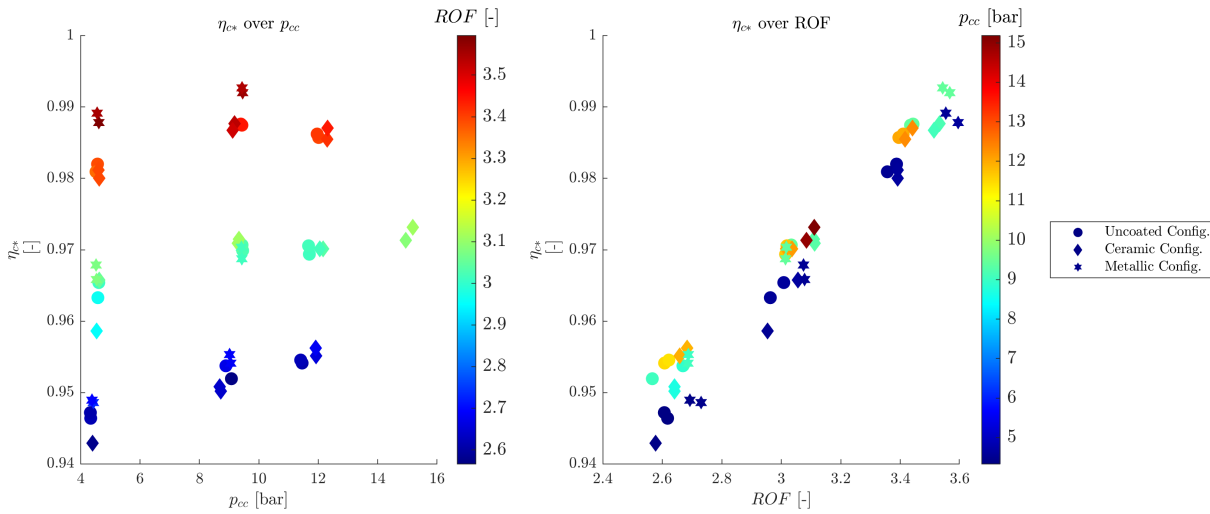


Figure 7.33.: η_{c^*} over p_{cc} and η_{c^*} over ROF for all tests and all configurations

Combustion efficiency, referred to as η_{c^*} in chemical rocketry, quantifies the ratio of actual energy released to the theoretical heat of reaction per unit of propellant mass. It serves as a measure of the effectiveness of the system in exploiting its energy source. In well-designed rocket propulsion systems, empirical data typically show energy release efficiencies in the range of 94 – 99%. Such high efficiencies imply quite thorough combustion, with some residual propellant left unreacted, because of not combusting at the stoichiometric condition. Then chemical equilibrium is closely attained. [43] This is the case for this engine, as can be taken from Figure 7.33.

η_{c^*} is calculated using Equation (7.7) and was employed as the metric for performance evaluation, quantifying the degree of completion of chemical energy release. Equation (7.7) was found using Equation (7.6), as the geometry and mass flow are equivalent in the theoretical and experimental case. The loss in performance is derived from a lower than ideal pressure that could be reached during the experiments. In this context, the theoretical combustion chamber pressure $p_{cc,theo}$ is derived from ideal chemical equilibrium reactions, determined through the NASA CEA program [38] and [39]. This theoretical pressure is correlated with the experimentally observed combustion chamber pressure $p_{cc,exp}$ attained during the hot fires.

$$\eta_{c^*} = \frac{c^*_{exp}}{c^*_{theo}} = \frac{p_{cc,exp}}{p_{cc,theo}} \quad (7.7)$$

In Figure 7.33, there is no remarkable dependency of the combustion efficiency visible concerning p_{cc} . From the left subfigure it is observable that the metallic configuration exhibits a marginally better efficiency, especially for low p_{cc} with a maximum of 1%. In contrast to that, a correlation of a rising ROF and an increasing η_{c^*} can be taken from the right subfigure. In general there is no large difference to be found between the ceramic and the uncoated configuration. This is most likely due to the under-prediction of the integral heat flux over the CC, which influences the calculation of η_{c^*} . Figure 7.33 emphasizes that the use of a coating is not detrimental for the combustion efficiency of the engine, yet even encouraged.

7.5.5. Specific Impulse

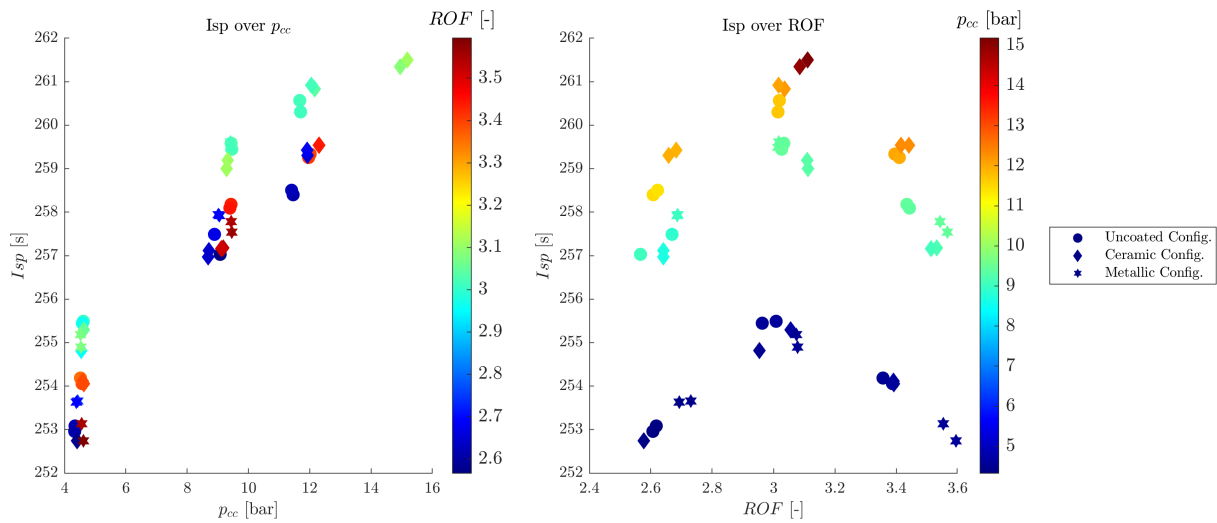


Figure 7.34.: Vacuum I_{sp} over p_{cc} and I_{sp} over ROF for all tests and all configurations

The specific impulse is a value that is influenced by the nozzle geometry and represents the thrust per unit propellant weighted flow rate. As altitude increases, atmospheric pressure decreases, increasing both thrust and specific impulse for the vehicle. [43] For this reason it is important to note, that the I_{sp} introduced here is the I_{sp} achieved in vacuum conditions.

In order to calculate the I_{sp} , the supersonic area ratio, ergo the exit area ration of 4.04 was derived from the geometry and used as an input in the performance calculation code. This value is derived using Equation (7.8), with F being the thrust and g_0 representing the standard gravitational acceleration of earth.

$$I_{sp} = \frac{F}{\dot{m}g_0} \quad (7.8)$$

A clear tendency of increase over p_{cc} can be observed for all configurations, evidence in Figure 7.34, although this increase only spans a few seconds over the examined pressure range. A peak in I_{sp} can be noted in the right subfigure for the nominal ROF of 3.1 for every pressure case. For the 5 bar load point and the nominal ROF the uncoated configuration performs the best, with the ceramic and metallic being nearly equal. For the 10 bar load point and the nominal ROF, the uncoated and metallic version lead. For the 12 bar load point and the nominal ROF, the ceramic coating exhibits a marginally better performance than the uncoated version. Also in this analysis it becomes apparent that the ceramic version is a favourable option in comparison to the uncoated engine.

7.6. Inverse Heat Conduction Method Error Analysis

To effectively assess experimental data it is essential to understand the various sources of error, their respective magnitudes and influence on the results. These errors typically stem from both statistical and systematic inaccuracies in the measured data, as well as uncertainties inherent in the modelling process. [32]

Typically, the uncertainty associated with heat flux measurements is influenced by the measuring chain associated with each variable. This chain typically includes the sensor, wiring, measuring transducers, and data acquisition device. Among these components, the sensor tends to have the highest measurement inaccuracy, consequently the thermocouples were the focus of this analysis. The manufacturer's guaranteed accuracy is often used as a reference (Section 7.6.1). Mounting techniques like spring loaded ferrules to keep the TC in place and maximize their contact condition with the to be measured material. [21]

In the context of the CGM code, measurements are primarily limited to thermocouple readings, who implement their own set of errors. Regarding the modeling aspect, the CGM code employs the heat conduction equation alongside appropriate boundary conditions (Section 6.4.3), which were not extensively evaluated. The material parameter model is another potential error source. The following aspects, definitions and formulas corresponding to [32], have been included into the error analysis:

- Thermocouple accuracy
- Thermocouple precision
- Thermocouple positioning
- Material properties
- Inverse method error

All the errors are relative heat flux errors evaluated at the respective six optimization points utilized by the CGM. In cases where it was necessary to differentiate between the hotfire configurations, it is indicated. To norm the error, the reference heat fluxes of the cases were taken.

7.6.1. Thermocouple Accuracy

The term measurement "accuracy" describes the deviation of the measured quantities from the "true value". To assess the accuracy of thermocouples, one can rely on the manufacturer's instrument accuracy, denoted as ΔT_{acc} . Solving the transient IHTP, the heat flux is not determined by absolute temperature values but by the temperature deviation within a certain evaluation time window. Consequently, the total temperature accuracy error attributable to this evaluation method is resulting in a magnitude of $2\Delta T_{acc}$. [32]

In agreement with the concept of linearity the heat flux error ΔP_{acc} can be calculated with the algebraic system in Equation (7.9). Since the SM is constant and ΔT_{acc} can be assumed to be a constant maximum offset of $\Delta T_{acc} = 1\text{ K}$ from the TC manufacturer [28], the error is time independent.

$$\Delta P_{acc} = 2J^{-1}\Delta T_{acc} \quad (7.9)$$

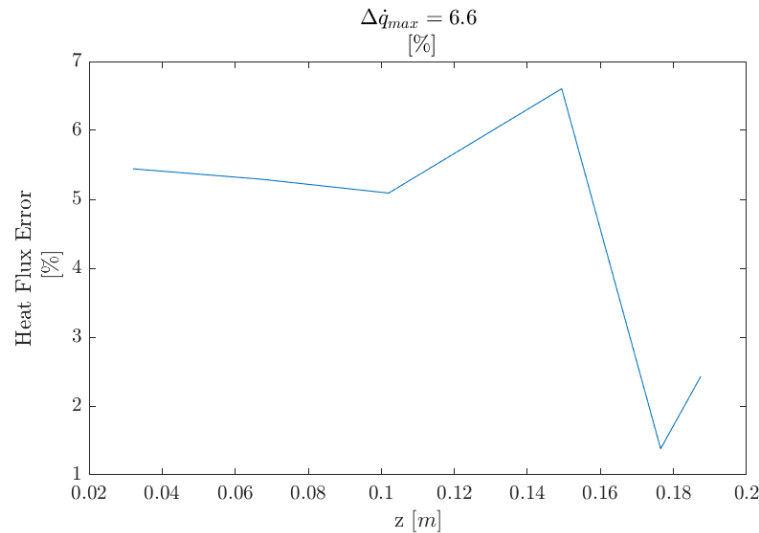


Figure 7.35.: Relative heat flux error due to a 1 K TC accuracy error

The result can be seen in Figure 7.35, where the highest influence of a measurement error of such sort is in the transitional zone from cylindrical to convergent, with 6.6 %. The smallest error is found in the throat. Since temperatures and heat fluxes are generally highest at this point, a 1 K deviation will not be a major contributor to the change in heat flux. A positive error correlates with a heat flux over-prediction.

7.6.2. Thermocouple Precision

For transient temperature measurements, the precision error refers to the random variation in thermocouple readings. Raw TC data often contains high frequency noise, so the transient profiles must be smoothed before the inverse method is applied. The precision error is quantified as the difference between the smoothed signal and the raw data, with the corresponding heat flux error defined accordingly in Equation (7.10). [32]

$$\Delta P_{prec} = J^{-1} \Delta T_{prec} = 0 \quad (7.10)$$

Referencing to Figure 6.2, the need for smoothing the data was not given and no significant effect was attributed to this phenomena, but is listed for the sake of completeness.

7.6.3. Thermocouple Positioning

A significant source of uncertainty in thermocouple measurements is the lack of precise knowledge of their exact locations. To address this error source a post-processing step in which a systematic spatial deviation Δr was assigned to all thermocouples. This deviation was added to the initial thermocouple positions r_0 , resulting in new set of TC positions. Since no extensive measurements of the depth of the drilling hole were conducted, like in [30], an offset of $\Delta r = 0.5 \text{ mm}$ following [32] was selected. The approach proposed in [30] by repeating the inverse calculation with an updated SM was not considered due to the almost identical result, to this method.

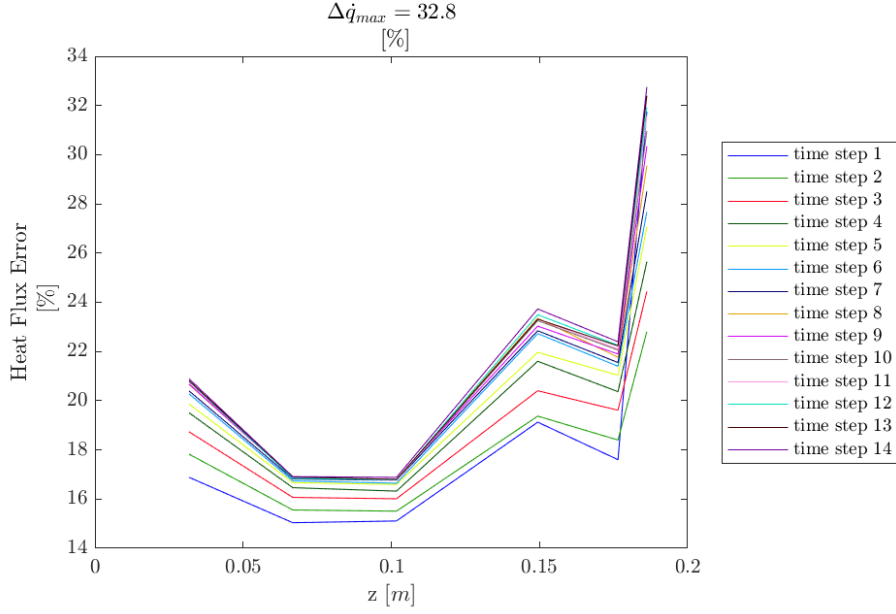


Figure 7.36.: Relative heat flux error due to a $\Delta r = 0.5\text{mm}$ TC positioning error for the uncoated case over time

For all three hotfire configurations, the respective converged solution of run 10 with ROF 3.1 and 10 bar was used. The temperature distribution within the domain was interpolated for the old and new sensor locations and were then used to estimate the temperature error. This happened for each sensor location at each point in time (i), using Equation (7.11). After iteratively using Equation (7.12), a heat flux error per optimization point per time increment resulted.

$$\Delta T_{pos,i} = T_{calc,i}(r_0) - T_{calc,i}(r_0 + \Delta r) \quad (7.11)$$

$$\Delta P_{pos,i} = J^{-1} \Delta T_{pos,i} \quad (7.12)$$

In Figure 7.36, Figure 7.37 and Figure 7.38, there is an apparent trend of a significant increase happening at the end of the domain, where there are only two sensors located directly at the optimization point, making it vulnerable position for the influence of errors. Except the first time step in Figure 7.37, the global picture of the error distribution for the coated cases are very similar. In Figure 7.36 a peak occurs in the cylindrical to convergent transitioning zone. A positive error correlates with a heat flux under-prediction.

In general it is observed that the error grows in magnitude with time, which is a consequence of the rising heat flux, especially over the first five time steps, for the uncoated case and the first four for the coated cases. This explains why at later points in time, when the heat flux is rather constant over a period in the hot fire, the errors are nearly equal. The proportional error for the positioning uncertainty is significant in comparison to the other error sources.

Figure 7.37 exhibits a nearly constant behaviour for the cylindrical part. The reason for the negative value is that for this specific time step the numerical solution found a negative heat flux value. This unphysical behaviour sometimes happens in the numerical solution for the first time step as the temperature differences

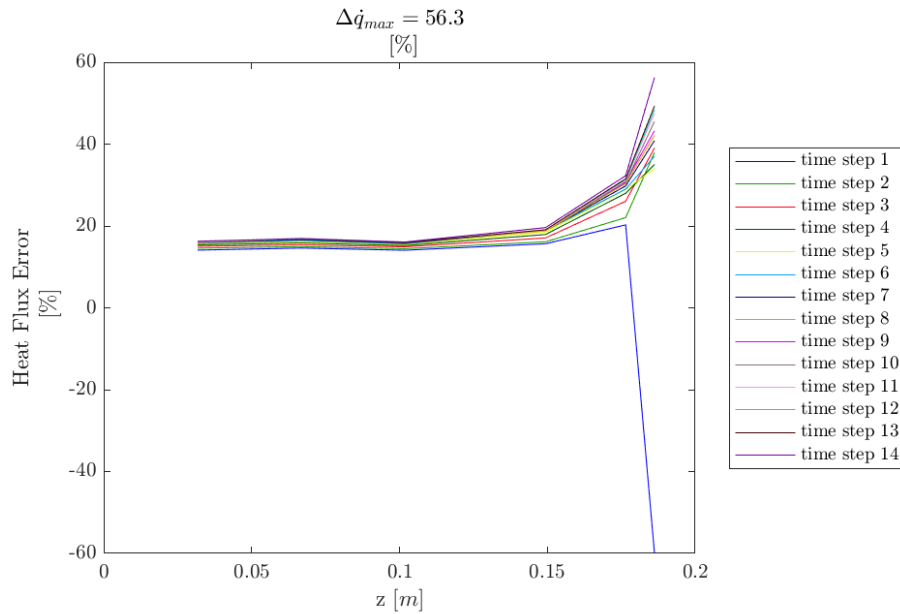


Figure 7.37.: Relative heat flux error due to a $\Delta r = 0.5\text{mm}$ TC positioning error for the ceramic case over time

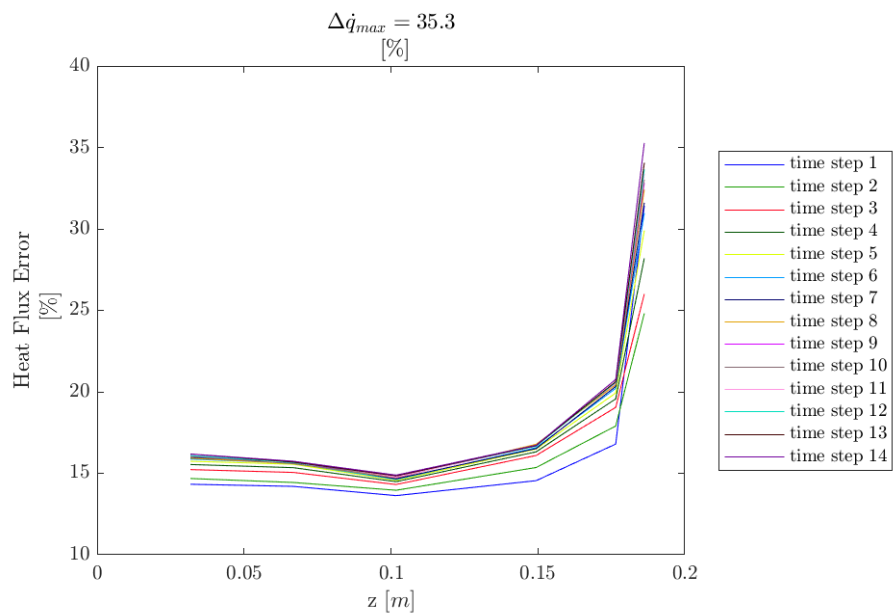


Figure 7.38.: Relative heat flux error due to a $\Delta r = 0.5\text{mm}$ TC positioning error for the metallic case over time

are very small, due to a marginal heat flux at the start up of the engine. The boundary end condition is set to a heat flux value of zero at the end-point of the domain. As a result the algorithm finds sectional negative heat fluxes to be able to in total end with a heat flux value of zero. The negative sign is owing to the negative heat flux, with a positive temperature difference in Equation (7.11). The maximum relative heat flux error for the ceramic case is in relation to the other cases is large as well.

Figure 7.38 displays a similar behaviour to Figure 7.37 albeit with lower error magnitude. Nevertheless the maximum relative error is still higher at the last optimization point as for the uncoated one.

7.6.4. Material Properties

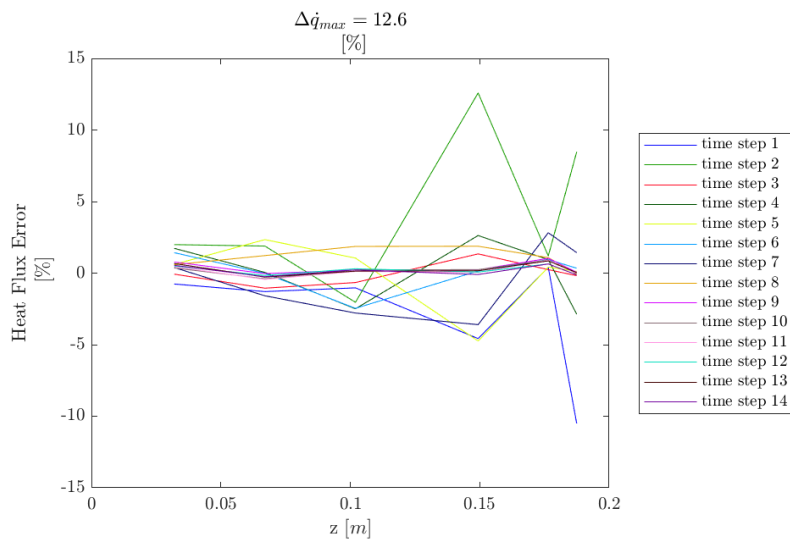


Figure 7.39.: Relative heat flux error due to a material uncertainties of $\Delta\alpha = 10\%$ for the uncoated case over time

This part of the analysis aims to observe effects of uncertainty of material parameters on the solution of the IHCM. The material properties used to solve the direct problem are taken from the data sheet of the CC material [6]. However, there may be uncertainty in the choice of thermal conductivity, density and heat capacity due to the manufacturing process. It is important to quantify the effect of this uncertainty on the converged heat flux values. [32]

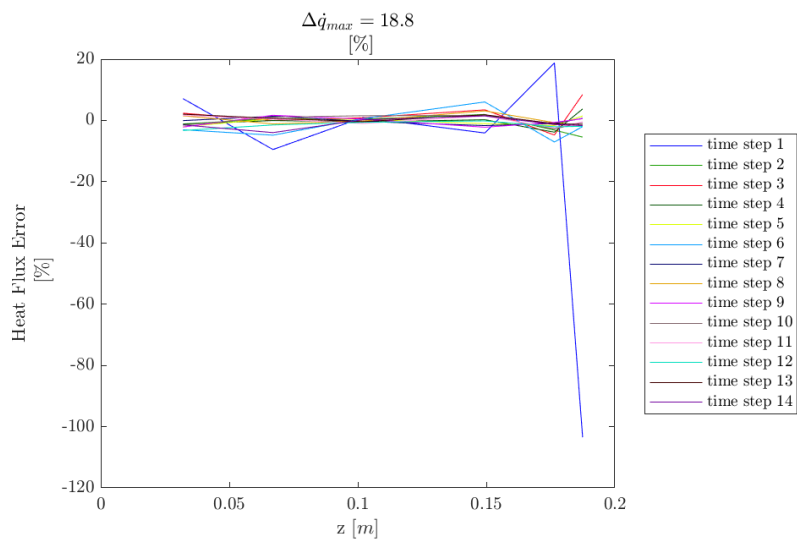


Figure 7.40.: Relative heat flux error due to a material uncertainties of $\Delta\alpha = 10\%$ for the ceramic case over time

The following is the procedure for calculating the material induced error. Similar as in the prior section, run 10 with ROF 3.1 and 10 *bar* of all three hot fire configurations was used. As this thesis deals with a transient IHTP, not only the thermal conductivity of the material, like in [30], had to be altered but the thermal diffusivity of the material model, see Equation (7.13). λ being the thermal conductivity, ρ

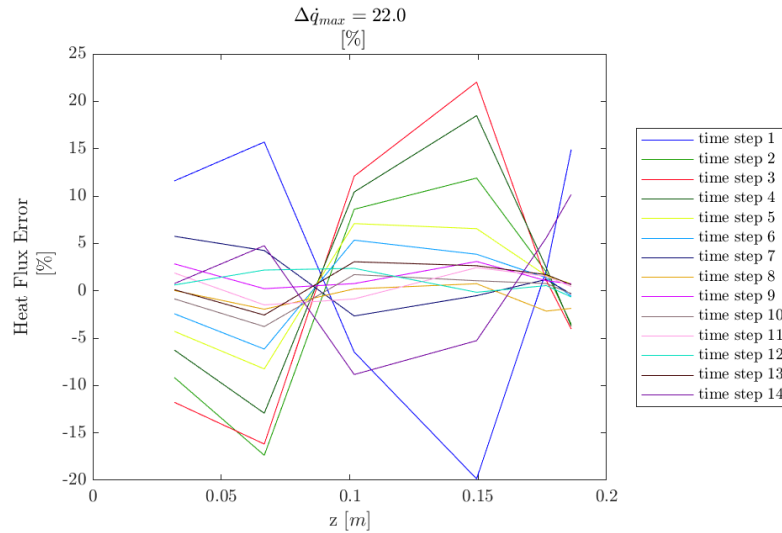


Figure 7.41.: Relative heat flux error due to a material uncertainties of $\Delta\alpha = 10\%$ for the metallic case over time

the density and c_p the specific heat capacity. A difference of 10% was used resulting in the factors in Equation (7.13), similar to [32]. The IHCM was performed with the new material model and for every time step, the temperature deviation was identified see Equation (7.14). In the next step, the HF error was determined by means of Equation (7.15) for every time step and every configuration.

$$\alpha_0 + \Delta\alpha = \frac{1.331\lambda}{1.1\rho \cdot 1.1c_p} \quad (7.13)$$

$$\Delta T_{mat,i} = T_{calc,i}(\alpha_0 + \Delta\alpha) - T_{calc,i}(\alpha_0) \quad (7.14)$$

$$\Delta P_{mat,i} = J^{-1}\Delta T_{mat,i} \quad (7.15)$$

Interpreting the unsteady heat conduction equation for constant properties Equation (7.16) from [34], the thermal diffusivity can be deciphered as the ratio of the time derivative of temperature to its curvature, the second derivative of the temperature. Quantifying the rate at which induced temperature differences are reduced. [34]

$$\frac{\delta T}{\delta t} = \alpha \nabla^2 T \quad (7.16)$$

A positive error correlates with a heat flux over-prediction. Figure 7.39 exhibits the biggest differences in the early time steps, in the unsteady start-up process, while positive deviations are an over-prediction of the heat flux, a negative ones an under-prediction. All in all the deviations are in a range of a few percentage. A similar behaviour for the first time step as in Figure 7.37 can be observed in Figure 7.40. The same explanation can be applied. The errors in Figure 7.41 vary more for the first time steps compared with the last, where they are all to be found in the vicinity of zero. Interestingly most of them cross at the same point in the coated par of CC1.

7.6.5. Inverse Method Error

The method itself contributes with two major error sources, the error related to the temporal discretization and the error of the spatial discretization.

Spatial IHCM Error Analogous to the process in Section 6.6.1, the relative error of the discretization, ΔP_{dz} alongside six optimization points in relation to a given Sinyarev-based heat flux distribution was resolved. As the resolution can be compared continuously the curve progression appears distinct from the previous errors. A positive error correlates with a heat flux over-prediction and gets interpolated for the total error.

Temporal IHCM Error Analogous to the process in Section 6.6.2, the relative error of a discretization of 14 time steps versus one of 20 steps, comparing the respective last time steps were taken. This was done for every hot fire, resulting in ΔP_{dt} . A positive error correlates with a heat flux under-prediction.

7.6.6. Total Error

Before summing up all the errors, using Equation (7.17) from [30], the material properties uncertainty and the positioning error got averaged in time reducing the dimension, as the other errors were only available as an arithmetic mean. ΔP_{tot} is available for every hot fire case.

$$\Delta P_{tot} = \sqrt{\Delta P_{acc}^2 + \Delta P_{pos}^2 + \Delta P_{mat}^2 + \Delta P_{dz}^2 + \Delta P_{dt}^2} \quad (7.17)$$

Due to different error definitions a positive error is defined as an over-prediction from now on in order to compare the contributions of each error, which means that the values of ΔP_{pos} and ΔP_{dt} are obverted. Such a step does not have to be done for the total error, as the heat flux values are squared. The results are presented on the following pages.

Relative Heat Flux Error of Uncoated Case The total error for the uncoated case varies between about 18% and 32%, being the most at the cylindrical to convergent transitional zone, depicted in Figure 7.42. Figure 7.43 exhibits the marginal influence of the time discretization error and the influence of material parameter uncertainties. The accuracy error is rather constant with a contribution of about 5% over-predicting. A major under-prediction is happening in the cylindrical to convergent transitional zone and the throat area for the spatial discretization error, while the positioning error due to its definition is always under-predicting.

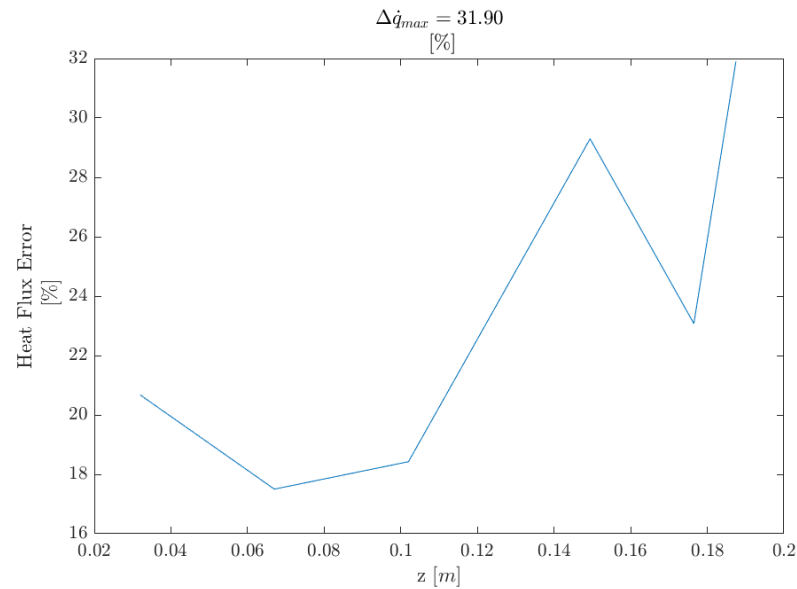


Figure 7.42.: Summed relative heat flux error uncoated case

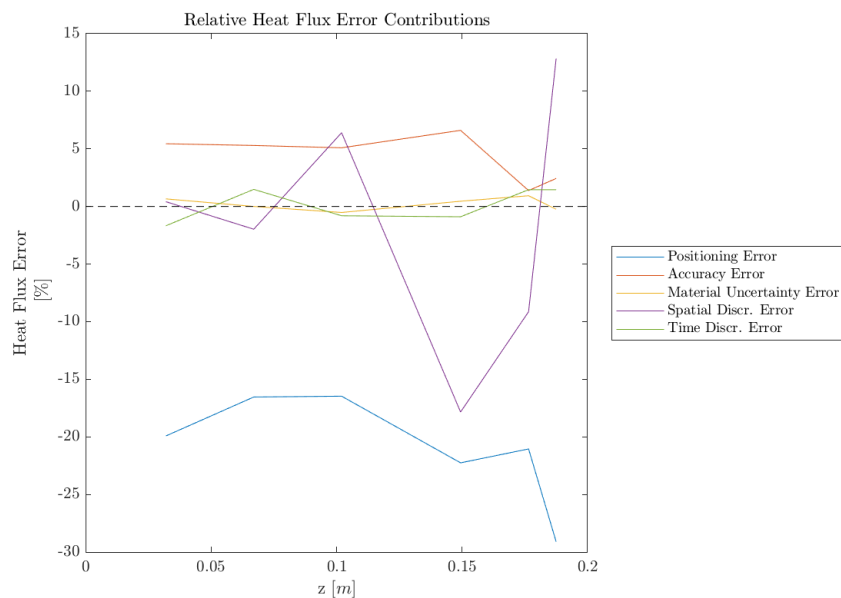


Figure 7.43.: Relative heat flux error contributions uncoated case

Relative Heat Flux Error of Ceramic Case The total error for the ceramic case varies between about 16% and 38%, being the most at the last optimization point, depicted in Figure 7.44. Figure 7.45 exhibits the marginal influence of the influence of material parameter uncertainties. Compared to uncoated case the time discretization error gains more influence, nearly as much as the accuracy error with a rather constant contribution of about 5% over-predicting. A major under-prediction is happening in the cylindrical to convergent transitional zone and the throat area for the spatial discretization error, while the positioning error due to its definition is always under-predicting.

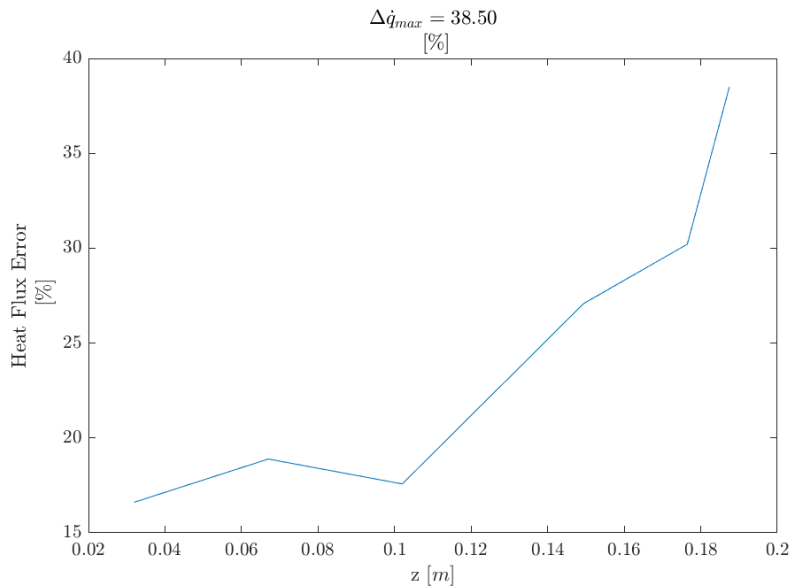


Figure 7.44.: Summed relative heat flux error ceramic case

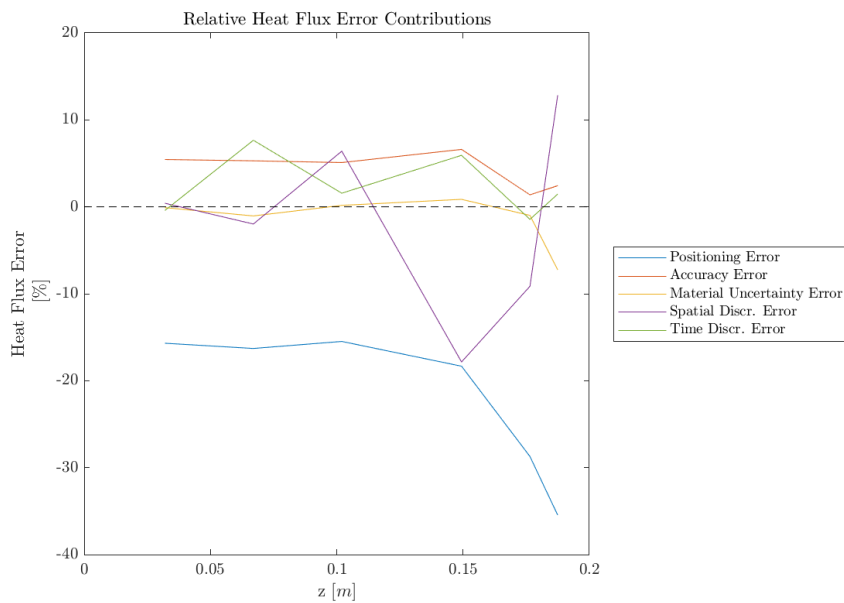


Figure 7.45.: Relative heat flux error contributions ceramic case

Relative Heat Flux Error of metallic Case The total error for the metallic case varies between about 17% and 34%, being the most at the last optimization point, depicted in Figure 7.46. The total error has more a similar form to the total error of the uncoated case than the ceramic one, with a drop at the throat area. Figure 7.47 exhibits the marginal influence of the influence of material parameter uncertainties and the time discretization error. The accuracy error over-predicts with a rather constant contribution of about 5%. A major under-prediction is happening in the cylindrical to convergent transitional zone and the throat area for the spatial discretization error, while the positioning error due to its definition is always under-predicting. In comparison with the ceramic case the positioning error is larger at the throat.

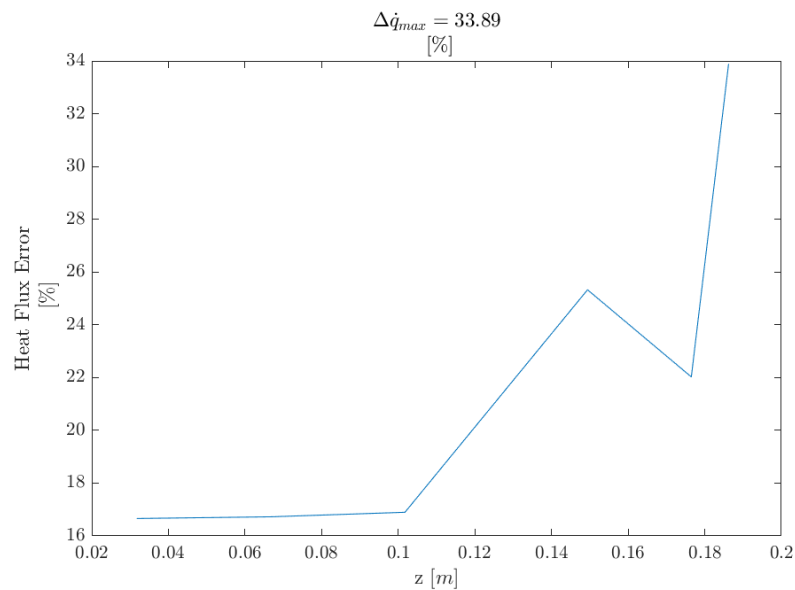


Figure 7.46.: Summed relative heat flux error metallic case

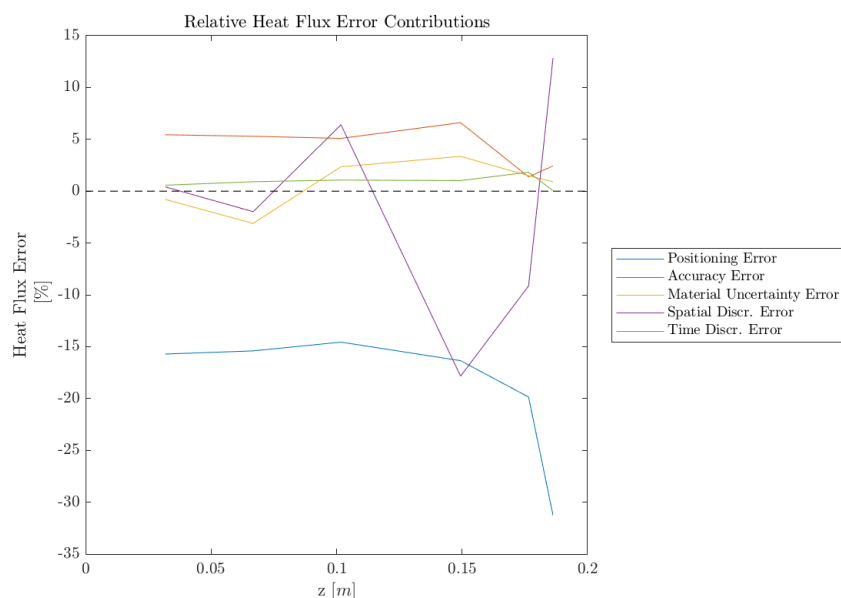


Figure 7.47.: Relative heat flux error contributions metallic case

8. Conclusion and Outlook

This chapter combines a summary of the findings of this thesis and a statement about future work that could develop from this project, as well as ideas about what could have been done better.

8.1. Conclusion

The aim of this research was to investigate the feasibility and effect of thermal barrier coatings on a small capacitive copper rocket combustion chamber at the Chair of Space Mobility and Propulsion at the Technical University of Munich. Two different coating systems were successfully applied, tested and evaluated.

Extensive research into coating applications, materials and manufacturing techniques was undertaken to select suitable coatings to withstand the extreme conditions found in a rocket engine. Two thermal barrier coating systems consisting of two material layers were selected. A ceramic system consisting of a YSZ/NiCrAlY and a metallic system consisting of a Rene80/NiCuCrAl material were applied to a cylindrical chamber segment that could be modularly assembled with a nozzle segment to form a complete combustion chamber. A key driver for the selection was to find a feasible manufacturing technique in combination with the challenges posed by the small internal geometry of the combustion chamber segment. Thermal simulation was used to determine the desired coating thickness for each coating system.

In order to gain experimental insight into the behaviour of the thermal barrier coatings under test conditions, hot fire tests were carried out on a mobile test rig. In addition to the two chamber configurations with the coatings, a reference case with an uncoated segment was tested. The ceramic configuration withstood all load points, whereas the metallic system failed at the second of three pressure load points due to a pre-existing weakness in the coating layer.

Since the thermal load on a rocket engine plays a significant role in the design of a chamber, an evaluation approach based on the inverse heat conduction method using a conjugate gradient method as an optimisation algorithm has been implemented and validated. Sensitivity analysis was carried out on different parts of the algorithm itself, the initial conditions and the temporal and spatial discretisation. Using this technique, the axial heat flux distribution was found and used as a medium to compare the effect of thermal barrier coatings on the chamber.

The application of a thermal barrier coating resulted in a reduction in the magnitude of the heat flux across the coated segment, the magnitude of the reduction varying with the load points. At the nominal load point of 12 *bar* and an ROF of 3.1, the average heat flux reduction over the segment for the ceramic coating was 18.9%, while the metallic case reached 11.3% at 10 *bar* and an ROF of 3.1. Not only the magnitude of the respective heat flux distributions was investigated, but also the temporal evolution of

this quantity over the duration of the hot fire experiment. The performance of the coated configuration was evaluated in terms of integral heat flux, combustion efficiency, characteristic velocity and specific impulse. The evaluation showed that the ceramic coating performed better than the metallic system in terms of heat load reduction, for example at 10 *bar* and an ROF of 3.1 of 22.8%. Both coating systems performed better with increasing chamber pressure. Due to an issue with the thermocouples in the throat area of the reference case, which were needed to calculate the integral heat load across the chamber, the performance assessment does not reflect the efficiency as clearly as the heat flux results.

The axial and circumferential temperature distributions were also of interest in estimating the effect on the copper. An error analysis of the evaluation method was carried out to assess the quality of the results. In particular, an error related to a deviation between the estimated and actual position of the thermocouple makes a large contribution to the total error. For each configuration the total error was greatest at the end of the nozzle due to lack of comparative data and had another peak in the throat area. The average total area was approximately 21 – 24% depending on the configuration.

8.2. Outlook

The results of this work can be used as a reference case for further investigation, for example at different coating thicknesses and in combination with regenerative cooling, with regard to the use of thermal barrier coatings in small methane-oxygen thrusters.

This work was able to highlight the insulation effect of a thermal barrier coating system in this context. The ceramic coating was easier to manufacture, the components are commercially available, showed greater reliability with no failures and had a greater effect in reducing the thermal load on the copper chamber. The metallic coating, although better suited to larger rocket engines, did not show its full potential due to premature material failure, although this was a post-processing issue and could have been avoided. Nevertheless, for the data that could be compared, the ceramic coating had a greater impact on the thermal loads of the chamber.

If a supplier could be found who could produce a similar coating using electron beam physical vapour deposition rather than plasma spraying, this could give even better results in terms of material strength, but could be more expensive. If a thermal barrier coating is chosen, it could also be applied to the cylindrical part of the nozzle, applying it from one side. However, if the chamber were to be made non-segmented or even smaller, the likelihood of applying a thermal barrier coating would be drastically reduced, as the small internal diameter of the chamber would already limit the application of this work.

However, where the application of a thermal barrier coating is feasible, it represents a good alternative or addition to more complex cooling methods such as regenerative cooling.

Bibliography

- [1] Bäker, M.; Fiedler, T.; Rösler, J.: Stress evolution in thermal barrier coatings for rocket engine applications. *Mechanics of Advanced Materials and Modern Processes*, Vol. 1, No. 1, p. 115, 2015.
- [2] Cao, X. Q.; Vassen, R.; Stoeber, D.: Ceramic materials for thermal barrier coatings. *Journal of the European Ceramic Society*, Vol. 24, No. 1, pp. 1–10, 2004.
- [3] D. Kowollik; P. Horst; M. Haupt: *Fluid-Structure Interaction Analysis Applied to Thermal Barrier Coated Cooled Rocket Thrust Chambers with Subsequent Local Investigation of Delamination Phenomena*, 2013.
- [4] D. R. Bartz: A Simple Equation for Rapid Estimation of Rocket Nozzle Convective Heat Transfer Coefficients. *Jet Propulsion*, No. 27.1, pp. 49–51, 1957.
- [5] Dalshad, R.: *Capacitive Chamber Hotfire Tests Documentation 2023: (unpublished)*, 2023.
- [6] Deutsches Kupferinstitut: *Cu-ETP: DKI Werkstoff-Datenblätter*, 2005.
- [7] Fiedler, T.; Rösler, J.; Bäker, M.: A new Metallic Thermal Barrier Coating System for Rocket Engines: Failure Mechanisms and Design Guidelines. *Journal of Thermal Spray Technology*, Vol. 28, No. 7, pp. 1402–1419, 2019.
- [8] Fiedler, T.: *Wärmedämmschichten für Raketentriebwerke*. PhD thesis.
- [9] Fiedler, T.; Bäker, M.; Rösler, J.: Large heat flux exposure of metallic coatings for rocket engine applications. *Surface and Coatings Technology*, Vol. 332, No. 5, pp. 30–39, 2017.
- [10] Fiedler, T.; Fedorova, T.; Rösler, J.; Bäker, M.: Design of a Nickel-Based Bond-Coat Alloy for Thermal Barrier Coatings on Copper Substrates. *Metals*, Vol. 4, No. 4, pp. 503–518, 2014.
- [11] Fiedler, T.; Groß, R.; Rösler, J.; Bäker, M.: Damage mechanisms of metallic HVOF-coatings for high heat flux application. *Surface and Coatings Technology*, Vol. 316, pp. 219–225, 2017.
- [12] Fiedler, T.; Rösler, J.; Bäker, M.: Development of a CuNiCrAl Bond Coat for Thermal Barrier Coatings in Rocket Combustion Chambers. *Journal of Thermal Spray Technology*, Vol. 24, No. 8, pp. 1480–1486, 2015.
- [13] Fiedler, T.; Rösler, J.; Bäker, M.; Hötte, F.; Sethe, C. von; Daub, D.; Haupt, M.; Haidn, O. J.; Esser, B.; Gülhan, A.: Mechanical Integrity of Thermal Barrier Coatings: Coating Development and Micromechanics. In: *Future Space-Transport-System Components under High Thermal and Mechanical Loads*. Springer, Cham, pp. 295–307, (cit. on pp. 3, 33, 36, 37), 2021.
- [14] Gleeson, B.: Thermal Barrier Coatings for Aeroengine Applications. *Journal of Propulsion and Power*, Vol. 22, No. 2, pp. 375–383, 2006.
- [15] Golikov, A. N.; Polyanskii, M. N.: Thermocyclic testing of heat-resistant coatings at megawatt three-phase plasmatron. *Journal of Engineering Thermophysics*, Vol. 17, No. 4, pp. 311–319, 2008.

- [16] Greuel, D.; Haidn, O.; Fritscher, K.: Thermal Barrier Coating for Cryogenic Rocket Engines. In: 38th AIAA/ASME/SAE/ASEE Joint Propulsion Conference & Exhibit, 2002.
- [17] Haidn, O. J.: Raumfahrtantriebe 1: Grundlagen Antriebe, 2017.
- [18] Hötte, F.; Sethe, C. von; Fiedler, T.; Haupt, M.; Haidn, O. J.; Rohdenburg, M.: Experimental lifetime study of regeneratively cooled rocket chamber walls. *International Journal of Fatigue*, Vol. 138, p. 105649, 2020.
- [19] Kevin Hemker; Sai Raj: Microsample Characterization of Coatings for GRCop-84 for High Heat Flux Applications, 2003.
- [20] Kirchberger, C.; Wagner, R.; Kau, H.-P.; Soller, S.; Martin, P.; Bouchez, M.; Bonzom, C.: Prediction and Analysis of Heat Transfer in Small Rocket Chambers. In: 46th AIAA Aerospace Sciences Meeting and Exhibit, 2008.
- [21] Kirchberger, C. U.: Investigation on Heat Transfer in Small Hydrocarbon Rocket Combustion Chambers. TU Munich, PhD thesis, 2014.
- [22] Lehrstuhl für Umformtechnik und Gießereiwesen: Geometriemessung.
- [23] Louis J. Ghosn; Sai V. Raj: Residual Stresses in Thermal Barrier Coatings for a Cu-8Cr-4Nb Substrate System. In: 26th Annual Conference on Composites, Advanced Ceramics, Materials, and Structures: B: Ceramic Engineering and Science Proceedings. John Wiley & Sons, Ltd, pp. 409–416, (cit. on p. 4), 2008.
- [24] Lukas Preis: Inverse Heat Transfer Method with Multi-Objective Optimization applied to Rocket Combustion Chambers with Regenerative Cooling Systems. TU Munich, Master thesis, 2018.
- [25] Mondal, K.; Nuñez III, L.; Downey, C. M.; van Rooyen, I. J.: Thermal Barrier Coatings Overview: Design, Manufacturing, and Applications in High-Temperature Industries. *Industrial & Engineering Chemistry Research*, Vol. 60, No. 17, pp. 6061–6077, 2021.
- [26] Nikolaos Perakis: Wall Heat Transfer Measurement and Prediction in Methane/Oxygen Rocket Engines. TU Munich, PhD thesis, 2021.
- [27] Oerlikon Metco: Atmospheric Plasma Spray Solutions, 2022.
- [28] Omega Engineering Inc.: Thermocouple types.
- [29] Özişik, M. N.; Orlande, H. R. B.: Inverse heat transfer: Fundamentals and applications, New York, NY: Taylor & Francis, ISBN 156032838X, 2000.
- [30] Perakis, N.; Haidn, O. J.: Inverse heat transfer method applied to capacitively cooled rocket thrust chambers. *International Journal of Heat and Mass Transfer*, Vol. 131, pp. 150–166, 2019.
- [31] Perakis, N.; Preis, L.; Haidn, O. J.: Wall Heat Flux Evaluation in Regeneratively Cooled Rocket Thrust Chambers. *Journal of Thermophysics and Heat Transfer*, Vol. 35, No. 1, pp. 127–141, 2021.
- [32] Perakis, N.; Strauß, J.; Haidn, O. J.: Heat flux evaluation in a multi-element CH₄/O₂ rocket combustor using an inverse heat transfer method. *International Journal of Heat and Mass Transfer*, Vol. 142, p. 118425, 2019.
- [33] Quentenmeyer, R.; KASPER, H.; KAZAROFF, J.: Investigation of the effect of ceramic coatings on rocket thrust chamber life. In: 14th Joint Propulsion Conference, 7251978.
- [34] Rajput, P.: Key Concepts in Thermal Conduction: Intro to Heat Transfer in Fluids – Lesson 4, 2020.

-
- [35] Robert Vassen; Xueqiang Cao; Frank Tietz; Debabrata Basu; Detlev Stöver: Zirconates as New Materials for Thermal Barrier Coatings. *Journal of the American Ceramic Society*, Vol. 83, No. 8, pp. 2023–2028, 2000.
- [36] Rybak + Hofmann rhv-Technik GmbH + Co. KG: rhv-technik: <https://www.rhv-technik.com>.
- [37] Rybak + Hofmann rhv-Technik GmbH + Co. KG: Thermische Beschichtungen: <https://www.rhv-technik.com/beschichtungen/verfahren/>.
- [38] S. Gordon, B. M.: Computer Program for Calculation of Complex Chemical Equilibrium Compositions and Applications, I. Analysis. NASA Reference Publication 1311, 1994.
- [39] S. Gordon, B. M.: Computer Program for Calculation of Complex Chemical Equilibrium Compositions and Applications_2, II. Users Manual and Program Description. NASA Reference Publication 1311, 1996.
- [40] Schloesser, J.; Bäker, M.; Rösler, J.: Laser cycling and thermal cycling exposure of thermal barrier coatings on copper substrates. *Surface and Coatings Technology*, Vol. 206, No. 7, pp. 1605–1608, 2011.
- [41] Schulz, U.; Fritscher, K.; Peters, M.; Greuel, D.; Haidn, O.: Fabrication of TBC-armored rocket combustion chambers by EB-PVD methods and TLP assembling. *Science and Technology of Advanced Materials*, Vol. 6, No. 2, pp. 103–110, 2005.
- [42] Silvestri, S.: Investigation of Heat Transfer and Injector Design Criteria for Methane/Oxygen Rocket Combustion Chambers. Technical University of Munich, PhD thesis, 2019.
- [43] Sutton, George P., Biblarz, Oscar: *Rocket Propulsion Elements*.
- [44] T. Fiedler; J. Schloesser; J. Rösler; M. Bäker: Development of a thermal-barrier coating-system for rocket combustion chambers. EUCASS, 2015.
- [45] Technical University of Braunschweig: Dr.-Ing. T. Fiedler: <https://www.tu-braunschweig.de/ifw/institut/mitarbeitende/tfiedler>, 22.03.2024.
- [46] Thakare, J. G.; Pandey, C.; Mahapatra, M. M.; Mulik, R. S.: Thermal Barrier Coatings—A State of the Art Review. *Metals and Materials International*, Vol. 27, No. 7, pp. 1947–1968, 2021.
- [47] The MathWorks, I.: ThermalModel: <https://de.mathworks.com/help/pde/ug/pde.thermalmodel.html>.
- [48] Zhou, Y.; Yang, L.; Zhu, W.: *Thermal barrier coatings: Failure theory and evaluation technology*, Singapore and Beijing: Springer and Science Press, ISBN 9789811927225, 2022.

A. Uncoated Configuration IHCM evaluation

Heat Flux of Uncoated Test $\overline{p_{CC}} = 4.35[\text{bar}]$ and $\overline{\dot{m}_{tot}} = 0.06[\text{kg/s}]$

Evaluation time of $t = 3.19 [\text{s}]$ and $\Delta t = 0.23 [\text{s}]$

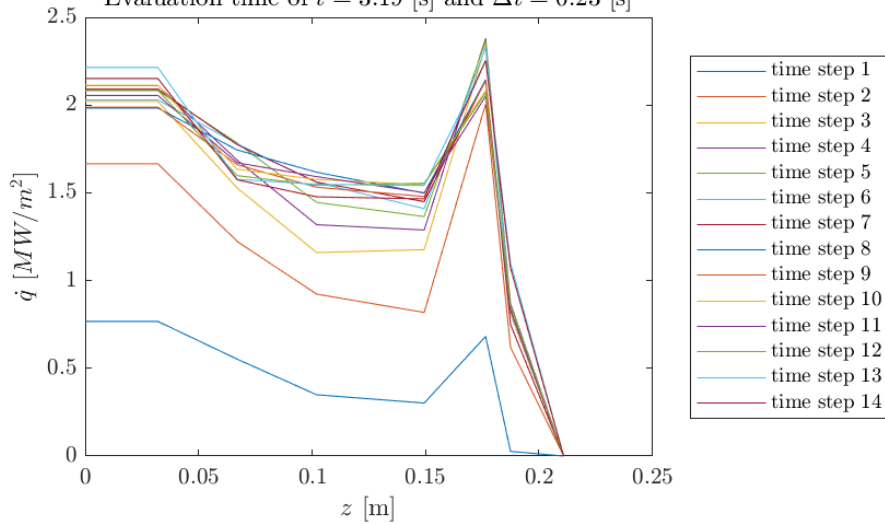


Figure A.1.: Run 1

Heat Flux of Uncoated Test $\overline{p_{CC}} = 4.34[\text{bar}]$ and $\overline{\dot{m}_{tot}} = 0.06[\text{kg/s}]$

Evaluation time of $t = 5.15 [\text{s}]$ and $\Delta t = 0.37 [\text{s}]$

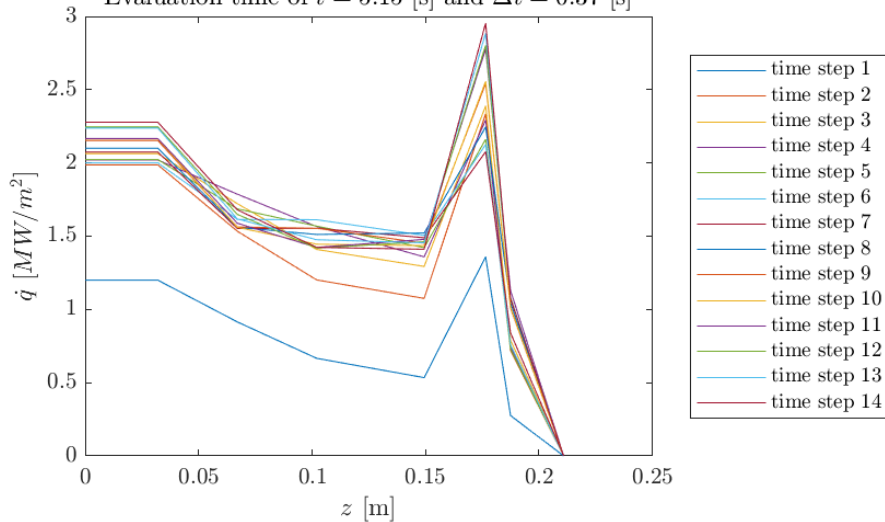


Figure A.2.: Run 2

Heat Flux of Uncoated Test $\overline{p_{CC}} = 4.64[\text{bar}]$ and $\overline{\dot{m}_{tot}} = 0.07[\text{kg/s}]$
 Evaluation time of $t = 3.15 [\text{s}]$ and $\Delta t = 0.22 [\text{s}]$

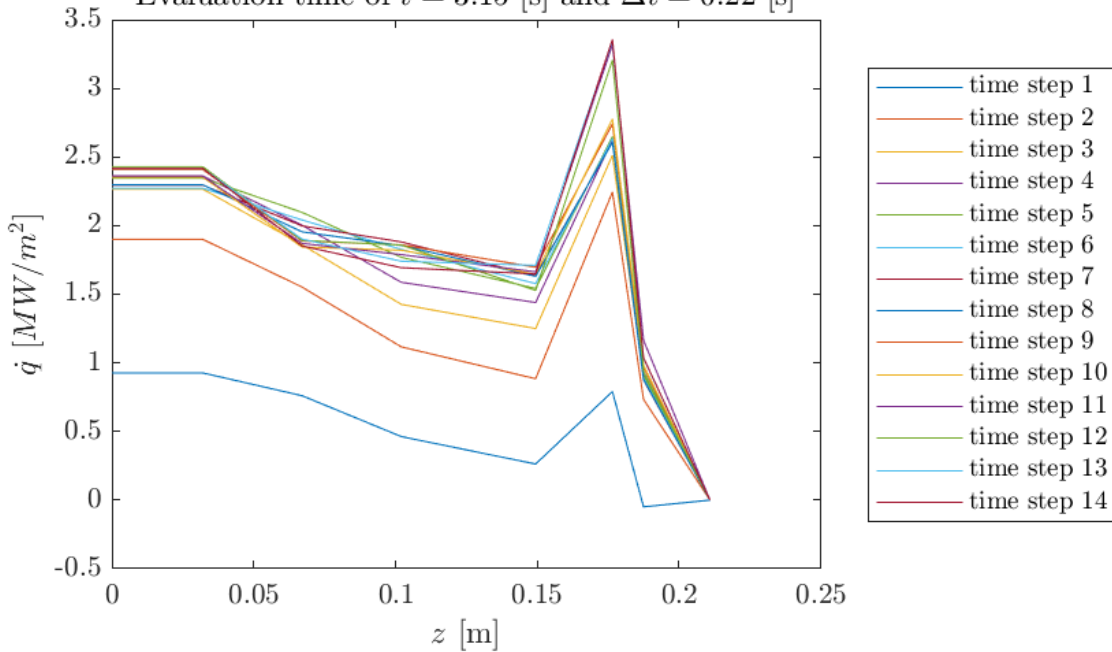


Figure A.3.: Run 3

Heat Flux of Uncoated Test $\overline{p_{CC}} = 4.61[\text{bar}]$ and $\overline{\dot{m}_{tot}} = 0.07[\text{kg/s}]$
 Evaluation time of $t = 3.15 [\text{s}]$ and $\Delta t = 0.22 [\text{s}]$

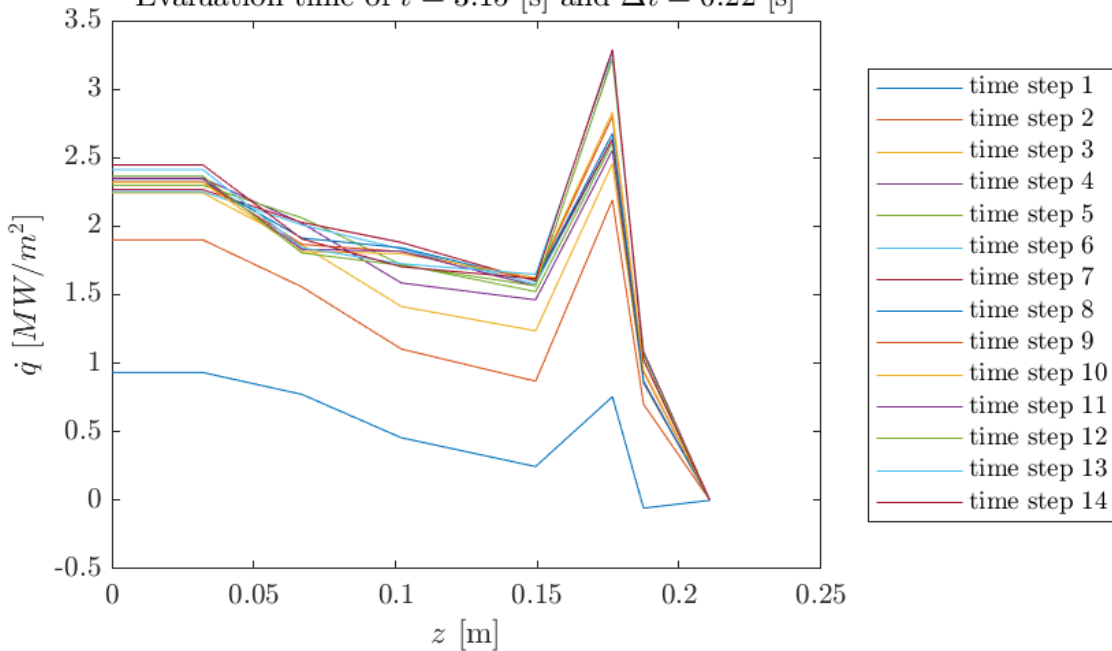


Figure A.4.: Run 4

Heat Flux of Uncoated Test $\overline{p_{CC}} = 4.60[\text{bar}]$ and $\overline{\dot{m}_{tot}} = 0.07[\text{kg/s}]$
Evaluation time of $t = 3.15 [\text{s}]$ and $\Delta t = 0.22 [\text{s}]$

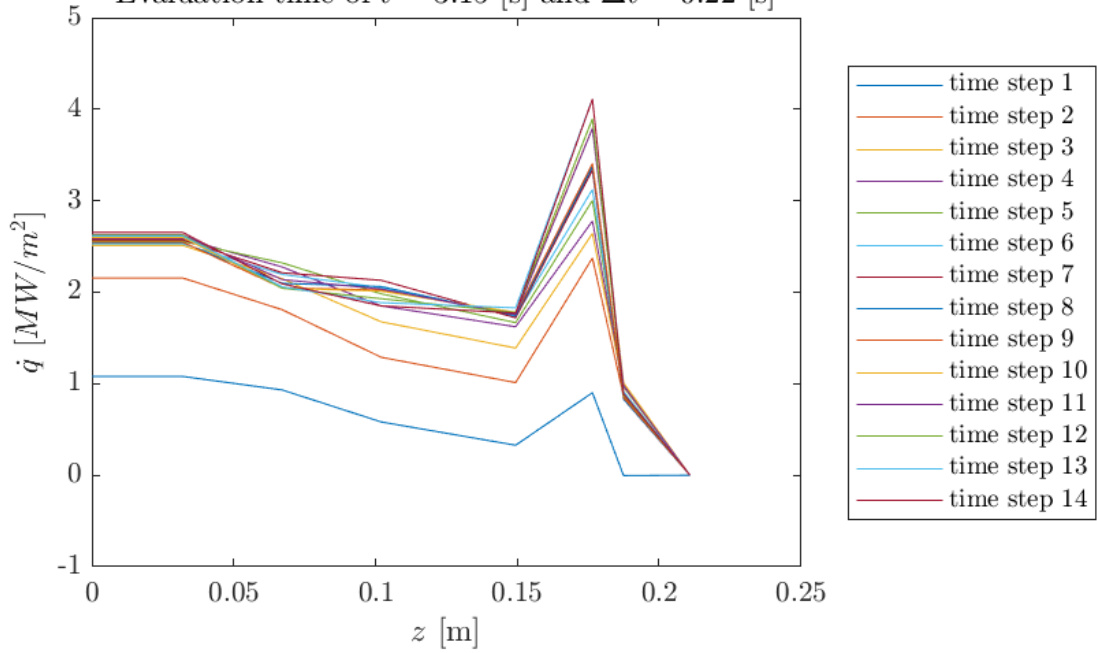


Figure A.5.: Run 5

Heat Flux of Uncoated Test $\overline{p_{CC}} = 4.56[\text{bar}]$ and $\overline{\dot{m}_{tot}} = 0.07[\text{kg/s}]$
Evaluation time of $t = 3.15 [\text{s}]$ and $\Delta t = 0.22 [\text{s}]$

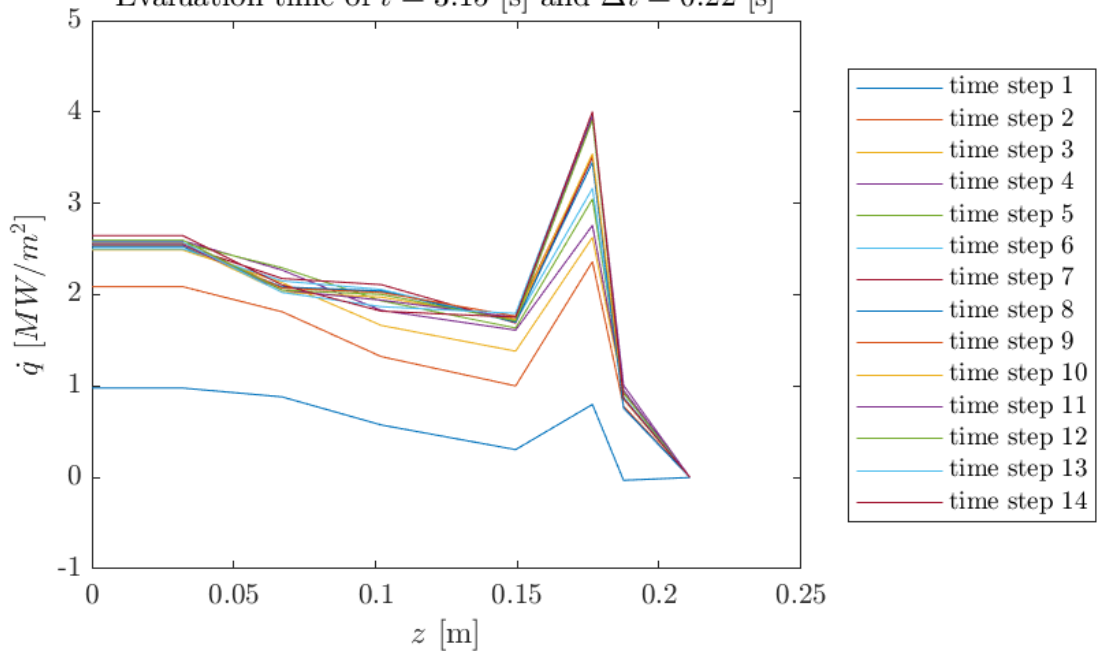


Figure A.6.: Run 6

Heat Flux of Uncoated Test $\overline{p_{CC}} = 8.83[\text{bar}]$ and $\overline{\dot{m}_{tot}} = 0.13[\text{kg/s}]$
 Evaluation time of $t = 3.17 [\text{s}]$ and $\Delta t = 0.23 [\text{s}]$

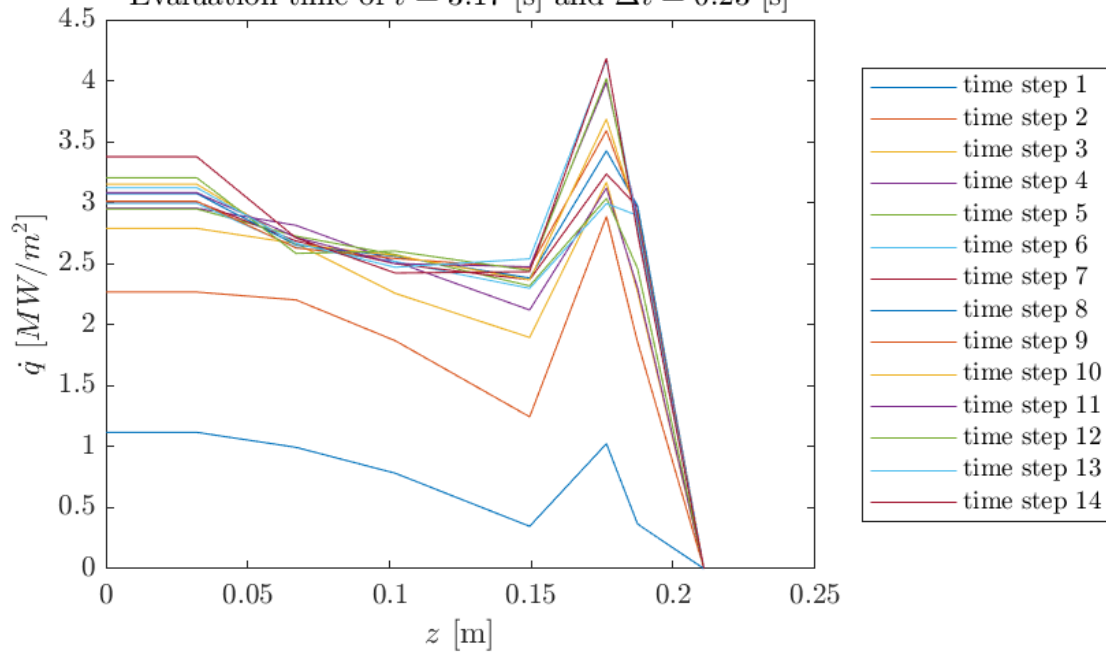


Figure A.7.: Run 7

Heat Flux of Uncoated Test $\overline{p_{CC}} = 9.03[\text{bar}]$ and $\overline{\dot{m}_{tot}} = 0.13[\text{kg/s}]$
 Evaluation time of $t = 3.19 [\text{s}]$ and $\Delta t = 0.23 [\text{s}]$

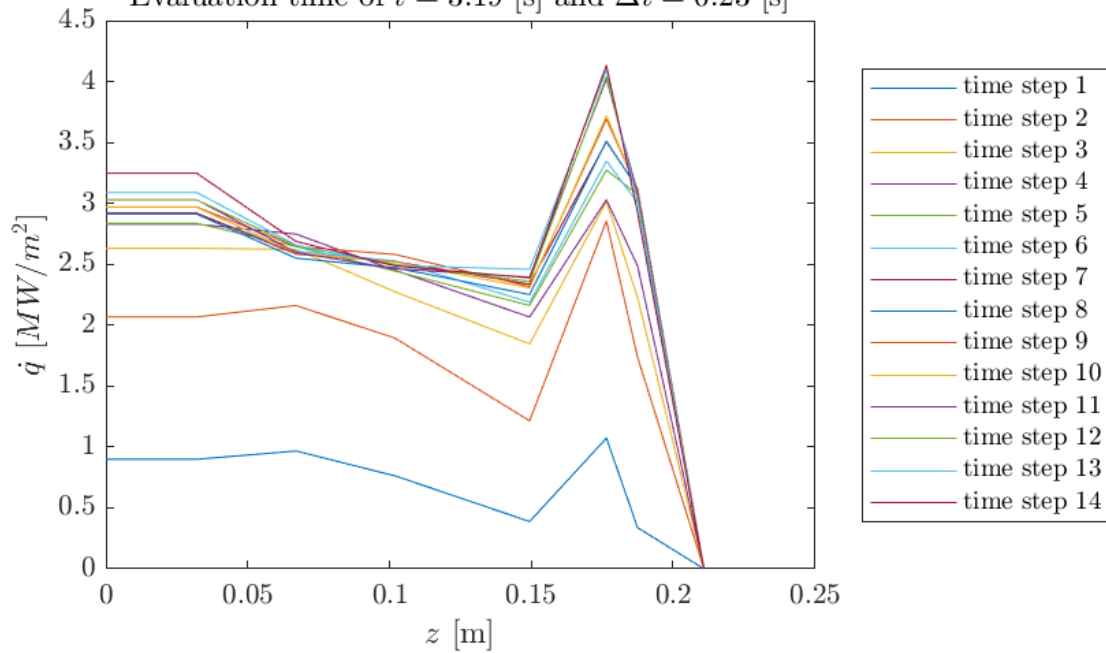


Figure A.8.: Run 8

Heat Flux of Uncoated Test $\overline{p_{CC}} = 9.41[\text{bar}]$ and $\overline{\dot{m}_{tot}} = 0.14[\text{kg/s}]$
 Evaluation time of $t = 3.17 [\text{s}]$ and $\Delta t = 0.23 [\text{s}]$

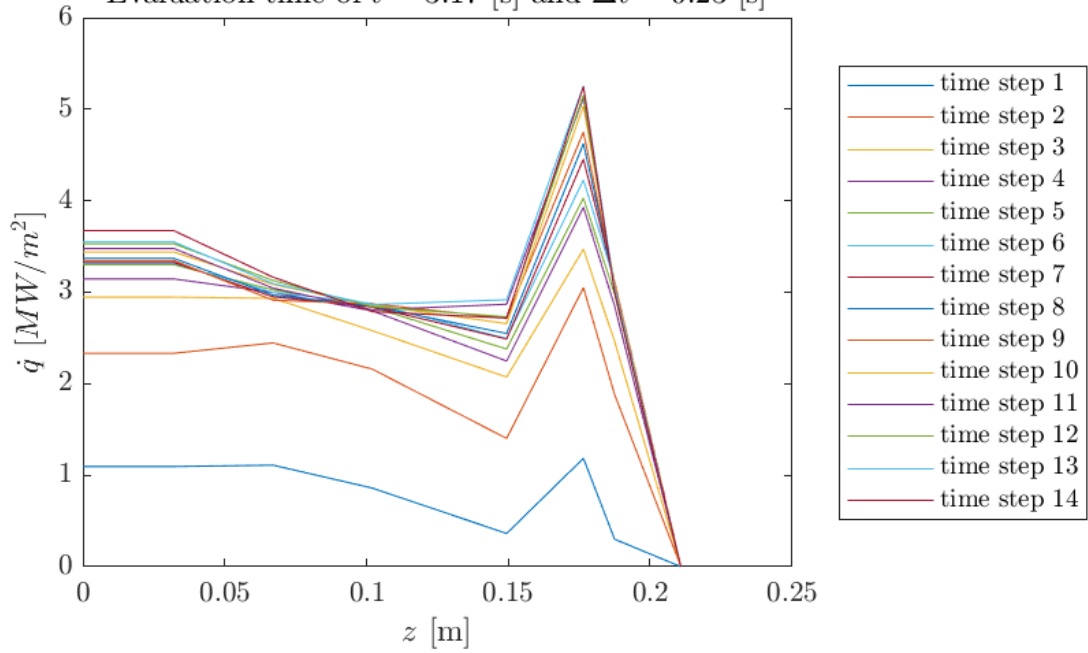


Figure A.9.: Run 9

Heat Flux of Uncoated Test $\overline{p_{CC}} = 9.39[\text{bar}]$ and $\overline{\dot{m}_{tot}} = 0.14[\text{kg/s}]$
 Evaluation time of $t = 3.17 [\text{s}]$ and $\Delta t = 0.23 [\text{s}]$

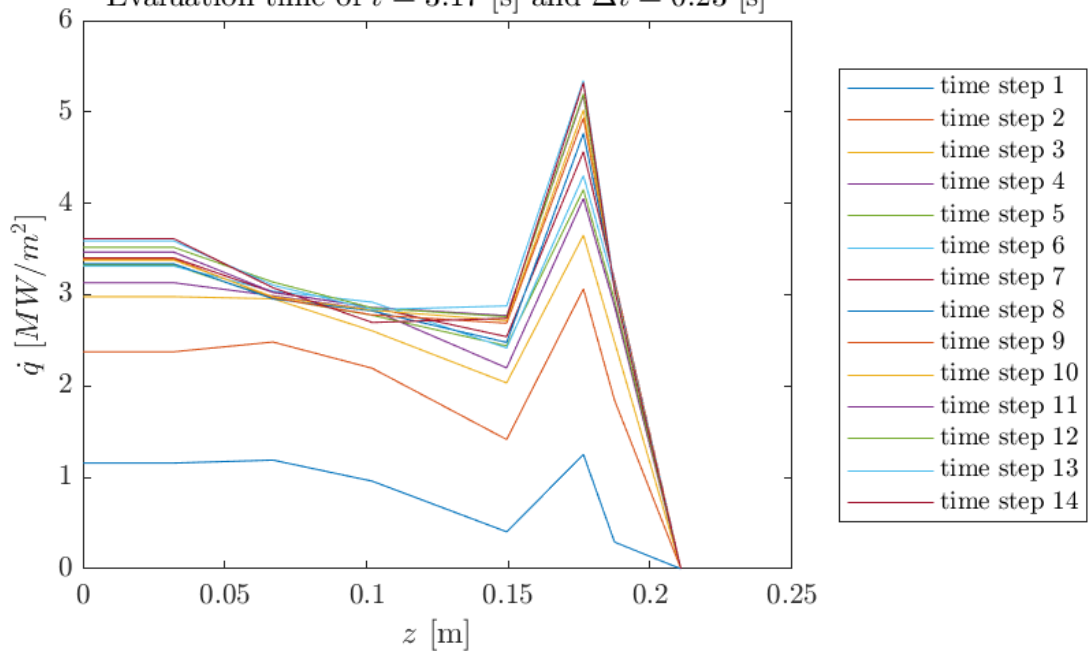


Figure A.10.: Run 10

Heat Flux of Uncoated Test $\overline{p_{CC}} = 9.39[\text{bar}]$ and $\overline{\dot{m}_{tot}} = 0.14[\text{kg/s}]$
 Evaluation time of $t = 3.17 [\text{s}]$ and $\Delta t = 0.23 [\text{s}]$

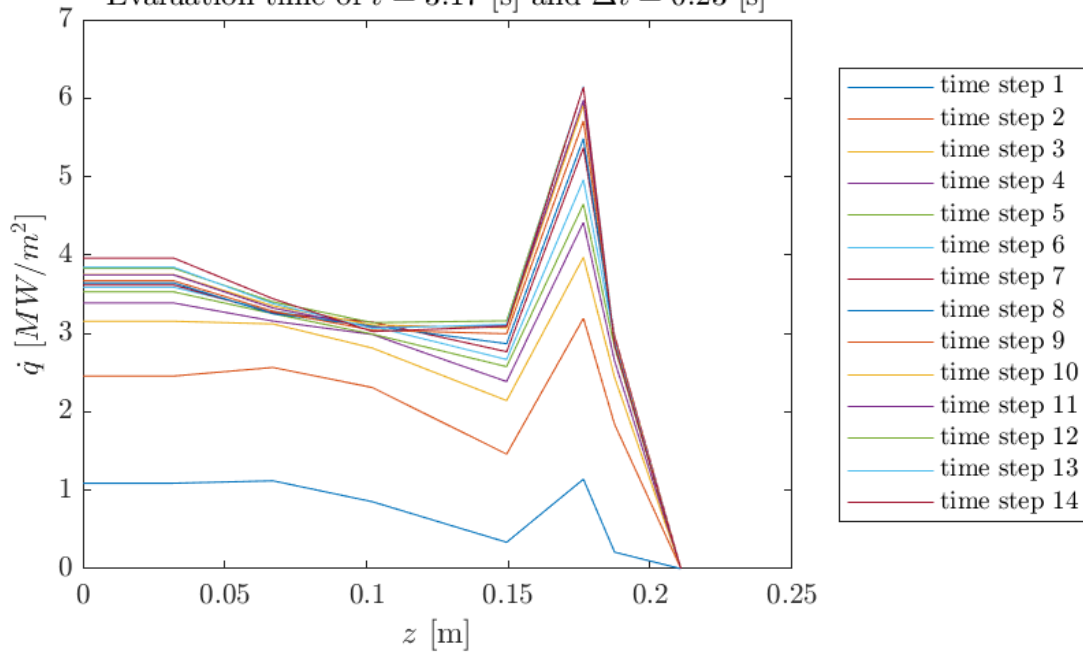


Figure A.11.: Run 11

Heat Flux of Uncoated Test $\overline{p_{CC}} = 9.36[\text{bar}]$ and $\overline{\dot{m}_{tot}} = 0.14[\text{kg/s}]$
 Evaluation time of $t = 3.17 [\text{s}]$ and $\Delta t = 0.23 [\text{s}]$

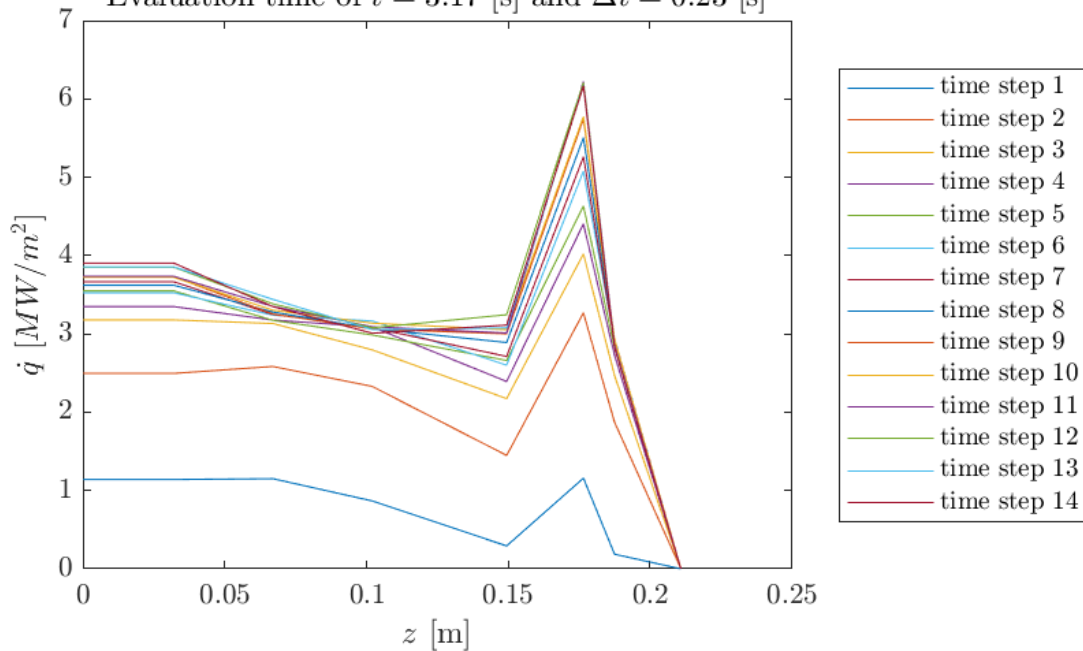


Figure A.12.: Run 12

Heat Flux of Uncoated Test $\overline{p_{CC}} = 11.40[\text{bar}]$ and $\overline{\dot{m}_{tot}} = 0.17[\text{kg/s}]$
 Evaluation time of $t = 3.19 [\text{s}]$ and $\Delta t = 0.23 [\text{s}]$

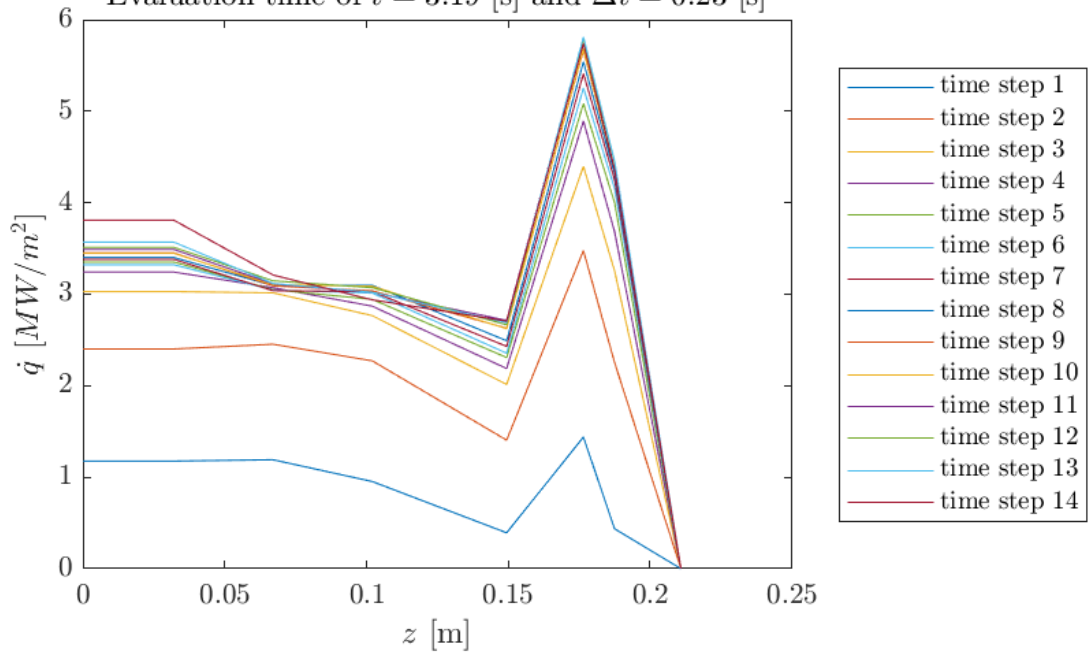


Figure A.13.: Run 13

Heat Flux of Uncoated Test $\overline{p_{CC}} = 11.36[\text{bar}]$ and $\overline{\dot{m}_{tot}} = 0.17[\text{kg/s}]$
 Evaluation time of $t = 3.19 [\text{s}]$ and $\Delta t = 0.23 [\text{s}]$

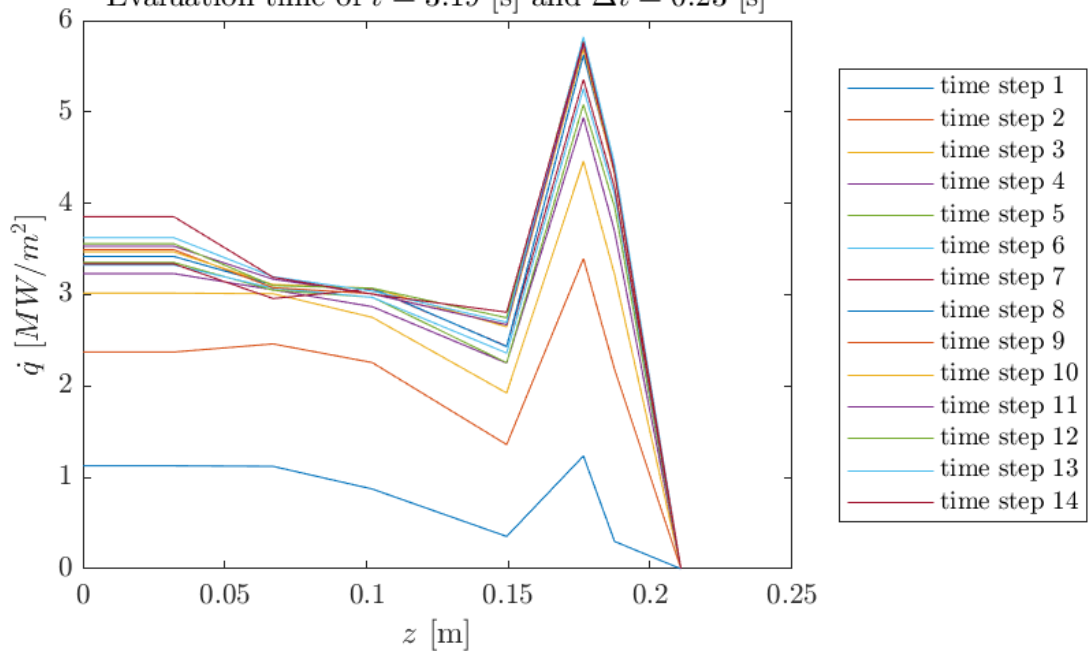


Figure A.14.: Run 14

Heat Flux of Uncoated Test $\overline{p_{CC}} = 11.67[\text{bar}]$ and $\overline{\dot{m}_{tot}} = 0.17[\text{kg/s}]$
 Evaluation time of $t = 3.17 [\text{s}]$ and $\Delta t = 0.23 [\text{s}]$

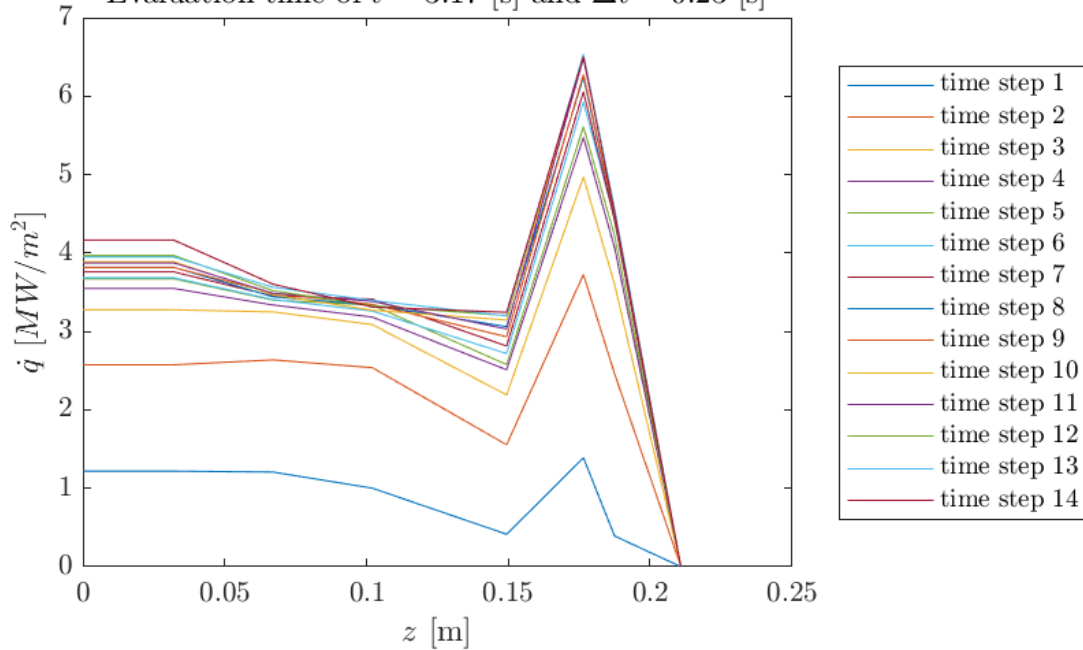


Figure A.15.: Run 15

Heat Flux of Uncoated Test $\overline{p_{CC}} = 11.64[\text{bar}]$ and $\overline{\dot{m}_{tot}} = 0.17[\text{kg/s}]$
 Evaluation time of $t = 3.17 [\text{s}]$ and $\Delta t = 0.23 [\text{s}]$

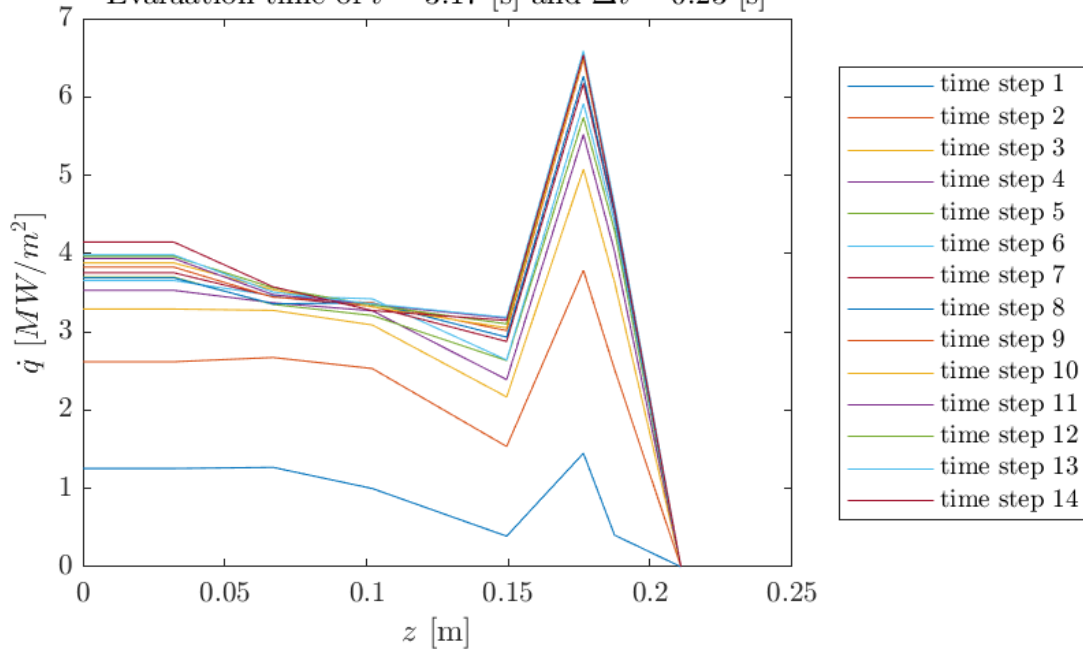


Figure A.16.: Run 16

Heat Flux of Uncoated Test $\overline{p_{CC}} = 12.00[\text{bar}]$ and $\overline{\dot{m}_{tot}} = 0.17[\text{kg/s}]$
 Evaluation time of $t = 3.17 [\text{s}]$ and $\Delta t = 0.23 [\text{s}]$

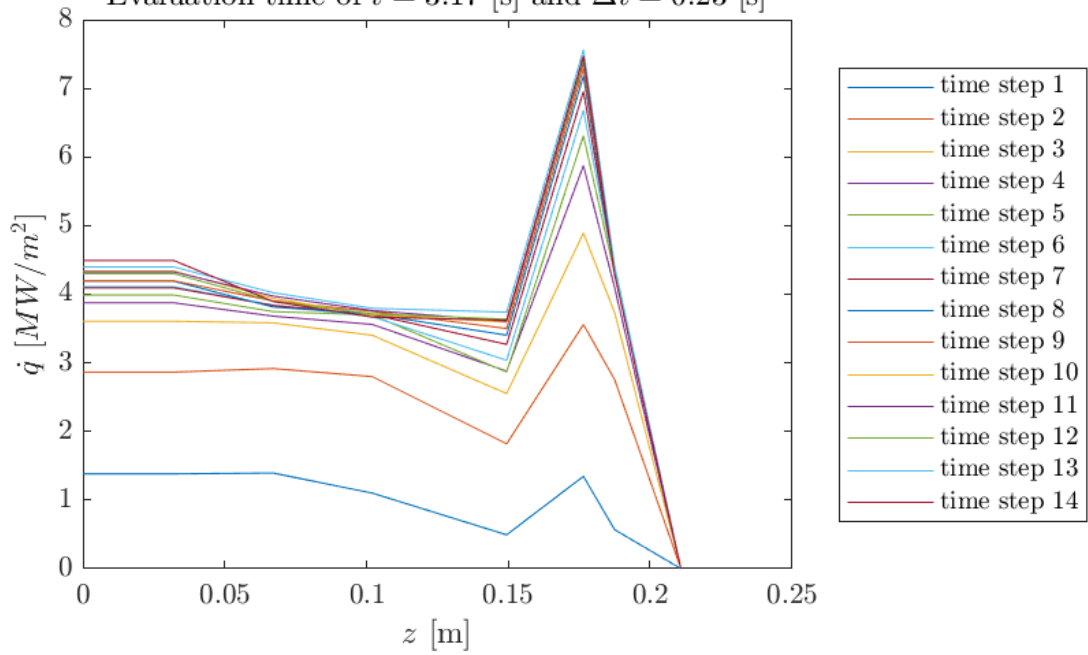


Figure A.17.: Run 17

Heat Flux of Uncoated Test $\overline{p_{CC}} = 11.95[\text{bar}]$ and $\overline{\dot{m}_{tot}} = 0.17[\text{kg/s}]$
 Evaluation time of $t = 3.17 [\text{s}]$ and $\Delta t = 0.23 [\text{s}]$

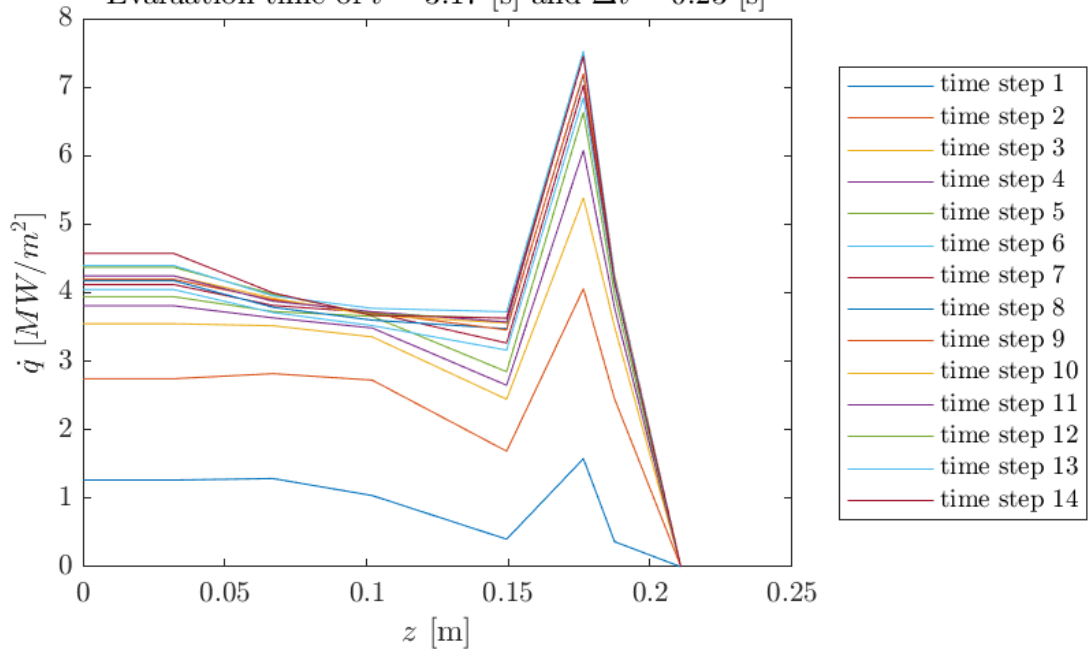


Figure A.18.: Run 18

B. Ceramic Configuration IHCM evaluation

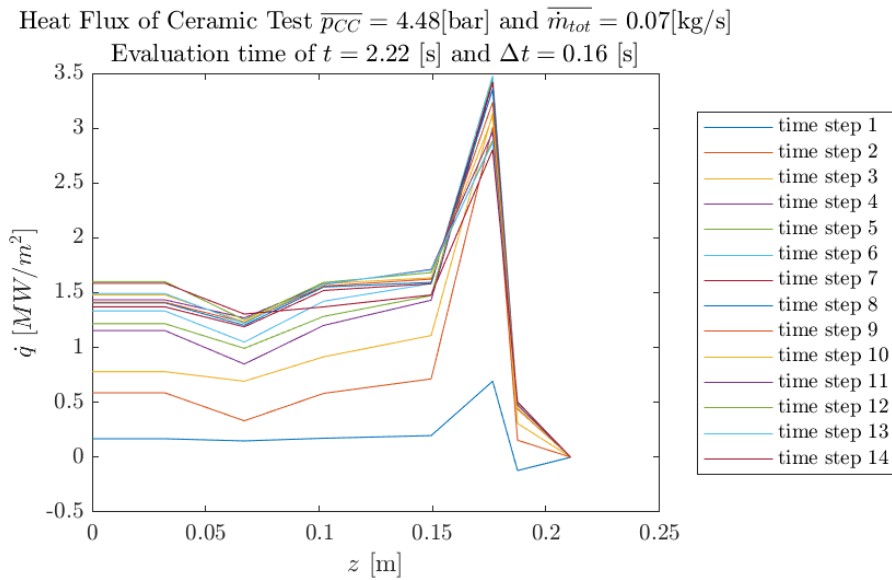


Figure B.1.: Run 1

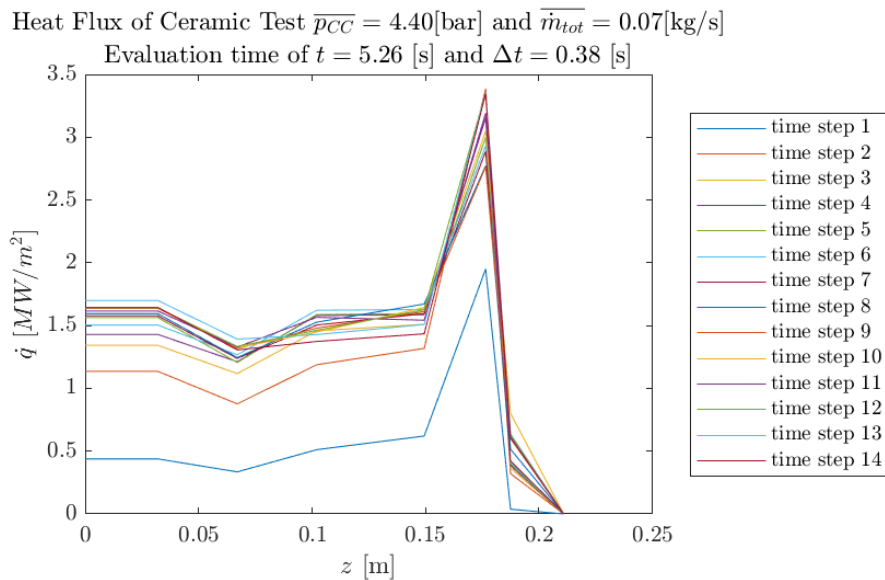


Figure B.2.: Run 2

Heat Flux of Ceramic Test $\overline{p_{CC}} = 4.50[\text{bar}]$ and $\overline{\dot{m}_{tot}} = 0.07[\text{kg/s}]$
 Evaluation time of $t = 3.26 [\text{s}]$ and $\Delta t = 0.23 [\text{s}]$

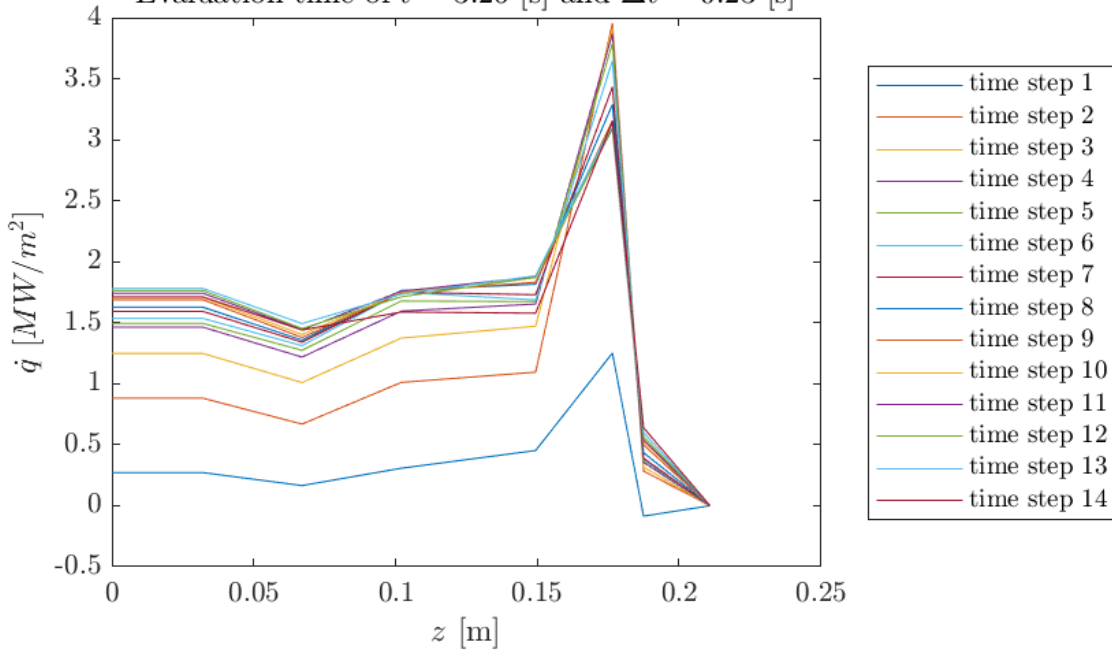


Figure B.3.: Run 3

Heat Flux of Ceramic Test $\overline{p_{CC}} = 4.63[\text{bar}]$ and $\overline{\dot{m}_{tot}} = 0.07[\text{kg/s}]$
 Evaluation time of $t = 5.24 [\text{s}]$ and $\Delta t = 0.37 [\text{s}]$

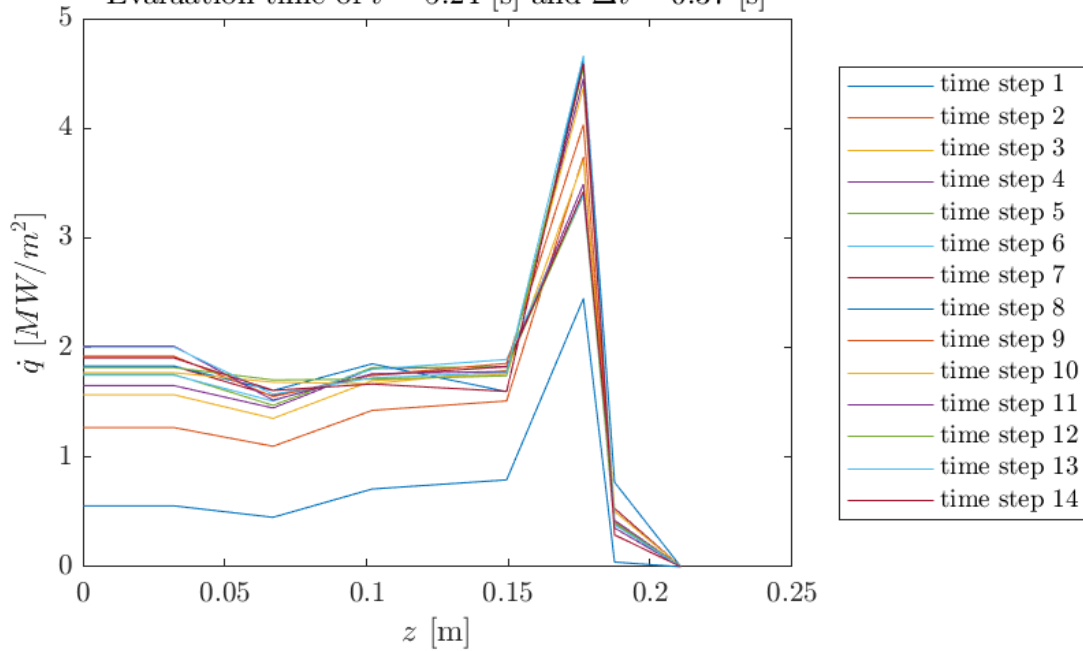


Figure B.4.: Run 4

Heat Flux of Ceramic Test $\overline{p_{CC}} = 4.66[\text{bar}]$ and $\overline{\dot{m}_{tot}} = 0.07[\text{kg/s}]$
 Evaluation time of $t = 3.23 [\text{s}]$ and $\Delta t = 0.23 [\text{s}]$

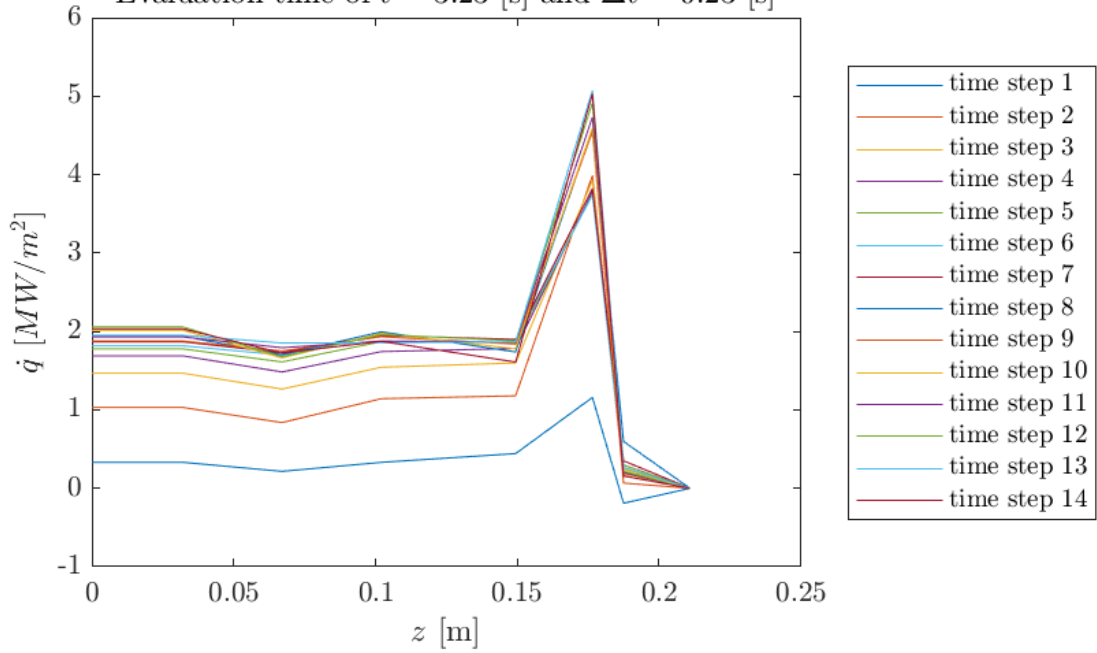


Figure B.5.: Run 5

Heat Flux of Ceramic Test $\overline{p_{CC}} = 4.59[\text{bar}]$ and $\overline{\dot{m}_{tot}} = 0.07[\text{kg/s}]$
 Evaluation time of $t = 5.26 [\text{s}]$ and $\Delta t = 0.38 [\text{s}]$

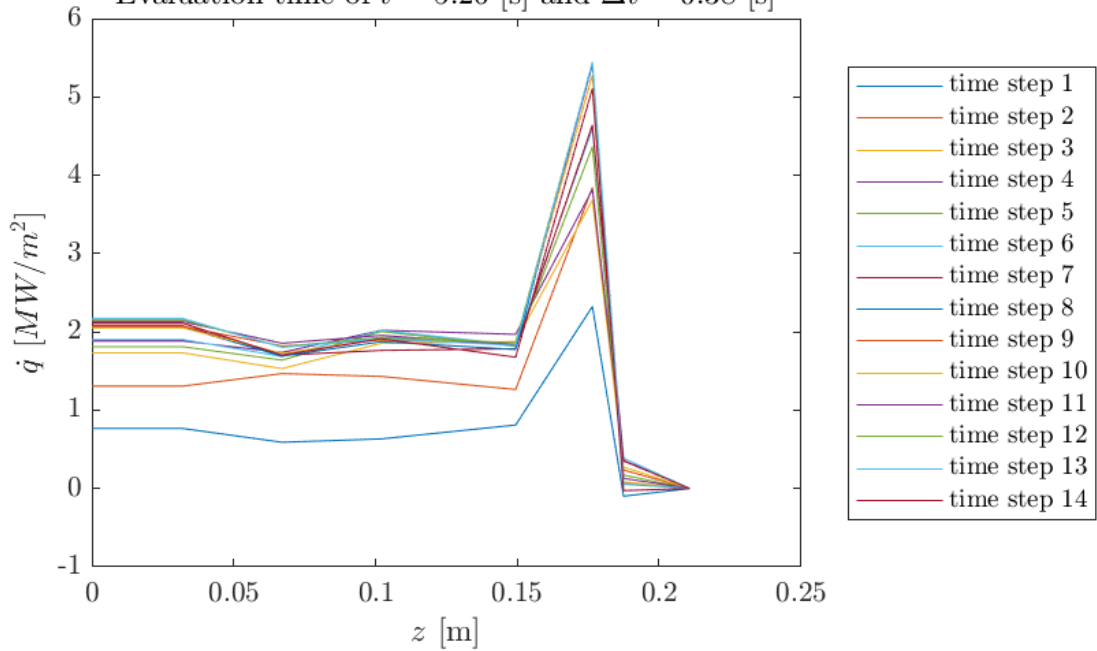


Figure B.6.: Run 6

Heat Flux of Ceramic Test $\overline{p_{CC}} = 8.68[\text{bar}]$ and $\overline{\dot{m}_{tot}} = 0.13[\text{kg/s}]$
 Evaluation time of $t = 3.28 [\text{s}]$ and $\Delta t = 0.23 [\text{s}]$

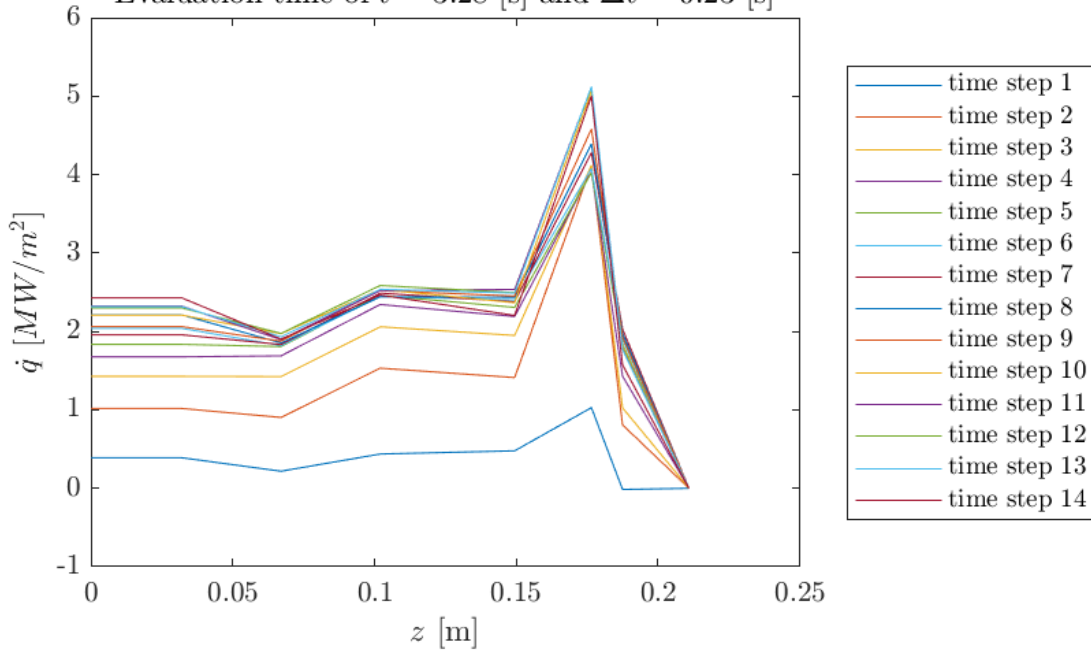


Figure B.7.: Run 7

Heat Flux of Ceramic Test $\overline{p_{CC}} = 8.67[\text{bar}]$ and $\overline{\dot{m}_{tot}} = 0.13[\text{kg/s}]$
 Evaluation time of $t = 5.28 [\text{s}]$ and $\Delta t = 0.38 [\text{s}]$

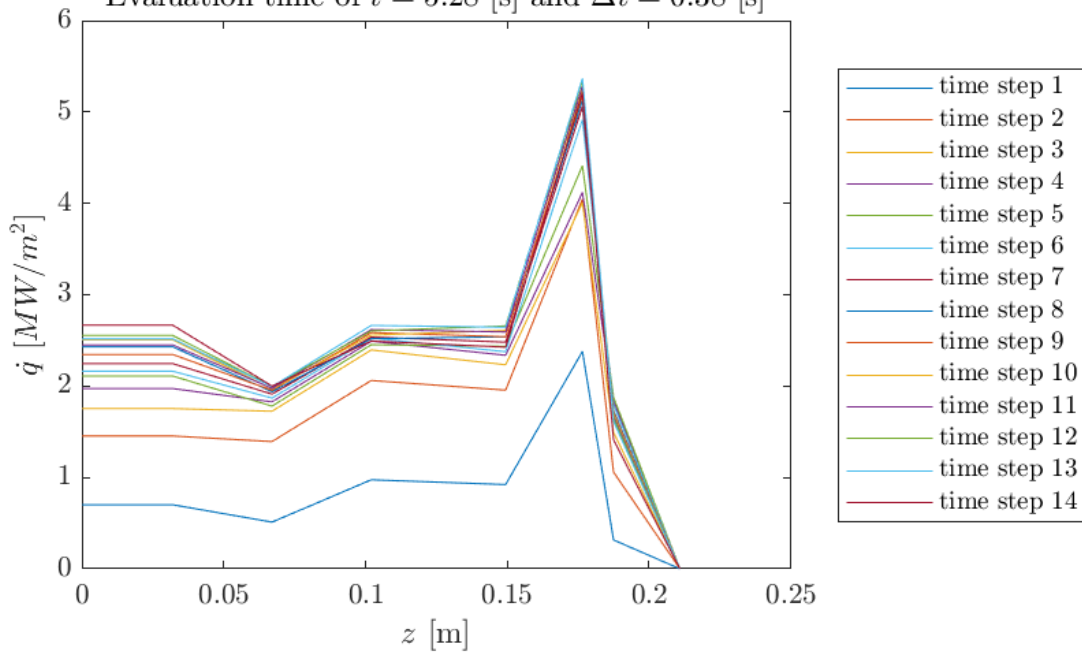


Figure B.8.: Run 8

Heat Flux of Ceramic Test $\overline{p_{CC}} = 9.30[\text{bar}]$ and $\overline{\dot{m}_{tot}} = 0.13[\text{kg/s}]$
 Evaluation time of $t = 3.23 [\text{s}]$ and $\Delta t = 0.23 [\text{s}]$

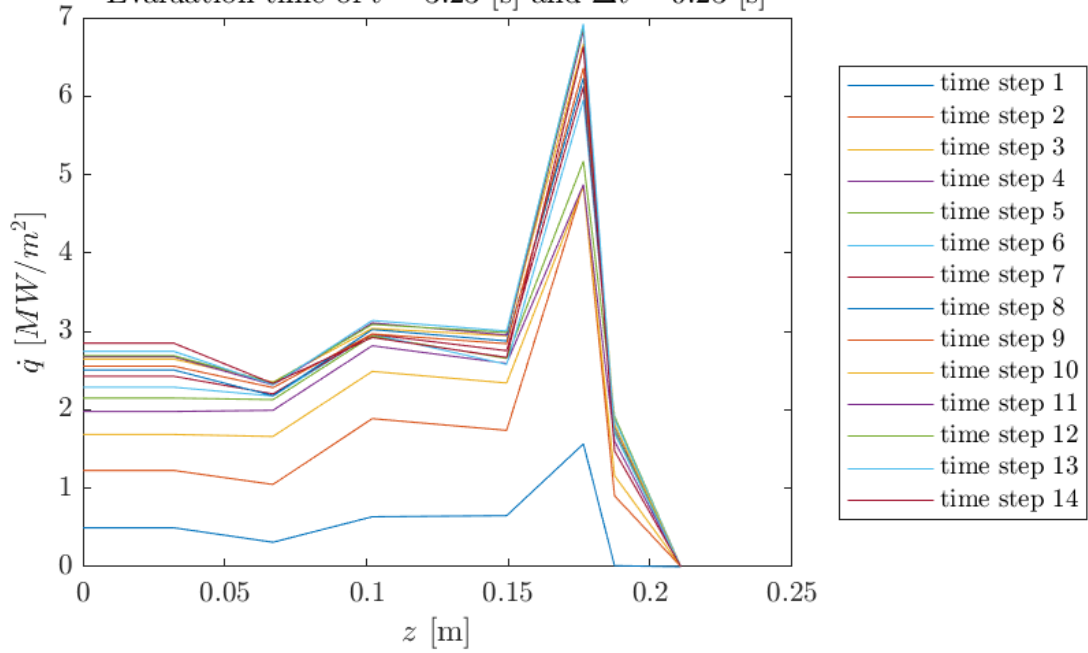


Figure B.9.: Run 9

Heat Flux of Ceramic Test $\overline{p_{CC}} = 9.27[\text{bar}]$ and $\overline{\dot{m}_{tot}} = 0.13[\text{kg/s}]$
 Evaluation time of $t = 3.26 [\text{s}]$ and $\Delta t = 0.23 [\text{s}]$

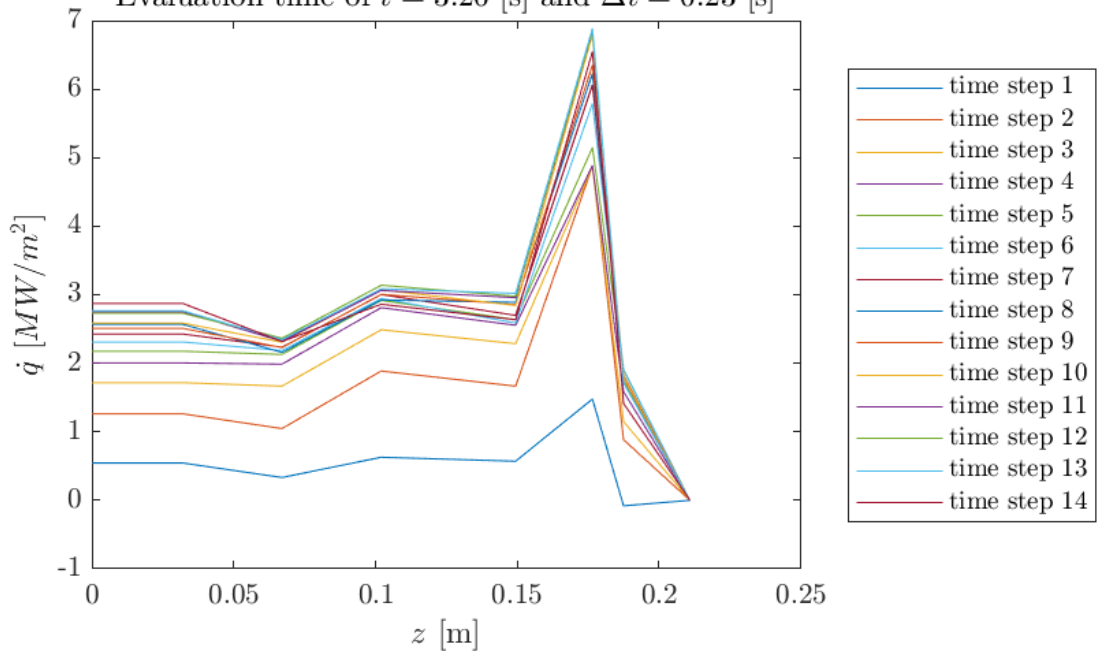


Figure B.10.: Run 10

Heat Flux of Ceramic Test $\overline{p_{CC}} = 9.16[\text{bar}]$ and $\overline{\dot{m}_{tot}} = 0.13[\text{kg/s}]$
 Evaluation time of $t = 3.23 [\text{s}]$ and $\Delta t = 0.23 [\text{s}]$

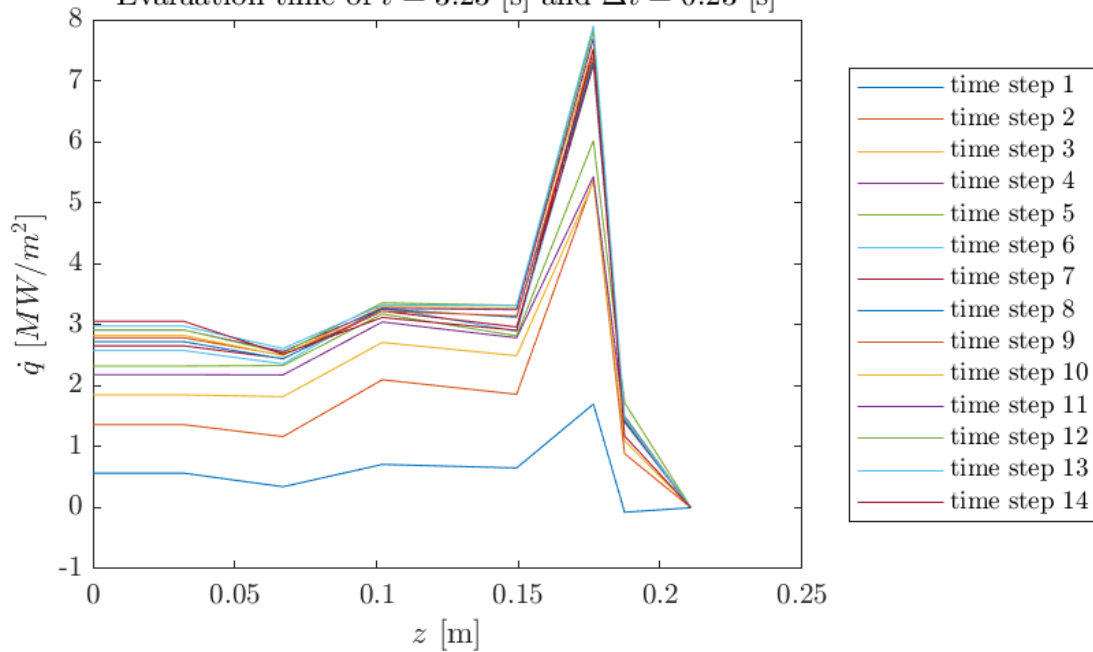


Figure B.11.: Run 11

Heat Flux of Ceramic Test $\overline{p_{CC}} = 9.11[\text{bar}]$ and $\overline{\dot{m}_{tot}} = 0.13[\text{kg/s}]$
 Evaluation time of $t = 3.23 [\text{s}]$ and $\Delta t = 0.23 [\text{s}]$

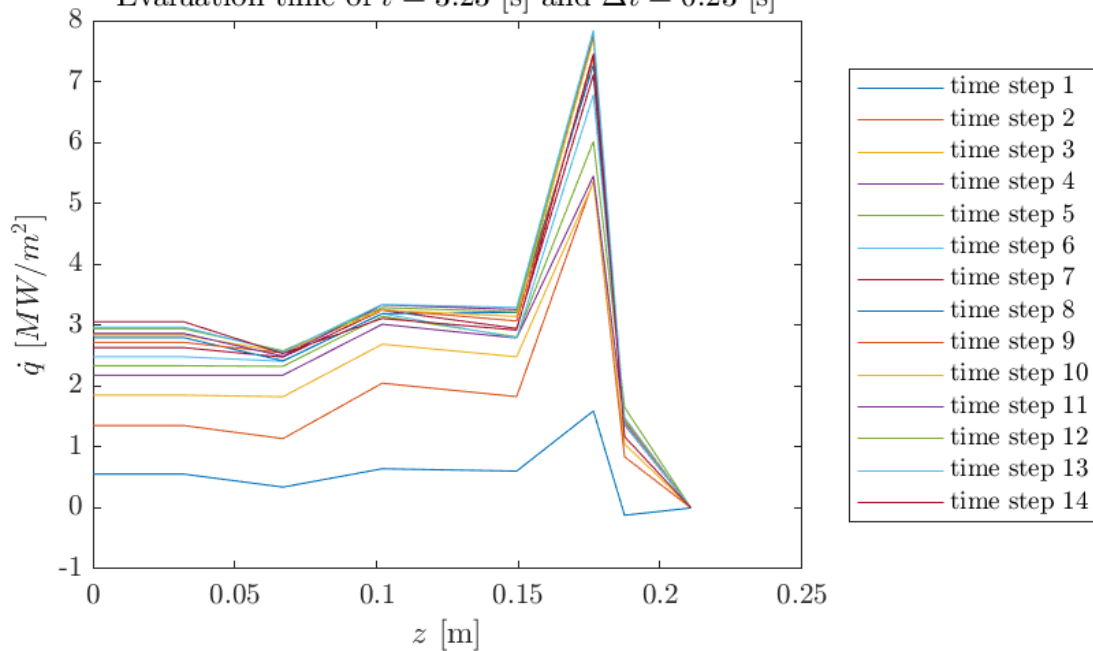


Figure B.12.: Run 12

Heat Flux of Ceramic Test $\overline{p_{CC}} = 11.81[\text{bar}]$ and $\overline{\dot{m}_{tot}} = 0.17[\text{kg/s}]$
 Evaluation time of $t = 3.28 [\text{s}]$ and $\Delta t = 0.23 [\text{s}]$

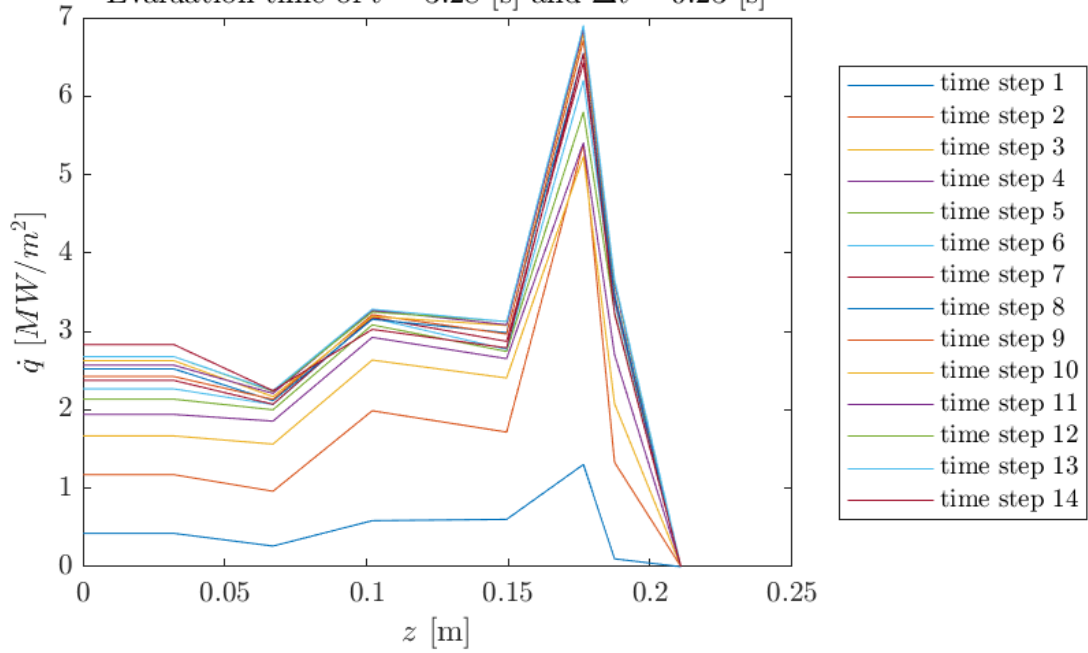


Figure B.13.: Run 13

Heat Flux of Ceramic Test $\overline{p_{CC}} = 11.88[\text{bar}]$ and $\overline{\dot{m}_{tot}} = 0.17[\text{kg/s}]$
 Evaluation time of $t = 4.97 [\text{s}]$ and $\Delta t = 0.36 [\text{s}]$

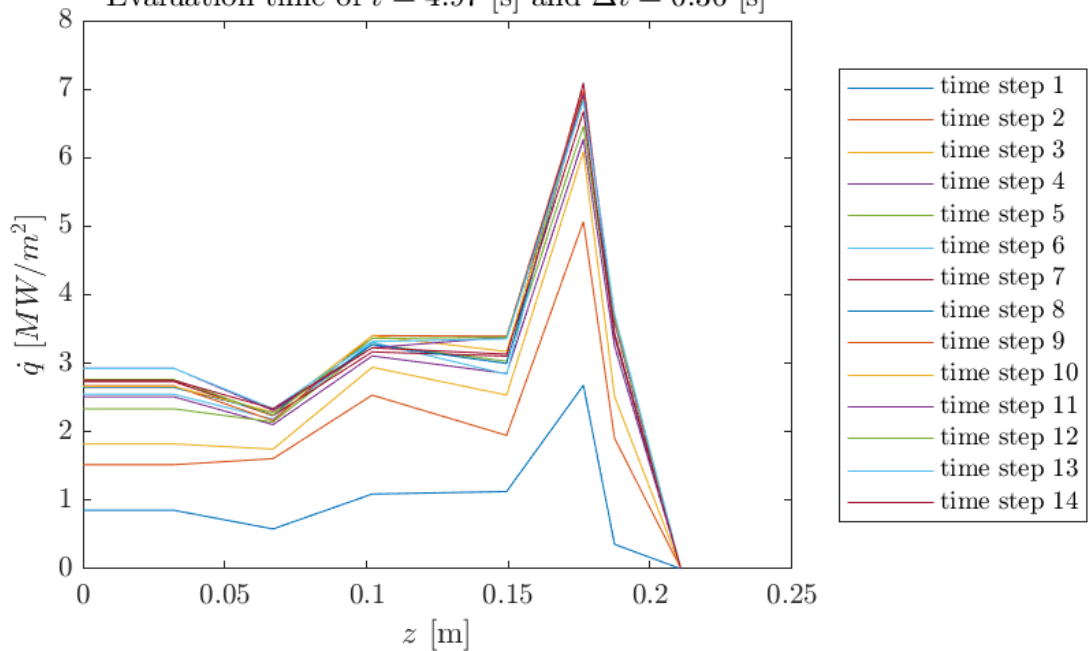


Figure B.14.: Run 14

Heat Flux of Ceramic Test $\overline{p_{CC}} = 12.02[\text{bar}]$ and $\overline{\dot{m}_{tot}} = 0.17[\text{kg/s}]$
 Evaluation time of $t = 3.23 [\text{s}]$ and $\Delta t = 0.23 [\text{s}]$

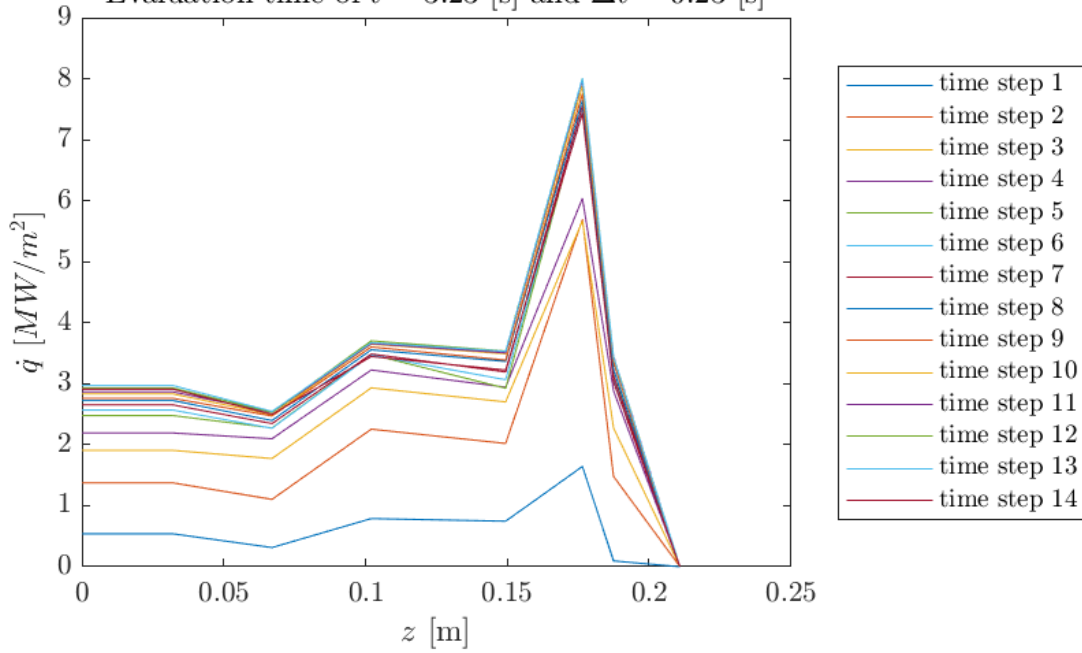


Figure B.15.: Run 15

Heat Flux of Ceramic Test $\overline{p_{CC}} = 12.00[\text{bar}]$ and $\overline{\dot{m}_{tot}} = 0.17[\text{kg/s}]$
 Evaluation time of $t = 4.33 [\text{s}]$ and $\Delta t = 0.31 [\text{s}]$

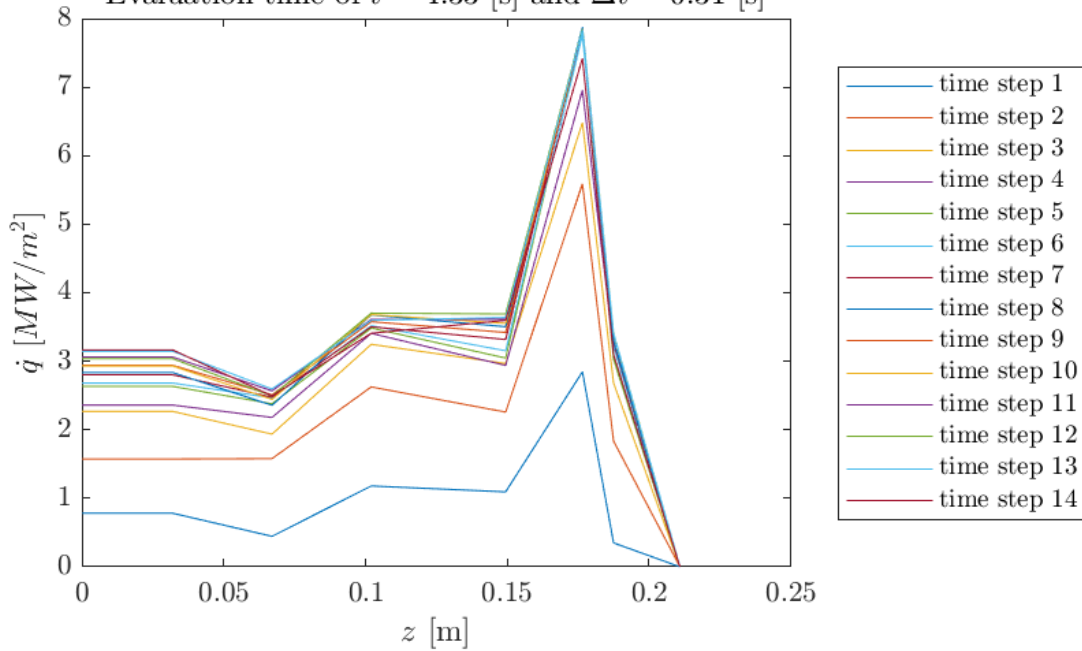


Figure B.16.: Run 16

Heat Flux of Ceramic Test $\overline{p_{CC}} = 12.18[\text{bar}]$ and $\overline{\dot{m}_{tot}} = 0.18[\text{kg/s}]$
 Evaluation time of $t = 3.23 [\text{s}]$ and $\Delta t = 0.23 [\text{s}]$

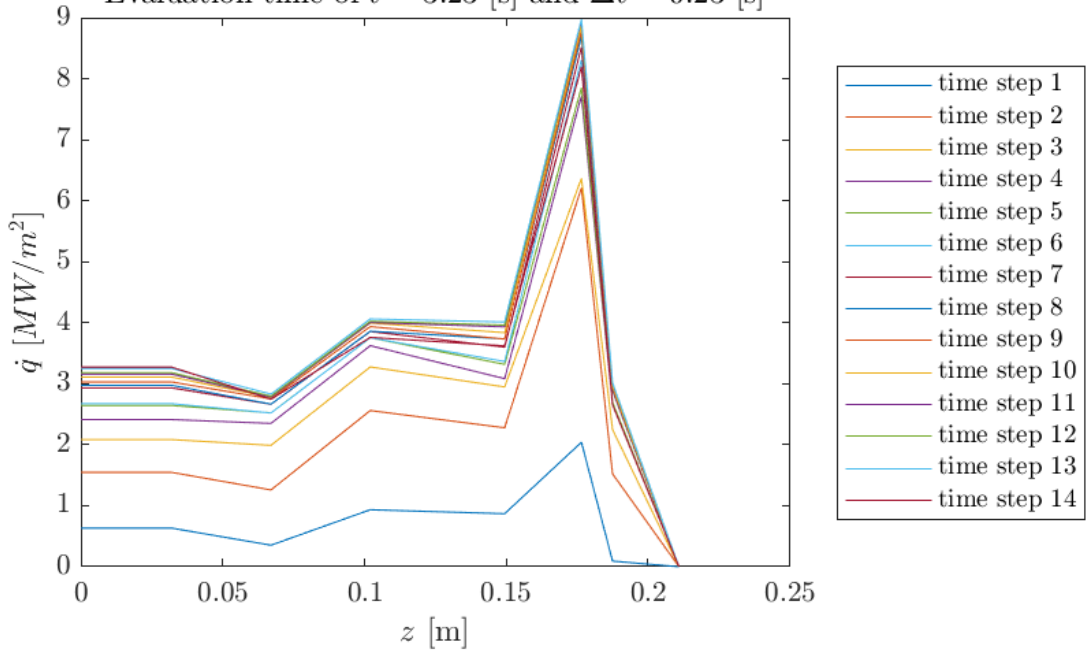


Figure B.17.: Run 17

Heat Flux of Ceramic Test $\overline{p_{CC}} = 12.20[\text{bar}]$ and $\overline{\dot{m}_{tot}} = 0.18[\text{kg/s}]$
 Evaluation time of $t = 3.67 [\text{s}]$ and $\Delta t = 0.26 [\text{s}]$

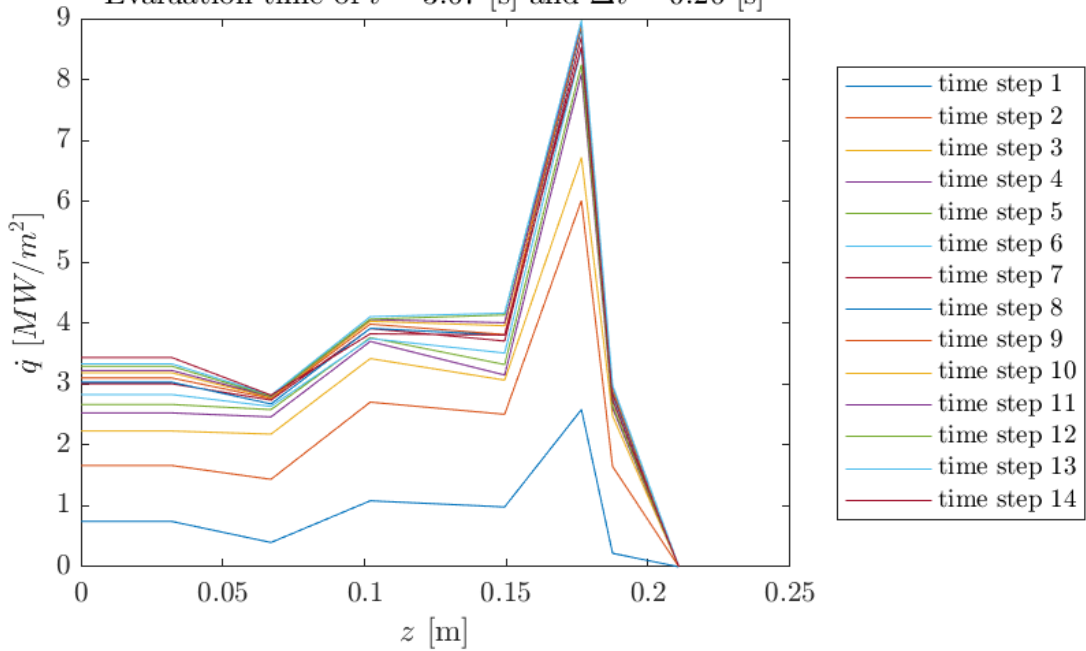


Figure B.18.: Run 18

Heat Flux of Ceramic Test $\overline{p_{CC}} = 15.04[\text{bar}]$ and $\overline{\dot{m}_{tot}} = 0.22[\text{kg/s}]$
 Evaluation time of $t = 3.26 [\text{s}]$ and $\Delta t = 0.23 [\text{s}]$

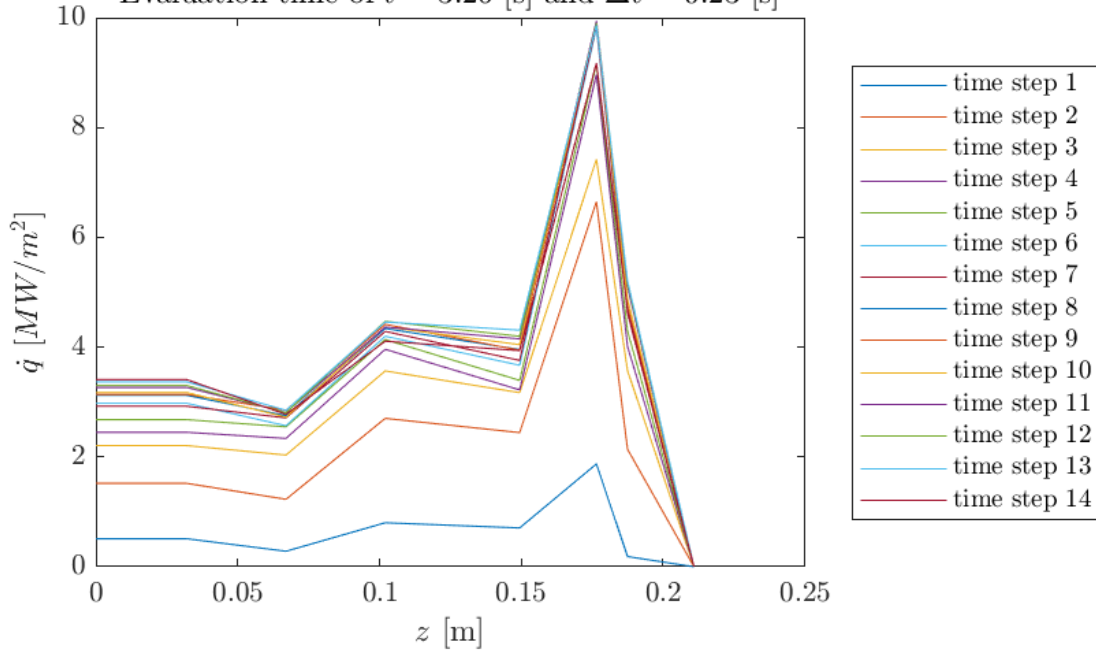


Figure B.19.: Run 19

Heat Flux of Ceramic Test $\overline{p_{CC}} = 14.83[\text{bar}]$ and $\overline{\dot{m}_{tot}} = 0.21[\text{kg/s}]$
 Evaluation time of $t = 3.34 [\text{s}]$ and $\Delta t = 0.24 [\text{s}]$

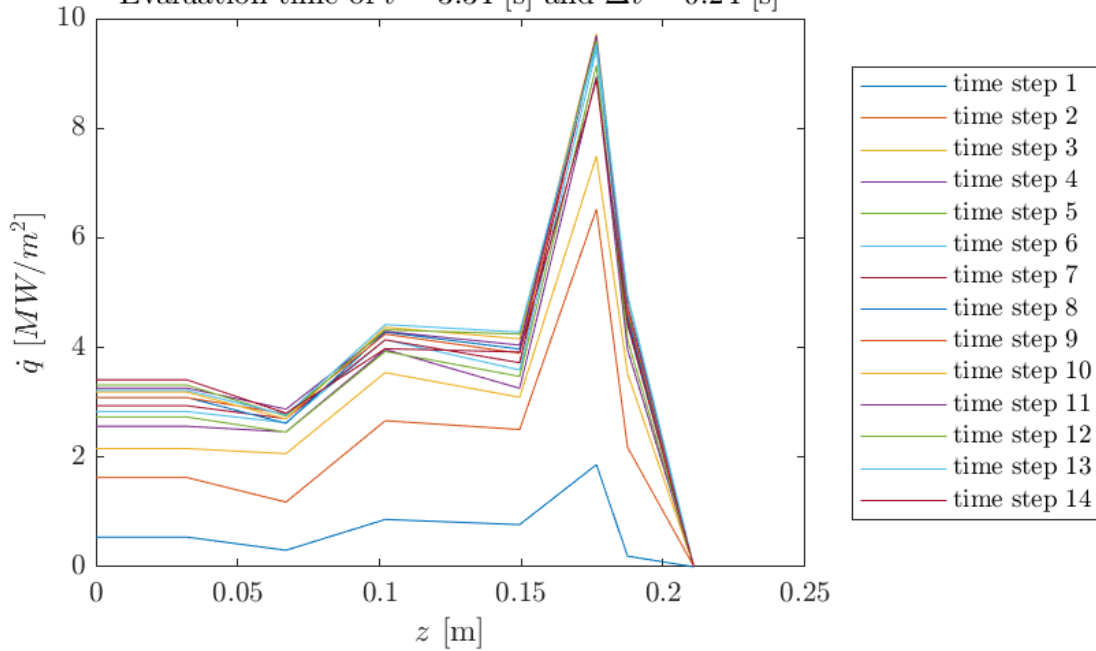


Figure B.20.: Run 20

C. Metallic Configuration IHCM evaluation

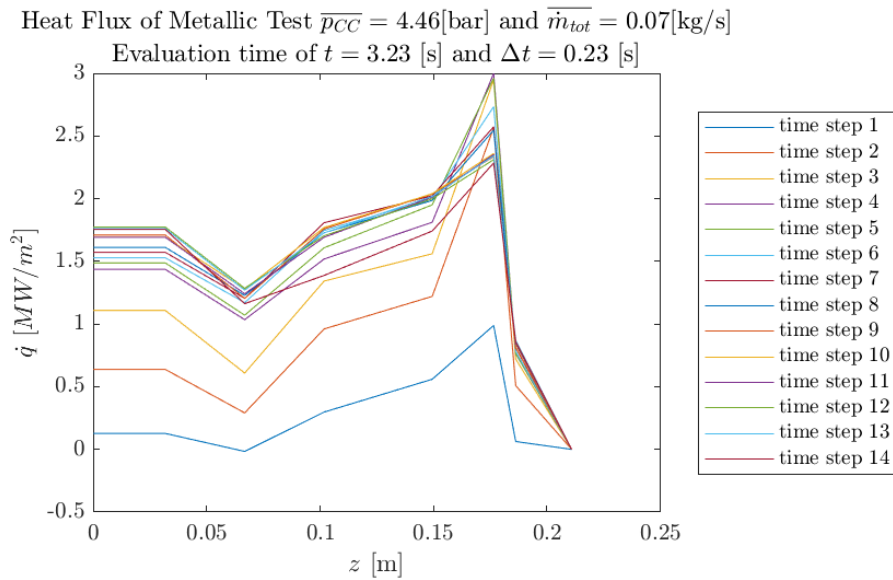


Figure C.1.: Run 1

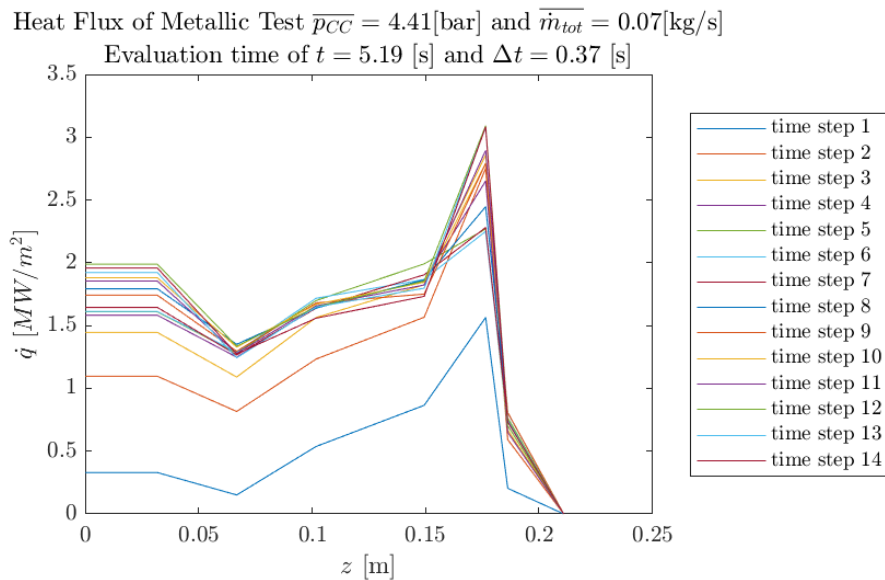


Figure C.2.: Run 2

Heat Flux of Metallic Test $\overline{p_{CC}} = 4.57[\text{bar}]$ and $\overline{\dot{m}_{tot}} = 0.07[\text{kg/s}]$
 Evaluation time of $t = 3.21 [\text{s}]$ and $\Delta t = 0.23 [\text{s}]$

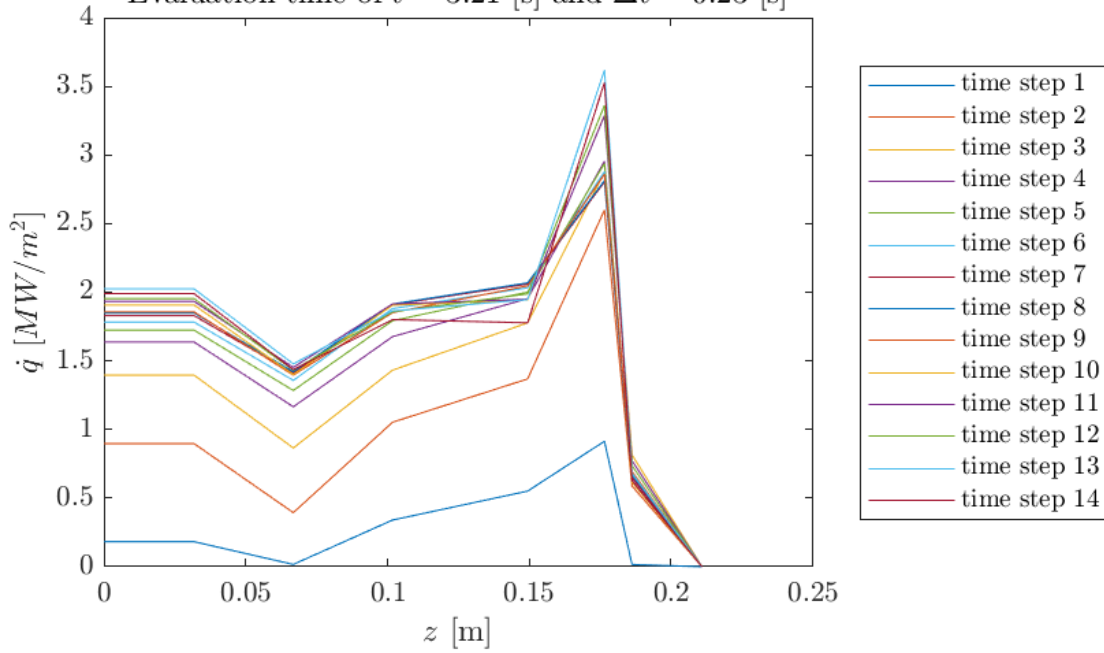


Figure C.3.: Run 3

Heat Flux of Metallic Test $\overline{p_{CC}} = 4.53[\text{bar}]$ and $\overline{\dot{m}_{tot}} = 0.07[\text{kg/s}]$
 Evaluation time of $t = 5.24 [\text{s}]$ and $\Delta t = 0.37 [\text{s}]$

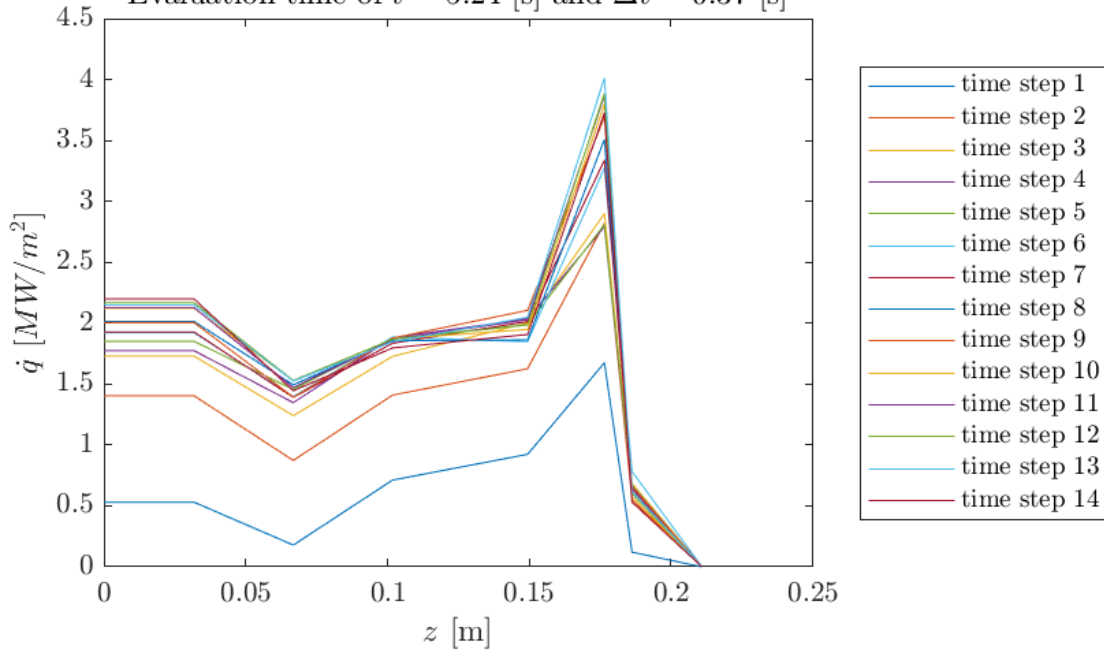


Figure C.4.: Run 4

Heat Flux of Metallic Test $\overline{p_{CC}} = 4.64[\text{bar}]$ and $\overline{\dot{m}_{tot}} = 0.07[\text{kg/s}]$
 Evaluation time of $t = 3.21 [\text{s}]$ and $\Delta t = 0.23 [\text{s}]$

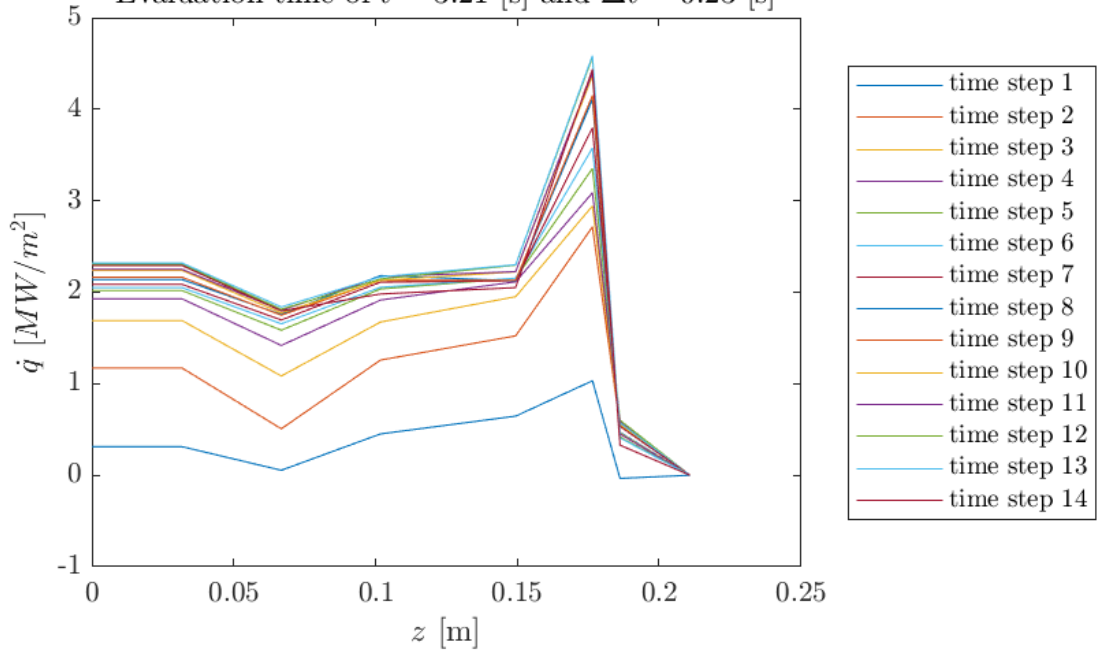


Figure C.5.: Run 5

Heat Flux of Metallic Test $\overline{p_{CC}} = 4.51[\text{bar}]$ and $\overline{\dot{m}_{tot}} = 0.07[\text{kg/s}]$
 Evaluation time of $t = 8.73 [\text{s}]$ and $\Delta t = 0.62 [\text{s}]$

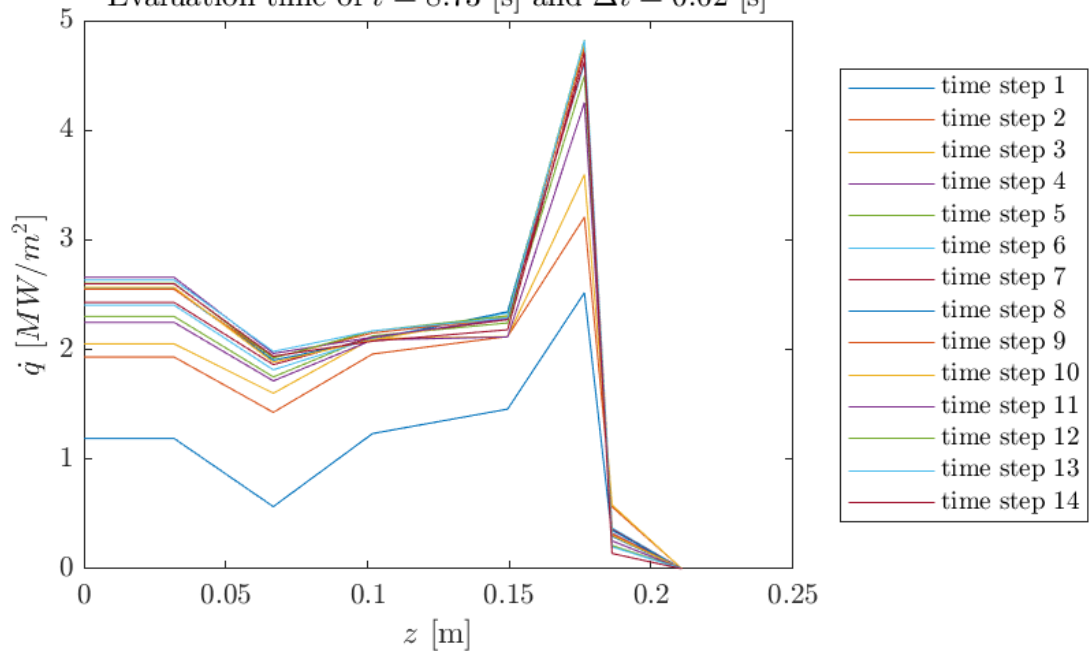


Figure C.6.: Run 6

Heat Flux of Metallic Test $\overline{p_{CC}} = 9.00[\text{bar}]$ and $\overline{\dot{m}_{tot}} = 0.13[\text{kg/s}]$
 Evaluation time of $t = 3.23 [\text{s}]$ and $\Delta t = 0.23 [\text{s}]$

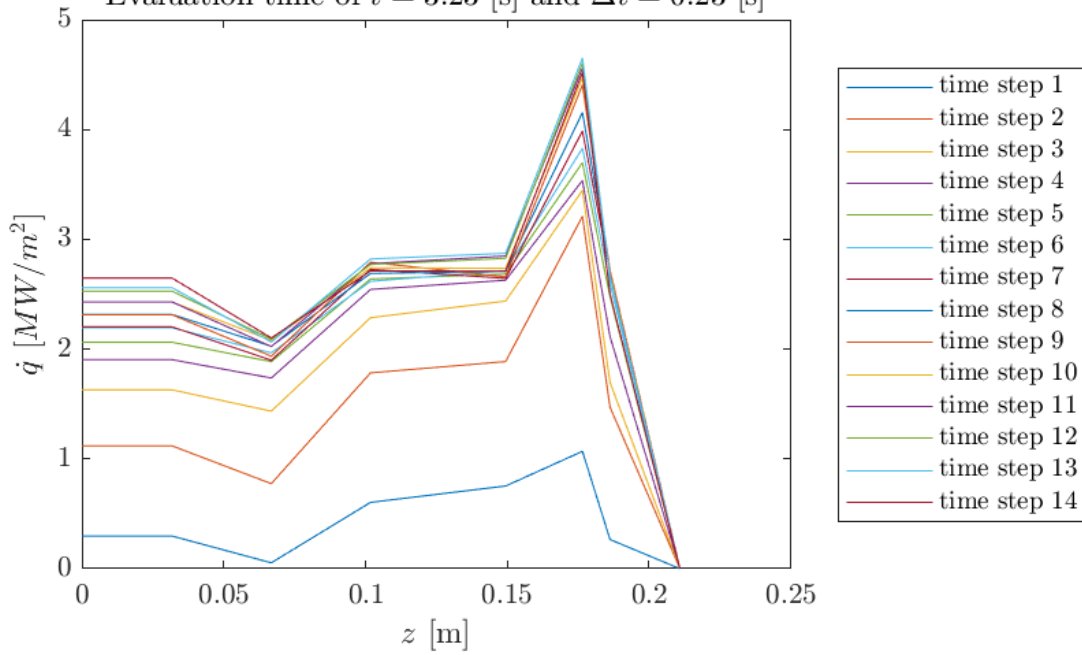


Figure C.7.: Run 7

Heat Flux of Metallic Test $\overline{p_{CC}} = 9.01[\text{bar}]$ and $\overline{\dot{m}_{tot}} = 0.13[\text{kg/s}]$
 Evaluation time of $t = 5.24 [\text{s}]$ and $\Delta t = 0.37 [\text{s}]$

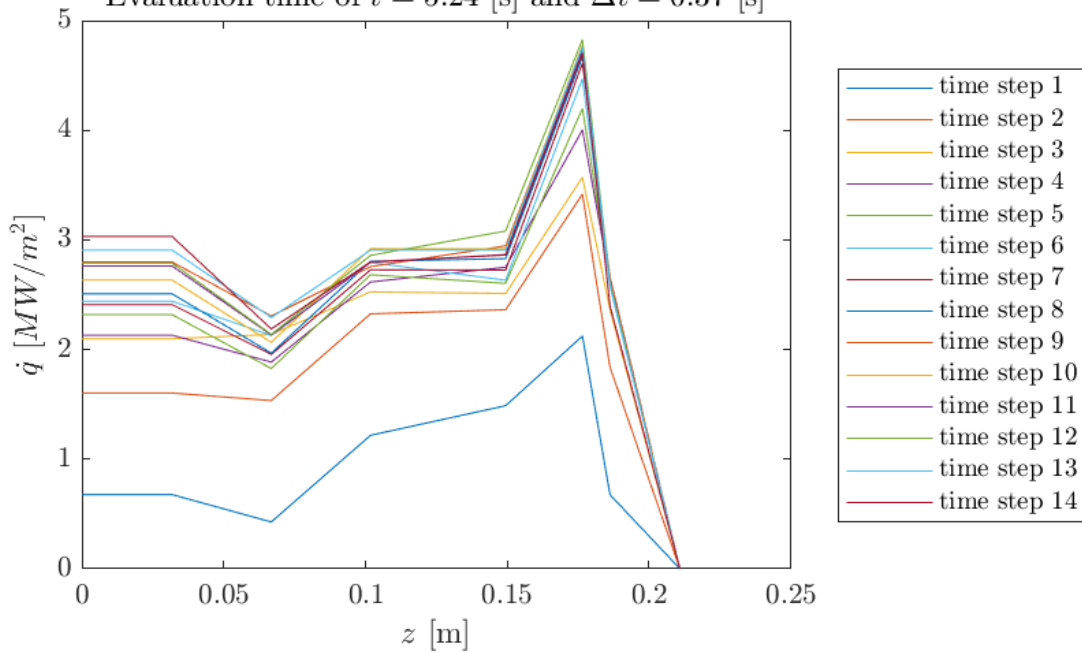


Figure C.8.: Run 8

Heat Flux of Metallic Test $\overline{p_{CC}} = 9.38[\text{bar}]$ and $\overline{\dot{m}_{tot}} = 0.14[\text{kg/s}]$
 Evaluation time of $t = 3.23 [\text{s}]$ and $\Delta t = 0.23 [\text{s}]$

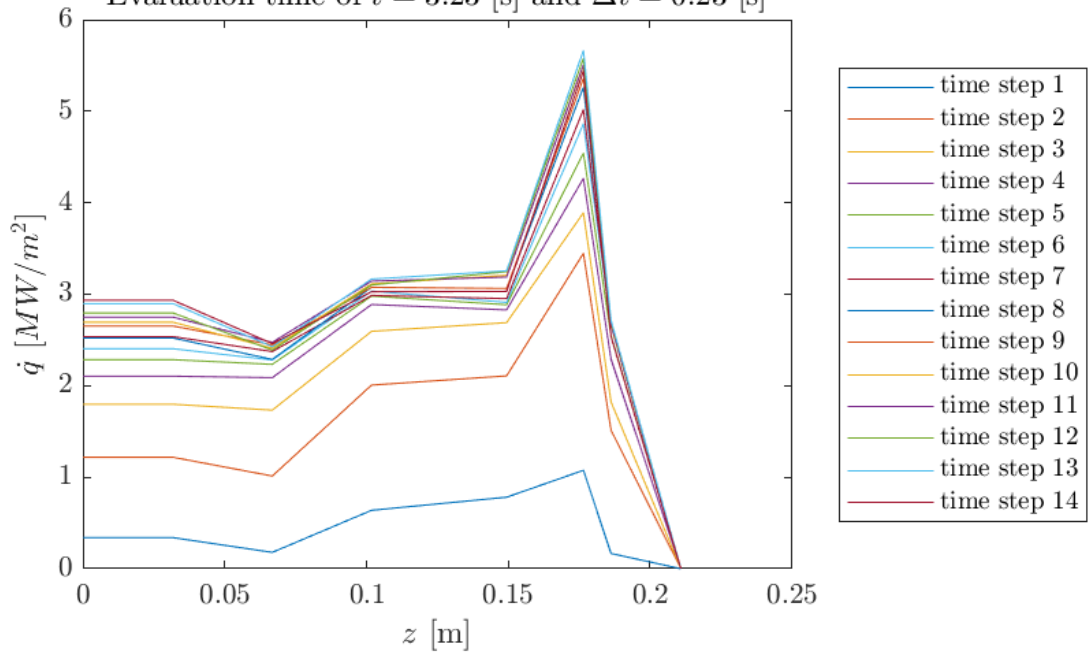


Figure C.9.: Run 9

Heat Flux of Metallic Test $\overline{p_{CC}} = 9.40[\text{bar}]$ and $\overline{\dot{m}_{tot}} = 0.14[\text{kg/s}]$
 Evaluation time of $t = 4.99 [\text{s}]$ and $\Delta t = 0.36 [\text{s}]$

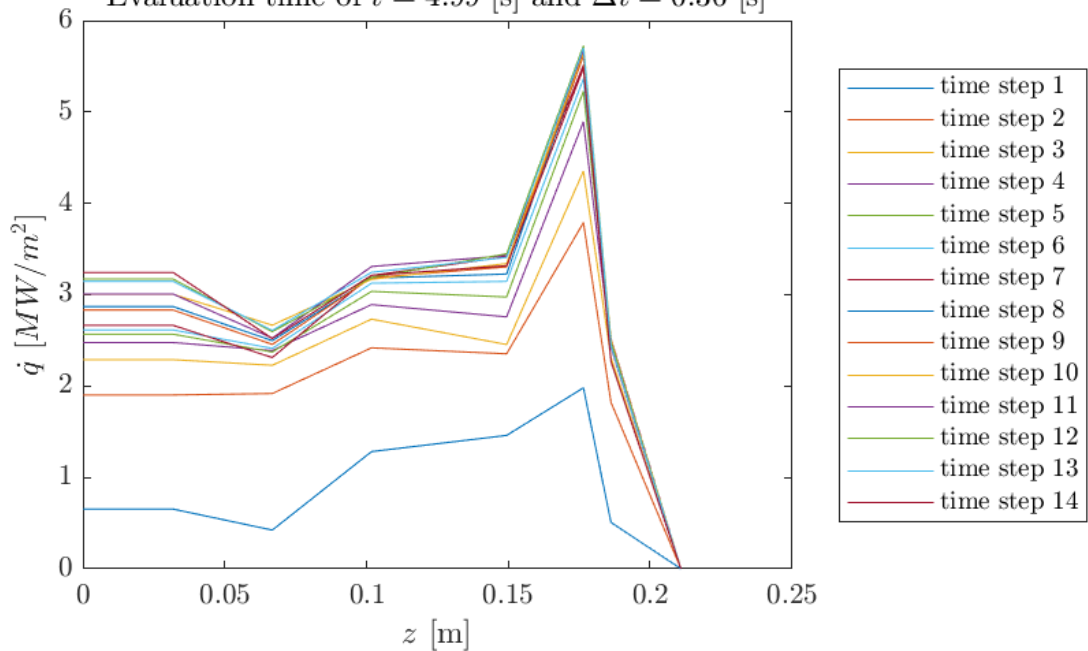


Figure C.10.: Run 10

Heat Flux of Metallic Test $\overline{p_{CC}} = 9.41[\text{bar}]$ and $\overline{\dot{m}_{tot}} = 0.14[\text{kg/s}]$
 Evaluation time of $t = 3.21 [\text{s}]$ and $\Delta t = 0.23 [\text{s}]$

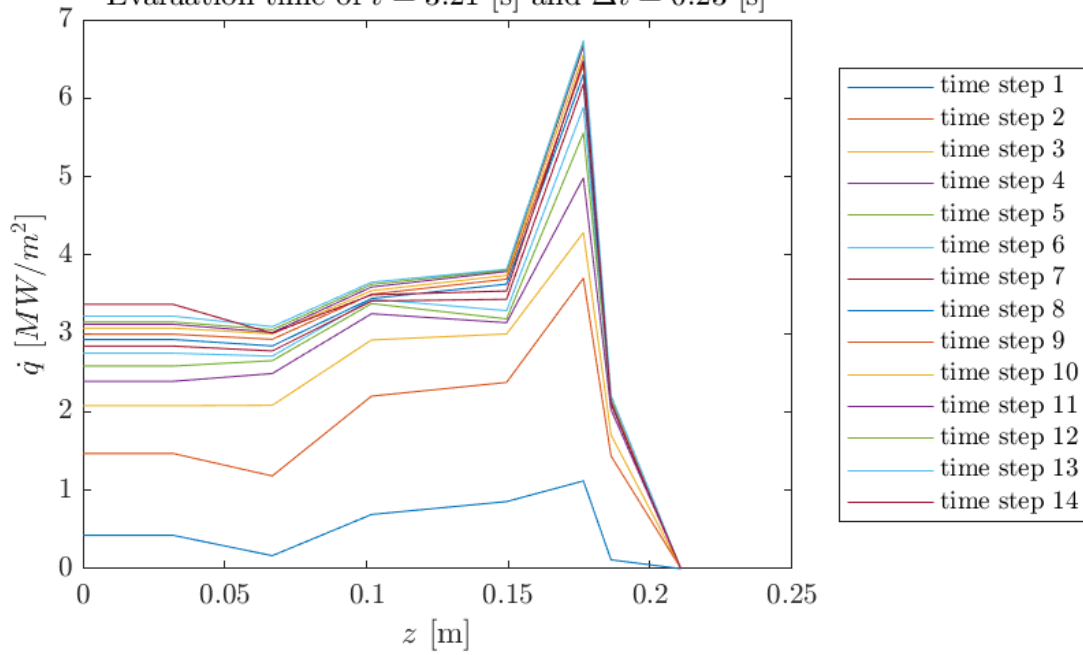


Figure C.11.: Run 11

Heat Flux of Metallic Test $\overline{p_{CC}} = 9.41[\text{bar}]$ and $\overline{\dot{m}_{tot}} = 0.14[\text{kg/s}]$
 Evaluation time of $t = 4.47 [\text{s}]$ and $\Delta t = 0.32 [\text{s}]$

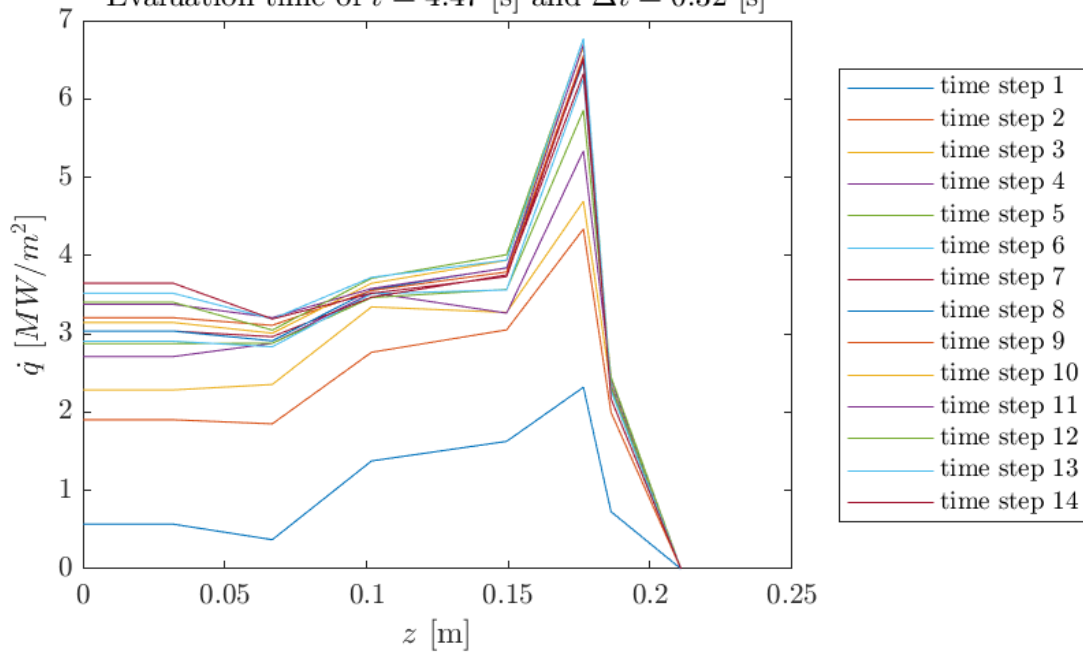


Figure C.12.: Run 12